Advanced Solid-State Dissimilar Material Joining and Additive Manufacturing for Enabling Multi-Material Lightweight Structures

by

Abdul Sayeed Khan

A dissertation submitted in partial fulfillment
of the requirements for the degree of
Doctor of Philosophy
(Naval Architecture and Marine Engineering)
in the University of Michigan
2024

Doctoral Committee:

Professor Pingsha Dong, Chair
Professor Zhan Chen
Professor Amit Misra
Professor Lei Zuo

Abdul Sayeed Khan

absk@umich.edu

ORCID iD: 0000-0002-8313-667X

© Abdul Sayeed Khan 2024

Dedication

Dedicated to the woman who brought me to this world and my family and friends who have been a constant source of motivation.

Acknowledgements

Ph.D. is a long voyage, and it always has high and low tides of time. My advisor, Professor Pingsha Dong has been the beacon of strong support, wisdom, immense knowledge, patience, and motivation to get me started on this journey and keep me on the right course since the first day of joining his research group. He has been a wonderful advisor and a great motivating mentor to me throughout this journey, and I can't imagine my Ph.D. degree and dissertation writing reaching this stage without his constant support. I would like to pay my sincere and deepest gratitude to Professor Pingsha Dong for all his support, motivation, advice, and mentorship, for sharing his encouraging and valuable experiences and curious and creative discussions, and for helping me steer the waves of this journey so far and beyond.

Secondly, I would like to thank Dr. Fengchao Liu with all my sincerity for introducing me to Professor Pingsha Dong's research. Dr. Liu introduced the concepts of solid-state advanced manufacturing to me and has been a source of constant support and motivation in dealing with the metallurgical aspects of this research work. His suggestions on thinking and applying my curiosity scientifically yet creatively have always made me think beyond common applications and expectations. I can't imagine the field of solid-state joining and additive manufacturing without him being my technical mentor, especially during the first half of my Ph.D. journey.

I would also like to express my sincere gratitude to my Ph.D. thesis committee members, Professor Lei Zuo, Professor Amit Misra, and Professor Zhan Chen, for their constant suggestions,

discussions, insightful comments, timely feedback, and encouragement in helping me realize the well-roundedness of this journey.

I would like to further express my sincere thanks to every staff member in the Michigan Center of Material Characterization (MC2) for their timely and constant support in every material characterization I performed during my research work. It would not have been possible without their insightful discussions on various material characterization techniques and upliftment for helping me learn various sophisticated material characterization techniques. Most specifically, I would like to thank Dr. Kai Sun for all his expertise, for his invaluable support on TEM analysis and data interpretation, and valuable insights.

Research work in the field of advanced manufacturing is impossible without the constant and consistent support from the machine shop staff and their contribution to resolving issues with engineering parts machining on time. I would like to express my sincere thanks to all the staff members at the Mechanical Engineering Machine Shops (Kent Pruss, Willam Kirkpatrick, Jonathon Yenkel, Charles Bradley, Michael Klein, and Jared Roy) and Machine Shop manager Donald Wirkner for enabling the due machining related support throughout the research work conducted during this dissertation.

I would also like to specially thank Professor Mihaela Banu for allowing me to use the Electrical Discharge Machine (EDM) for our timely needs of metallic material precision machining in-house at the University of Michigan, Ann Arbor. It has helped us tremendously in various aspects of our engineering part machining and new conceptual design developments.

To embark on such a voyage, it’s not possible to get to the shore smoothly without constant and timely support from the departmental staff and fellow colleagues. I would like to extend my sincere thanks to the Department of Naval Architecture and Marine Engineering for hosting me,

getting us all through the taxing pandemic era, and providing all the necessary support and feedback needed to navigate more productively. Specifically, I would like to thank Ms. Lisa Kisabeth for her “always there for students” way of helping, Ms. Nathalie Fiveland for her right and fast feedback for any academic question, Ms. Nicole Cheeseman for all her timely support on technical purchasing-related queries, and Mr. Chris Eckmeter for his ingenious support on anything related to IT systems.

I would also like to thank all of my previous and current colleagues, Dr. Xianjun Pei, Dr. Sandipp K Ravi, Dr. Shengjia Wu, Zetao Jin, and Yuning Zhang for their encouragement, curious discussions, and due support and comfort since the day I joined the research group. I would like to especially thank my colleagues Jiyuan Cheng (Josh) and Ben Houle for giving me the opportunity to be their mentor and work with them as a team to take various conceptual experimental designs from scratch to the final applications and trials in the laboratory for due successes.

Furthermore, I would like to sincerely thank the almighty for all ***His*** grace upon me and, finally, my parents and my family for their constant unconditional support, encouragement, and patience in helping me go through this journey for the past several years. I would like to especially thank my wife for her constant patience and support in helping me complete this journey through thick and thin. I would also like to extend my warm thanks to all my friends and colleagues at Michigan (Dr. Hoang N Minh, Dr. Avin Vijay, Dr. Mohammad Umar Farooq Khan, Dr. Rana Dabaja, Dr. Xhulija Biraku, Dr. Touheed Anwar Atif, and Aamir Sohail), and from India (Mr. Prakhar Gupta, Dr. Ananth S M, Mr. Ramaiah Chowdary, and Mr. Jeevraj Hejmadi) for their valuable suggestions, discussions, and helping me throughout this journey.

Table of Contents

Dedication ii

Acknowledgements iii

List of Tables x

List of Figures xi

Abstract xviii

Chapter 1 Introduction 1

1.1 Background 1

1.2 Advanced Manufacturing Processes 3

1.2.1 Dissimilar material direct joining 3

1.2.2 Solid-state additive manufacturing 5

1.3 Major Challenges 7

1.4 Objectives of the Current Research 8

1.5 Outline of the Dissertation 9

1.6 Brief Summary and Highlights of Major Contributions 11

References 13

Chapter 2 State of the Art Review and Research Needs 16

2.1 Introduction 16

2.2 Promising Direct Joining Techniques 21

2.2.1 Laser-assisted joining processes 22

2.2.2 Friction-based joining processes 25

2.2.3 Roles of chemical bonding 29

2.3 Direct Chemical Bonding Between Polymer and Metal 31
2.3.1 Role of functional groups 31
2.3.2 Thermomechanical conditions 33
2.3.3 Bonding and joint strength enhancement methods 38
2.4 Joint Design and Joint Property Evaluation Methods 42
2.4.1 Mesh-insensitive traction stress method 42
2.4.2 Joint strength property 44
2.4.3 Joint fatigue property 48
2.4.4 Optimum joint design 49
2.5 Unresolved Critical Issues for Industrial Applications 51
2.5.1 Dominant chemical bond formation mechanism 52
2.5.2 Joint property development 53
2.5.3 Quantitative joint design methods 53
2.6 Closure 54
References 56
Chapter 3 Direct Joining of Metal and Non-Polar Polypropylene Thermoplastic Composite 68
3.1 Introduction 68
3.2 Materials and Methods 71
3.3 Results 73
3.3.1 Bonding enabled by carbonyl group seeding 74
3.3.2 Joint strengths, failure modes, and key welding parameters 76
3.3.3 Interfacial microstructure characterization 77
3.3.4 Fracture surface analysis 82
3.4 Discussions 85
3.4.1 Bonding mechanisms 85

3.4.2 Process Characteristics 88
3.5 Conclusions 89
References 91
Chapter 4 Direct Spot Joining of Thin Gauge Aluminum Alloy to Stainless Steel 95
4.1 Introduction 95
4.2 Materials and Methods 98
4.3 Results 102
4.3.1 Al/Steel interfacial bond formation characteristics 102
4.3.2 Interface chemical composition and nanoscale structure 105
4.3.3 Joint strength and failure characteristics 107
4.4 Discussions 111
4.4.1 Suppression of IMCs 111
4.4.2 Corrosion effects 115
4.5 Conclusions 118
References 120
Chapter 5 Novel Solid-State Additive Friction Extrusion Deposition Method 125
5.1 Introduction 125
5.2 Materials and Methods 128
5.3 Results and Discussion 131
5.4 Conclusions 145
References 147
Chapter 6 Further Exploratory Study on Friction Extrusion-Based Solid-State Deposition of Dissimilar Material Systems 149
6.1 Background 149
6.2 Results and Implications 151
6.2.1 Stainless steel 316 deposition on carbon steel AISI1018 151

6.2.2 Aluminum alloy-6061 deposition on stainless steel 304 substrate 156
6.3 Summary 165
References 167
Chapter 7 Conclusions 169
7.1 Key Research Findings 169
7.2 Contributions to Existing Body of Knowledge and Broad Impacts 174
7.3 Future Work 175

List of Tables

Table 2.1: Test data and corresponding membrane and total traction structural stress values 48

Table 3.1: Mechanical and physical properties of AA6061-T6, 40GFRP-PP, and PA6 71

Table 3.2: Elemental composition of AA6061-T6 sheet (wt.%) 71

Table 3.3: Summary of welding trials to join AA6061 and GFRP-PP without PA6 thin film inter-layer and any special surface or material pre-treatment 74

Table 4.1: Chemical compositions of stainless steel 316 (wt%). 98

Table 4.2: Chemical compositions of AA6061-T6 alloy (wt%). 98

Table 4.3: Mechanical properties of base metals 99

List of Figures

Figure 1.1: Existing challenges and prospective solutions for automotive lightweighting [15] 2

Figure 1.2: (a) General schematic of laser powder bed fusion (LPBF) additive manufacturing [19] (GEPs = Gas-entrapped Pores, KHs = Key Holes), and (b) typical presence of defects in a simple cylindrical structure micro-CT image [18] (LOF = Lack of Fusion) 3

Figure 1.3: Challenges faced by traditional adhesive joining and fastening applications [22,23]. 4

Figure 1.4: Solid-state additive manufacturing schematics; (a) AFSD module commercialized by MELD Inc. [32], and (b) novel AFED process schematic invented by Liu et al. [31] 6

Figure 2.1: Structural lightweighting through a multi-material concept [13] 17

Figure 2.2: (a) A lightweight liftgate concept made of GFPP of passenger van [43], and (b) A lightweight truck cargo bed made of metal-polymer hybrid structure [gmauthority.com] 19

Figure 2.3: Schematic of localized heat and pressure conditions to join metal and polymer. 22

Figure 2.4: Variants of laser assisted joining, (a) conduction joining, (b) transmission joining. . 24

Figure 2.5: Nd:YAG vs diode laser (LD) joining method characteristics [23] 24

Figure 2.6: Effect of laser process parameters on joint load capacity [60] 25

Figure 2.7: (a) Fiat panda roof grill made of steel-PA composite using laser and induction joining [www.compositesworld.com], (b) Aircraft fuselage structure made of Al-PPS composite using friction spot joining [17,68] 26

Figure 2.8: Schematic of friction-based spot joining method 27

Figure 2.9: Spot joints made using FSpJ method, cross-section and process temperature characteristics [71] 28

Figure 2.10: Friction lap joining schematic for metal-polymer joining [17] 29

Figure 2.11: Temperature and cross-section characteristics under friction lap joining method [78] 30

Figure 2.12: (a) Non-polar polypropylene, (b)PA6 with carbonyl group, (c)chemical interaction at the joining interface of metal and polymer, (d) AA6061 and Nylon joining under FLW and

cross-section views [20], (e & f) XPS spectra confirming C-O-Al bonds at 0.8 nm and 3.2 nm depths respectively [78] 31

Figure 2.13: Chemical bond formation via MD simulation [96] 32

Figure 2.14: ToF-SIMS spectra near weld line for Al-PA joint and proposed model chemical reaction [100] 34

Figure 2.15: Hydrogen bond formation during Al-PA joining and IR spectra at Al-PA joint interface [97] 34

Figure 2.16: Schematic of functional group seeding methodology. 36

Figure 2.17: Al-GFPP joint formation using functional group seeding and substrate failure [21] 36

Figure 2.18: Bonding interface in Al-GFPP joints [21] 37

Figure 2.19: Metal surface pre-treatment methods: (a) laser texturing on the metal surface [22], (b) chemical etching method to generate micro mechanical anchoring effect [107] , (c) surface anodization in aluminum to provide honeycomb pores [108], (d) mechanism of silane coupling [109] 38

Figure 2.20: Polymer pre-treatment methods: (a) effect of plasma treatment on PP surface conditions [131], and (b) effect of MAH grafting on PP [132] 40

Figure 2.21: Existing testing schematics for dissimilar material joint property measurement [156] 41

Figure 2.22: Effect of mesh size on joint strength evaluation due to inherent singularities 41

Figure 2.23: Traction based mesh-insensitive structural stress and effect of mesh size on SCF [157,158] 42

Figure 2.24:Failure modes in a typical bi-material joint 43

Figure 2.25: Illustration of traction stress definition controlling failure Modes A versus B 44

Figure 2.26:Fillet formation in PA66/AA6061 joint [174] 45

Figure 2.27: Fillet feature approximations for FE modeling using mesh-insensitive structural stress method [174] 45

Figure 2.28:Traction stress-based joint shear strength results – (a) without considering the fillet features, and (b) after considering fillet features [174] 45

Figure 2.29: Analytical traction structural modeling of a lap-shear joint specimen between AA 6061 and PP (GFRP) 47

Figure 2.30:Membrane and bending interaction diagram for determining static strength and applications in interpreting AA 6061/PP (GFRP) joint test data 48

Figure 2.31:Traction structural stress modeling of fatigue in dissimilar material joints [156] 49

Figure 2.32:Effect of joining length on mode-I and mode-II stress intensity factor K (a fracture mechanics parameter) 50

Figure 2.33: Validation of Mode A failure - aluminum to steel welded lap shear tests 50

Figure 2.34: Failure Mode A versus Mode B in various joint types in which Mode A offers the best static and fatigue load capacity and should be ensured through optimum joint sizing 51

Figure 3.1:Chemical structure of (a) Polypropylene (PP) without any functional group, (b) nylon-6 (PA6) containing carbonyl functional group 72

Figure 3.2: (a) Schematic of a friction spot joining method, (b) non-consumable steel tool, (c) forge force and depth variation during the main phase of friction assisted joining process, (d) non-joinable AA6061 and GFRP-PP by conventional method 72

Figure 3.3: (a) Schematic of friction spot joining method using thin film insert, (b) detailed view of material placement during joining, (c) 50 µm thick PA6 insert film, (d) top view of the AA6061/GFRP-PP joint produced using thin PA6 film [1800 RPM, 12-sec and, (f) bottom view and base material failure of the joint produced after the lap shear tensile test 74

Figure 3.4: (a) Lap shear tensile test schematic, (b) & (c) major dimensions of the specimen used, (d) summary of the peak loads at failure during lap shear tensile test 75

Figure 3.5: (a-i) Failure patterns after lap shear tensile test of AA6061/GFRP-PP joints produced using PA6 thin film inter-layer [1800 RPM, various forge depth and spot weld time], (j) comparison of the bonding region lengths measured as the outer diameters of the bonding region lengths measured as the outer diameters of the melting zone (MZ). 76

Figure 3.6: Cross-sectional SEM images of AA6061/GFRP-PP joint [1800 rpm, 12-sec and 0.10 mm], (a) low magnification SEM micrograph with visible cavities, (b) high magnification SEM micrograph depicting bonding interface and PA6-fibers-PP network 78

Figure 3.7: SEM images of bonding interfaces in AA6061/GFRP-PP joint [1800 rpm, 0.10 mm and 12 sec], (a-c) Al-PA6 interface, (d-f) PA6-fiber interface 79

Figure 3.8: SEM images showing possible PA6-PP interface in AA6061/GFRP-PP joint [1800 rpm, 12-sec and 0.10 mm] 79

Figure 3.9: Interfacial temperature measurement, (a-b) schematic of thermocouple (TC) placement, (c) temperature measurements for AA6061/GFRP-PP joint [1800 rpm, 12 sec, 0.10 mm] and, (d) ratios of MZ to DZ for various process parameters. 80

Figure 3.10: Failure features of the produced joints [1800 rpm, 0.10 mm] at, (a) 3-sec spot weld time, (b) 6-sec spot weld time, (c) SEM micrograph of R1 on aluminum side, (d) SEM micrograph of R2 on aluminum side 82

Figure 3.11: Resolidified PA6 near fracture origin in the joint [1800 rpm, 0.10 mm and 12 sec], (a) global view, (b) local view of PA6+PP reconsolidation near through crack fracture region, (c) SEM micrograph of crack front location and ridges, (d) ridges pattern on the aluminum side 84

Figure 3.12: (a) Schematic representation of multi-material composite network formation at the cross-section of AA6061/GFRP-PP joint (T = 12-sec), (b) schematic representation of the fully developed bonding regions for a 12-sec spot-welded joint 88

Figure 4.1: Friction spot joining process schematic: (a) tool placement with respect to the aluminum and steel sheets, and (b) critical dimensions of the friction stir tool 99

Figure 4.2: Joining process temperature measurements, (a) thermocouple placement schematic, and (b) temperature profile 100

Figure 4.3: Al/Steel joints: (a) & (b) before the corrosion cycle, front and back sides of the sample, respectively, and (c) & (d) post-corrosion cycle, front and back sides of the sample, respectively. 101

Figure 4.4: Lap shear tensile experimental schematic, (a) & (b) sample dimensions and shims/tab placement, (c) experimental setup with Al/Steel joint sample 102

Figure 4.5: Cross-sectional SEM images of Al/Steel joint nugget shoulder, (a) before corrosion cycles; (b) after corrosion cycles; (c) high resolution detailed view from (a); (d) high resolution detailed view (b); and (e) high resolution detailed view near the not..... 103

Figure 4.6: Cross-sectional SEM micrographs at the nugget center of Al/Steel joints, (a) & (b) low resolution images before corrosion cycles, and (c) & (d) high resolution images after corrosion cycles 104

Figure 4.7: High-resolution cross-sectional STEM images of the Al/Steel joints at the nugget center, (a) (c) & (e) high-angle annular dark field (HAADF) images, and (b) (d) & (f) bright-field images, (c) and (d) showing the high-magnification images near the red arrows marked in (a). 105

Figure 4.8: STEM HAADF image at the nugget center cross-section of the Al/Steel joint and EDS elemental maps 106

Figure 4.9: Al/Steel joint load capacity during lap shear tensile loading before and after corrosion conditions: S1-S3 represent the samples before corrosion cycles, and C1-C3 represent the samples after corrosion cycles..... 108

Figure 4.10: Failure features after lap shear tensile experiments, (a) & (b) global and local views before corrosion, and (c) & (d) global and local views after corrosion..... 109

Figure 4.11: SEM micrographs at locations (i) and (ii) near the aluminum nugget shown in Figure 4.10, respectively. 110

Figure 4.12: Fracture morphologies around the button failure at the nugget boundary, (a) global views, (b) schematic of nugget, (c) failure locations and failure paths during lap shear tensile experiments, (i-iv) detailed views of the locations i-iv shown in (a)..... 110

Figure 4.13: (a) EDS line analysis location across Al/Steel interface, and (b) elemental distribution across Al/Steel joint interface..... 113

Figure 4.14: Schematic representation of the amorphous phase formation at the aluminum to steel joining interface produced via friction stir spot joining: (a) pre-melting layer formation due to intense friction induced high shear strain rate above the steel faying surface, and (b) amorphous phase formation as a graded reaction zone (or reaction layer) due to rapid quenching effect. 114

Figure 4.15: Schematic illustration of corrosion resistance via amorphous reaction zone at the aluminum/steel joining interface achieved via NSSLIA: (a) schematic representing spot joining configuration, (b) representation of corrosive media electrolytic ions penetration through grain boundaries of crystalline grain boundaries in IMCs, and (c) barrier effect to prevent the penetration of corrosive media electrolytic ions via the amorphous phase reaction zone..... 117

Figure 5.1: Principle of AFED (or SoftTouch deposition). 127

Figure 5.2: Schematic diagram showing the location of the end of the thermocouple during the deposition of the second layer..... 130

Figure 5.3: AFED: (a) prototype machine, (b) 6061 aluminum alloy feedstock within the system. A snapshot of AFED (c) before and (d) during printing..... 132

Figure 5.4: Photographs of deposited aluminum alloy in the shape of spot (a), linear (b), curvilinear linear (c), and multiple layers (d). (e) Cross-sectional observation of the deposited metal and (f) a zoom-in view of the deposited metal..... 133

Figure 5.5: Thermal history of the metal in the middle of the first deposited layer during the second layer deposition. 134

Figure 5.6: Grain structure of (a) 6061aluminum alloy substrate, (b) at the interface between the deposited layer and substrate, at the center of the first printed layer (c) after the first layer of printing, and (d) after 10 layers of printing..... 135

Figure 5.7: Distribution of grain boundary and texture at the center of the first printed layer (a) after the first layer of printing, and (b) after 10 layers of printing (TRD: tool rotation direction; DPN: die plane normal). 136

Figure 5.8: Tensile deformation behavior of the as-deposited dense aluminum alloys: (a) schematic showing the locations and dimensions of the tensile test specimens, (b) ultimate tensile strength of each deposited layer in X and Y directions, (c) a comparison of the stress-

strain curves in X, Y, and Z directions, and (d) typical fractography of the failed tensile specimen tested in the Z direction. 137

Figure 5.9: Hardness map for the cross-section of the as-deposited sample and the adjacent substrate. 138

Figure 5.10: TEM micrographs of the tenth layer of the as-deposited sample at (a) low and (b) high magnification; TEM micrographs of the first layer of the as-deposited sample at (c) low and (d) high magnification. 140

Figure 5.11: Microstructure and element distribution of the first layer of the as-deposited sample. 140

Figure 5.12: Hardness map for the cross-section of the deposited sample and the adjacent substrate after T6 heat treatment. 141

Figure 5.13: Tensile deformation behavior of the deposited alloy and the nearby BM (wrought aluminum alloy) after T6 heat treatment: (a) ultimate tensile strength of each deposited layer in X and Y directions, (b) a comparison of the tensile deformation behavior of the nearby BM and the deposited alloy in X, Y, and Z directions. 142

Figure 5.14: TEM micrographs of the (a) BM and (b) the first layer of the deposited sample after T6 heat treatment. 143

Figure 5.15: Effect of printing layer thickness on the printing process and bonding quality: (a) compression pressure applied on the substrate during AFED, and (b) compression pressure as a function of printing layer thickness. Photographs of as-deposited aluminum alloy with a deposition layer thickness of 1.5 mm (c) and 3 mm (d), respectively. Cross-section of as-deposited aluminum alloy with a layer thickness of 1.5 mm (e) and 3 mm (f), respectively. 143

Figure 6.1:(a) Schematic of the AFED (SoftTouch AM^{TM}) process, (b) bow-tie extrusion profile, (c) off-the-shelf round feedstock of aluminum alloy 6061 (AA6061) and stainless steel 316 (SS316), (d) anti-locking feature on the top end of feedstocks 150

Figure 6.2: (a) SS316 deposition on AISI1018, (b) cross-sectional SEM image showing a global view of deposition, (c) detailed features of flash overhang indicated in (b), (d) higher magnification image showing banded structure between SS316 deposition and AISI1018 substrate, (e) higher magnification image showing inter-penetration of SS316 deposited layer with AISI1018 substrate top surface indicated in (d) 151

Figure 6.3: (a) EBSD scanning locations in the SS316 deposited layer and top of the AISI1018 substrate, (b) EBSD IPF maps for SS316 base material, (c) inverse pole figure (IPF) maps at the location shown for the SS316 deposited layer, (d) IPF maps at the top of the AISI1018 layer adjacent to the SS316 deposited layer, (e) IPF triangle 153

Figure 6.4: (a) Texture plot for the IPF maps shown in Figure 6.3(c), (b) texture plot for the IPF maps shown in Figure 6.3(d), (c) grain size distribution w.r.t. area fraction for the IPF

maps shown in Figure 6.3(c), (d) grain size distribution w.r.t. area fraction for the IPF maps shown in Figure 6.3(d) 154

Figure 6.5: Illustration of three-point bending test; (a) testing setup before the loading begins, (b) sample under 5kN loading condition, and (c) optical image showing bonding and delamination between SS316 deposited layer and AISI1018 substrate. 155

Figure 6.6: (a) Top view of multi-layer 6061 aluminum deposition on SS304 substrate, (b) front of view of multi-layer 6061 aluminum deposition on SS304 substrate. 156

Figure 6.7: Cross-sectional SEM images of multi-layer 6061 aluminum alloy deposition on SS304 substrate; (a) multi-layer deposited sample cross-section with marked layers 1-5 and locations (i) and (ii) for EBSD scanning, (b) intimately bonded AA6061/SS304 interface, (c) higher magnification image showing tightly bonded interface, dispersion of white Mg_2Si precipitates, and surface unevenness of SS304, (d) inter-layer bonding features near the overhang shown in (a), and (e) nanoscale interfacial reaction zone indicated in (c) with location (iii) marked for TEM sample analysis 157

Figure 6.8: EBSD IPF (a) AA6061 base material, (b) IPF triangle, (c) IPF maps showing grain refinement at location (i) in L5 shown in Figure 6.7(a), (d) IPF maps showing grain refinement at location (ii) in L1 shown in Figure 6.7(a) 159

Figure 6.9: (a) Texture plots for IPF maps in 6.8(c), (b) texture plots for IPF maps in 6.8(d), (c) grain size distribution and area fraction for IPF maps in 6.8(c), and (d) rain size distribution and area fraction for IPF maps in 6.8(d) 159

Figure 6.10: (a) dotted lines showing the location for mini-tensile sample machining, (b) configuration of the mini-tensile sample extraction, (c) dimensions for the mini-tensile samples, (d) physical sample after EDM machining and surface cleaning, and (e) stress-strain curves obtained after tensile testing 161

Figure 6.11: Post-tensile failure features of mini-tensile samples: (a) and (b) SEM images showing global failure features, (c) local ductile failure features indicated in (a), (d), ductile and shear failure features indicated at aluminum side in (b), and (e) residual 6061 aluminum alloy on SS304 indicated in (b) 162

Figure 6.12: (a) TEM dark field image taken at the location (iii) shown in Figure 6.7(e), showing the interface between aluminum alloy 6061 and SS304 with small grains, reaction zone, and distorted crystals on SS304 side, and (b) detailed view of reaction zone indicated in (a) 163

Figure 6.13: Elemental distribution across the reaction zone developed between aluminum 6061 ally and SS304 during AFED 164

Abstract

Multi-material lightweight structures by "using the right material at the right place" have become increasingly important for ensuring environmental sustainability. Conventional mechanical fastening and/or adhesive bonding processes can be inefficient, unreliable, and time-consuming, therefore unable to take full advantage of multi-material structures and emerging advanced manufacturing processes, such as additive manufacturing (AM). Due to material incompatibility between some of the dissimilar material combinations, e.g., between aluminum alloy and steel or between polymer composite and metal, there have been major challenges in achieving direct welding or joining. For instance, fusion-based dissimilar metal joining or AM, e.g., between aluminum alloy and steel, introduces brittle intermetallic compounds (IMCs) between the aluminum-steel interface, which can cause severe cracking and galvanic corrosion or stress corrosion cracking. However, there have been some promising developments over the recent years. Some solid-state dissimilar material joining and AM processes, e.g., friction-based processes for producing direct bonding between dissimilar metals, e.g., between aluminum alloy and steel and between polar polymer (PA66) and aluminum, and friction-based solid-state additive manufacturing (additive friction stir deposition or AFSD). However, the direct joining between non-polar polymer (such as polypropylene or PP) and metal and suppression of IMCs for improving corrosion resistance in bimetallic joints is still not achieved. The solid-state additive manufacturing method available to date (e.g., AFSD) imparts severe compression force and overheats the substrate, making the process challenging for relatively thin substrates and

safety-critical applications.

In this research, solid-state friction-based dissimilar material direct joining and additive manufacturing methods are investigated. Using the friction-based solid-state method, it first achieved a novel metal to hard-to-weld polypropylene (PP) composite direct joining using a functionally active interface modulator insert layer under localized temperature and pressure conditions. Utilizing carbon-oxygen-aluminum (C-O-Al) type covalent bonding between aluminum alloy and polypropylene composite, it eliminated fasteners and adhesives for a robust joint stronger than the base composite material. Subsequently, it utilized previously discovered, nanoscale shear localization-induced amorphization (NSLIAA) to join thin gauge aluminum to steel materials directly under controlled friction spot joining configuration for the suppression of IMCs and increased corrosion resistance.

It has then demonstrated a novel friction-based solid-state metal additive manufacturing method to enable melt-less dissimilar material additive manufacturing of metals and alloys directly at a large scale without solidification defects and minimal substrate compression force-induced instabilities. It was termed SoftTouch AM^{TM} due to its low temperature and low compression force features and defined as an additive friction extrusion deposition (AFED) process due to its friction-based extrusion and additive processing features. SoftTouch AM^{TM} utilizes super-plasticity to soften the feedstock in two steps, eliminating the need for direct contact between substrate and feedstock and providing grain refinement and severe cold working (severe plastic deformation) below the melting temperatures of metallic materials. It avoids using pricy powders and is fully capable of utilizing off-the-shelf metallic bars as feedstock. It has proven crucial for future demands of large-area additive manufacturing, energy sectors, and sustainability.

With the above accomplishments, the following describes the major intellectual merits and broad engineering impacts of this research:

- It proposed a new carbon-oxygen-metal or C-O-M type covalent bond formation mechanism between non-polar polypropylene composite and metals through an intermediary functional layer.

- Discovered a mechanistic description that if the amorphous phase is present at the Al/Steel joining interface, then the electrolytic ions from the corrosive media are not able to penetrate the amorphous phase, which occurs through the grain boundaries in crystalline intermetallic compounds.

- Developed novel SoftTouch AM^{TM} process concepts and laboratory implementation for consistent solid-state deposition of aluminum to aluminum, aluminum to stainless steel, carbon steel to carbon steel, and stainless steel to carbon steel, which potentially offers rapid large-area solid-state additive manufacturing of similar and dissimilar material systems.

- Introduced a novel modular multi-material insert die design and rotational stability requirements in the SoftTouch AM^{TM} system for achieving consistent solid-state deposition of aluminum to aluminum, aluminum to stainless steel, and stainless steel to carbon steel.

The dissimilar material direct joining discovered during this research provides process development platforms for automotive lightweighting. It is intended to support the Department

of Energy's (DOE) multi-material lightweight vehicle (MMLV) initiatives in the coming years. It will further enable using metal to hard-to-weld polymer dissimilar and aluminum to steel-type bi-metallic pairs in severe and harsh environmental conditions without significantly losing structural strength. The research work was supported by the National Science Foundation (NSF – CMMI – 2126163) and the Electric Power Research Institute (EPRI) and is intended for multi-material structural lightweighting and rapid, defect-free, large-area solid-state additive manufacturing for diverse industrial applications, including light water reactor (LWR) and energy sectors for sustainability.

Chapter 1 Introduction

1.1 Background

The global share of transport sector greenhouse gas (GHG) emissions was 8.5Gt CO_2 eq which amounted to around 14% of all emissions in the year 2018 [1]. Road transport, international shipping, and international aviation amounted to 73%, 8%, and 7%, respectively of the total sector emissions [1], out of which the bulk is during the use phase of the transport vehicles [2]. Such growth in GHGs and future sustainability have demanded to rethink the transportation vehicular designs and significantly reduce greenhouse gases in the recent decade [2-6]. Studies have shown that up to 50% of the fuel consumption can be due to the mass of the vehicle [2,7], and lightweighting strategies are thus highly sought-after [7,8]. A multi-material approach to achieve demand-based structural lightweighting has been gaining ample attention in recent years [3,9-12]. Aerospace manufacturers have significantly adopted the use of lightweight metals in combination with fiber-reinforced composites to reduce the weight and achieve this goal [13]. Shipbuilding industries have been adopting modular and multi-material structures to achieve weight reduction and, therefore, fuel economy [14]. Auto manufacturers have been aggressively pursuing structural lightweighting to achieve increasingly stringent fuel economy requirements by regulators, in addition to vehicle electrification, manufacturing cost, and recyclability [9] through utilizing advanced structural designs, lightweight alloys such as magnesium and aluminum alloys, high-strength steel, and fiber-reinforced composites in conjunction with advanced materials as shown in Figure 1.1 [15].

The advent of fusion-based additive manufacturing (AM) of metallic materials has provided major breakthroughs in the manufacturing of near-net-shape metallic components for

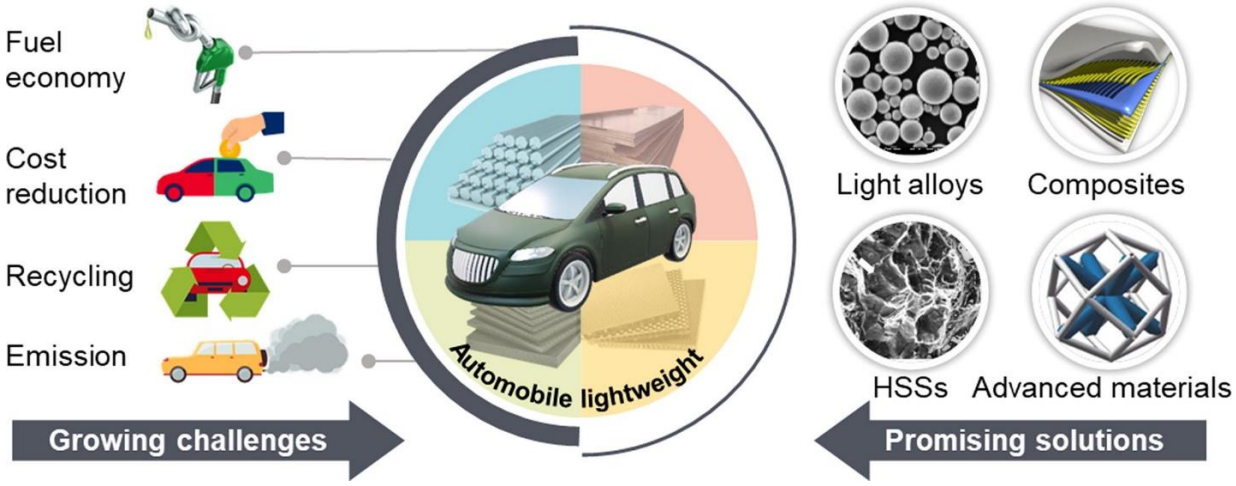


Figure 1.1: Existing challenges and prospective solutions for automotive lightweighting [15]

both structural and non-structural applications [16] aimed at future sustainability through effective usage of materials, energy, and optimal structural design through topology optimization [17]. However, metallic AM processes today are not suited for large-volume build and mass-produced transportation systems [18]. Another major limitation for broadly deploying fusion-based metal AM technology is its inherent solidification-induced defects, such as gas-entrapped pores (GEPs), keyholes (KHs), and lack of fusion (LOF), as illustrated in Figure 1.2, for the laser powder bed fusion (LPBF) process. It further faces complications and downside of expensive powders and feedstock availability, restrictions to reuse the materials, part size limitations, and explosive natures for easily volatile metallic materials have made it challenging for large-area additive manufacturing [16,19]. Inspired by such limitations, researchers and industries sided towards fusion-less additive manufacturing for specific applications to build circular economies and sustainable ecosystems [20]. Such future sustainability-driven initiatives have culminated in solid-state additive manufacturing processes in recent years and have been dominating large-area

additive manufacturing applications such as joint-less hulls, large rocket engines, and on-demand repair capabilities [21].

1.2 Advanced Manufacturing Processes

1.2.1 Dissimilar material direct joining

The success of multi-material lightweighting structures depends heavily on the robustness and cost-effectiveness of joining technologies to achieve dissimilar material joining between

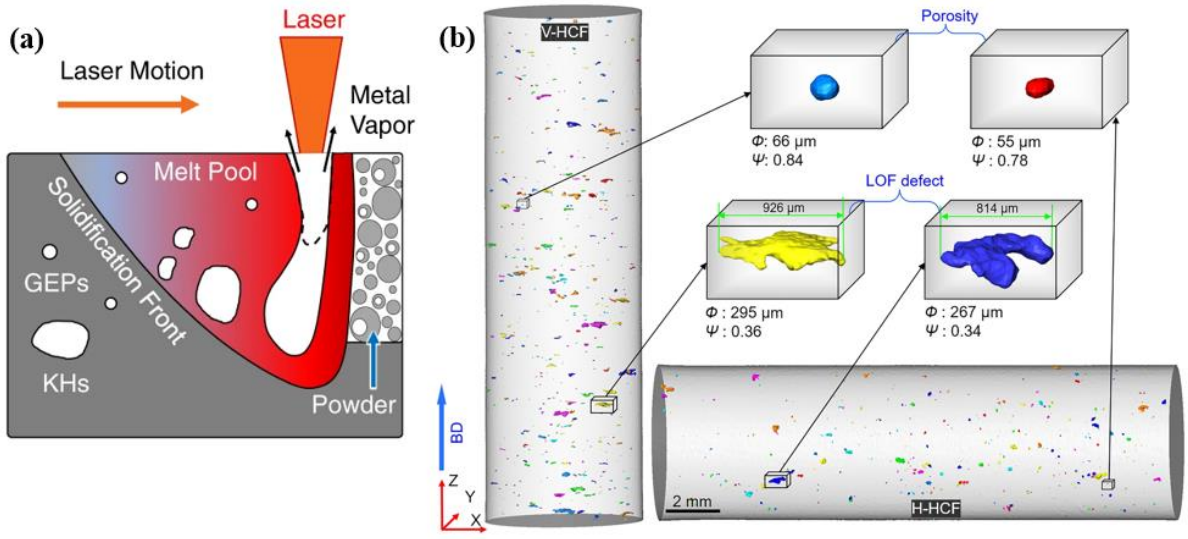


Figure 1.2: (a) General schematic of laser powder bed fusion (LPBF) additive manufacturing [19] (GEPs = Gas-entrapped Pores, KHs = Key Holes), and (b) typical presence of defects in a simple cylindrical structure micro-CT image [18] (LOF = Lack of Fusion)

a metal and a polymer/polymer composite or between two different and incompatible metals [22]. Conventional joining methods such as riveting, adhesive joining, resistance spot welding, and advanced joining methods such as self-piercing rivets have been in application for decades to achieve such joining between dissimilar materials [22,23]. However, as shown in Figure 1.3, due to their weight penalties, non-recyclability, susceptivity to fatigue failure, and environmental corrosion, there has been an increased demand to achieve the joining between two dissimilar materials without adhesives and fasteners in the recent decade [24]. Deformation, temperature, and

friction-based joining technologies have been providing very apt solutions to achieve direct joining between metal and polymer composites via physical, chemical, or mechanical interlocking effects [25].

Metal-to-polymer joining has been primarily achieved using adhesives and mechanical fasteners for structural and non-structural applications. However, the advent of electric vehicles has driven auto manufacturers to investigate metal-to-polymer welding or direct joining without relying on adhesives and fasteners for a rapid turn-around, weight reduction for fuel efficiency, and utilization of thermoplastic polymers for the circular economy. Various structural polymers such as polyamide (PA) or nylon, polypropylene (PP), polyether ether ketone (PEEK), and polycarbonates (PC) and their glass fiber and carbon fiber composites have been introduced for the structural and non-structural components not only for automotive applications, but for aerospace, and marine structural applications as well [9].

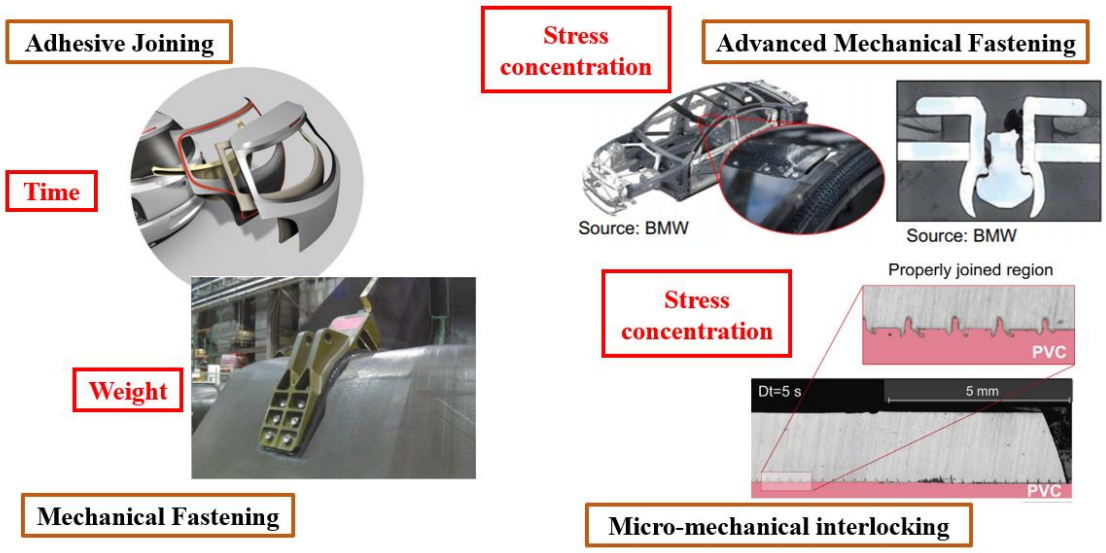


Figure 1.3: Challenges faced by traditional adhesive joining and fastening applications [22,23].

On the other hand, bimetallic dissimilar material joints and their structural applications vary vastly from marine structures, aerospace, and automotive industries [26]. Aluminum alloys and steel stand out among all and have amounted to more than 70% of the structural parts in

shipbuilding and automotive components [27]. However, their long-term usage has been enabled by either adhesive, fasteners, fusion-based, or friction-based welding methods. The direct joining between two dissimilar metals such as fusion-based or friction-based welding methods, suffer from the formation of brittle intermetallic compounds (IMCs) at the joining interface due to interatomic diffusion [28]. Due to the presence of IMCs, they suffer additional accelerated corrosion at the joining interface, and manufacturing industries seek active solutions to avoid such accelerated corrosion phenomenon.

1.2.2 Solid-state additive manufacturing

In the past decade, solid-state additive manufacturing (SSAM or S2AM) methods have enabled multiple avenues for additively depositing materials or 3D printing without solidification or melting-induced defects [21]. It has become one of the major thrust areas for sustainable manufacturing due to its solid-state nature, leveraging off-the-shelf feedstocks as raw material, minimal material waste, and higher energy efficiency compared to fusion-based additive manufacturing processes. Utilizing the defect-free nature of the S2AM, significant efforts have been made to deposit metallic materials on a base material or component surface either in the single line of deposition or multiple parallel passes (cladding) for strengthening, protecting, repairing, or increasing the wear resistance of the base surface [29]. Cold spray and additive friction stir deposition (AFSD) have been largely employed to achieve seamless engine block repair and reusable and long-lasting off-shore component surfaces repaired for in-service or on-demand applications [30].

Additive friction extrusion deposition (AFED), shown in Figure 1.4(b) is a relatively new form of additive manufacturing, invented by Liu et al. [31] recently and termed SoftTouch Additive Manufacturing (SoftTouch AM^{TM}). It can provide a dense microstructure through a solid-

state grain refinement process without severely compressing the substrate or the previously printed layers compared to AFSD (Figure 1.4a). As Liu et al. [31] described, it utilizes grain refinement to soften the feedstock material in a flowable state, and simultaneous extrusion prints the paste-like softened material through the nozzle. AFED is different from other friction-stir-based additive manufacturing [21,31] in which the feedstock is actively compressed on the substrate or the previously printed layer to engage under pressure and generate frictional heating to plasticize the feedstock. The applied pressure in both the processes are significantly different and the SoftTouch AM^{TM} deposition process provides the advantage of securing the previously printed layer or the substrate. With the low compression force needed in the SoftTouch deposition process, it is possible to control and further utilize the deposition process for structural repair without overheating and over-compressing the substrate as a suitable alternative to other solid-state additive manufacturing processes [21,30,31].

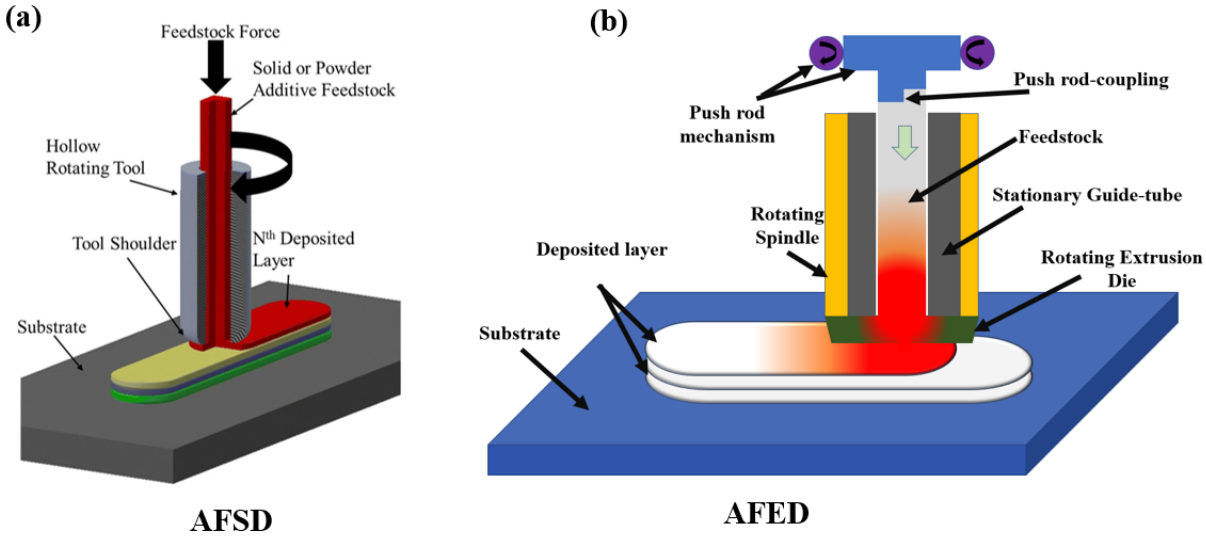


Figure 1.4: Solid-state additive manufacturing schematics; (a) AFSD module commercialized by MELD Inc. [32], and (b) novel AFED process schematic invented by Liu et al. [31]

1.3 Major Challenges

Although conventional manufacturing processes such as adhesive bonding, mechanical fastening, and fusion-based welding methods have been the mainstream approaches to joining dissimilar materials, they have failed to provide efficient weight reduction, corrosion resistance, and cost benefits in multi-material structural components. Major challenges remaining for directly joining dissimilar materials without adhesives or fasteners are:

i. Suitable manufacturing processes
ii. Material compatibility at the metal-to-polymer joining interface
iii. Lack of underlying bonding mechanism explanations
iv. Occurrence of IMCs at the bimetallic interfaces
v. Joint design for static and structural fatigue applications
vi. Mechanical property extraction and transferability for other joint types
vii. Corrosion resistance of the directly bonded dissimilar-material joints

Similarly, fusion-based additive manufacturing methods have produced dissimilar material additively manufactured components for non-structural and limited structural applications. Due to the liquid-to-solid transition phenomenon during molten pool solidification, such components have suffered from size/scale limitations, thermal shrinkage, and major material incompatibility issues. To eliminate the fusion-induced defects and address large-area additive manufacturing challenges, the additive friction stir deposition (AFSD) based solid-state additive manufacturing method has been adopted in recent years. However, the AFSD methods introduced in recent years have been utilized primarily for similar material deposition and pose major challenges as:

a. Sever compression-induced instability of the substrate material
b. Special square shape feedstock preparation

c. Lack of controlled material interaction at the joining interface for incompatible materials
d. Excessive substrate plate heating and plasticization before feedstock material deposition
e. Lack of controlled dissimilar material deposition for structural applications

1.4 Objectives of the Current Research

Based on the above critical review of the research needs and challenges faced by the industry for realizing the enormous benefits of multi-material lightweight structures, we conclude that it is of paramount importance to develop direct joining and solid-state additive manufacturing processes to achieve multi-material structural lightweighting. These processes and strategies should not only be capable of developing metal-to-polymer, dissimilar metal direct bonding, and dissimilar material solid-state additively manufacturable components but also provide robust joints and ease of translational capabilities for direct industrial applications. Achieving metal-to-polymer direct joining significantly differs from metal-to-metal dissimilar material direct joining, although they share similar material incompatibility and joint design issues. Hence, the dissimilar material direct joining processes should not only provide specific material-dependent joining solutions but should also be able to translate between various joining configurations, such as localized spot or linear joining configurations for broader structural lightweighting applications. On the other hand, the friction-based solid-state additive manufacturing methods should not only eliminate the compression force-induced instabilities in the substrate but should also provide intermetallic free or intermetallic suppressed joining interface capable of corrosion resistance and large area additive manufacturing. Driven by these motivations, this dissertation research aims at developing a fundamental understanding of solid-state dissimilar material joining and additive manufacturing processes and novel process implementation for enabling the design and manufacture of next-generation multi-material structures through these four major research undertakings:

i. Direct method for direct joining polymer composite to metal and underlying bonding mechanisms.
ii. Direct method for direct joining between dissimilar metals (e.g., aluminum to steel or stainless steel to carbon steel) and underlying bonding mechanisms.
iii. Robust solid-state dissimilar metal additive manufacturing.
iv. Characterize bond quality and joint properties.

1.5 Outline of the Dissertation

The four tasks mentioned above for achieving dissimilar material joints and enabling structural lightweighting for sustainability via solid-state manufacturing processes are addressed through the seven chapters of this dissertation. This doctoral thesis follows a multi-manuscript format, with Chapter 1 serving as an integrated introduction and Chapter 7 as an integrated conclusion. Chapters 2 [22,23], 3 [34], 4 [35], and 5 [36] are four separate manuscripts that have been published in peer-reviewed international journals. These chapters are thus presented in the format submitted with minor changes to abide by the formatting requirements. As a result, there may be a few overlaps between the material presented in these chapters. These overlapping materials make the individual chapters completely self-contained. Chapter 6 further substantiates the solid-state dissimilar material deposition processes by presenting exploratory studies using both ferrous and non-ferrous alloys.

The dissertation begins with background information on the structural lightweighting demands of the transportation sectors and the role of a multi-material approach in achieving sustainability, supported by relevant literature reviews. It later emphasizes the importance of direct joining processes vs. traditional joining processes and solid-state manufacturing processes vs. fusion-based additive manufacturing processes. Based on the combined literature review, Chapter

1 lays the foundation for major challenges and objectives of the current research work and outlines the strategic plan to tackle the current shortcomings.

Chapter 2 of the dissertation provides a critical review of advanced joining processes for dissimilar materials focusing on metal-to-polymer direct joining. It identifies the suitable joining processes, critical and affecting process parameters, importance of pressure and temperature conditions, material chemistry, and use cases for various industrial applications. It further emphasizes the importance and nuances of joint design for the eventual success of dissimilar material joining processes for structural lightweighting applications. It ends with recommendations for C-O-M type covalent bonding formation mechanism and structural stress methods for joint strength evaluations and transferrable joint property evaluations.

With the scientific rationales presented in Chapter 2 to select the friction-based solid-state joining processes, Chapter 3 builds upon identifying the suitable joining process parameters and joint formation mechanism between aluminum alloy and glass fiber reinforced polypropylene (GFRP-PP) composite intended for automotive structural applications. It provides a detailed examination of the joint formation mechanism using C-O-M type covalent bonding, joint load capacity, and joint failure characteristics to achieve a joint stronger than the base PP composite material sheet.

Following a successful metal-polymer direct joining in Chapter 3, nano-scale shear localization-induced amorphization (NSLIAA) developed previously by Liu et al [33] for thick sheets has been implemented to generate the direct bonding between thin gauge aluminum alloy and steel material sheets in Chapter 4. It utilizes a systematic approach to suppress the formation of IMCs at the joining interface of aluminum and steel. Chapter 4 further assesses the joint load capacities under a well-accepted automotive corrosion cycle GMW 14872 and provides critical

findings behind the corrosion resistance nature of bimetallic joints with suppressed IMCs at the bonding interface.

Utilizing the successful direct joining of dissimilar materials in the previous chapters, Chapter 5 presents a novel solid-state additive friction extrusion deposition (AFED) process to additively manufacture metallic alloys at a large scale. It first lays the foundation of a novel AFED process schematic, the effect of process parameters, grain refinement, and the effect of layer thickness on the substrate reaction force while 3D printing aluminum alloy 6061-T6. Later, it assesses the noteworthy mechanical properties of below-melting deposition of AA6061-T6, highlighting improved hardness, isotropic nature, and ductility behavior.

Following the AFED process concept development and implementation presented in Chapter 5, Chapter 6 provides a novel exploratory study on dissimilar material deposition processes using aluminum alloy 6061-T6 on stainless steel 304 substrate and stainless steel 316 material on carbon steel AISI-1018 substrate. Chapter 6 further evaluates the suppression of IMCs at the AA6061/SS316 interface and provides a detailed analysis of bonding strength and microstructures for AA6061/SS316 and SS316/AISI-1018 interfaces through hierarchical material characterization using various microscopy techniques. The dissertation is then concluded in Chapter 7 with an integrated summary of the research work completed so far and recommendations for possible future research directions.

1.6 Brief Summary and Highlights of Major Contributions

In this research, solid-state friction-based dissimilar material direct joining and additive manufacturing methods are investigated. Using the friction-based solid-state method, it first achieved a novel metal to hard-to-weld polypropylene (PP) composite direct joining using a functionally active interface modulator insert layer under localized temperature and pressure

conditions. Utilizing C-O-Al type covalent bonding between aluminum alloy and PP-GFRP composite, it eliminated fasteners and adhesives for a robust joint stronger than the base composite material. Subsequently, it utilized previously discovered, nanoscale shear localization-induced amorphization (NSLIAA) to join thin gauge aluminum alloy to steel materials directly under controlled friction spot joining configuration for the suppression of IMCs and increased corrosion resistance.

It has then demonstrated a novel friction-based solid-state metal additive manufacturing method to enable dissimilar material additive manufacturing of metals and alloys directly at a large scale without solidification defects and minimal substrate compression force-induced instabilities. It was termed SoftTouch AM^{TM} due to its low temperature and low compression force features and defined as an additive friction extrusion deposition (AFED) process due to its friction-based extrusion and additive processing features. SoftTouch AM^{TM} utilizes super-plasticity to soften the feedstock in two steps, eliminating the need for direct contact between substrate and feedstock and providing grain refinement and severe cold working (plastic deformation) below the melting temperatures of metallic materials. It avoids using pricy powders and is fully capable of utilizing off-the-shelf metallic bars as feedstock. It has proven crucial for future demands of large-area additive manufacturing, energy sectors, and sustainability.

References

[1] Lamb WF, Wiedmann T, Pongratz J, Andrew R, Crippa M, Olivier JGJ, et al. A review of trends and drivers of greenhouse gas emissions by sector from 1990 to 2018. Environ Res Lett 2021;16. https://doi.org/10.1088/1748-9326/abee4e.

[2] Lewis GM, Buchanan CA, Jhaveri KD, Sullivan JL, Kelly JC, Das S, et al. Green Principles for Vehicle Lightweighting. Environ Sci Technol 2019;53:4063–77. https://doi.org/10.1021/acs.est.8b05897.

[3] Kawajiri K, Kobayashi M, Sakamoto K. Lightweight materials equal lightweight greenhouse gas emissions?: A historical analysis of greenhouse gases of vehicle material substitution. J Clean Prod 2020;253:119805. https://doi.org/https://doi.org/10.1016/j.jclepro.2019.119805.

[4] Gearhart C. Implications of sustainability for the United States light-duty transportation sector. MRS Energy Sustain 2016;3:1–15. https://doi.org/10.1557/mre.2016.8.

[5] Kelly JC, Sullivan JL, Burnham A, Elgowainy A. Impacts of Vehicle Weight Reduction via Material Substitution on Life-Cycle Greenhouse Gas Emissions. Environ Sci Technol 2015;49:12535–42. https://doi.org/10.1021/acs.est.5b03192.

[6] Keoleian GA, Sullivan JL. Materials challenges and opportunities for enhancing the sustainability of automobiles. MRS Bull 2012;37:365–72. https://doi.org/10.1557/mrs.2012.52.

[7] Kim HC, Wallington TJ. Life-cycle energy and greenhouse gas emission benefits of lightweighting in automobiles: Review and harmonization. Environ Sci Technol 2013;47:6089–97. https://doi.org/10.1021/es3042115.

[8] Luk JM, Kim HC, De Kleine R, Wallington TJ, MacLean HL. Review of the Fuel Saving, Life Cycle GHG Emission, and Ownership Cost Impacts of Lightweighting Vehicles with Different Powertrains. Environ Sci Technol 2017;51:8215–28. https://doi.org/10.1021/acs.est.7b00909.

[9] Taub A, De Moor E, Luo A, Matlock DK, Speer JG, Vaidya U. Materials for Automotive Lightweighting. Annu Rev Mater Res 2019;49:327–59. https://doi.org/10.1146/annurev-matsci-070218-010134.

[10] BİLGE Ç, AYDINER T, AKDENİZ Ç, SOYER AM, AKSEL L. Weight Reduction of Automobile Using Glass-Mat Thermoplastic Composites in Spare-Wheel Well. Eur Mech Sci 2020;4:7–11. https://doi.org/10.26701/ems.573687.

[11] Czerwinski F. Current trends in automotive lightweighting strategies and materials. Materials (Basel) 2021;14. https://doi.org/10.3390/ma14216631.

[12] Tofail SAM, Koumoulos EP, Bandyopadhyay A, Bose S, O'Donoghue L, Charitidis C. Additive manufacturing: scientific and technological challenges, market uptake and opportunities. Mater Today 2018;21:22–37. https://doi.org/10.1016/J.MATTOD.2017.07.001.

[13] Blanco D, Rubio EM, Marín MM, Davim JP. Advanced materials and multi-materials applied in aeronautical and automotive fields: a systematic review approach. Procedia CIRP 2021;99:196–201. https://doi.org/https://doi.org/10.1016/j.procir.2021.03.027.

[14] Daidola JC. Modularity: Facilitator for commercial shipyards in naval shipbuilding. J Sh Prod Des 2021;37:97–108. https://doi.org/10.5957/JSPD.11190059.

[15] Zhang W, Xu J. Advanced lightweight materials for Automobiles: A review. Mater Des 2022;221:110994. https://doi.org/10.1016/j.matdes.2022.110994.

[16] DebRoy T, Wei HL, Zuback JS, Mukherjee T, Elmer JW, Milewski JO, et al. Additive manufacturing of metallic components – Process, structure and properties. Prog Mater Sci 2018;92:112–224. https://doi.org/10.1016/j.pmatsci.2017.10.001.
[17] Langelaar M. Topology optimization of 3D self-supporting structures for additive manufacturing. Addit Manuf 2016;12:60–70. https://doi.org/10.1016/j.addma.2016.06.010.
[18] Wu Z, Wu S, Bao J, Qian W, Karabal S, Sun W, et al. The effect of defect population on the anisotropic fatigue resistance of AlSi10Mg alloy fabricated by laser powder bed fusion. Int J Fatigue 2021;151:106317. https://doi.org/10.1016/j.ijfatigue.2021.106317.
[19] Poudel A, Yasin MS, Ye J, Liu J, Vinel A, Shao S, et al. Feature-based volumetric defect classification in metal additive manufacturing. Nat Commun 2022;13:1–12. https://doi.org/10.1038/s41467-022-34122-x.
[20] Leino M, Pekkarinen J, Soukka R. The role of laser additive manufacturing methods of metals in repair, refurbishment and remanufacturing - Enabling circular economy. Phys Procedia 2016;83:752–60. https://doi.org/10.1016/j.phpro.2016.08.077.
[21] Shao J, Samaei A, Xue T, Xie X, Guo S, Cao J, et al. Additive friction stir deposition of metallic materials: Process, structure and properties. Mater Des 2023;234:112356. https://doi.org/10.1016/j.matdes.2023.112356.
[22] KHAN AS, DONG P, LIU F, ZHANG Y. A State-of-the-Art Review on Direct Welding of Polymer to Metal for Structural Applications: Part 2 — Joint Design and Property Characterization. Weld J 2024;103:142–50. https://doi.org/10.29391/2024.103.013.
[23] Khan AS, Dong P, Liu F, Zhang Y. A State-of-the-Art Review on Direct Welding of Polymer to Metal for Structural Applications: Part 1 — Promising Processes. Weld J 2024;103:117S-136S. https://doi.org/10.29391/2024.103.011.
[24] Lambiase F, Balle F, Blaga LA, Liu F, Amancio-Filho ST. Friction-based processes for hybrid multi-material joining. Compos Struct 2021;266:113828. https://doi.org/10.1016/j.compstruct.2021.113828.
[25] Lambiase F, Scipioni SI, Lee CJ, Ko DC, Liu F. A state-of-the-art review on advanced joining processes for metal-composite and metal-polymer hybrid structures. Materials (Basel) 2021;14. https://doi.org/10.3390/ma14081890.
[26] S. Kleinbaum, C. Jiang, S. Logan, Enabling sustainable transportation through joining of dissimilar lightweight materials, MRS Bull. 44 (2019) 608–612, https:// doi.org/10.1557/mrs.2019.178.
[27] A. Gullino, P. Matteis, F.D. Aiuto, Review of aluminum-to-steel welding technologies for car-body applications, Metals (Basel) 9 (2019) 1–28, https://doi. org/10.3390/met9030315.
[28] B. Pan, H. Sun, S.L. Shang, M. Banu, P.C. Wang, B.E. Carlson, et al., Understanding formation mechanisms of intermetallic compounds in dissimilar Al/steel joint processed by resistance spot welding, J. Manuf. Process. 83 (2022) 212–222, https://doi.org/10.1016/j.jmapro.2022.08.062.
[29] Hartley WD, Garcia D, Yoder JK, Poczatek E, Forsmark JH, Luckey SG, et al. Solid-state cladding on thin automotive sheet metals enabled by additive friction stir deposition. J Mater Process Technol 2021;291:117045. https://doi.org/10.1016/j.jmatprotec.2021.117045.
[30] Gottwald RB, Griffiths RJ, Petersen DT, Perry MEJ, Yu HZ. Solid-State Metal Additive Manufacturing for Structural Repair. Accounts Mater Res 2021;2:780–92. https://doi.org/10.1021/accountsmr.1c00098.
[31] Liu F, Dong P, Khan AS, Zhang Y, Cheng R. 3D printing of fine-grained aluminum alloys

through extrusion-based additive manufacturing: Microstructure and property characterization. J Mater Sci Technol 2022. https://doi.org/10.1016/J.JMST.2022.08.017.

[32] Avery DZ, Phillips BJ, Mason CJT, Palermo M, Williams MB, Cleek C, et al. Influence of Grain Refinement and Microstructure on Fatigue Behavior for Solid-State Additively Manufactured Al-Zn-Mg-Cu Alloy. Metall Mater Trans A Phys Metall Mater Sci 2020;51:2778–95. https://doi.org/10.1007/s11661-020-05746-9.

[33] Liu FC, Dong P. From thick intermetallic to nanoscale amorphous phase at Al-Fe joint interface: roles of friction stir welding conditions. Scr Mater 2021;191:167–72. https://doi.org/10.1016/j.scriptamat.2020.09.031.

[34] Khan AS, Liu F, Dong P. Joining of metal and non-polar polypropylene composite through a simple functional group seeding layer. J Manuf Process 2023;85:90–100. https://doi.org/10.1016/J.JMAPRO.2022.11.022.

[35] Khan AS, Dong P, Sun K, Larsen D. Direct spot joining of thin gauge aluminum alloy to stainless steel and joint performance in a corrosion environment. Thin-Walled Struct 2024;200:111919. https://doi.org/10.1016/j.tws.2024.111919.

[36] Liu F, Dong P, Khan AS, Zhang Y, Cheng R. 3D printing of fine-grained aluminum alloys through extrusion-based additive manufacturing: Microstructure and property characterization. J Mater Sci Technol 2022. https://doi.org/10.1016/J.JMST.2022.08.017.

Chapter 2 State of the Art Review and Research Needs

2.1 Introduction

To ensure sustainability of the environment and quality of life, effective use and reuse of existing materials have become increasingly important in transitioning to a circular economy [1–3]. As part of such an effort, major automotive manufacturers have been leading the drive towards structural lightweighting over the last decade or so [4–7]. The consensus resulted from recent major research initiatives is that multi-material structure, i.e., "using the right material at the right place", offers the most effective lightweighting in addition to achieving multi-functionalities [8–12]. For instance, the US Department of Energy (DOE) multi-material lightweight vehicle (MMLV) autobody structure [13] made of high strength steel, aluminum, and magnesium alloys, and carbon fiber polymer composites can offer up to 40% weight reduction versus all high strength steel structures, as highlighted in Figure 2.1. However, the challenge has been how to cost-effectively manufacture such multi-material structures in a mass-production environment while ensuring structural durability, and recyclability. Traditional mechanical fastening incurs additional part counts and adds weight while adhesive bonding increases production cycle time in addition to its implications for long-term durability and recyclability of adhesive-bonded components [14–16]. To mitigate some of the major concerns, direct welding of dissimilar materials (polymer to metal or between incompatible metals, e.g., aluminum to steel) has gained growing attention in the research community over recent years [17–19].

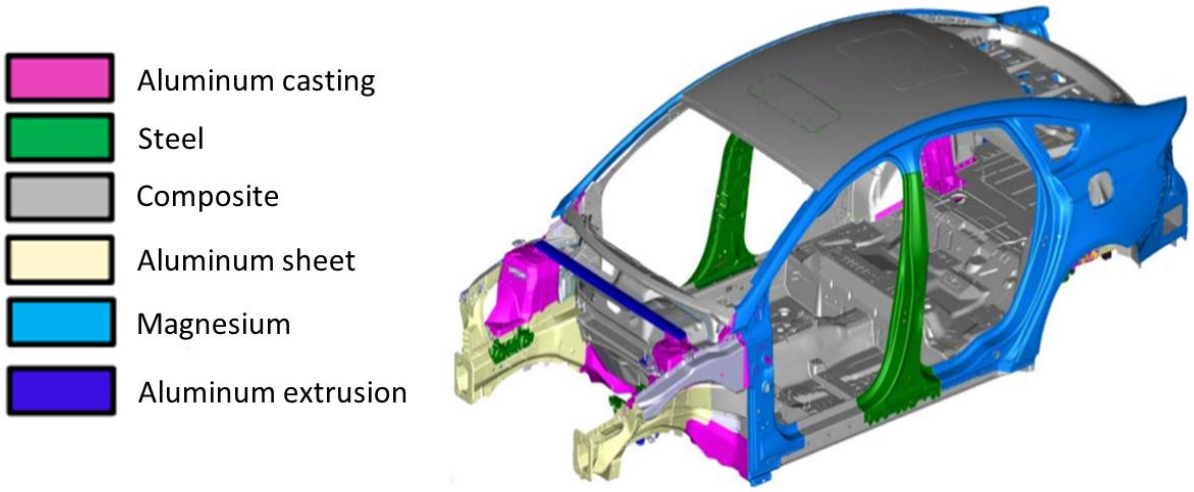


Figure 2.1: Structural lightweighting through a multi-material concept [13]

There have been some promising successes in developing methods for direct welding of polymer or polymer-composite to metal. For instance, Liu et al, [20] demonstrated that the functional groups in polyamide (PA) or nylon enabled its direct welding with aluminum alloy without any surface or material pre-treatment through a carbon-oxygen-metal (aka C-O-M) chemical bond formation under localized heating and pressure conditions, e.g., via a friction-assisted lap welding technique. Using friction assisted spot method, Khan et al [21], recently demonstrated that a nonpolar polypropylene (PP) composite can be directly welded using a thin layer of functional group seeding material between the PP composite and metal partner without special surface treatments. Han et al, [22] have shown the joining of PP sheet with aluminum alloy using a metal surface laser texturing by micromechanical interlocking under friction-assisted spot joining. Kawahito et al, [23] have shown successful joining of steel and PA under pulsed laser joining and achieved strong joints. The combination of PA or PP and aluminum or steel can be used for reducing weight in some of the automotive interior components. As shown in Figure 2.2a, recent applications of PP in GM liftgates and PA composites in GMC Sierra trucks (Figure 2.2b)

have shown the importance of directly joining polymer composites with aluminum and steel structures for structural lightweight applications in mass production environments.

It should be noted that the direct joining of incompatible dissimilar metals such as aluminum alloys to steel (involved in MMLV in Figure 2.1) has been facing similar challenges due to the formation of brittle intermetallic compounds (IMCs) at the joining interface [24–26]. Recent research efforts have shown that brittle IMCs can be effectively avoided through a nanoscale shear localization process beyond a threshold strain rate under certain friction stir welding conditions. As a result, the aluminum-steel interface exhibits a dominantly amorphous microstructure which offers high interfacial bonding strength and excellent thermal stability [27–30]. A good thermal stability is important to restrict the nucleation and growth of IMCs at thermal cyclic loading conditions [148].

The use of fiber-reinforced thermoplastics has been a prime mover in the automotive industries due to recyclability [31–34] and has been seeing an uptake in aerospace and marine structures as well [35–38]. It is expected that the need for recyclable polymers and lightweighting requirements will enable the use of thermoplastics for as much as up to 40% of the total material in automotive structures [13,39]. PA and PP are the most common polymer materials being used in the automotive industries due to their formability, low cost, and recyclability [40–43]. PP, due to its low density comparing with other industrial polymers and high corrosion resistance, is widely used in automotive industry [44–47]. The direct joining of metals with polymer or polymer composites thus eliminates multiple process steps, mechanical fasteners, and adhesives and provides strong joints capable of hermetic sealing required for applications under pressure and severe weather environment [17–19]. As recently suggested from some recent studies [48–50],

direct dissimilar material joining also offers improved structural reliability under dynamic and fatigue loading conditions.

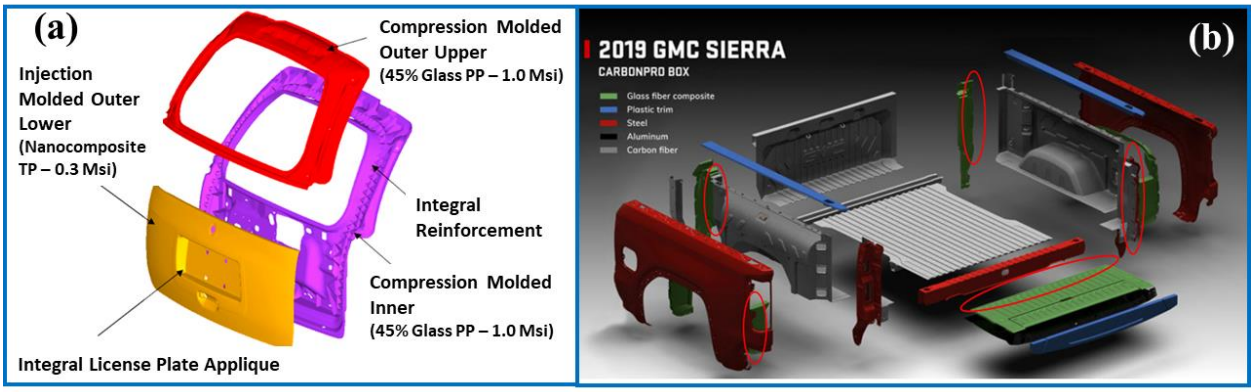


Figure 2.2: (a) A lightweight liftgate concept made of GFPP of passenger van [43], and (b) A lightweight truck cargo bed made of metal-polymer hybrid structure [gmauthority.com]

As highlighted above, multi-material or mixed-material structures made of dissimilar metals, polymers, and polymeric composites have been becoming increasingly important for meeting today's increasingly stringent weight reduction, energy efficiencies, and recyclability requirements [51,52]. However, robust, reliable, and cost-effective joining methods are still in the early research and development stage. Among various new dissimilar material joining methods under exploration today, direct joining of polymer to metal is of the most interest for mass-production environment and can be a key enabler for realizing the advanced multi-material structures (e.g., the one shown in Figure 2.1) in a cost-effective manner.

In addition to the need of ensuring adequate chemical bonding at polymer and metal interface as a result of direct joining methods, effective methodologies for extracting joint properties from simple lab specimen testing are also of critical importance for supporting computer-aided engineering (CAE) evaluation of multi-material structures for industrial applications. However, one additional major challenge remains: how to determine the mechanical properties of these joints in such a way that these properties can be used in the design and

evaluation of actual structures. Most of the aforementioned investigations have been relying on simple lap-shear (Figure 2.21a) or coach peel (Figure 2.21b) by performing either static tensile strength or fatigue tests. The resulting test data are typically presented in terms of nominal stress (F/A) corresponding to load at failure, where A can be either defined as the loaded base plate cross-section area or the bonded area at the dissimilar material interface of a simple lab specimen, depending upon where the failure actually occurs in the test. As such, the test data cannot be directly adopted in a finite element (FE) model for structural design and optimization purposes. This is because in actual structures, the load carrying area A is typically ill-defined. To remove such limitations, the test data based on F/A obtained from simple lab specimens must be transformed into a joint level property, e.g., tensile strength or fatigue strength. This would typically require rigorous mechanics-based modeling, e.g., through FE analysis. The major difficulty in performing FE analysis for welded joints is how to suppress mesh-size induced sensitivity when stresses are computed at sharp corner locations (see the red arrow lines in Figure 2.21) where stress and strain possess singularity. This is illustrated in Figure 2.22 in which two lap-shear specimens were analyzed using commercial code ABAQUS [156]. The stresses at the sharp corner locations suffer severe mesh size sensitivity, just like in welded components as discussed in some recent publications [156-162]. This issue must be resolved in order to reliably extract joint properties not only for evaluating dissimilar material joint design, but also for optimizing structural performance in product development process involving multi-materials.

Along this line, this chapter is structured as follows: after a brief introduction of the needs in direct joining methods for effectively integrate polymer composites to metal for structural applications, some of the promising direct joining methods will be critically reviewed and assessed in Section 2.2. Their process characteristics, bonding mechanisms involved, as well chemical

bonding enhancement techniques are discussed in Section 2.3. Then, in Section 2.4, joint property characterization methods, particularly those that are relevant for supporting computer-aided engineering (CAE) for design and structural performance evaluation will be discussed. One of the key outcomes of the section is mechanics-based principles for achieving optimal design for dissimilar material joints for improved jointability and joint performance in load-bearing structures. Finally, some of the unresolved research issues for enabling reliable structural applications will be summarized for considerations by the research community.

2.2 Promising Direct Joining Techniques

Here, a direct joining technique is defined as a method by which a polymer or its composite forms (e.g., reinforced through glass or carbon fibers) can be joined with a metal substrate by forming chemical bonds without needing any separate surface or material pretreatment or curing process [48]. Among all promising direct joining processes reported in the literature to date, localized heat and pressure are the necessary ingredients (Figure 2.3) for providing favorable thermomechanical conditions for the formation of chemical bonds. In this regard, thermoplastic polymers and their composites including glass fibers and carbon fiber composites are often considered for joining with metals and their alloys. Among them, polymers with carbonyl functional groups, such as polyamide (PA) or nylon, polycarbonate (PC), and polyether ether ketone (PEEK) have been shown to possess weldability with aluminum 5xxx, 6xxx, and 7xxx alloys for automotive and aerospace applications, i.e., without needing any special surface or material treatment before joining. Whereas polymers lacking carbonyl functional groups, such as PP, and PE, typically require special surface treatment such as metal surface laser texturing for mechanical interlocking or chemical treatment to enable chemical bonding with metal

counterparts, therefore, continuing to pose significant challenges for achieving direct joining with metals.

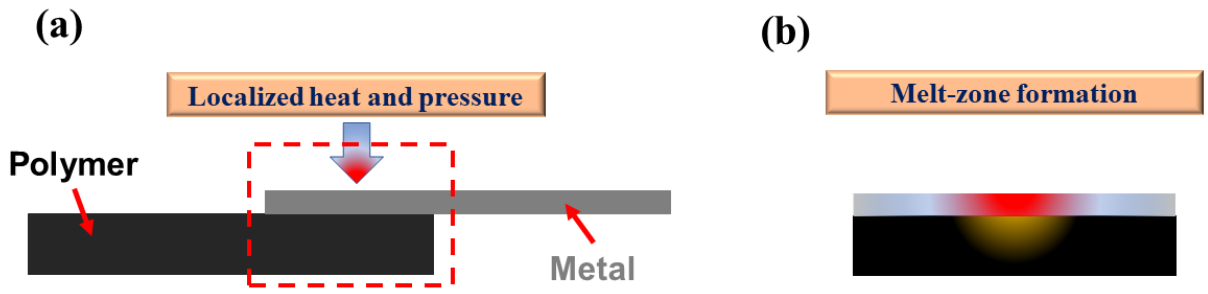


Figure 2.3: Schematic of localized heat and pressure conditions to join metal and polymer.

For dissimilar material combinations discussed above, localized heating and pressure can be achieved through a variety of means, e.g., laser, electrical resistance, induction, ultrasonic vibration, and friction. Some of the promising direct joining processes are described and discussed below, based on their process capability, particularly for structural applications.

2.2.1 Laser-assisted joining processes

2.2.1.1 Process description

It utilizes a laser source to generate laser beams of suitable wavelength to project onto the metallic sheet and locally heat the interacted area. A customized clamping system is often used to provide localized pressure conditions for the molten polymer to interact with the metal sheet and form the joint. The laser beam can be projected directly on the metal surface to heat and melt the plastic underneath (conduction joining CJ, Figure 2.4a) or it can pass through a transparent polymer to heat the metal at the assembly interface (transmission joining TJ, Figure 2.4b) [23,53]. Conduction joining (CJ) can be implemented for opaque polymers when the laser wavelength can't penetrate the polymer sheet without significantly damaging it. Laser beams can be applied either

in spot configuration or linear configuration per the joint design requirements and shielding gases such as Argon (Ar) or Nitrogen (N2) are often used to protect material surfaces and control the temperature.

2.2.1.2 Key process parameters and joint formation mechanisms

Laser beam shape, power density, laser wavelength, and scanning speed combinedly affect the joining quality between a given metal and polymer combination. Laser power density is a function of laser power and defocused distance. Combined with laser beam shape and wavelength, the interaction volume or fusion zone can be controlled to provide sufficient wetting of the metal surface with polymer. The directed laser heats the metal and the localized rapid heating further melts and often generates inherent bubbles at the metal/polymer interface. One key consideration in such laser-assisted polymer-metal joining is the amount of bubbles formed during localized rapid heating. Such bubbles, although can help by generating pressure between the molten layer of polymer and metal substrate, however in excess, lead to a poor bonding quality. For example, Kawahito et al [23] used a continuous wave (CW) 1.5 kW Nd:YAG laser beam with a 1064 nm wavelength and a 200W laser diode (LD) laser beam with an 807 nm wavelength to join stainless steel with PA, polyethylene terephthalate (PET) and polycarbonate (PC) and used Ar and N2 as shielding gases for continuous wave and laser diode mode respectively. Gas bubble formation was found be minimal under CJ mode for linear configuration using laser diode laser beam while joining SUS304 and PA (Figure 2.5).

Furthermore, a defocused laser beam can be used to regulate heating zone size, geometry, and beam/material interaction volume [54–56]. Consequently, a larger defocus distance increases the weld width and spreads the temperature and energy uniformly. However, an optimal defocus distance, laser power density and spot size are often necessary, and the optimum values change for

the material combination provided [57–59]. Jung et al [60] found that there is always an optimal laser power and scanning speed to obtain the strongest joint made of steel and nylon (PA6) composite (Figure 2.6). The clamping pressure plays an indirect role during weld formation process and can be generated by a mechanical, pneumatic or servo-electronically driven device. It is found that a minimum contact pressure to keep the joining counterparts closely in contact is necessary to achieve a good interfacial bonding, resulting in stronger joints demonstrated through mechanical testing [61–63]. Applying a too-high pressure can deteriorate interfacial bond quality. Metal and polymer usually have a very high thermal conductance difference and the application of pressure also ensures a continuous heat diffusion between these highly different materials. It also affects bubble formation and thus controls the final bond to a significant extent [64,65].

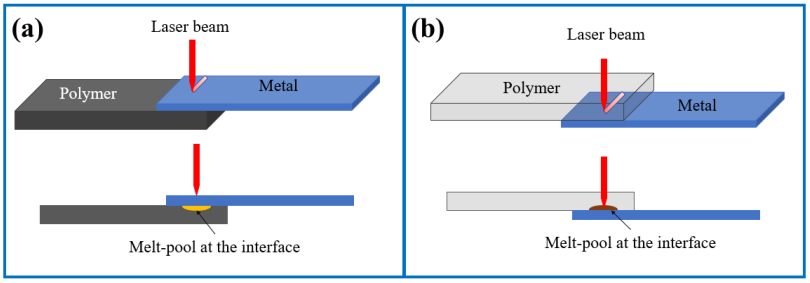


Figure 2.4: Variants of laser assisted joining, (a) conduction joining, (b) transmission joining.

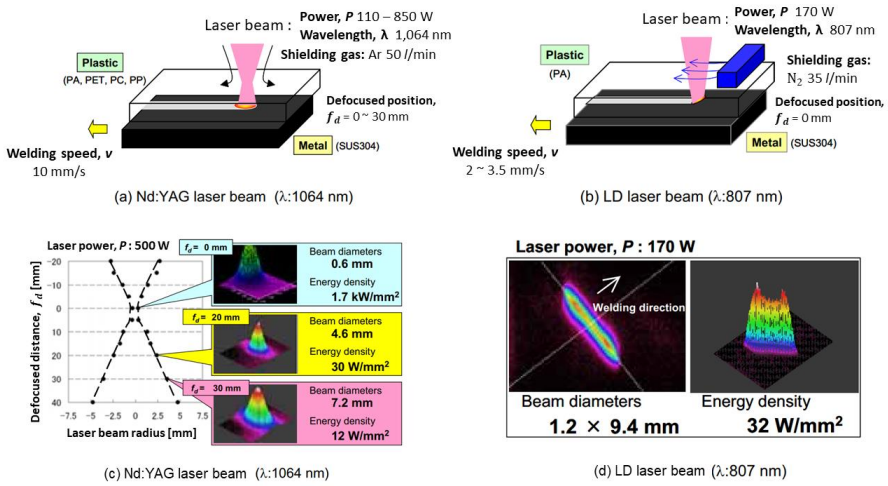


Figure 2.5: Nd:YAG vs diode laser (LD) joining method characteristics [23]

2.2.1.3 Joint strength and structural applications

The joint strength is primarily governed by the material interaction volume and interface quality at the metal/polymer joining interface which in turn is controlled by localized heating [66,67]. Figure 2.7a shows a recent application of laser joining of steel with PA composite for a FIAT panda roof grill and represents the adaptability of laser joining method in automotive structures. To develop a continuous production throughput, the laser joining method further requires due automation and qualification for load bearing applications.

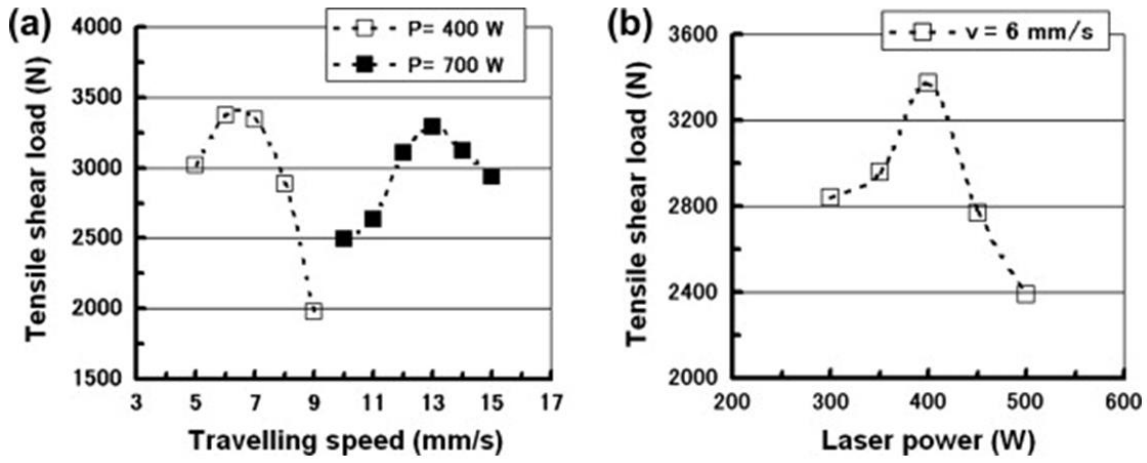


Figure 2.6: Effect of laser process parameters on joint load capacity [60]

2.2.2 Friction-based joining processes

2.2.2.1 Process description

Friction based direct joining between metal and polymer shares a great deal of similarities with friction stir welding (FSW) but differs in fundamentals. The major difference is not only in the tooling pin functionality, but also in geometry [17,69–72]. It generates friction heating by rotating the friction tool against the metal part of the joint. The resulting local heating rapidly diffuses to metal/polymer interface to cause the melting of polymer in contact with the metal underneath the rotating friction tool. By design, such friction-based direct joining processes using

rotational friction tool simultaneously produces both localized heating and pressure through the rubbing action between the rotating tool head and the metal surface. A sufficient closing contact pressure at the joint interface is necessary to keep the joining counterparts in close contact as in the case of the laser joining.

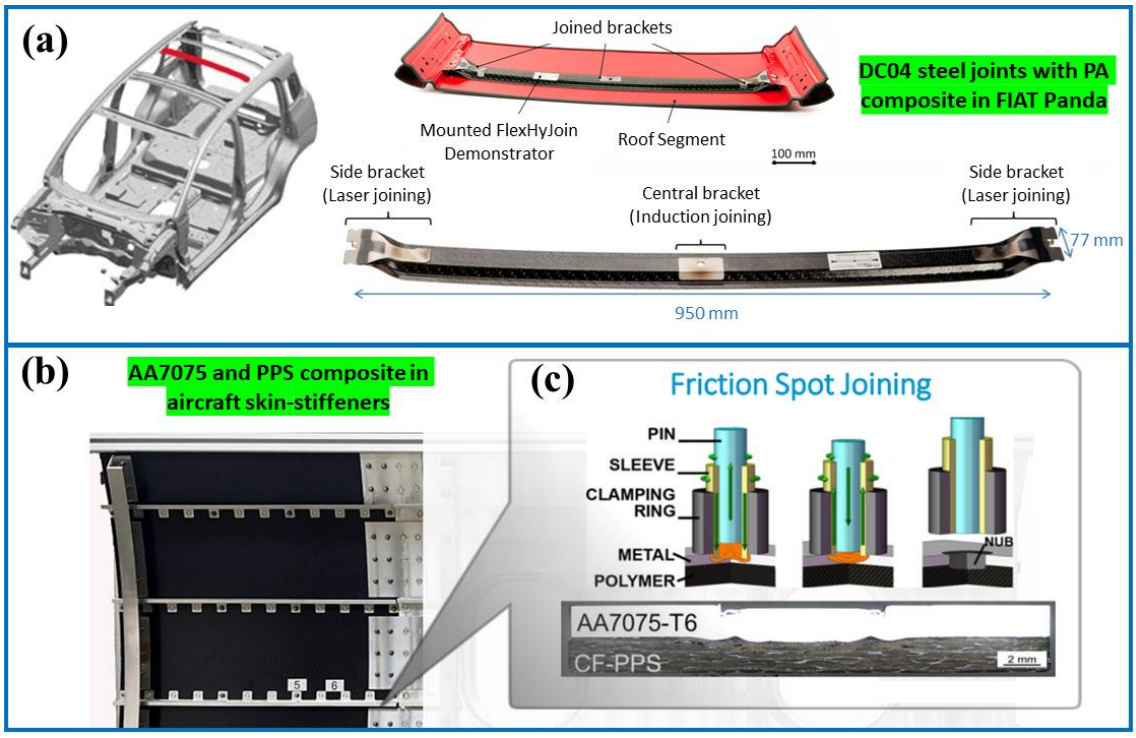


Figure 2.7: (a) Fiat panda roof grill made of steel-PA composite using laser and induction joining [www.compositesworld.com], (b) Aircraft fuselage structure made of Al-PPS composite using friction spot joining [17,68]

Such a contact pressure can be achieved through the same unitary system (embedded with the tooling system) or by a binary system (externally via clamps or temporary fixtures). It can be used either for spot (Figure 2.8 and Figure 2.9) or linear (Figure 2.10) joining configurations under the same principal. The linear joining configuration has been termed as friction lap welding (FLW) or friction lap processing (FLP) and was initially used by Okada et al [147] to join metal and polymer sheets. The spot joining configuration has been termed friction spot joining (FSpJ) and has been found considerably advantageous due to its ease of process control.

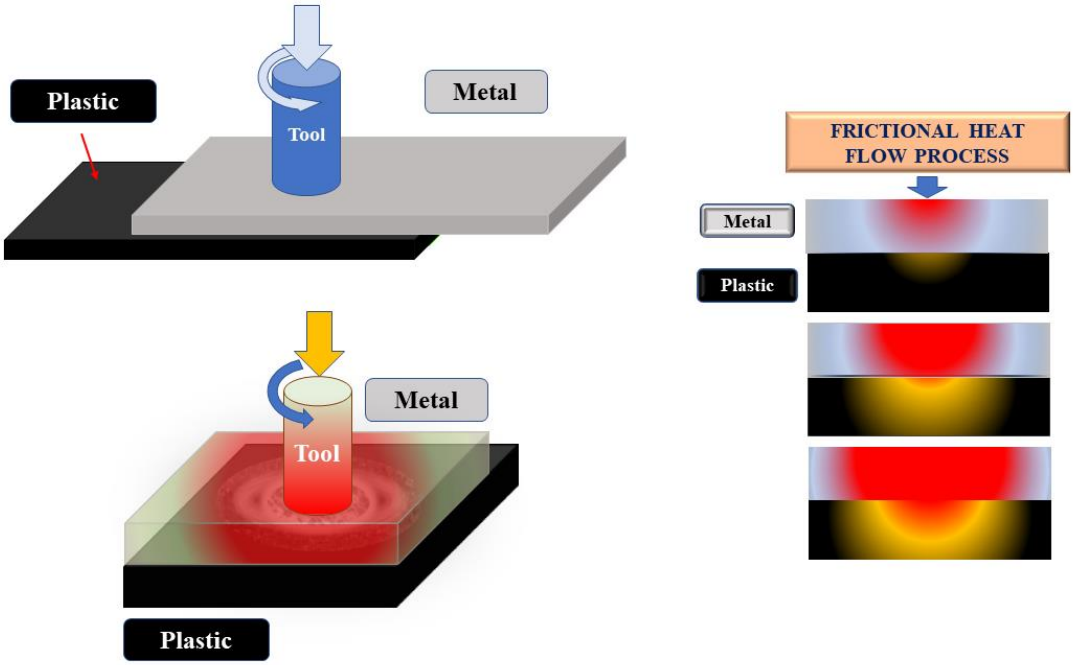


Figure 2.8: Schematic of friction-based spot joining method

2.2.2.2 Key process parameters and joint formation mechanisms

The tool impression area, tool rotation rate, plunge force or depth, and weld time (spot time in spot joining configuration or linear welding speed in linear joining configuration) play important roles to achieve desired joining between a given metal and polymer combination. The diffusing heat resulted from friction heating rapidly raises the polymer temperature, and the continuous heat generation raises the volumetric temperature above the bulk melting point of the polymer (Figure 2.8 and Figure 2.9). Thus, this molten polymer reacts with the metal surface present at the vicinity forming the chemical bond at the joint interface under the localized heat and pressure conditions. Excess temperature thermally decomposes the polymer material and deteriorates the joining interface by introducing gaseous bubbles both in friction spot joining (FSpJ) and friction lap welding (FLW) unequivocally [73–75]. For example, Khan et al [21] used spot joining configuration to achieve good interfacial direct bonding between AA6061 and PP composite and

found that an initial minimum contact pressure achievable through fine-tuning the friction tool forge depth, for which 1800 RPM and 12-sec spot time seemed to provide high quality interfacial bonding, as shown in Figure 2.17b. The spot weld time was found to be affecting the joint formation at a constant tool rotation rate and forge depth. Liu et al [72] utilized the FLW (Figure 2.10) to join AA6061 and MC Nylon-6 (PA6) and achieved superior quality joints at 3000 rpm and 200 mm/min linear welding speed. The welding speed for linear welding was seen to be affecting the polymer melt pool and interfacial bond formation differently. A higher linear welding speed, although, reduced the thermal energy (Figure 2.11) and bubble volumes, it also reduced the polymer melt pool volume. A further examination of the linear welding speed effects on joint strengths suggested that the joint strength decreased with increasing welding speed, however, not more than 22% for a 5 m/min welding speed compared to a 1 m/min welding speed [76].

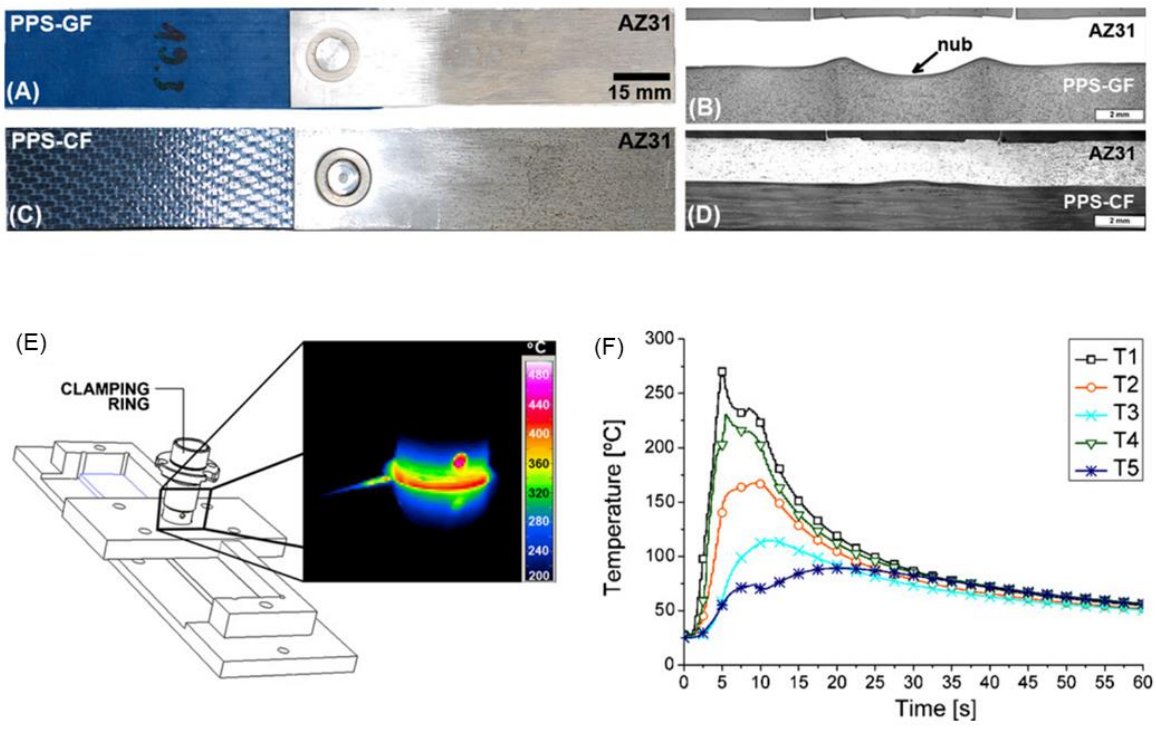


Figure 2.9: Spot joints made using FSpJ method, cross-section and process temperature characteristics [71]

2.2.2.3 Joint strengths and structural applications

Due to lack of joint design guidelines and well-accepted strength testing methods, a common practice of using the nominal area defined by friction tool impression has been used in literature for joint strength estimation [17,71,72,77,78]. In case of FSpJ, using the outer sleeve area the joint strength was found to be over 20 MPa for AZ31/PPS-CF joint under optimal parameters of 1950 rpm, 0.25 mm plunge depth and 8 sec spot time [71]. Under the same tooling configuration AA2024/CF-PPS joints provided similar results although at 2900 rpm and 4.8 sec spot time [77]. Figure 2.9 demonstrates aluminum alloy joined with the PPS composite using FSpJ in an aircraft skin panel to emphasize the adoptability of friction based joining methods in aircraft manufacturing industry.

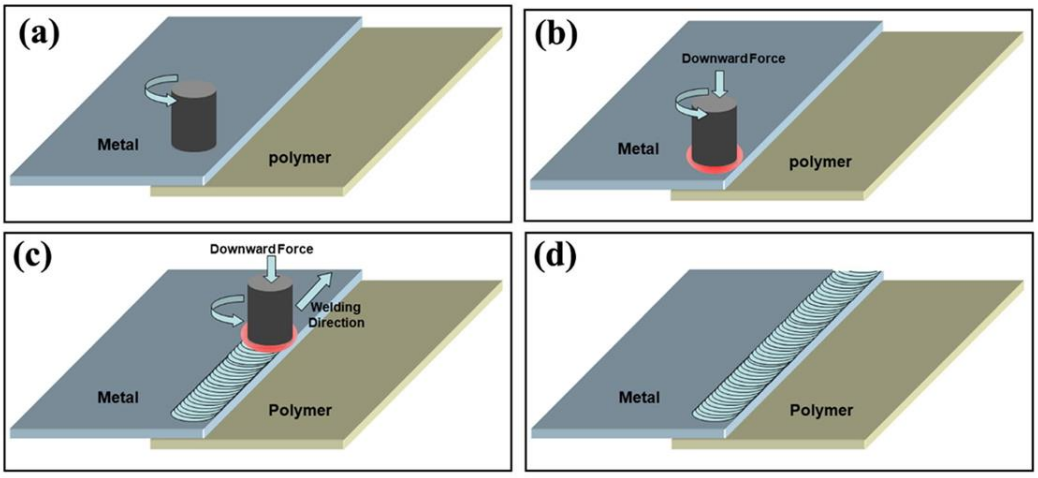


Figure 2.10: Friction lap joining schematic for metal-polymer joining [17]

2.2.3 Roles of chemical bonding

To achieve maximum joint strength in a metal to polymer joint, one straight forward way adopted in some of the publications is to demonstrate that a polymer to metal joint under lap-shear condition fails away from the weld area, e.g., across the polymer substrate, which is referred to here as base material (BM) [21,78]. Although this may be achieved through some of the traditional

joining processes, such as adhesive bonding with sufficiently large bonding area design and/or introducing mechanical interlocking, chemical bonding at molecular level is highly desirable for hermetic sealing purposes. Along this line, Liu et al [20] provided some direct evidence of Al-O-C type chemical bond formation at the joining interface between PA6 and aluminum alloy, resulted in a joint strength higher than PA polymer base material. Khan et al [21] further achieved similar results for PP/6061 joints with a PA6 type seeding layer placed at the interface between aluminum alloy and PP composite. Such type of covalent bonds can also act as a barrier for moisture penetration through the interface to provide strong hermitic sealings. Based on these promising results, a brief discussion on various types of chemical bonding at the interface is provided in the ensuing section.

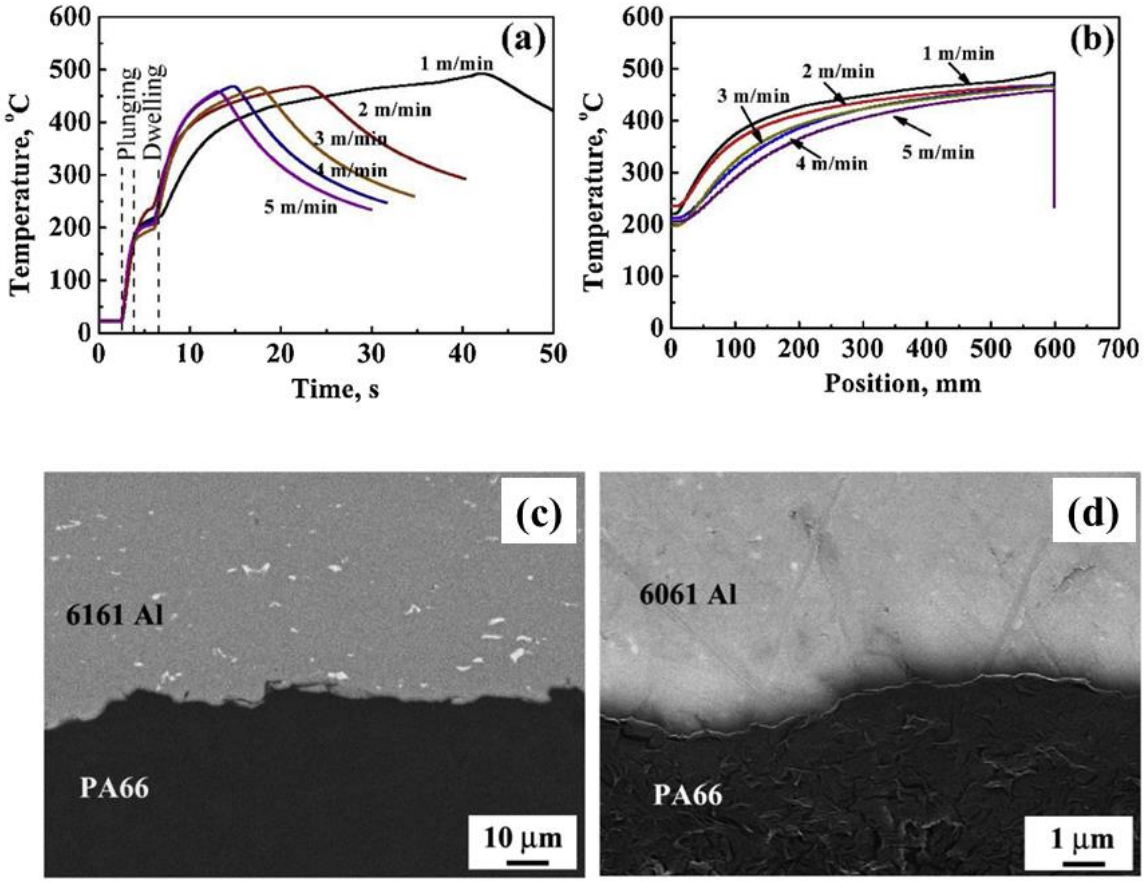


Figure 2.11: Temperature and cross-section characteristics under friction lap joining method [78]

2.3 Direct Chemical Bonding Between Polymer and Metal

2.3.1 Role of functional groups

Once the necessary localized heat and pressure conditions can be achieved to melt the polymer at polymer/metal interface, the ability for forming chemical bonds is dependent on the chemical structure of the polymer under consideration. Based on the electronic charge affinity, polymers can be either functional polymers (polar polymers) or polyolefins (functionally inert or non-polar polymers) [79]. Functional polymers have active functional groups made of electronegative species, such as oxygen, (-O) or nitrogen (-N) attached to the main chain or branching chain of the polymer, are hydrophilic and polar in nature, such as PA-6 (Figure 2.12b). On the other hand, polyolefins don't possess any active functional group or electronegative species in or around the main chain of polymer, and are hydrophobic, functionally inert, or non-polar in nature, such as PP (Figure 2.12a).

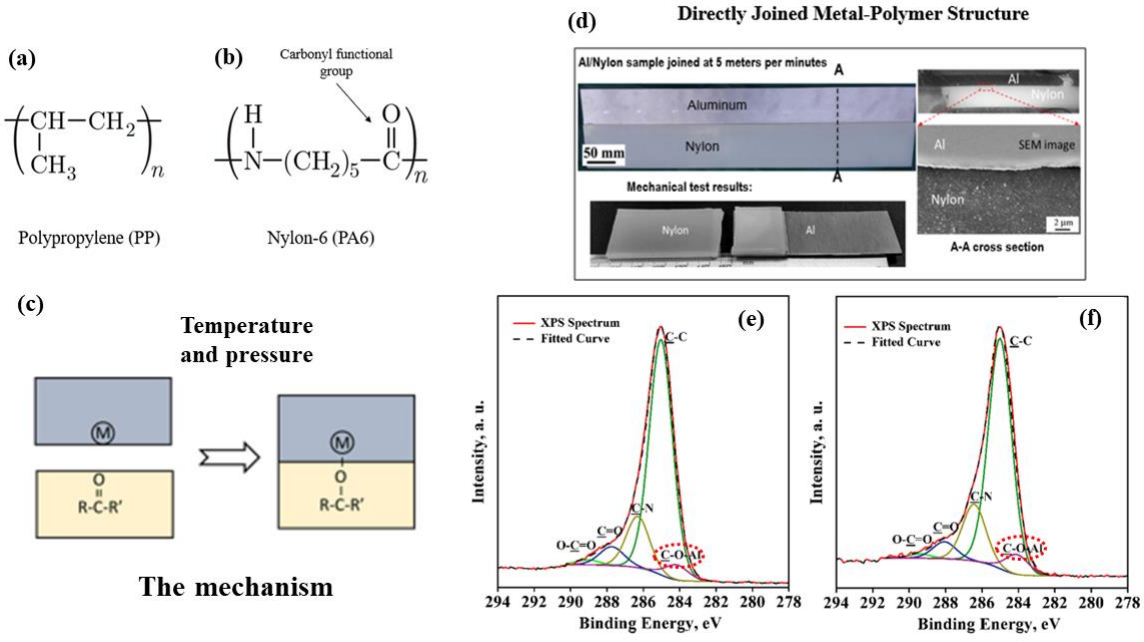


Figure 2.12: (a) Non-polar polypropylene, (b)PA6 with carbonyl group, (c)chemical interaction at the joining interface of metal and polymer, (d) AA6061 and Nylon joining under FLW and cross-section views [20], (e & f) XPS spectra confirming C-O-Al bonds at 0.8 nm and 3.2 nm depths respectively [78]

Various researchers have shown successful direct joining of polymethylmethacrylate (PMMA) [57,80–82], polycarbonate (PC) [83,84], polyethylene terephthalate (PET) [85–88], polyamide (PA) [72,89–91], polyether ether ketone (PEEK) [56,92,93], and polyetherimide (PEI) [94,95] polymers with metals. These polymers have at least one active functional group, made of oxygen (-O) and thus are polar and functionally active. Liu et. al. [20], illustrated that functional groups like carbonyl (C=O) help developing chemical bonds with metals under optimal conditions. Thus, the direct joining with metals without any surface modifications can be effectively achieved if carbonyl (or like) functional groups are present in the main chain of the polymer such as nylon-6 (PA6) shown in Figure 2.12b. A molecular dynamic simulation was developed which showed that 80% of the reacted C=O bonds form linear Al-O-C bonds and rest develop a triangular Al-O-C bonding structure Figure 2.13. A further analysis using the XPS was subsequently performed, and the formation of Al-O-C chemical bond was confirmed as shown in Figure 2.12 e & f.

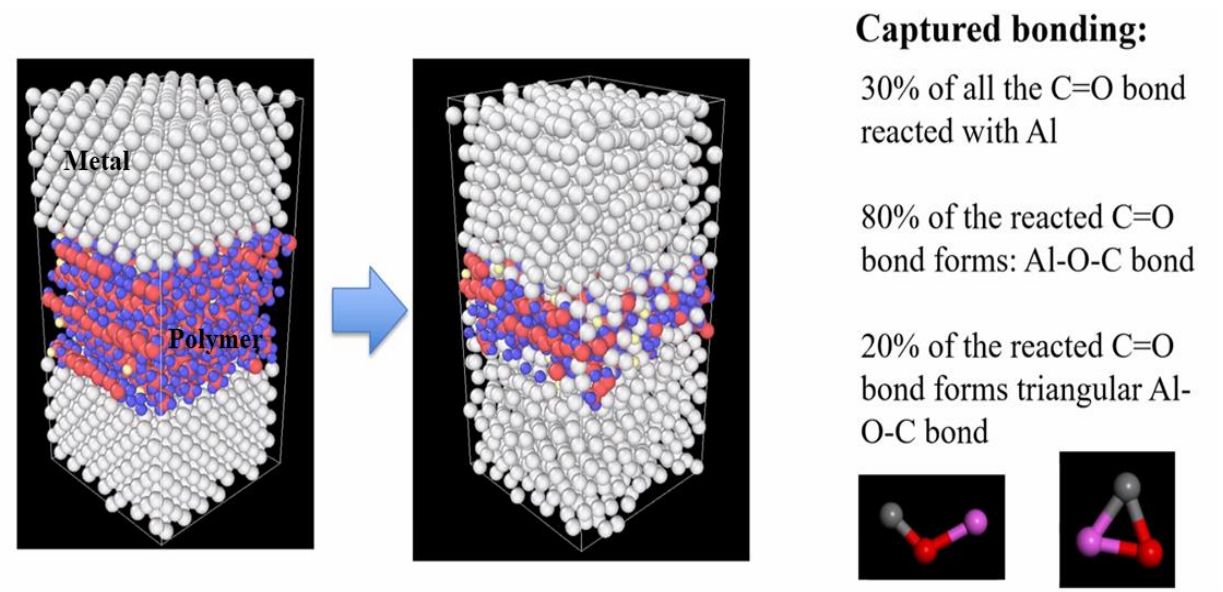


Figure 2.13: Chemical bond formation via MD simulation [96]

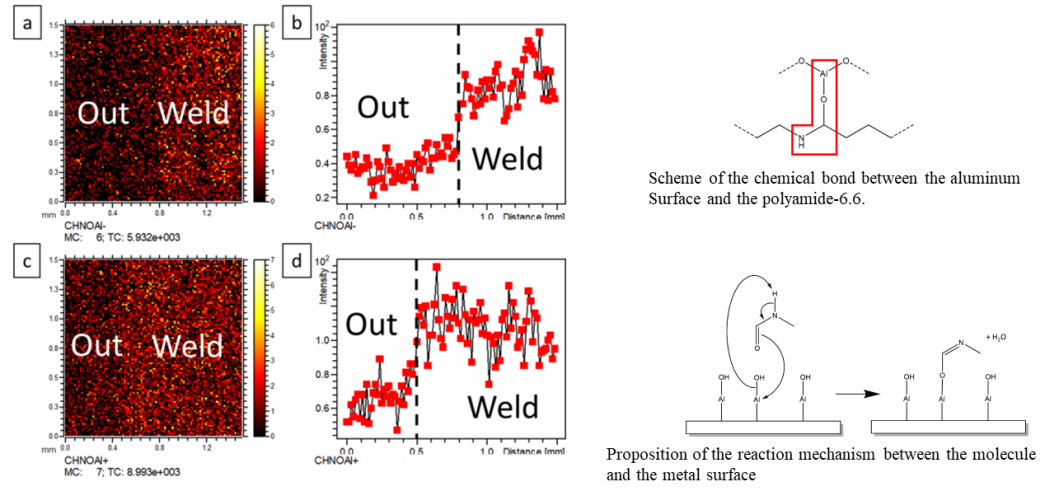
2.3.2 Thermomechanical conditions

2.3.2.1 Chemical kinetics and C-O-M bond formation

Chemical bonding at the joining interface can be defined when the covalent bond formation takes place between the metal and the polymer. Physical bonding such as Van der Waals forces or hydrogen bonding can also appear at the joining interface [18,48,97]. Once the localized heating raises the polymer temperature to its flowable state (melting point), its polymeric chains with functional groups gain energy to actively interact with metals at the molecular level. At the same time, surface energy increases on the heated metal surface and the available carbonyl groups in the polymer develop chemical bonding to form an intimately bonded interface. Chemical bonds have much higher bonding energy (250-1000 kJ/mol) compared to either the physical forces (2-40 kJ/mol) or hydrogen bonds (50 kJ/mol) [98]. Covalent bonds are the strongest bonds after ionic bonds among other types of bonds [98,99]. Which further substantiated the conclusion by Liu et al [20] that the C-O-M type covalent bonding must have taken place between metal (-M) and polymer (=C-O-) joining counterparts at the joining interface owing to its considerably high bonding energy (Figure 2.12 e & f) observed at the joint interface [20,78].

Another important attribute of covalent bonds is the length of the chemical bonds at the polymer-metal interface. Generally, the covalent bonds are much smaller than the water molecule (≈ 0.27 nm across) and if joining interface is well-developed by forming the chemical bonds at the interface, it becomes impervious to water or moisture molecules [48]. Such an interface provides strong hermetic sealing along with good load bearing capacity to metal-polymer hybrid joint demanded for pressure containment structural applications. Additionally, the chemical bonds at the joining interface become unstable when re-heated at a sufficiently high temperature above the

melting point but below the degradation temperature of polymers. Such a reversible process provides an advantage to disassembly of metal-polymer hybrid joints for repair and reuse.



ToF-SIMS large area images and their area integration along the x-axis (a and b) for CHNOAl- and (c and d) CHNOAl+

Figure 2.14: ToF-SIMS spectra near weld line for Al-PA joint and proposed model chemical reaction [100]

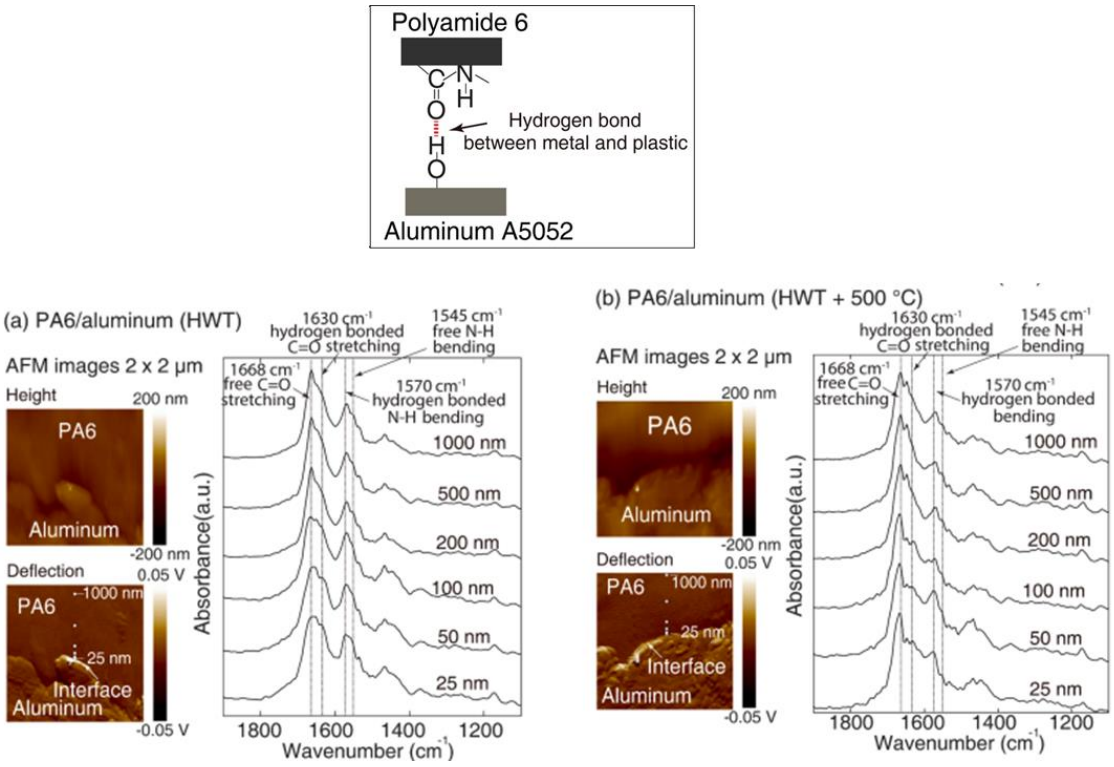


Figure 2.15: Hydrogen bond formation during Al-PA joining and IR spectra at Al-PA joint interface [97]

2.3.2.2 Alternative chemical bonding possibilities

Hirchenhahn et al [100] have performed an interesting study and proposed another chemical bonding theory between PA66 and the native oxide of aluminum sheet when joined using laser joining process. They suggested that the native oxide layer gets transformed into surface hydroxyl groups and then this hydroxyl group reacts with the available carbonyl group (-C=O-) group in the PA66 chain to formulate $CHNOAl^{+-}$ type species (Figure 2.14). They further investigated the covalent chemical bonding between the aluminum and polymer chain using XPS and time of flight secondary electron microscopy (ToF-SIMS). In their investigation they concluded that C-O-Al chemical bonds were indeed formed between the carbonyl group and the available aluminum by the means of ToF-SIMS rather XPS. Zhao et al [97] have further illustrated a different bonding mechanism under injection molding of PA6 polymer over AA5052 sheets. Due to the presence of inherent oxide on the aluminum surface and susceptibility towards hydrocarbons, the formation of metal hydroxide is probable. Under such circumstances, the metal hydroxide can also contribute towards chemical reaction sights. Although there appeared a significant level of mechanical interlocking at the joint interface, they concluded that the observed joint strength was significantly enhanced by the hydrogen bonding between the -CONH (containing -C=O- carbonyl group) group of the PA6 and the hydroxyls (-OH) on the aluminum surface. Using AFM-IR, they confirmed the formation of hydrogen bonds at 1630 cm^{-1} wavenumber conforming with the IR spectra at the joining interface (Figure 2.15). All these studies further demonstrates that the presence of carbonyl group (-C=O-) is critically important to achieving a strong chemical bonding between metal and polymer substrates.

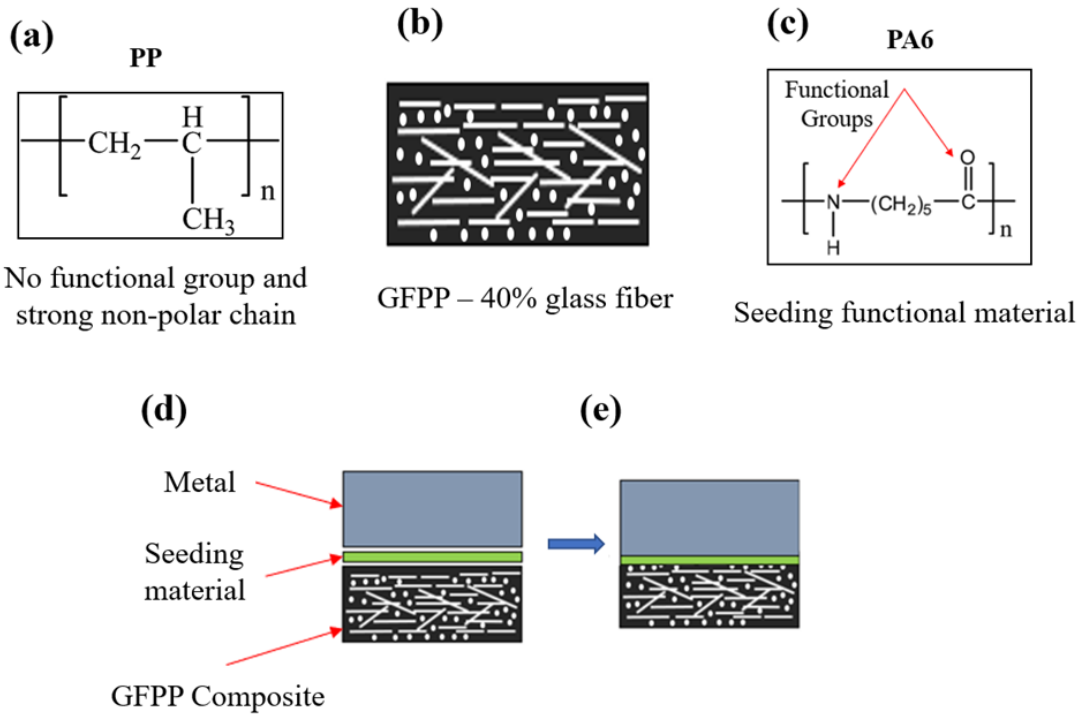


Figure 2.16: Schematic of functional group seeding methodology.

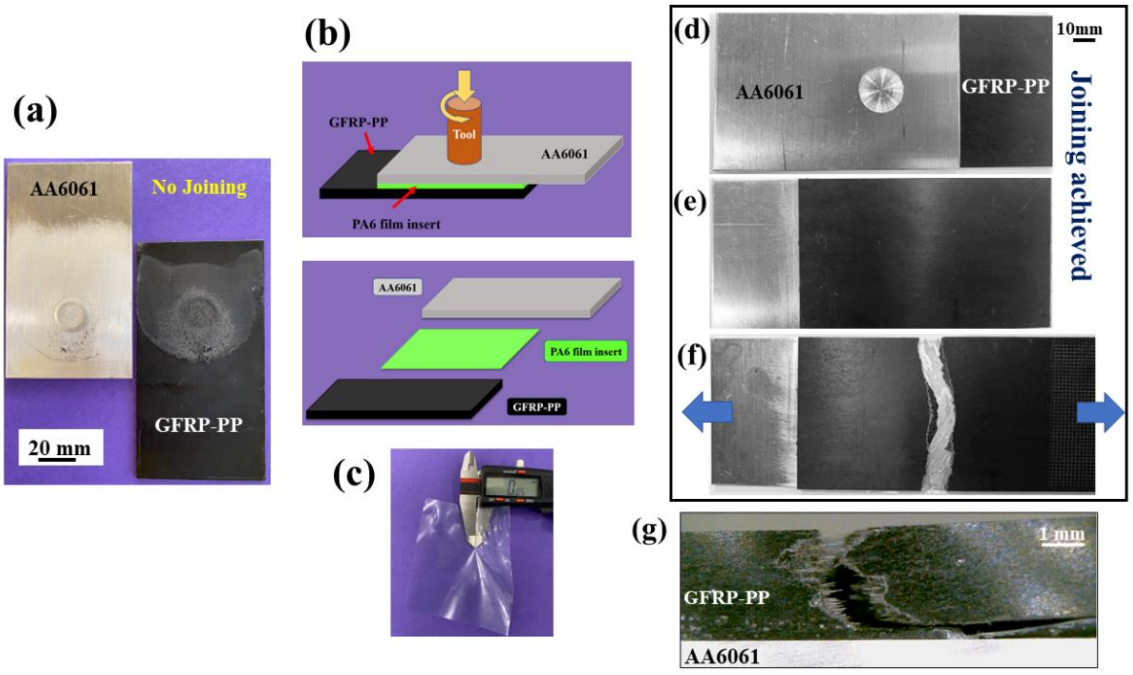


Figure 2.17: Al-GFPP joint formation using functional group seeding and substrate failure [21]

2.3.2.3 Functional group seeding

Non-polar polymers, i.e., polymers without functional groups in their chemical structure, are not capable of directly forming chemical bonds at the metal-polymer interface [20,101–105]. One cost-effective solution was to introduce functional group seeding either in-situ or ex-situ. Along this line, Liu et al [48,106] have recently proposed that 3D distributed chemical bonds (3D ChemBonds) can be produced in-situ between metal and polymer through trapped air pockets at the joint interface. These air-pockets induce the necessary carbonyl groups in the inert polymer which in turn helps form the chemical bond observed.

Khan et al [21] recently developed a simple and effective functional group seeding method via using a readily available PA6 thin film between aluminum alloy and PP composite to enable the metal-PP composite joining under friction based joining process, as illustrated in Figure 2.16. This technique is shown working well for polymer composites with inert polymer resins and any combination of reinforced fibers. Once the seeding material is placed between the metal and the inert polymer composite sheets, suitable conditions of temperature and pressure need to be imposed to melt both polymers and formulate an intermixed multi-material fiber composite at the interface. Using an off-the-shelf 50 µm thin PA6 film not only the joining was enabled between aluminum alloy and GFRP-PP composite (Figure 2.17), but the load bearing capability was also maximized such that the joint did not fail under the lap shear tensile condition, rather, the base GFRP-PP material failed at the bulk material through-thickness (Figure 2.17).

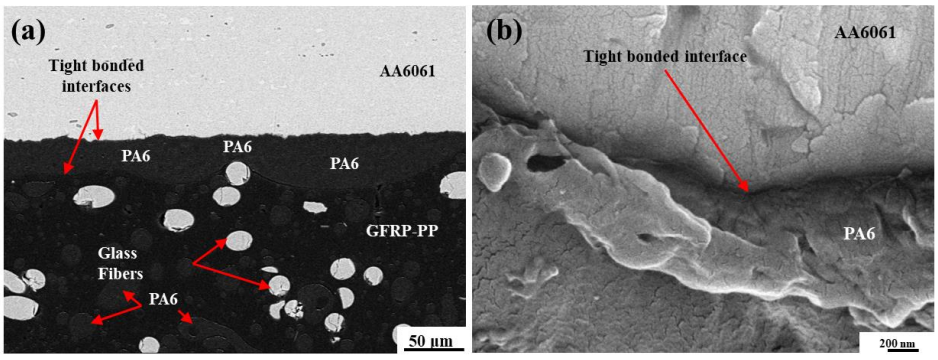


Figure 2.18: Bonding interface in Al-GFPP joints [21]

Their investigations showed that the joint interface between PP and aluminum alloy was intimately bonded through the thin PA6 intermediate layer forming an inter-mixed composite network among the available glass fibers and the PP matrix (Figure 2.18). A closer look at the Al-PA interface (Figure 2.18) revealed that the joining interface is indistinguishable at a 200 nm length scale suggesting strong possibility of chemical or molecular level bonding at the joint interface between Al and PA materials.

2.3.3 Bonding and joint strength enhancement methods

Although direct chemical bonding between metal and polymer substrates can be achieved if inherent functional groups are present in the polymers (polar polymers such as PA or PC), for engineering applications, additional measures for ensuring a sufficient joint strength is required. This is because chemical reaction sights at a joint interface can be limited or nonuniformly distributed, due to process variability. There are numerous metal or polymer surface or bulk material pre-treatment techniques being reported in the literature, as briefly highlighted below.

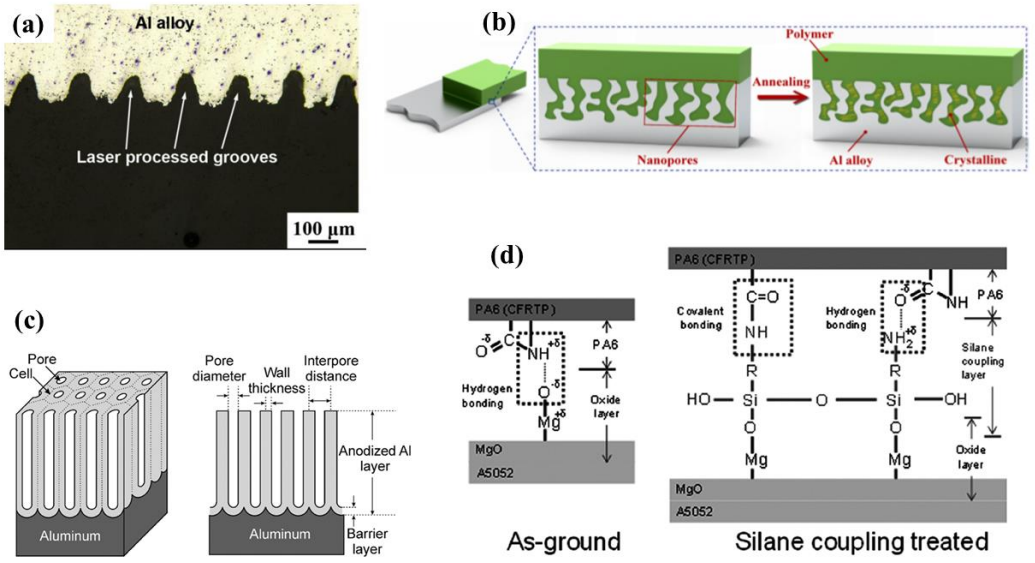


Figure 2.19: Metal surface pre-treatment methods: (a) laser texturing on the metal surface [22], (b) chemical etching method to generate micro mechanical anchoring effect [107] , (c) surface anodization in aluminum to provide honeycomb pores [108], (d) mechanism of silane coupling [109]

2.3.3.1 Metal pre-treatment

Metal pre-treatment can be used to generate mechanical features at various length scales to assist and increase mechanical interlocking effects [110–115]. When performed at micro or nano scale [116–119], this also increases the surface energy of the metal surface and provides higher wettability. Laser texturing (Figure 2.19a) has been efficient to develop mechanical grooves to provide anchoring effect and increase joining between metal and polymers [22,120–122]. A sequence of chemical etching using sodium hydroxide (NaOH), hydrochloric acid (HCl) and hydrazine (N_2H_4) is another way to locally dissolve metal surface (usually soft metals such as aluminum alloys) and generate nanopores (Figure 2.19b) to assist seeping in the polymer melt and form micro-mechanical interlocking effects [107]. Electrochemical etching (surface anodizing) has also been an effective method to generate a controlled honeycomb morphology (Figure 2.19c) on aluminum alloys for joining with non-polar polymers [108,123–125]. Alternatively, silane type chemical coupling agents [126–128] and plasma electrolytic oxidation [129,130] can be used on the metal surface when mechanical anchoring features are not desirable. Silane is a chemical coupling agent with multiple carbonyl (-C=O-) type functional groups. Due to a strong polar nature (Figure 2.19d), it reacts with the metal surface (or native oxide when available) to form strong linkages between the metal and the polymer joining partners. For example, it generates chemical reaction sites by formulating a covalent bonding in addition to the proposed hydrogen bonding compared to the untreated condition (Figure 2.19d) when joining aluminum alloy with PA6 [109].

2.3.3.2 Polymer pre-treatment

Other than micro-mechanical interlocking methods, the polymer side can be treated either on the surface or in a bulk manner [133–137]. These processes share the same principle of either inducing or providing functional groups (-C=O-) on the surface or in the bulk of the polymer

matrix and are called polymer functionalization. For example, using controlled atmospheric and inert vacuum plasma treatments distinguishable carbonyl groups (-C=O-) can be generated on the PP surface (confirmed by XPS in Figure 2.20a) [104,131,138–140]. On the other hand, a bulk grafting of PP using anhydride has also proven very vital to functionalize PP and enable joining with metal counterparts [141–145].

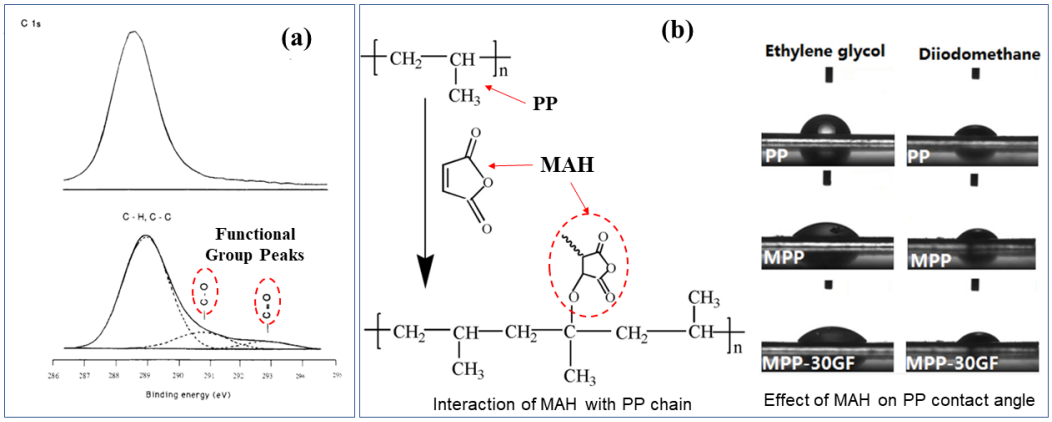


Figure 2.20: Polymer pre-treatment methods: (a) effect of plasma treatment on PP surface conditions [131], and (b) effect of MAH grafting on PP [132]

Maleic anhydride (MAH) is one of the most used grafting compounds which contains multiple carbonyl type (-C=O-) functional groups in its cyclic chemical structure (Figure 2.20b). Untreated PP can be used in small pellets in a blend with MAH and the blend can be co-extruded to form a modified grafted PP (MAH-g-PP) below the decomposition temperature of PP. Carbonyl-type functional groups thus can be grafted in the PP and the surface energy of such grafted-PP increases [101,137,146]. Surface energy increase and introduction of functional groups make it possible for grafted PP to react chemically with the metal joining partner under the prescribed localized heat and pressure conditions.

2.3.3.3 Limitations of bonding enhancement methods

Most of the surface treatment methods discussed above are still cost- and time-prohibitive for use in mass production environment. For instance, mechanical or physical surface modification

of metal side is time-consuming. The resulting mechanical protrusions tend to serve stress concentration sites in structural applications. Chemical bulk structure modification or chemical surface treatment on polymer side involves various steps to be followed to achieve a reasonable bonding strength in metal polymer hybrid (MPH) joints. The process of functionalizing non-functional (non-polar) polymers generates a very thin layer of such carbonyl groups, usually of few hundreds of nanometers, and requires immediate joining operation before degradation occurs. This can be a major limitation for its use in a production environment.

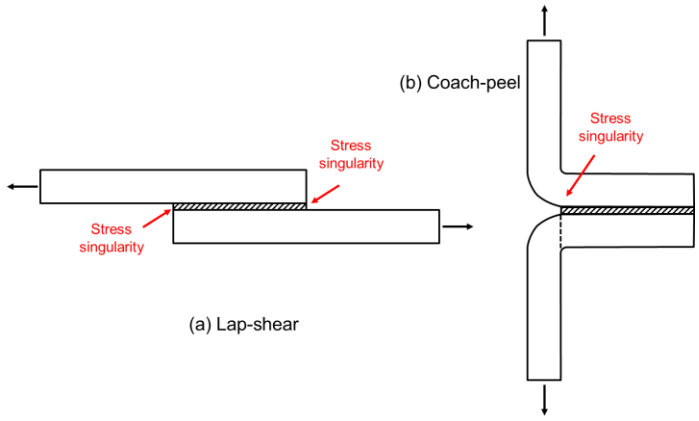


Figure 2.21: Existing testing schematics for dissimilar material joint property measurement [156]

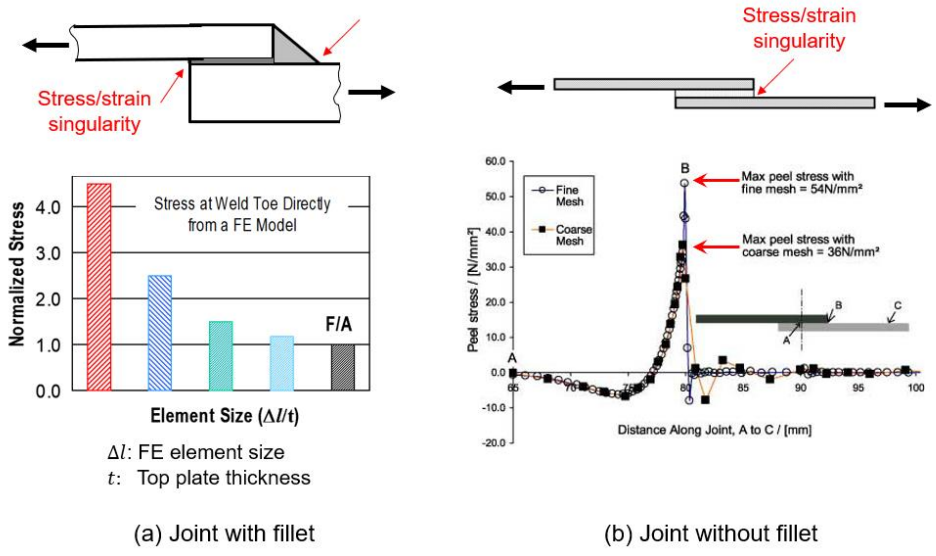


Figure 2.22: Effect of mesh size on joint strength evaluation due to inherent singularities

2.4 Joint Design and Joint Property Evaluation Methods

There have been two major developments in robust finite element methods for dealing with the aforementioned mesh-sensitivity problems caused by stress or strain singularity. One is referred to as the mesh-insensitive structural stress method (also known as a traction structural stress method) for welded structures [158-159] and the other is direct fracture mechanics approach [156]. For the latter, it would require a clearly defined crack size which can be difficult to implement for structural design evaluations. Both methods are critically reviewed here, with the focus on their applications in determining critical joint design dimensions and their use in extracting joint properties for supporting engineering design.

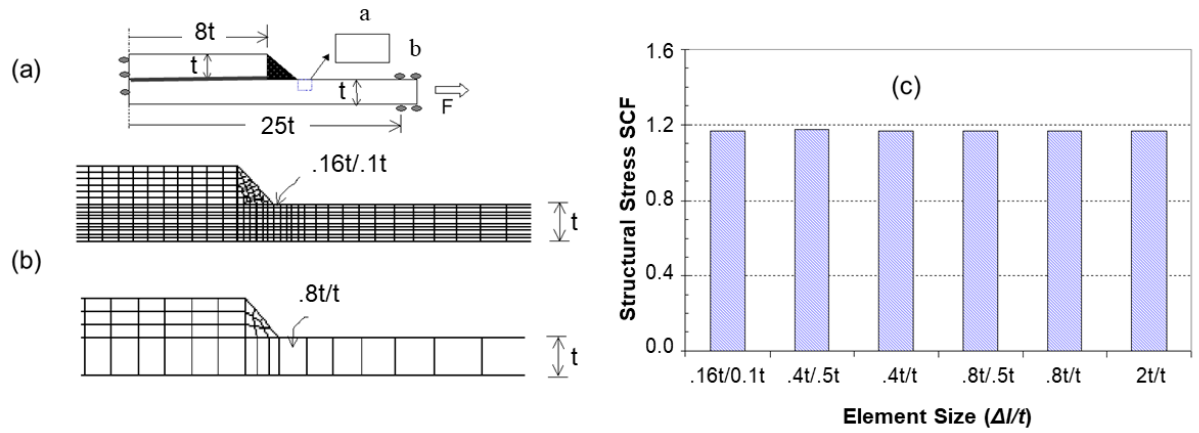


Figure 2.23: Traction based mesh-insensitive structural stress and effect of mesh size on SCF [157,158]

2.4.1 Mesh-insensitive traction stress method

There have been a number of publications over the last decade on the effectiveness of the mesh-insensitive traction stress method [160-167] and its adoption in ASME B&PV International Code [168] for design and evaluation of pressure vessel and piping components. The mechanics basis and computational procedures can be found in the aforementioned references, e.g., [158, 161, 167] and will not be repeated here due to space limitation. In essence, the key reason behind the

method's mesh-insensitivity for computing stresses at sharp corner locations (see Figure 2.21 and Figure 2.22) is that nodal forces and moments from FE computation are used by imposing an equilibrium-equivalent argument if two dimensional (2D) stress problems are considered or work-equivalent argument in the form of a matrix equation if general 3D stress problems are considered. The effectiveness for a similar lap joint shown in Figure 2.21a is summarized in Figure 2.23. For the given loading conditions and the substrate thickness combination, the resulting normalized stress (i.e., stress concentration factor, SCF) by the remotely applied stress (F/A) remains essentially the same regardless of the relative element size ($\Delta l/t$) used, as shown in Figure 2.23c.

It should be noted that another advantage of the traction structural stress method is that the stress calculated has a clear definition in terms of the failure mode (position and orientation) being considered. The traction structural stress results given in Figure 2.23c, corresponding to failure initiated at the fillet corner (often referred to as toe) position into base plate thickness, referred to failure Mode A. As explained in Figure 2.24, the traction structural stress can be computed for Mode A which has two possibilities, while Mode B represents interfacial failure [156,169,170]. Mode A is controlled by normal traction stress along its arrow line with respect to each of the substrate thickness and Mode B is controlled by the interfacial traction stress along the arrow line along the interface between Substrates 1 and 2, as further illustrated in Figure 2.25. More detailed discussions on filled welded components on how to treat Mode A versus Mode B failure mode can be found in [170-173].

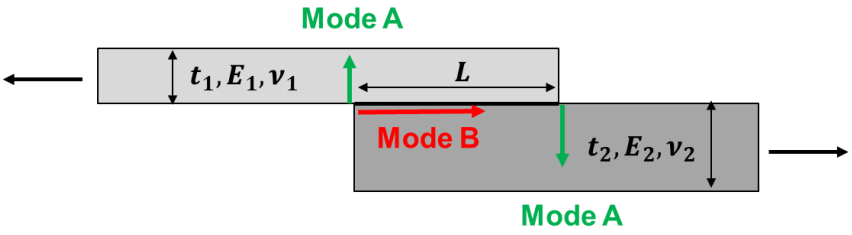


Figure 2.24:Failure modes in a typical bi-material joint

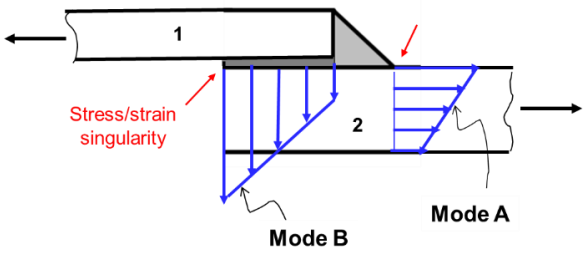


Figure 2.25: Illustration of traction stress definition controlling failure Modes A versus B

2.4.2 Joint strength property

For the dissimilar material joints, Liu et al [174] used the mesh-insensitive traction stress method discussed above to prove that PA66/AL 6061 joint shear strengths are essentially the same (up to about 5%) as welding speed varied from 1m/min to 5m/min (see Figure 2.28b), even though the nominal shear strengths measured in F/A exhibited a significant variation up to 22% (see Figure 2.28a). The joint cross-section profiles are shown in Figure 2.26, corresponding to welding speed 1m/min, 3m/min, and 5m/min, respectively. Upon a closer examination, the only difference among the three welding conditions given in Figure 2.26 was the fillet size (see the arrow lines). After the actual fillet sizes were considered in their finite element models, as shown in Figure 2.27, the shear traction stresses computed corresponding to interfacial failure (i.e., Mode B, as described in Figure 2.24) between PA66 and aluminum substrate were used for correlating the same test data given in Figure 2.28(a). This was done by multiplying the shear traction stress SCFs corresponding to the joint fillet profiles shown in Figure 2.27 against their respective F/A values in Figure 2.28(a). The results are shown in Figure 2.28(b) which shows that all three welding conditions exhibit essentially the same joint shear strengths within a scatter band of 5%. The shear strengths so calculated offer transferability, regardless of test specimen geometries and loading conditions

and therefore can be directly used in complex structural models for design and performance optimization purposes.

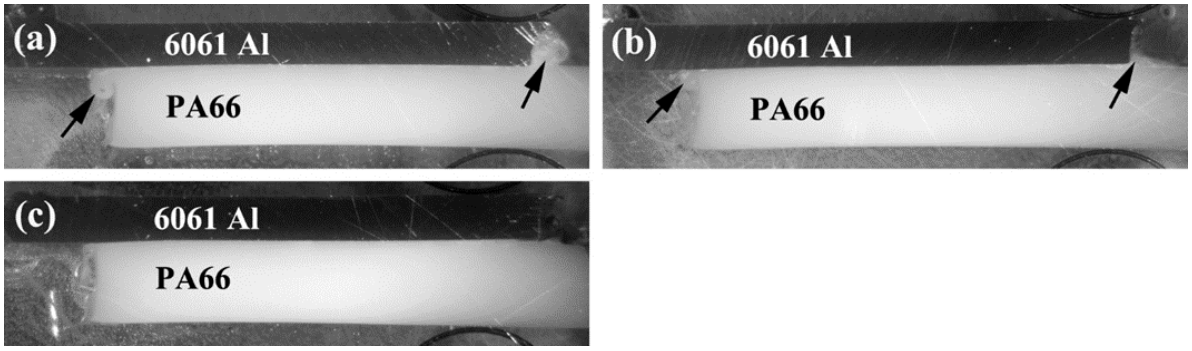


Figure 2.26:Fillet formation in PA66/AA6061 joint [174]

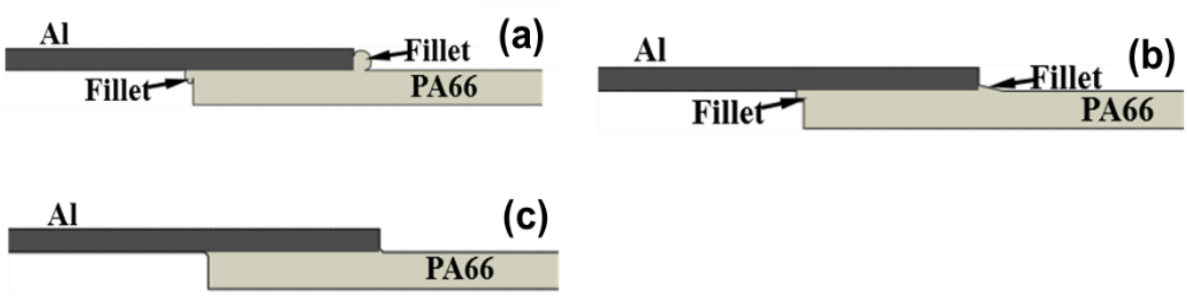


Figure 2.27: Fillet feature approximations for FE modeling using mesh-insensitive structural stress method [174]

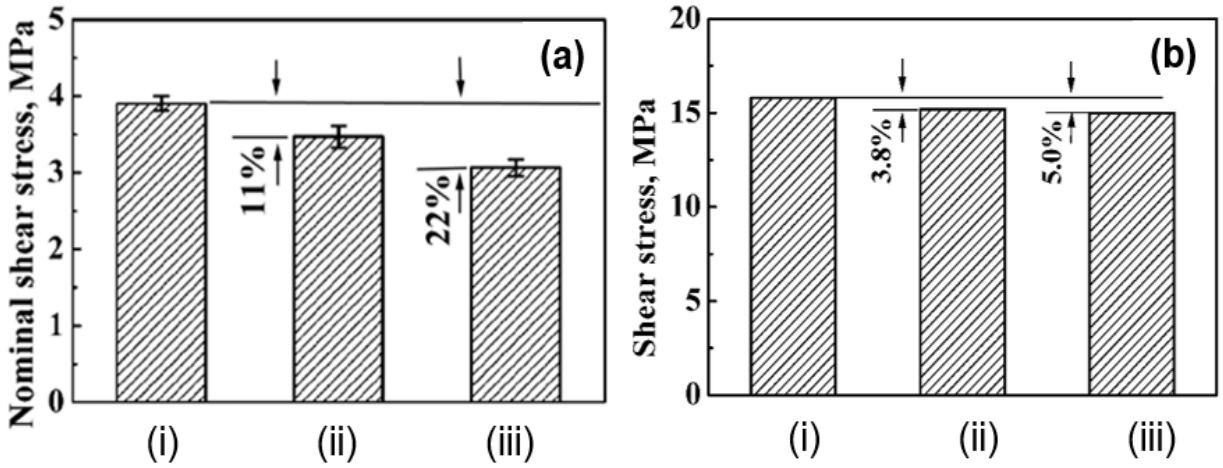


Figure 2.28:Traction stress-based joint shear strength results – (a) without considering the fillet features, and (b) after considering fillet features [174]

As another example for demonstrating the effectiveness of the mesh-insensitive traction stress method in interpreting joint strength test data, we consider the test specimens shown in Khan et al [154] for GFRP-PP to aluminum alloy 6061 joints, which resulted in Mode A failure along the PP base plate/material width (or BM failure). Although these specimens are of spot weld types, their Mode A failures along PP base plate can be approximately treated as 2D traction stress problems for illustration purpose here, so that simple closed-form analytical solutions can be readily obtained for gaining insights on how the mesh-insensitive traction method described above works.

As shown in Figure 2.29, the equilibrium condition with respect to moments leads to:

$$M_1 = P \times \left(\frac{t_1+t_2}{2} - \frac{t_1}{2}\right) = \frac{Pt_2}{2} \quad (1)$$

$$M_2 = P \times \left(\frac{t_1+t_2}{2} - \frac{t_2}{2}\right) = \frac{Pt_1}{2} \quad (2)$$

where P represents applied line load (i.e., remote load divided by Substrate 2 width) at failure. Then, the traction structural stress corresponding to a given failure mode is a linear combination of the membrane and bending stresses. For the cases shown in Figure 2.29, the traction structural stress acting on the planes indicated by Line A-A with respect to substrate-1 (AA 6061) and Line B-B with respect to substrate-2 (PP) can be expressed for per unit specimen width (into the paper) as:

$$\sigma_{s1} = \sigma_{m1} + \sigma_{b1} = \frac{P}{t_1} + 6\frac{M_1}{t_1^2} \quad (3)$$

and,

$$\sigma_{s2} = \sigma_{m2} + \sigma_{b2} = \frac{P}{t_2} + 6\frac{M_2}{t_2^2} \quad (4)$$

respectively. Since $t_1 = 2.00\,mm,\ t_2 = 2.70\,mm$, as given in Khan et al [154], the traction stress acting on the plane described by line B-B is becomes $\sigma_{s2} = 0.370P + 0.823P$ which corresponds to the failure position observed in experiments.

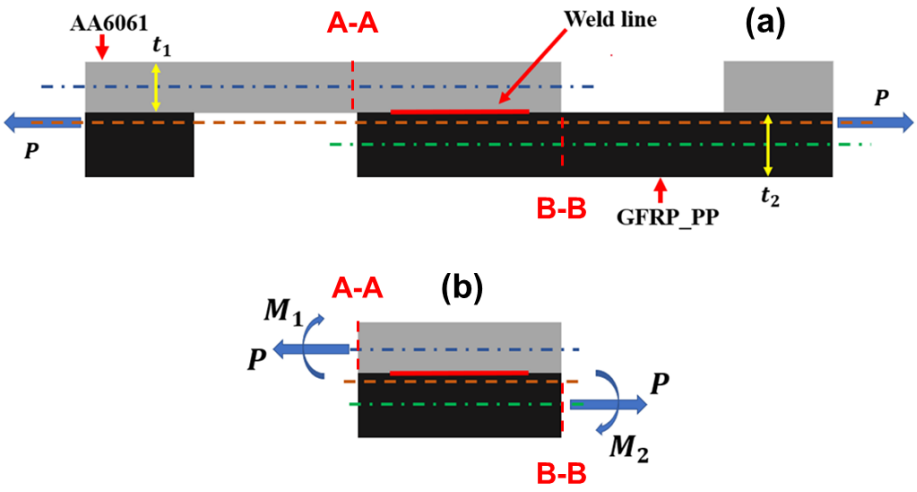


Figure 2.29: Analytical traction structural modeling of a lap-shear joint specimen between AA 6061 and PP (GFRP)

To determine the static strength in terms of the membrane and bending parts of the traction stress given in Eq. (4), a well-established membrane and bending interaction diagram in terms of $(\sigma_m + \sigma_b)/S$ versus σ_m/S (see ASME B&PV code Section VIII Division 2) can be used here, as illustrated in Figure 2.30, where S presents the tensile strength of PP from simple tensile strip tests. The curve and vertical straight line represent the theoretical static failure envelope. The AA6061/PP joint test results from Khan et al [154] expressed in terms of $(\sigma_m + \sigma_b)/S$ versus σ_m/S are summarized in Figure 2.30 below. These results are also plotted against the interaction diagram in Figure 2.30, which shows that the failure envelope provides a reasonable estimation of the failure conditions observed from the test data, demonstrating the effectiveness of the mesh-insensitive traction stress in establishing test data transferability.

Table 2.1: Test data and corresponding membrane and total traction structural stress values

Sample	σ_m/S	$(\sigma_m + \sigma_b)$/S
Sample-1	0.50	1.59
Sample-2	0.52	1.67
Sample-3	0.53	1.70

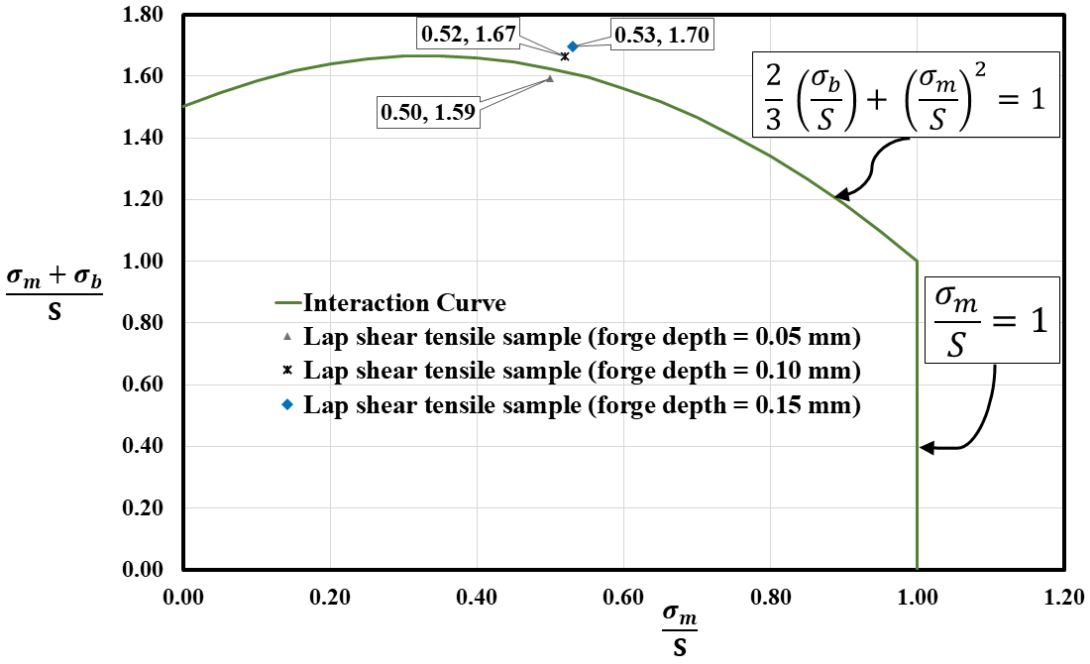


Figure 2.30:Membrane and bending interaction diagram for determining static strength and applications in interpreting AA 6061/PP (GFRP) joint test data

2.4.3 Joint fatigue property

In addition to facilitating the extraction of joint static strength properties as discussed in the previous section, the traction structural stress method has been shown effective in extraction of dissimilar material joint fatigue properties. One example along this line is the recent work by Zhang and Dong [156] on modeling of adhesive-bonded test specimens in the form of lap shear (LS) and coach-peel (CP) configurations, as shown in Figure 2.31a. If the nominal stress (F/A)

range is used, it can be seen that the lap-shear and coach-peel test data follow their own scatter band in the form of an S-N plot in the log-log scale (Figure 2.31b). Once the traction structural stress method is used, the same test data points are collapsed into a single narrow band in Figure 2.31c, indicating fatigue test data transferability. As a result, the single scatter band, and its statistical values (e.g., mean-2σ) can be used for structural fatigue evaluation of dissimilar material joints. Here σ represents the standard deviation with respect to cycles to failure.

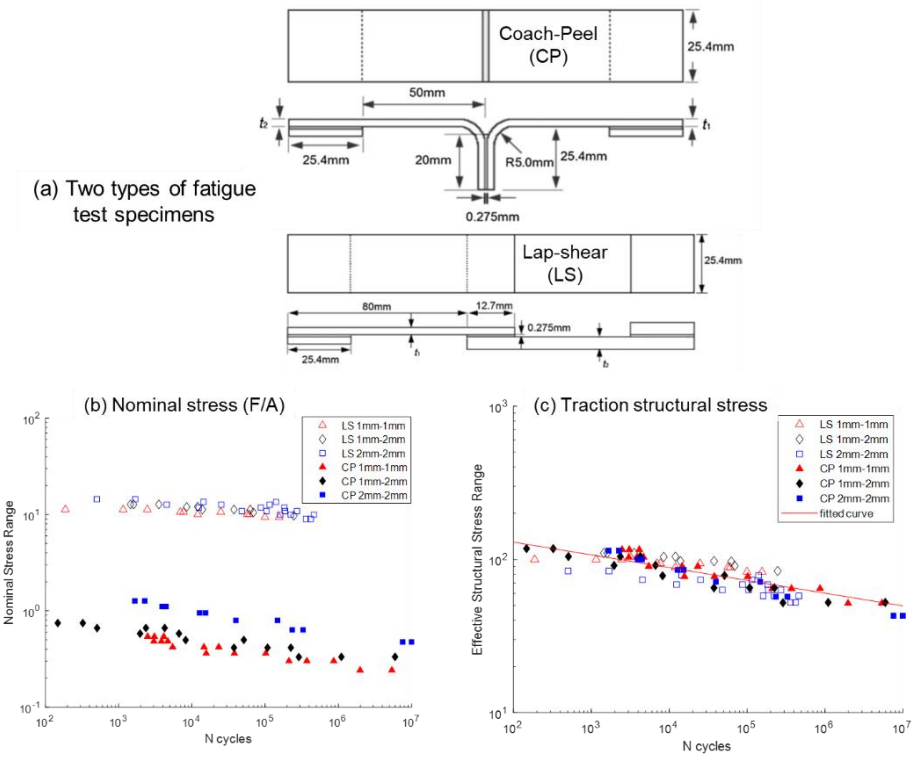


Figure 2.31:Traction structural stress modeling of fatigue in dissimilar material joints [156]

2.4.4 Optimum joint design

In addition to joint property extraction, optimum design of dissimilar material joints can be quantitatively determined by means of the new computational methods for structural applications. Both the computational fracture mechanics modeling and simplified analytical solutions recently developed by Zhang and Dong [156] have shown that there exists a threshold

value about $L/h \approx 2$ beyond which fatigue driving force in terms of stress intensity factor (K_I corresponding to Mode-I, e.g., in coach peel tests and K_{II} corresponding to Mode-II, e.g., in lap shear tests) remains constant, as shown in Figure 2.32. This indicates that a further increasing in bond area size (e.g., L) no longer offers any additional fatigue capacity.

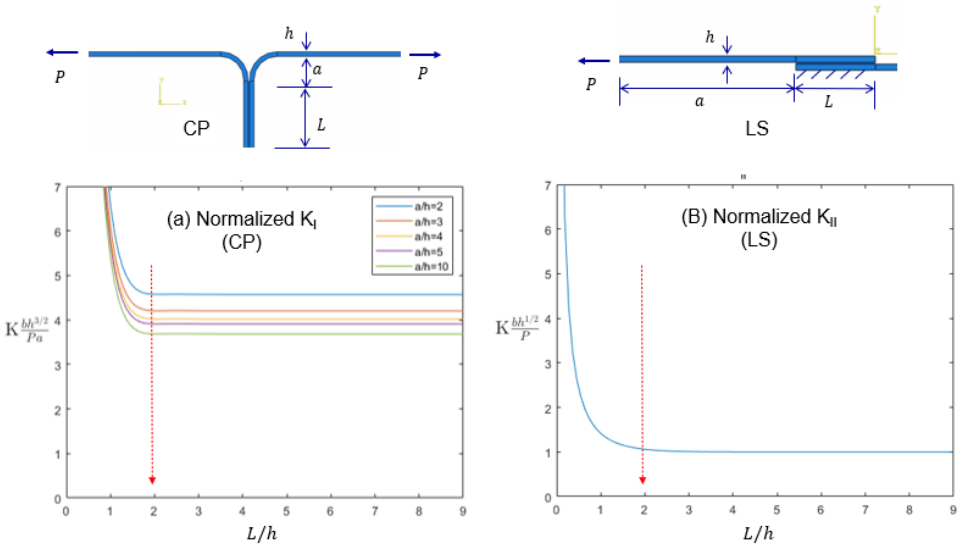


Figure 2.32:Effect of joining length on mode-I and mode-II stress intensity factor K (a fracture mechanics parameter)

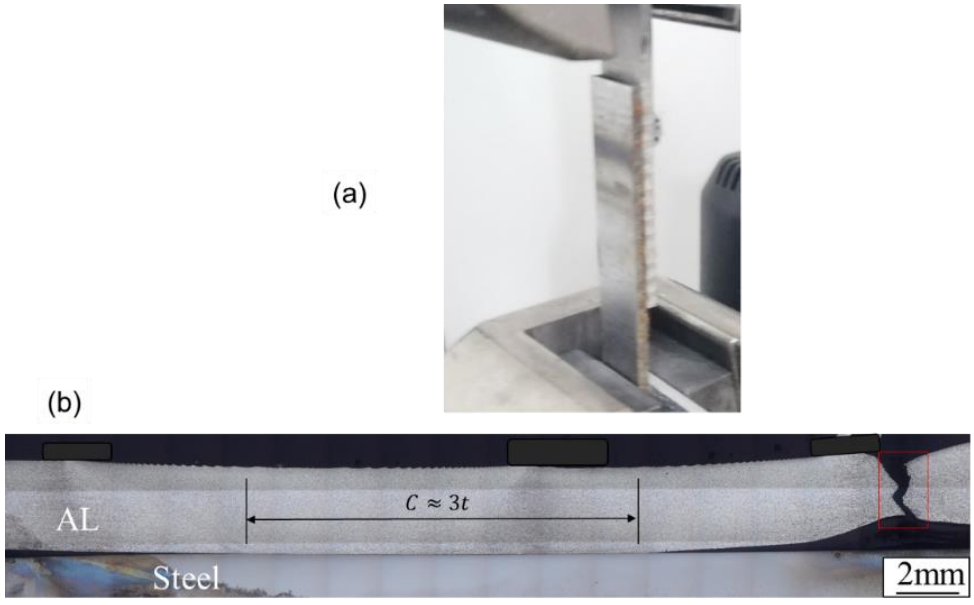


Figure 2.33: Validation of Mode A failure - aluminum to steel welded lap shear tests

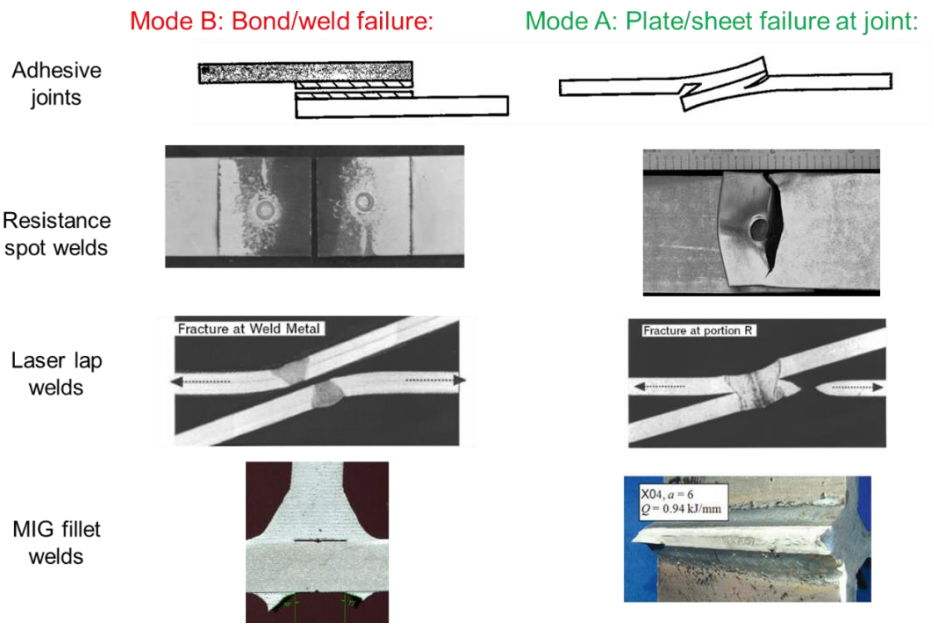


Figure 2.34: Failure Mode A versus Mode B in various joint types in which Mode A offers the best static and fatigue load capacity and should be ensured through optimum joint sizing

Indeed, the results shown in Figure 2.31 has been confirmed by experimental test data ($L/h \approx 3$), as shown in Figure 2.33 for direct welding aluminum to steel by the means of a new shear localization procedure described in [175-177]. In fact, joint design rules can be simply stated as: prevention of Mode B failure, if possible, regardless of static loading or fatigue loading. As such, Mode A failure mode provides the best load capacity under given joint type and joint position, as illustrated in Figure 2.34 covering both dissimilar and similar material joints. If the best load capacity is still not sufficient for a given structural applications, alternative joint type and/or joint position needs to be considered, as discussed in [178,179].

2.5 Unresolved Critical Issues for Industrial Applications

As discussed in sections 2.2 and 2.3, there have been numerous promising developments for achieving robust polymer to metal welding (e.g., either direct or through an intermediate carbonyl functional agent), industrial scale adoption of some of these dissimilar materials joining technologies is still at its infancy, particularly in mass-production environment. To accelerate a

broad adoption of these novel joining techniques for supporting industry's drive towards multi-material lightweighting, three major hurdles need to be overcome. These are: (1) an improved understanding of C-O-M chemical bond development mechanisms and their controlling parameters; (2) effective procedures for extracting joint properties from simple lab test specimens for supporting computer-aided engineering of multi-material structures; (3) joint design guidelines for improved jointability in process and joint performance in structural context. These are further discussed below.

2.5.1 Dominant chemical bond formation mechanism

Carbonyl functional group (C=O) has been the most important chemical component for achieving the strong direct joining between the metals and the polymers (plastic). However, there are multiple theories on the bond formation mechanisms. Al-O-C type covalent bond formation between the aluminum and the polymer chain via carbonyl group, covalent bond formation between native aluminum oxide and the polymeric chain, and hydrogen bonding between the native aluminum oxide and the polymeric chain via hydrolysis of hydrocarbons in conjunction with the carbonyl group are among the top. The Van der Waals effect at the bonding interface is also considered a contributing factor. How to experimentally confirm one dominant bonding mechanism and to what extent over others under a given direct joining process condition remains to be challenging. The ability to do so is important for developing optimized direct joining process for promoting the uniformity and sufficient length scale of the resulting covalent chemical bond. In addition to capable measurement and characterization techniques, novel experimental approaches (e.g., the alumina/PA66 coating experiment by Liu et al [180]) to isolate and promote some of the bonding mechanisms can be rather effective for elucidating favorable bond formation environment. Such insights played a key role in their subsequent process development [154,174].

2.5.2 Joint property development

As discussed in Sec. 1, once a capable direct joining process has been established, it is important to establish a mechanics-based procedure for extracting mechanical properties from lab specimen test data for supporting CAE of multi-material structures. It should be emphasized here that any joint properties, e.g., joint tensile strengths, fatigue strengths (typically expressed in terms of S-N curve in stress life or E-N curve in strain life context) must satisfy transferability requirements, i.e., properties that must exhibit invariance over specimen types (e.g., different thickness combinations of polymer and metal substrates) and loading mode (e.g., lap-shear versus coach-peel, see Figure 2.31). This aspect has not been adequately addressed, as demonstrated in Section 2.4. The recent developments in computational methods, e.g., the mesh-insensitive traction structural stress method, can be an effective tool for extracting joint properties from simple lab specimen tests for use in CAE based design optimization of complex structures. Once an effective joint property extraction procedure is in place, another benefit is that bond quality and its effect on a specific joint property parameter can be determined through either lap specimen testing or finite element modeling (see Figs. 2.29-2.330).

2.5.3 Quantitative joint design methods

Design of dissimilar material joints, particularly for direct joining methods (versus traditional mechanical fastening, as an example), is mostly done through empirical means today. As described in some recent investigations (see [154,156,174]), a proper joint design can significantly improve not only jointability and cost in manufacturing, but also joint performance in structures. Here, by joint design, we refer to three essential aspects: (1) joint location, (2) joint type (e.g., lap versus butt-seam); (3) joint detailing (bonding area size, end fillet (see Figure 2.26), and nearby geometry (see [154,156,174]). As demonstrated in Figure 2.32, for a given dissimilar

material combination, there exists an optimum interfacial bonding area or size, beyond which any benefit becomes rapidly diminished. As discussed in Section 2.4, advanced computational modeling methods are now available for quantitatively evaluating the three aspects above for structural applications. A longer-term objective should be the development of industry-wide joint design guidelines for typical dissimilar joint types and joining processes for mass-produced products for supporting a broader application of some of advanced joining processes, which will facilitate confidence building, reduce development costs, and ensure product safety.

2.6 Closure

A state-of-the-art assessment of polymer-metal joining research and promising techniques have been presented, with a particular emphasis on their potential for structural applications in the mass-produced marketplace. Direct welding of polymer to metal is not only possible but also shows the potential for applications in mass-production environments, in addition to its simplicity and excellent joint performance for some dissimilar material combinations. To accelerate a broad adoption of these novel joining techniques for supporting the industry's drive towards multi-material lightweighting, three major hurdles need to be overcome. These are: (1) an improved understanding of C-O-M chemical bond development mechanisms and their controlling parameters; (2) effective procedures for extracting joint properties from simple lab test specimens for supporting computer-aided engineering of multi-material structures; (3) joint design guidelines for improved jointability in process and joint performance in structural context.

Regarding the C-O-M chemical bond mechanisms, the carbonyl functional group (-C=O-) has been the most important chemical component for achieving the strong direct joining between the metals and the polymers (plastic). However, there are multiple theories on the bond formation mechanisms. Al-O-C type covalent bond formation between the aluminum and the polymer chain

via carbonyl group, covalent bond formation between native aluminum oxide and the polymeric chain, and hydrogen bonding between the native aluminum oxide and the polymeric chain via hydrolysis of hydrocarbons in conjunction with the carbonyl group are among the top. The Van der Waals effect at the bonding interface is also considered a contributing factor. How to experimentally confirm one dominant bonding mechanism and to what extent over others under a given direct joining process condition remains to be challenging. The ability to do so is important for developing an optimized direct joining process for promoting the uniformity and sufficient length scale of the resulting covalent chemical bond. In addition to capable measurement and characterization techniques, novel experimental approaches to isolate and promote some of the bonding mechanisms can be rather effective for elucidating a favorable bond formation environment. Such insights played a key role in their subsequent process development.

With an improved understanding of the C-O-M bonding mechanisms and some of the chemical bond quality improvement techniques reviewed in this article, some main-stream structural applications are expected to be realized in the near future for achieving ever-increasingly structural lightweight goals by the transportation industry. Along this line, the research needs for supporting the technology transition are also highlighted, particularly in the area of joint property development and effective methodologies for optimum joint design for jointability and joint performance. Some of the recently developed computational methods are demonstrated through a number of detailed examples. Then, “using the right material at the right place” can become a reality for mass-produced products for meeting today’s structural lightweighting needs.

References

[1] Lamb WF, Wiedmann T, Pongratz J, Andrew R, Crippa M, Olivier JGJ, et al. A review of trends and drivers of greenhouse gas emissions by sector from 1990 to 2018. Environ Res Lett 2021;16. https://doi.org/10.1088/1748-9326/abee4e.

[2] Keoleian GA, Sullivan JL. Materials challenges and opportunities for enhancing the sustainability of automobiles. MRS Bull 2012;37:365–72. https://doi.org/10.1557/mrs.2012.52.

[3] Kelly JC, Sullivan JL, Burnham A, Elgowainy A. Impacts of Vehicle Weight Reduction via Material Substitution on Life-Cycle Greenhouse Gas Emissions. Environ Sci Technol 2015;49:12535–42. https://doi.org/10.1021/acs.est.5b03192.

[4] Taub A, De Moor E, Luo A, Matlock DK, Speer JG, Vaidya U. Materials for Automotive Lightweighting. Annu Rev Mater Res 2019;49:327–59. https://doi.org/10.1146/annurev-matsci-070218-010134.

[5] Goede M, Stehlin M, Rafflenbeul L, Kopp G, Beeh E. Super Light Car—lightweight construction thanks to a multi-material design and function integration. Eur Transp Res Rev 2009;1:5–10.

[6] Hürkamp A, Dér A, Gellrich S, Ossowski T, Lorenz R, Behrens B-A, et al. Integrated computational product and production engineering for multi-material lightweight structures. Int J Adv Manuf Technol 2020;110:2551–71.

[7] Meschut G, Janzen V, Olfermann T. Innovative and highly productive joining technologies for multi-material lightweight car body structures. J Mater Eng Perform 2014;23:1515–23.

[8] Dong P. Quantitative weld quality acceptance criteria: an enabler for structural lightweighting and additive manufacturing. Weld J 2020;99.

[9] Conklin J, Beals R, Brown Z. BIW Design and CAE MMLV Lightweight Body in White Structure Multi Material Lightweight Vehicle (MMLV). SAE Int 2015. https://doi.org/10.4271/2015-01-0408.Copyright.

[10] Jaranson J, Ahmed M. MMLV: Lightweight Interior Systems Design 2015. https://doi.org/https://doi.org/10.4271/2015-01-1236.

[11] Blanco D, Rubio EM, Marín MM, Davim JP. Advanced materials and multi-materials applied in aeronautical and automotive fields: A systematic review approach. Procedia CIRP 2021;99:196–201. https://doi.org/10.1016/j.procir.2021.03.027.

[12] Martinsen K, Hu SJ, Carlson BE. Joining of dissimilar materials. CIRP Ann - Manuf Technol 2015;64:679–99. https://doi.org/10.1016/j.cirp.2015.05.006.

[13] Skszek T, Conklin J. Multi-Material Lightweight Vehicles Acknowledgement 2014.

[14] Pramanik A, Basak AK, Dong Y, Sarker PK, Uddin MS, Littlefair G, et al. Joining of carbon fibre reinforced polymer (CFRP) composites and aluminium alloys – A review. Compos Part A Appl Sci Manuf 2017;101:1–29. https://doi.org/10.1016/j.compositesa.2017.06.007.

[15] Galińska A. Mechanical Joining of Fibre Reinforced Polymer Composites to Metals—A Review. Part I: Bolted Joining. Polymers (Basel) 2020;12. https://doi.org/10.3390/polym12102252.

[16] Lißner M, Erice B, Alabort E, Thomson D, Cui H, Kaboglu C, et al. Multi-material adhesively bonded structures: Characterisation and modelling of their rate-dependent performance. Compos Part B Eng 2020;195:108077. https://doi.org/10.1016/j.compositesb.2020.108077.

[17] Lambiase F, Balle F, Blaga LA, Liu F, Amancio-Filho ST. Friction-based processes for

hybrid multi-material joining. Compos Struct 2021;266:113828. https://doi.org/10.1016/J.COMPSTRUCT.2021.113828.
[18] Lambiase F, Scipioni SI, Lee CJ, Ko DC, Liu F. A state-of-the-art review on advanced joining processes for metal-composite and metal-polymer hybrid structures. Materials (Basel) 2021;14. https://doi.org/10.3390/ma14081890.
[19] Lambiase F, Liu F. Recent advances in metal-polymer joining processes. First Edit. Elsevier Ltd.; 2021. https://doi.org/10.1016/B978-0-323-85399-6.00007-2.
[20] Liu FC, Dong P, Lu W, Sun K. On formation of AlOC bonds at aluminum/polyamide joint interface. Appl Surf Sci 2019;466:202–9. https://doi.org/https://doi.org/10.1016/j.apsusc.2018.10.024.
[21] Khan AS, Liu F, Dong P. Joining of metal and non-polar polypropylene composite through a simple functional group seeding layer. J Manuf Process 2023;85:90–100. https://doi.org/10.1016/J.JMAPRO.2022.11.022.
[22] Han SC, Wu LH, Jiang CY, Li N, Jia CL, Xue P, et al. Achieving a strong polypropylene/aluminum alloy friction spot joint via a surface laser processing pretreatment. J Mater Sci Technol 2020;50:103–14. https://doi.org/10.1016/j.jmst.2020.02.035.
[23] Kawahito Y, Tange A, Kubota S, Katayama S. Development of direct laser joining for metal and plastic. ICALEO 2006 - 25th Int Congr Appl Laser Electro-Optics, Congr Proc 2006;604. https://doi.org/10.2351/1.5060840.
[24] Shang S-L, Sun H, Pan B, Wang Y, Krajewski AM, Banu M, et al. Forming mechanism of equilibrium and non-equilibrium metallurgical phases in dissimilar aluminum/steel (Al–Fe) joints. Sci Rep 2021;11:24251.
[25] Watanabe M, Feng K, Nakamura Y, Kumai S. Growth manner of intermetallic compound layer produced at welding interface of friction stir spot welded aluminum/steel lap joint. Mater Trans 2011;52:953–9. https://doi.org/10.2320/matertrans.L-MZ201120.
[26] Wang K, Shang S-L, Wang Y, Vivek A, Daehn G, Liu Z-K, et al. Unveiling non-equilibrium metallurgical phases in dissimilar Al-Cu joints processed by vaporizing foil actuator welding. Mater Des 2020;186:108306.
[27] Liu FC, Dong P. From thick intermetallic to nanoscale amorphous phase at Al-Fe joint interface: roles of friction stir welding conditions. Scr Mater 2021;191:167–72. https://doi.org/10.1016/j.scriptamat.2020.09.031.
[28] Liu FC, Dong P, Khan AS, Sun K, Lu W, Taub A, et al. Amorphous interfacial microstructure and high bonding strength in Al-Fe bimetallic components enabled by a large-area solid-state additive manufacturing technique. J Mater Process Technol 2022;308:117721. https://doi.org/10.1016/J.JMATPROTEC.2022.117721.
[29] Liu FC, Dong P, Zhang J, Lu W, Taub A, Sun K. Alloy amorphization through nanoscale shear localization at Al-Fe interface. Mater Today Phys 2020;15:100252. https://doi.org/https://doi.org/10.1016/j.mtphys.2020.100252.
[30] Liu F, Zhang Y, Dong P. Large area friction stir additive manufacturing of intermetallic-free aluminum-steel bimetallic components through interfacial amorphization. J Manuf Process 2022;73:725–35. https://doi.org/10.1016/j.jmapro.2021.11.042.
[31] Friedrich K. Carbon fiber reinforced thermoplastic composites for future automotive applications. AIP Conf Proc 2016;1736. https://doi.org/10.1063/1.4949575.
[32] Holbery J, Houston D. Natural-fiber-reinforced polymer composites in automotive applications. JOM 2006;58:80–6. https://doi.org/10.1007/s11837-006-0234-2.

[33] Elmarakbi A. Advanced composite materials for automotive applications: Structural integrity and crashworthiness. John Wiley & Sons; 2013.
[34] Stewart R. Thermoplastic composites - Recyclable and fast to process. Reinf Plast 2011;55:22–8. https://doi.org/10.1016/S0034-3617(11)70073-X.
[35] Bel Haj Frej H, Léger R, Perrin D, Ienny P. A Novel Thermoplastic Composite for Marine Applications: Comparison of the Effects of Aging on Mechanical Properties and Diffusion Mechanisms. Appl Compos Mater 2021;28:899–922. https://doi.org/10.1007/s10443-021-09903-0.
[36] Shanmugam L, Kazemi ME, Rao Z, Yang L, Yang J. On the metal thermoplastic composite interface of Ti alloy/UHMWPE-Elium® laminates. Compos Part B Eng 2020;181:107578. https://doi.org/10.1016/j.compositesb.2019.107578.
[37] da Costa AP, Botelho EC, Costa ML, Narita NE, Tarpani JR. A review of welding technologies for thermoplastic composites in aerospace applications. J Aerosp Technol Manag 2012;4:255–65. https://doi.org/10.5028/jatm.2012.04033912.
[38] Roux M, Dransfeld C, Eguémann N, Giger L. Processing and recycling of a thermoplastic composite fibre/peek aerospace part. 16th Eur Conf Compos Mater ECCM 2014 2014:22–6.
[39] Wagner D, Conklin JL, Zaluzec M, Skszek TW. The Multi Material Lightweight Vehicle (MMLV) Project. 2015. https://doi.org/10.4271/pt-170.
[40] Pradeep SA, Iyer RK, Kazan H, Pilla S. Automotive Applications of Plastics: Past, Present, and Future. Second Edi. Elsevier Inc.; 2017. https://doi.org/10.1016/B978-0-323-39040-8.00031-6.
[41] Patil A, Patel A, Purohit R. An overview of Polymeric Materials for Automotive Applications. Mater Today Proc 2017;4:3807–15. https://doi.org/10.1016/j.matpr.2017.02.278.
[42] Mallick PK. Thermoplastics and thermoplastic–matrix composites for lightweight automotive structures. LTD; 2020. https://doi.org/10.1016/B978-0-12-818712-8.00005-7.
[43] Foss PH, Mentzer CC, Franklin DW. Design and valifation of a thermoplastic composite liftgate. Glass 2004.
[44] Hisham A. Maddah. Polypropylene as a Promising Plastic: A Review. Am J Polym Sci 2016. https://doi.org/10.5923/j.ajps.20160601.01.
[45] Lorenzo L, Naughton P. Structural Front-End Carrier Using Long Glass Fiber Polypropylene. SAE Technical Paper; 2002.
[46] Hariprasad K, Ravichandran K, Jayaseelan V, Muthuramalingam T. Acoustic and mechanical characterisation of polypropylene composites reinforced by natural fibres for automotive applications. J Mater Res Technol 2020;9:14029–35. https://doi.org/10.1016/j.jmrt.2020.09.112.
[47] Burn DT. Long Discontinuous Carbon Fibre / Polypropylene Composites for High Volume Automotive Applications 2016.
[48] Liu F, Dong P. Directly and Reliably Welding Plastic to Metal. Weld J 2022;101:45–8.
[49] Staab F, Liesegang M, Balle F. Local shear strength distribution of ultrasonically welded hybrid Aluminium to CFRP joints. Compos Struct 2020;248:112481. https://doi.org/10.1016/j.compstruct.2020.112481.
[50] Staab F, Balle F. Fatigue and fracture of ultrasonically welded aluminum alloys to carbon fiber reinforced thermoplastics. Fatigue Fract Eng Mater Struct 2022;45:607–16. https://doi.org/10.1111/ffe.13622.

[51] Wagner D. Multi Material Lightweight Vehicle (MMLV) Architecture 2015.
[52] Kleinbaum S, Jiang C, Logan S. Enabling sustainable transportation through joining of dissimilar lightweight materials. MRS Bull 2019;44:608–12. https://doi.org/DOI: 10.1557/mrs.2019.178.
[53] Khayoon MA, Hubeatir KA, Al-Khafaji MM. Laser Transmission Welding is a promising joining technology technique–A Recent Review. J. Phys. Conf. Ser., vol. 1973, IOP Publishing; 2021, p. 12023.
[54] Huang Y, Gao X, Zhang Y, Ma B. Laser joining technology of polymer-metal hybrid structures - A review. J Manuf Process 2022;79:934–61. https://doi.org/10.1016/j.jmapro.2022.05.026.
[55] Jiao J, Xu Z, Wang Q, Sheng L, Zhang W. CFRTP and stainless steel laser joining: Thermal defects analysis and joining parameters optimization. Opt Laser Technol 2018;103:170–6. https://doi.org/10.1016/j.optlastec.2018.01.023.
[56] Su J, Tan C, Wu Z, Wu L, Gong X, Chen B, et al. Influence of defocus distance on laser joining of CFRP to titanium alloy. Opt Laser Technol 2020;124:106006.
[57] Huang Y, Gao X, Ma B, Zhang Y. Interface formation and bonding mechanisms of laser welding of pmma plastic and 304 austenitic stainless steel. Metals (Basel) 2021;11. https://doi.org/10.3390/met11091495.
[58] Wang H, Xiao X, Xiao G, Fan H-T, Arinez J. Laser Joining of Carbon-Fiber-Reinforced Polymer and Metal with High-Strength and Corrosion-Resistant Bonds. Procedia Manuf 2019;34:42–8. https://doi.org/https://doi.org/10.1016/j.promfg.2019.06.112.
[59] Jung K-W, Kawahito Y, Takahashi M, Katayama S. Laser direct joining of carbon fiber reinforced plastic to aluminum alloy. J Laser Appl 2013;25:032003. https://doi.org/10.2351/1.4794297.
[60] Jung KW, Kawahito Y, Takahashi M, Katayama S. Laser direct joining of carbon fiber reinforced plastic to zinc-coated steel. Mater Des 2013;47:179–88. https://doi.org/https://doi.org/10.1016/j.matdes.2012.12.015.
[61] Rodríguez-Vidal E, Lambarri J, Soriano C, Sanz C, Verhaeghe G. A combined experimental and numerical approach to the laser joining of hybrid polymer - Metal parts. Phys Procedia 2014;56:835–44. https://doi.org/10.1016/j.phpro.2014.08.101.
[62] Tamrin KF, Nukman Y, Zakariyah SS. Laser lap joining of dissimilar materials: A review of factors affecting joint strength. Mater Manuf Process 2013;28:857–71. https://doi.org/10.1080/10426914.2013.792413.
[63] Tillmann W, Elrefaey A, Wojarski L. Toward process optimization in laser welding of metal to polymer. Materwiss Werksttech 2010;41:879–83. https://doi.org/10.1002/mawe.201000674.
[64] Farazila Y, Miyashita Y, Hua W, Mutoh Y, Otsuka Y. YAG Laser Spot Welding of PET and Metallic Materials. J Laser Micro/Nanoengineering 2011;6.
[65] MIYASHITA Y, TAKAHASHI M, TAKEMI M, OYAMA K, MUTOH Y, TANAKA H. Dissimilar Materials Micro Welding between Stainless Steel and Plastics by Using Pulse YAG Laser. J Solid Mech Mater Eng 2009;3:409–15. https://doi.org/10.1299/jmmp.3.409.
[66] Rodríguez-Vidal E, Sanz C, Lambarri J, Renard J, Gantchenko V. Laser joining of different polymer-metal configurations: Analysis of mechanical performance and failure mechanisms. Phys Procedia 2016;83:1110–7. https://doi.org/10.1016/j.phpro.2016.09.002.
[67] Murzin SP, Palkowski H, Melnikov AA, Blokhin M V. Laser Welding of Metal-Polymer-Metal Sandwich Panels. Metals (Basel) 2022;12. https://doi.org/10.3390/met12020256.

[68] Borba NZ. Use of Cfrp Composites and New Joining Processes in Aircraft Fuselage 2018.
[69] Liu FC, Ma ZY. Influence of Tool Dimension and Welding Parameters on Microstructure and Mechanical Properties of Friction-Stir-Welded 6061-T651 Aluminum Alloy. Metall Mater Trans A 2008;39:2378–88. https://doi.org/10.1007/s11661-008-9586-2.
[70] Ma N, Geng P, Ma Y, Shimakawa K, Choi JW, Aoki Y, et al. Thermo-mechanical modeling and analysis of friction spot joining of Al alloy and carbon fiber-reinforced polymer. J Mater Res Technol 2021;12:1777–93. https://doi.org/10.1016/j.jmrt.2021.03.111.
[71] Amancio-Filho ST, Bueno C, dos Santos JF, Huber N, Hage E. On the feasibility of friction spot joining in magnesium/fiber-reinforced polymer composite hybrid structures. Mater Sci Eng A 2011;528:3841–8. https://doi.org/10.1016/j.msea.2011.01.085.
[72] Liu FC, Liao J, Nakata K. Joining of metal to plastic using friction lap welding. Mater Des 2014;54:236–44. https://doi.org/10.1016/j.matdes.2013.08.056.
[73] Liu FC, Nakata K, Liao J, Hirota S, Fukui H. Reducing bubbles in friction lap welded joint of magnesium alloy and polyamide. Sci Technol Weld Join 2014;19:578–87. https://doi.org/10.1179/1362171814Y.0000000228.
[74] Lambiase F, Grossi V, Scipioni SI, Paoletti A. Prediction of the power supplied in friction-based joining process of metal-polymer hybrids through machine learning. J Manuf Process 2021;68:750–60. https://doi.org/10.1016/J.JMAPRO.2021.06.001.
[75] Tan X, Zhang J, Shan J, Yang S, Ren J. Characteristics and formation mechanism of porosities in CFRP during laser joining of CFRP and steel. Compos Part B Eng 2015;70:35–43. https://doi.org/10.1016/j.compositesb.2014.10.023.
[76] Liu FC, Dong P, Pei X. A high-speed metal-to-polymer direct joining technique and underlying bonding mechanisms. J Mater Process Technol 2020;280:116610. https://doi.org/10.1016/j.jmatprotec.2020.116610.
[77] Goushegir SM, dos Santos JF, Amancio-Filho ST. Friction Spot Joining of aluminum AA2024/carbon-fiber reinforced poly(phenylene sulfide) composite single lap joints: Microstructure and mechanical performance. Mater Des 2014;54:196–206. https://doi.org/https://doi.org/10.1016/j.matdes.2013.08.034.
[78] Liu FC, Dong P, Pei X. A high-speed metal-to-polymer direct joining technique and underlying bonding mechanisms. J Mater Process Technol 2020;280:116610. https://doi.org/10.1016/j.jmatprotec.2020.116610.
[79] McIntyre D. Characterisation. 2015. https://doi.org/10.1017/CBO9781139237031.013.
[80] Bauernhuber A, Markovits T, Trif L, Csanády Á. Adhesion of steel and PMMA by means of laser radiation. Mater Sci Forum 2017;885:61–6. https://doi.org/10.4028/www.scientific.net/MSF.885.61.
[81] Csiszér T, Temesi T, Borbás L, Molnár L. Laser-assisted joining of steel and cellulose fiber-reinforced pmma. Acta Polytech Hungarica 2021;18:237–53. https://doi.org/10.12700/APH.18.2.2021.2.13.
[82] Hussein FI, Akman E, Genc Oztoprak B, Gunes M, Gundogdu O, Kacar E, et al. Evaluation of PMMA joining to stainless steel 304 using pulsed Nd:YAG laser. Opt Laser Technol 2013;49:143–52. https://doi.org/10.1016/j.optlastec.2012.12.028.
[83] Barakat AA, Darras BM, Nazzal MA, Ahmed AA. A Comprehensive Technical Review of the Friction Stir Welding of Metal-to-Polymer Hybrid Structures. Polymers (Basel) 2023;15. https://doi.org/10.3390/polym15010220.
[84] Meiabadi MSSM, Kazerooni A, Moradi M, Torkamany MJ. Laser assisted joining of St12 to polycarbonate: Experimental study and numerical simulation. Optik (Stuttg)

2020;208:164151.
[85] Ai Y, Zheng K, Shin YC, Wu B. Analysis of weld geometry and liquid flow in laser transmission welding between polyethylene terephthalate (PET) and Ti6Al4V based on numerical simulation. Opt Laser Technol 2018;103:99–108. https://doi.org/https://doi.org/10.1016/j.optlastec.2018.01.022.
[86] Chan CW, Smith GC. Fibre laser joining of highly dissimilar materials: Commercially pure Ti and PET hybrid joint for medical device applications. Mater Des 2016;103:278–92. https://doi.org/10.1016/j.matdes.2016.04.086.
[87] Wahba M, Kawahito Y, Katayama S. Laser direct joining of AZ91D thixomolded Mg alloy and amorphous polyethylene terephthalate. J Mater Process Technol 2011;211:1166–74. https://doi.org/10.1016/j.jmatprotec.2011.01.021.
[88] Yusof F, Miyashita Y, Seo N, Mutoh Y, Moshwan R. Utilising friction spot joining for dissimilar joint between aluminium alloy (A5052) and polyethylene terephthalate. Sci Technol Weld Join 2012;17:544–9. https://doi.org/10.1179/136217112x13408696326530.
[89] Balle F, Wagner G, Eifler D. Ultrasonic metal welding of aluminium sheets to carbon fibre reinforced thermoplastic composites. Adv Eng Mater 2009;11:35–9. https://doi.org/10.1002/adem.200800271.
[90] Jung KW, Kawahito Y, Katayama S. Laser direct joining of carbon fibre reinforced plastic to stainless steel. Sci Technol Weld Join 2011;16:676–80. https://doi.org/10.1179/1362171811Y.0000000060.
[91] Nagatsuka K, Kitagawa D, Yamaoka H, Nakata K. Friction lap joining of thermoplastic materials to carbon steel. ISIJ Int 2016;56:1226–31. https://doi.org/10.2355/isijinternational.ISIJINT-2016-042.
[92] Lambiase F, Paoletti A. Mechanical behavior of AA5053/polyetheretherketone (PEEK) made by friction assisted joining. Compos Struct 2018;189:70–8.
[93] Tao W, Su X, Chen Y, Tian Z. Joint formation and fracture characteristics of laser welded CFRP/TC4 joints. J Manuf Process 2019;45:1–8. https://doi.org/10.1016/J.JMAPRO.2019.05.028.
[94] Ageorges C, Ye L. Resistance welding of metal/thermoplastic composite joints. J Thermoplast Compos Mater 2001;14:449–75. https://doi.org/10.1106/PN74-QXKH-7XBE-XKF5.
[95] Feistauer EE, Guimarães RPM, Ebel T, dos Santos JF, Amancio-Filho ST. Ultrasonic joining: A novel direct-assembly technique for metal-composite hybrid structures. Mater Lett 2016;170:1–4. https://doi.org/https://doi.org/10.1016/j.matlet.2016.01.137.
[96] Gao T et al., An Internal Res Report, Univ Michigan.
[97] Zhao S, Kimura F, Wang S, Kajihara Y. Chemical interaction at the interface of metal–plastic direct joints fabricated via injection molded direct joining. Appl Surf Sci 2021;540:148339.
[98] Arenas JM, Alía C, Narbón JJ, Ocaña R, González C. Considerations for the industrial application of structural adhesive joints in the aluminium–composite material bonding. Compos Part B Eng 2013;44:417–23.
[99] Pletincx S, Fockaert LLI, Mol JMC, Hauffman T, Terryn H. Probing the formation and degradation of chemical interactions from model molecule/metal oxide to buried polymer/metal oxide interfaces. Npj Mater Degrad 2019;3:1–12. https://doi.org/10.1038/s41529-019-0085-2.
[100] Hirchenhahn P, Al Sayyad A, Bardon J, Felten A, Plapper P, Houssiau L. Highlighting

Chemical Bonding between Nylon-6.6 and the Native Oxide from an Aluminum Sheet Assembled by Laser Welding. ACS Appl Polym Mater 2020;2:2517–27. https://doi.org/10.1021/acsapm.0c00015.
[101] Liu Y, Shigemoto Y, Hanada T, Miyamae T, Kawasaki K, Horiuchi S. Role of Chemical Functionality in the Adhesion of Aluminum and Isotactic Polypropylene. ACS Appl Mater Interfaces 2021;13:11497–506. https://doi.org/10.1021/acsami.0c22988.
[102] Ochoa-Putman C, Vaidya UK. Mechanisms of interfacial adhesion in metal–polymer composites – Effect of chemical treatment. Compos Part A Appl Sci Manuf 2011;42:906–15. https://doi.org/https://doi.org/10.1016/j.compositesa.2011.03.019.
[103] RAMARATHNAM G, LIBERTUCCI M, SADOWSKI M, NORTH T. Joining of polymers to metal. Weld Journal-New York- 1992;71:483-s.
[104] Mandolfino C, Lertora E, Gambaro C, Pizzorni M. Functionalization of neutral polypropylene by using low pressure plasma treatment: Effects on surface characteristics and adhesion properties. Polymers (Basel) 2019;11. https://doi.org/10.3390/polym11020202.
[105] Melentiev R, Yudhanto A, Tao R, Vuchkov T, Lubineau G. Metallization of polymers and composites: State-of-the-art approaches. Mater Des 2022;221:110958. https://doi.org/10.1016/J.MATDES.2022.110958.
[106] Liu F, Dong P. High-Speed Polymer-To-Metal Direct Joining System And Method 2023.
[107] Xie Y, Zhang J, Zhou T. Large-area mechanical interlocking via nanopores: Ultra-high-strength direct bonding of polymer and metal materials. Appl Surf Sci 2019;492:558–70. https://doi.org/10.1016/j.apsusc.2019.06.246.
[108] Sulka GD. Highly ordered anodic porous alumina formation by self-organized anodizing. Nanostructured Mater Electrochem 2008:1–116.
[109] Kimiaki N, Hironobu T, Bolyu X, Atsuki T, Kazuhiro N. Effect of silane coupling on the joint characteristics of friction lap joined Al alloy/CFRP. Weld Int 2018;32:328–37. https://doi.org/10.1080/09507116.2017.1346819.
[110] Zhao S, Kimura F, Kadoya S, Kajihara Y. Experimental analysis on mechanical interlocking of metal–polymer direct joining. Precis Eng 2020;61:120–5. https://doi.org/https://doi.org/10.1016/j.precisioneng.2019.10.009.
[111] Saborowski E, Dittes A, Steinert P, Lindner T, Scharf I, Schubert A, et al. Effect of metal surface topography on the interlaminar shear and tensile strength of aluminum/polyamide 6 polymer-metal-hybrids. Materials (Basel) 2019;12:2963.
[112] Rodríguez-Vidal E, Sanz C, Lambarri J, Quintana I. Experimental investigation into metal micro-patterning by laser on polymer-metal hybrid joining. Opt Laser Technol 2018;104:73–82.
[113] Kim W-S, Yun I-H, Lee J-J, Jung H-T. Evaluation of mechanical interlock effect on adhesion strength of polymer–metal interfaces using micro-patterned surface topography. Int J Adhes Adhes 2010;30:408–17.
[114] Yusof F, Muhamad MR bin, Moshwan R, Jamaludin MF bin, Miyashita Y. Effect of surface states on joining mechanisms and mechanical properties of aluminum alloy (A5052) and polyethylene terephthalate (PET) by dissimilar friction spot welding. Metals (Basel) 2016;6:101.
[115] Dawei Z, Qi Z, Xiaoguang F, Shengdun Z. Review on Joining Process of Carbon Fiber-Reinforced Polymer and Metal: Methods and Joining Process. Rare Met Mater Eng 2018;47:3686–96. https://doi.org/https://doi.org/10.1016/S1875-5372(19)30018-9.

[116] Zou X, Sariyev B, Chen K, Jiang M, Wang M, Hua X, et al. Enhanced interfacial bonding strength between metal and polymer via synergistic effects of particle anchoring and chemical bonding. J Manuf Process 2021;68:558–68.
[117] Nasreen A, Shaker K, Nawab Y. Effect of surface treatments on metal–composite adhesive bonding for high-performance structures: an overview. Compos Interfaces 2021;28:1221–56.
[118] Elahi MA, Koch M, Bardon J, Addiego F, Plapper P. Failure mechanism analysis based on laser-based surface treatments for aluminum-polyamide laser joining. J Mater Process Technol 2021;298:117318.
[119] Steinert P, Dittes A, Schimmelpfennig R, Scharf I, Lampke T, Schubert A. Design of high strength polymer metal interfaces by laser microstructured surfaces. IOP Conf. Ser. Mater. Sci. Eng., vol. 373, IOP Publishing; 2018, p. 12015.
[120] Heckert A, Singer C, Zaeh MF, Daub R, Zeilinger T. Gas-tight Thermally Joined Metal-thermoplastic Connections by Pulsed Laser Surface Pre-treatment. Phys Procedia 2016;83:1083–93. https://doi.org/https://doi.org/10.1016/j.phpro.2016.08.114.
[121] Lambiase F, Yanala PB, Leone C, Paoletti A. Influence of laser texturing strategy on thermomechanical joining of AA7075 aluminum alloy and PEEK. Compos Struct 2023;315:116974. https://doi.org/https://doi.org/10.1016/j.compstruct.2023.116974.
[122] TAN C, SU J, FENG Z, LIU Y, CHEN B, SONG X. Laser joining of CFRTP to titanium alloy via laser surface texturing. Chinese J Aeronaut 2021;34:103–14. https://doi.org/https://doi.org/10.1016/j.cja.2020.08.017.
[123] Martínez-Viademonte MP, Abrahami ST, Hack T, Burchardt M, Terryn H. A review on anodizing of aerospace aluminum alloys for corrosion protection. Coatings 2020;10:1–30. https://doi.org/10.3390/coatings10111106.
[124] Buijnsters JG, Zhong R, Tsyntsaru N, Celis JP. Surface wettability of macroporous anodized aluminum oxide. ACS Appl Mater Interfaces 2013;5:3224–33. https://doi.org/10.1021/am4001425.
[125] Ramarathnam G, Libertucci M, Sadowski MM, North TH. Joining of polymers to metal. Weld JOURNAL-NEW YORK- 1992;71:483-s.
[126] Nagatsuka K, Xiao B, Wu L, Nakata K, Saeki S, Kitamoto Y, et al. Resistance spot welding of metal/carbon-fibre-reinforced plastics and applying silane coupling treatment. Sci Technol Weld Join 2018;23:181–6. https://doi.org/10.1080/13621718.2017.1362159.
[127] Lee SH, Yashiro H, Kure-Chu SZ. Effect of Silane Coupling Treatment on the Joining and Sealing Performance between Polymer and Anodized Aluminum Alloy. Korean J Mater Res 2021;31:122–31. https://doi.org/10.3740/MRSK.2021.31.3.122.
[128] Uetsuji Y, Yagi T, Nakamura Y. Interfacial adhesive strength of a silane coupling agent with metals: A first principles study. Mater Today Commun 2020;25:101397. https://doi.org/https://doi.org/10.1016/j.mtcomm.2020.101397.
[129] Aliasghari S, Ghorbani M, Skeldon P, Karami H, Movahedi M. Effect of plasma electrolytic oxidation on joining of AA 5052 aluminium alloy to polypropylene using friction stir spot welding. Surf Coatings Technol 2017;313:274–81. https://doi.org/https://doi.org/10.1016/j.surfcoat.2017.01.084.
[130] Liu FC, Liao J, Gao Y, Nakata K. Effect of plasma electrolytic oxidation coating on joining metal to plastic. Sci Technol Weld Join 2015;20:291–6. https://doi.org/10.1179/1362171815Y.0000000012.
[131] Guezenoc H, Segui Y, Thery S, Asfardjani K. Adhesion characteristics of plasma-treated

polypropylene to mild steel. J Adhes Sci Technol 1993;7:953–65. https://doi.org/10.1163/156856193X00943.
[132] Chen J, Du K, Chen X, Li Y, Huang J, Wu Y, et al. Influence of surface microstructure on bonding strength of modified polypropylene/aluminum alloy direct adhesion. Appl Surf Sci 2019;489:392–402. https://doi.org/10.1016/j.apsusc.2019.05.270.
[133] Bahrami M, Lavayen-Farfan D, Martínez MA, Abenojar J. Experimental and numerical studies of polyamide 11 and 12 surfaces modified by atmospheric pressure plasma treatment. Surfaces and Interfaces 2022;32:102154.
[134] Liston EM, Martinu L, Wertheimer MR. Plasma surface modification of polymers for improved adhesion: a critical review. J Adhes Sci Technol 1993;7:1091–127. https://doi.org/10.1163/156856193X00600.
[135] Shang SL, Sun H, Pan B, Wang Y, Krajewski AM, Banu M, et al. Forming mechanism of equilibrium and non-equilibrium metallurgical phases in dissimilar aluminum/steel (Al–Fe) joints. Sci Rep 2021;11:1–15. https://doi.org/10.1038/s41598-021-03578-0.
[136] Takenaka K, Machida R, Bono T, Jinda A, Toko S, Uchida G, et al. Development of a non-thermal atmospheric pressure plasma-assisted technology for the direct joining of metals with dissimilar materials. J Manuf Process 2022;75:664–9. https://doi.org/https://doi.org/10.1016/j.jmapro.2022.01.041.
[137] Liang CS, Lv ZF, Bo Y, Cui JY, Xu SA. Effect of modified polypropylene on the interfacial bonding of polymer-aluminum laminated films. Mater Des 2015;81:141–8. https://doi.org/10.1016/j.matdes.2015.05.021.
[138] Tao W, Su X, Chen Y, Tian Z. Joint formation and fracture characteristics of laser welded CFRP/TC4 joints. J Manuf Process 2019;45:1–8. https://doi.org/10.1016/j.jmapro.2019.05.028.
[139] Kornacka EM, Przybytniak G, Fuks L, Walo M, Łyczko K. Functionalization of polymer surfaces by radiation-induced grafting for separation of heavy metal ions. Radiat Phys Chem 2014;94:115–8. https://doi.org/10.1016/j.radphyschem.2013.05.047.
[140] Ku JH, Jung IH, Rhee KY, Park SJ. Atmospheric pressure plasma treatment of polypropylene to improve the bonding strength of polypropylene/aluminum composites. Compos Part B Eng 2013;45:1282–7. https://doi.org/10.1016/j.compositesb.2012.06.016.
[141] Chen MA, Li HZ, Zhang XM. Improvement of shear strength of aluminium-polypropylene lap joints by grafting maleic anhydride onto polypropylene. Int J Adhes Adhes 2007;27:175–87. https://doi.org/10.1016/j.ijadhadh.2006.01.008.
[142] Astigarraga V, Gondra K, Valea Á, Pardo Aurrekoetxea G. Improvement of adhesive bonding of polypropylene and maleic anhydride grafted polypropylene blends to aluminium by means of addition of cyclic butylene terephthalate. J Adhes 2019;95:286–307. https://doi.org/10.1080/00218464.2018.1437415.
[143] Li C, Zhang Y, Zhang Y. Melt grafting of maleic anhydride onto low-density polyethylene/polypropylene blends. Polym Test 2003;22:191–5. https://doi.org/https://doi.org/10.1016/S0142-9418(02)00079-X.
[144] Tan X, Xu Y, Jia G, Qian J. Ultrasonically Initiated Grafting of Maleic Anhydride onto Poly(propylene). Macromol React Eng 2007;1:185–90. https://doi.org/https://doi.org/10.1002/mren.200600012.
[145] Zhou J, Yan F. Effect of polyethylene-graft-maleic anhydride as a compatibilizer on the mechanical and tribological behaviors of ultrahigh-molecular-weight polyethylene/copper composites. J Appl Polym Sci 2004;93:948–55.

https://doi.org/https://doi.org/10.1002/app.20489.
[146] Chen MA, Zhang XM, Huang R, Lu X Bin. Mechanism of adhesion promotion between aluminium sheet and polypropylene with maleic anhydride-grafted polypropylene by γ-aminopropyltriethoxy silane. Surf Interface Anal 2008;40:1209–18. https://doi.org/10.1002/sia.2871.
[147] Okada T, Uchida S, Nakata K. Direct joining of aluminum alloy and plastic sheets by friction lap processing. Mater Sci Forum 2014;794–796:395–400. https://doi.org/10.4028/www.scientific.net/MSF.794-796.395.
[148] Zhang M, Liu FC, Liu ZY, Xue P, Dong P, Zhang H, et al. Highly stable nanoscale amorphous microstructure at steel-aluminum interface enabled by a new solid-state additive manufacturing method. Scr Mater 2023;227. https://doi.org/10.1016/j.scriptamat.2023.115300.
[149] Khan, A. S., Dong, P., Liu, F., Zhang Y. Directly Welding Plastic to Metal for Structural Applications: a state-of-the-art review – Part I Promising Processes. Weld J 2023.
[150] Amancio-Filho ST, Bueno C, dos Santos JF, Huber N, Hage E. On the feasibility of friction spot joining in magnesium/fiber-reinforced polymer composite hybrid structures. Mater Sci Eng A 2011;528:3841–8. https://doi.org/10.1016/j.msea.2011.01.085.
[151] Liu FC, Liao J, Nakata K. Joining of metal to plastic using friction lap welding. Mater Des 2014;54:236–44. https://doi.org/10.1016/j.matdes.2013.08.056.
[152] Kawahito Y, Tange A, Kubota S, Katayama S. Development of direct laser joining for metal and plastic. ICALEO 2006 - 25th Int Congr Appl Laser Electro-Optics, Congr Proc 2006;604. https://doi.org/10.2351/1.5060840.
[153] Lambiase F, Paoletti A, Grossi V, Ilio A Di. Friction assisted joining of aluminum and PVC sheets. J Manuf Process 2017;29:221–31. https://doi.org/10.1016/J.JMAPRO.2017.07.026.
[154] Khan AS, Liu F, Dong P. Joining of metal and non-polar polypropylene composite through a simple functional group seeding layer. J Manuf Process 2023;85:90–100. https://doi.org/10.1016/J.JMAPRO.2022.11.022.
[155] Goushegir SM, dos Santos JF, Amancio-Filho ST. Friction Spot Joining of aluminum AA2024/carbon-fiber reinforced poly(phenylene sulfide) composite single lap joints: Microstructure and mechanical performance. Mater Des 2014;54:196–206. https://doi.org/https://doi.org/10.1016/j.matdes.2013.08.034.
[156] Zhang Y, Dong P, Pei X. Fracture Mechanics Modeling of Fatigue Behaviors of Adhesive-Bonded Aluminum Alloy Components. Metals (Basel) 2022;12. https://doi.org/10.3390/met12081298.
[157] Dong P. A robust structural stress procedure for characterizing fatigue behavior of welded joints. SAE Tech Pap 2001;110:89–100. https://doi.org/10.4271/2001-01-0086.
[158] Dong P. A structural stress definition and numerical implementation for fatigue analysis of welded joints. Int J Fatigue 2001;23:865–76. https://doi.org/https://doi.org/10.1016/S0142-1123(01)00055-X.
[159] Dong P, Zhang J, Hong JK. Structural stress analysis 2005.
[160] Dong P. A Robust Structural Stress Method for Fatigue Analysis of Ship Structures 2003:199–211. https://doi.org/10.1115/OMAE2003-37313.
[161] Dong P. A Robust Structural Stress Method for Fatigue Analysis of Offshore/Marine Structures . J Offshore Mech Arct Eng 2005;127:68–74. https://doi.org/10.1115/1.1854698.
[162] Nie C, Dong P. A traction stress based shear strength definition for fillet welds. J Strain Anal Eng Des 2012;47:562–75.

[163] Dong P. A robust structural stress procedure for characterizing fatigue behavior of welded joints. SAE Trans 2001:89–100.
[164] Wang P, Pei X, Dong P, Song S. Traction structural stress analysis of fatigue behaviors of rib-to-deck joints in orthotropic bridge deck. Int J Fatigue 2019;125:11–22. https://doi.org/https://doi.org/10.1016/j.ijfatigue.2019.03.038.
[165] Dong P, Hong JK, Cao Z. A mesh-insensitive structural stress procedure for fatigue evaluation of welded structures. International Institute of Welding; 2001.
[166] Kang HT, Dong P, Hong JK. Fatigue analysis of spot welds using a mesh-insensitive structural stress approach. Int J Fatigue 2007;29:1546–53. https://doi.org/10.1016/J.IJFATIGUE.2006.10.025.
[167] Kyuba H, Dong P. Equilibrium-equivalent structural stress approach to fatigue analysis of a rectangular hollow section joint. Int J Fatigue 2005;27:85–94. https://doi.org/https://doi.org/10.1016/j.ijfatigue.2004.05.008.
[168] Dong P, Hong JK, De Jesus AMP. Analysis of Recent Fatigue Data Using the Structural Stress Procedure in ASME Div 2 Rewrite. J Press Vessel Technol 2006;129:355–62. https://doi.org/10.1115/1.2748818.
[169] Zhang L, Dong P, Wang Y, Mei J. A Coarse-Mesh hybrid structural stress method for fatigue evaluation of Spot-Welded structures. Int J Fatigue 2022;164:107109. https://doi.org/https://doi.org/10.1016/j.ijfatigue.2022.107109.
[170] Xing S, Dong P, Wang P. A quantitative weld sizing criterion for fatigue design of load-carrying fillet-welded connections. Int J Fatigue 2017;101:448–58. https://doi.org/https://doi.org/10.1016/j.ijfatigue.2017.01.003.
[171] Xing S, Dong P, Threstha A. Analysis of fatigue failure mode transition in load-carrying fillet-welded connections. Mar Struct 2016;46:102–26. https://doi.org/https://doi.org/10.1016/j.marstruc.2016.01.001.
[172] Xing S, Pei X, Mei J, Dong P, Su S, Zhen C. Weld toe versus root fatigue failure mode and governing parameters: A study of aluminum alloy load-carrying fillet joints. Mar Struct 2023;88:103344. https://doi.org/https://doi.org/10.1016/j.marstruc.2022.103344.
[173] Wang P, Pei X, Dong P, Yu Y, Li X. Analysis of weld root fatigue cracking in load-carrying high-strength aluminum alloy cruciform joints. Int J Fatigue 2020;139:105735. https://doi.org/https://doi.org/10.1016/j.ijfatigue.2020.105735.
[174] Liu FC, Dong P, Pei X. A high-speed metal-to-polymer direct joining technique and underlying bonding mechanisms. J Mater Process Technol 2020;280:116610. https://doi.org/10.1016/j.jmatprotec.2020.116610.
[175] Liu FC, Dong P, Zhang J, Lu W, Taub A, Sun K. Alloy amorphization through nanoscale shear localization at Al-Fe interface. Mater Today Phys 2020;15:100252. https://doi.org/https://doi.org/10.1016/j.mtphys.2020.100252.
[176] Liu FC, Dong P. From thick intermetallic to nanoscale amorphous phase at Al-Fe joint interface: roles of friction stir welding conditions. Scr Mater 2021;191:167–72. https://doi.org/10.1016/j.scriptamat.2020.09.031.
[177] Liu FC, Dong P, Khan AS, Sun K, Lu W, Taub A, et al. Amorphous interfacial microstructure and high bonding strength in Al-Fe bimetallic components enabled by a large-area solid-state additive manufacturing technique. J Mater Process Technol 2022;308. https://doi.org/10.1016/j.jmatprotec.2022.117721.
[178] Dong P. Quantitative weld quality acceptance criteria: an enabler for structural lightweighting and additive manufacturing. Weld J 2020;99.

[179] Bingzhi C, Zhengping H, Dong P, Song S, Wenzhong Z. Quantitative fatigue evaluation of complex welded connections and application in a train traction motor frame component. Proc Inst Mech Eng Part F J Rail Rapid Transit 2022;236:1252–61.
[180] Liu FC, Dong P, Lu W, Sun K. On formation of AlOC bonds at aluminum/polyamide joint interface. Appl Surf Sci 2019;466:202–9. https://doi.org/https://doi.org/10.1016/j.apsusc.2018.10.024.

Chapter 3 Direct Joining of Metal and Non-Polar Polypropylene Thermoplastic Composite

3.1 Introduction

Concerns for environmental sustainability and demands for vehicle performance continue to drive major vehicle manufacturers to pursue more advanced lightweight structure solutions [1,2]. Most recent studies have shown that multi-material structures are the most effective way of achieving structural lightweighting in transportation vehicular systems by "using the right material at the right place". Cost-effective manufacture of reliable multi-material structures, e.g., made of lightweight metals and polymer composites, has been considered one of the major challenges for realizing the benefits of these advanced lightweight vehicular structures [3,4]. These multi-material structural design scenarios often require combining steels, and aluminum alloys with various polymeric composites through either direct or indirect welding and joining methods.

One of the key challenges in manufacturing multi-material structures in a mass-production environment is how to cost-effectively achieve strong bonding between metal and polymer composite. Traditionally, metals and polymers were typically joined together using adhesives and/or mechanical fastening methods. Adhesive joining requires significant curing time under the support of special fixtures, and its byproducts sometimes can be hazardous to the environment [5]. Mechanical fastening using rivets, nuts, bolts, and mechanical engraving, adds additional weight to the hybrid structure, creates stress concentration sites that are prone to fatigue failures, and cannot attain hermetic sealing [6,7]. These issues can be addressed to a large degree by developing robust welding methods capable of joining metal and polymer composites directly [8,9]. In the

past decade, some advanced welding concepts were investigated for joining metals and polymer/polymer composites, such as friction lap welding (FLW) [10–14], ultrasonic welding [15,16], laser direct welding [17–20], induction welding [21], and resistance spot welding [22]. Among these newly developed welding methods, FLW has the advantages of high welding speed, good bonding strength, fewer process parameters to control, low material and mechanical property losses, and absence of environmental hazards [10,11]. It should be noted that some of these welding methods mentioned above have been demonstrated to be able to produce considerable high bonding strength between metal and polyamide (PA) based materials without special preprocessing or surface modifications [10,23,24]. However, to our best knowledge, none of them can be used successfully for joining metal and polypropylene (PP) based composite materials which are widely used in auto-body closures [13,25].

The major difficulty can be attributed to the PP polymer's molecular structure [24]. It has been shown that various metals can be welded directly to polymethylmethacrylate (PMMA) [26], polycarbonate (PC) [27], polyethylene terephthalate (PET) [17,28], PA [10,15,22,29–32], polyether ether ketone (PEEK) [21,33–36], and polyetherimide (PEI) [16]. All these polymers contain carbonyl functional groups (C=O). Liu et. al., [24] demonstrated that the carbonyl group on the thermoplastic surface reacted with aluminum atoms on the surface of aluminum alloys once an intimate contact can be created during the welding, leading to the formation of strong C-O-Al chemical bonds at the bonding interface. Liu et. al., [24] also concluded that it is difficult to directly weld metals to thermoplastics that do not contain polar functional groups, such as polypropylene, and polyethylene without any surface or material modifications.

To overcome the difficulties associated with the lack of polar functional groups, special surface modifications of metal and/or PP sides, therefore, have been explored for increasing their

weldability. Additional physical and chemical treatments have also been examined to introduce geometrical features at a microscopic scale on the metal surface to promote micro-mechanical interlocking between metals and PP under different welding conditions [25,37]. Along this line, the application of silane coupling agent on the metal surface has been proven beneficial for enabling the bonding between the metal and PP [22]. Surface modification of PP by plasma treatment [38] and bulk polymer modification by maleic anhydride grafting [39,40] have also been useful for joining PP with metals. These promising outcomes were attributed to the contributions of plasma treatment which generated transient functional groups on the PP surface and maleic anhydride grafting that contains carbonyl functional groups [41,42]. On the other hand, micro-mechanical anchoring provided by laser texturing has also become a suitable means to provide the joining through mechanical interlocking mechanism when the functional groups are absent in the polymer [25] or when to fulfill the requirement of joint strength improvement [33].

PP has the lowest polymer density and its composites have been very cost-effective among other available thermoplastic composites [43–45]. Demands for PP-based composites for producing metal-polymer hybrid structures have been surging in recent years in the automotive industry due to the significant advancements in thermoplastic composite manufacturing[46,47]. Even though the surface modification methods mentioned above have shown their efficiency in enhancing the bonding strength between metals and PP, these methods are still less attractive for the mass-production industry for which low manufacturing cost and production throughput are the main drivers.

To address some of the challenges mentioned above, this study is focused on the development of a robust and direct PP to metal joining method. Specifically, here we consider the combination of 6061 aluminum alloy (AA6061) and PP-based glass fiber reinforced polymer

composite (GFRP-PP) through a spot weld configuration. Through a simple and inexpensive carbonyl group seeding technique, it can be shown that strong chemical bonding at the GFRP-PP and AA6061 interface can be consistently established, resulting in strong bonding strengths. Both mechanical and interfacial microstructure characterizations are then performed for characterizing the resulting bonding interface quality and effects of various process parameters. The underpinning bond formation mechanisms at the joint interface between AA6061 and PP-based GFRP-PP are also discussed.

Table 3.1: Mechanical and physical properties of AA6061-T6, 40GFRP-PP, and PA6

	AA6061-T6	**40GFRP-PP**	**PA6**
Ultimate tensile strength (MPa)	310	115	85
Yield strength (MPa)	242	-	-
Elastic modulus (GPa)	68.9	8.66	3.30
Elongation at break (%)	12.50	4.50	40
Melting temperature (°C)	476-660	165	230
Thermal conductivity (W m^{-1} K^{-1})	167	0.30	0.25
Coefficient of thermal expansion (μm m^{-1} K^{-1})	23.6	45	90

Table 3.2: Elemental composition of AA6061-T6 sheet (wt.%)

	Al	Si	Zn	Fe	Cu	Mg	Ni	Mn	Ag	Cr	Others
AA6061	Balance	0.17	0.11	0.11	0.10	0.08	0.03	0.03	0.01	0.05	<0.025

3.2 Materials and Methods

AA6061 and GFRP-PP containing 40% glass fiber were used in this study. The physical and mechanical properties of both materials are listed in Table 3.1. As a point of reference, the conventional friction-assisted joining process is demonstrated in Figure 3.2(a) and a non-consumable heat-treated flat head steel tool of 20 mm diameter used is shown in Figure 3.2(b). Corresponding forge force and forge depth variations as a function of weld time are shown in Figure 3.2(c). A modified version of the friction-assisted spot joining schematic is shown in Figure 3.3(a), in which an off-the-shelf 50-μm thin PA6 film was placed for seeding the functional group

as an inter-layer between AA6061 and GFRP-PP (Figures 3.3b and 3.3c). Note that the color of the PA6 film is chosen only for providing a sufficient contrast in subsequent bonding surface examination. The physical and thermal properties of the PA6 film are listed in Table 3.1 and the chemical composition of AA6061-T6 is listed in Table 3.2. The dimensions of the specimen used are shown in Figure 3.4(b-c). The aluminum sheet was polished with P400 sandpaper and then degreased with ethanol before joining. No special surface or bulk material modification was performed on the GFRP-PP composite.

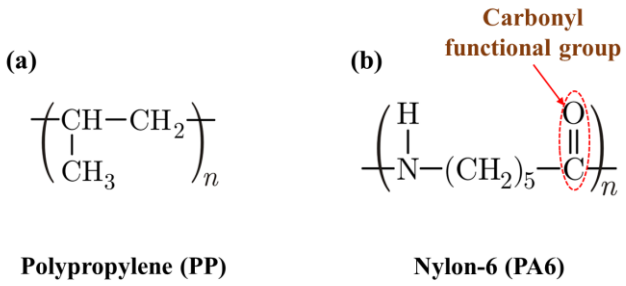


Figure 3.1:Chemical structure of (a) Polypropylene (PP) without any functional group, (b) nylon-6 (PA6) containing carbonyl functional group

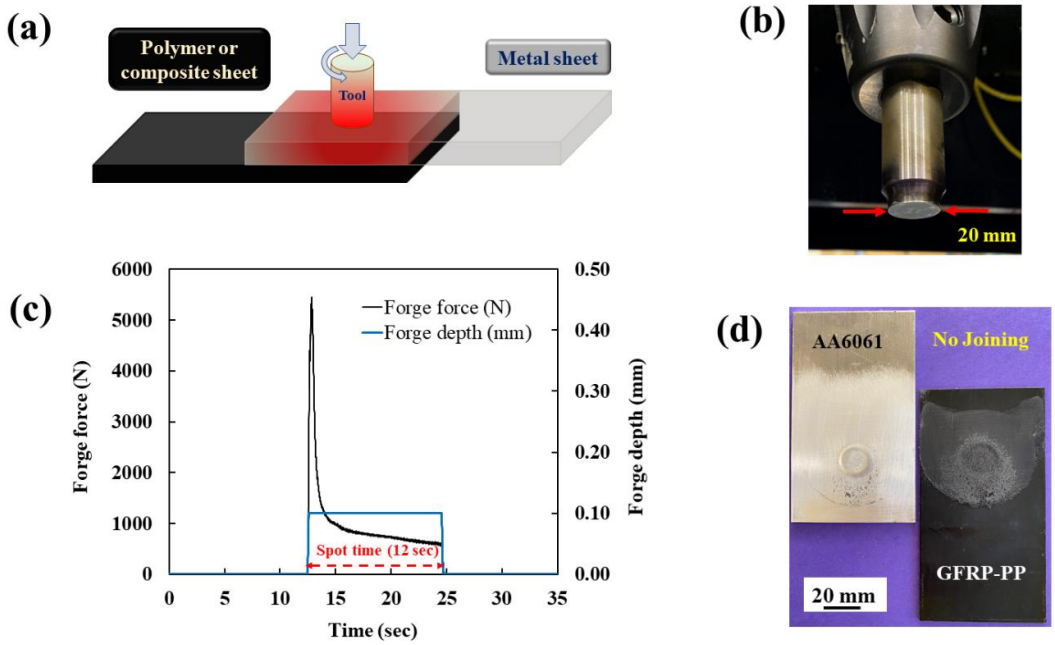


Figure 3.2: (a) Schematic of a friction spot joining method, (b) non-consumable steel tool, (c) forge force and depth variation during the main phase of friction assisted joining process, (d) non-joinable AA6061 and GFRP-PP by conventional method

Sandwich assembly using PA6 inter-layer was prepared as shown in Figures 3.3(a-b) and an initial force of 150N using the said flat head tool were applied to maintain close contact between metal and composite sheets. Friction-assisted spot joining was then performed at a constant tool rotation rate of 1800 rpm under displacement control mode. Forge depth was varied from 0.05 to 0.15 mm and spot weld times of 3, 6, and 12-sec were used.

Three K-type thermocouples were used to measure the interface temperatures and their embedded arrangements are shown in Figure 3.8(a-b). Lap shear tensile experiments were performed to obtain the joint strength in an MTS load frame at a displacement rate of 1 mm/min (Figure 3.4a). Cross-sectional analyses at macro and microscopic levels were performed along the section BB' (Figure 3.8a) using Nikon DIC optical microscope (OM) and a JEOL IT500 scanning electron microscope (SEM). SEM observations were carried out at 5kV – 15kV accelerating voltage under secondary electron detector (SED) mode and at 15kV accelerating voltage under back electron detector (BED) mode. The lengths of the bonding regions were measured along the aluminum surface at the cross-sections and the depths of the melting region were measured under the nugget center (Figure 3.6a-c).

3.3 Results

As stated in the previous section, due to its non-polar nature (Figure 3.1a), low surface energy, and hydrophobicity, PP-based composite does not join with any metal without any special surface or material pre-treatment. After the initial polishing and degreasing, several welding trials were conducted to join AA6061 and GFRP-PP using the reference welding parameter variation as shown in Figure 3.2c, and the resulting scenarios are presented in Table 3.3. As can be seen in Table 3.3, none of the welding parameter combinations could produce the joining between AA6061 and GFRP-PP, and sheets of both materials fell apart (Figure 3.2d) as soon as the tool

was lifted from the metal surface. Consequently, no significant polymer residue was observed on the metal side (Figure 3.2d).

Table 3.3: Summary of welding trials to join AA6061 and GFRP-PP without PA6 thin film inter-layer and any special surface or material pre-treatment

Spot Weld Time (sec)	900 RPM 0.10 mm	1800 RPM 0.10 mm	1800 RPM 0.15 mm
3	No Joining	No Joining	No Joining
6	No Joining	No Joining	No Joining
12	No Joining	No Joining	No Joining
25	No Joining	No joining	No joining

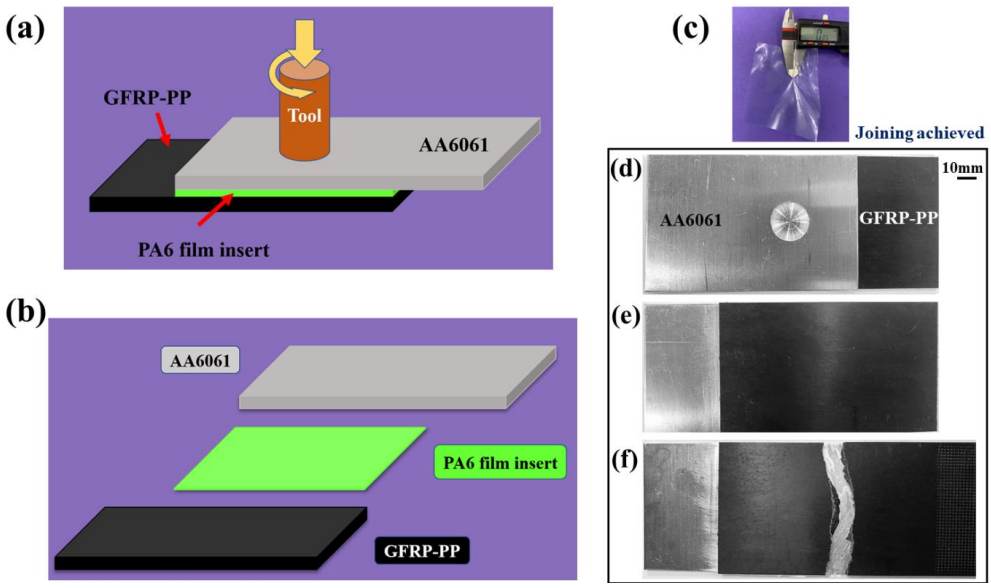


Figure 3.3: (a) Schematic of friction spot joining method using thin film insert, (b) detailed view of material placement during joining, (c) 50 µm thick PA6 insert film, (d) top view of the AA6061/GFRP-PP joint produced using thin PA6 film [1800 RPM, 12-sec and, (f) bottom view and base material failure of the joint produced after the lap shear tensile test

3.3.1 Bonding enabled by carbonyl group seeding

Figures 3.3(d-f) illustrate a strongly bonded joint between AA6061 and GFRP-PP composite substrates, in contrast to Figure 3.2(d) which shows no signs of bonding at all. The inter-layer of PA6 thin film enabled the formation of a strong bond between these two materials without requiring any special surface or material modifications either on the metal or GFRP-PP

side. Figure 3.3(d-f) represent a specimen produced at 1800 rpm, 12-sec spot weld time, and 0.10 mm forge depth before and after the lap shear tensile experiment. Except for the plastically deformed region under the tool impression, no noticeable thermo-mechanical distortion was seen on either side of the specimens (Figures 3.4d-f). Figure 3.4(f) shows the base material failure, suggesting a much stronger joint than the base GFRP-PP composite material.

The failure location is at some distance away from the tool center, indicating a sufficiently developed interfacial bonding between both materials, which offers sufficient joint strength. It should be emphasized here that the joining method demonstrated here requires no special bulk or surface modifications on either material side, unlike the existing methods either using surface treatments [25] or bulk material modification methods [39,41,48]. It should be pointed out that maximum loads at failure not the joint strengths are compared to determine the maximum load capacity of the joints. For deriving joint strength in terms of stress at failure for comparing with other specimen types (e.g., cross-tension [49,50]) or structural applications, the mesh-insensitive structural stress methods [51–53] can be used, which is beyond the scope of this study.

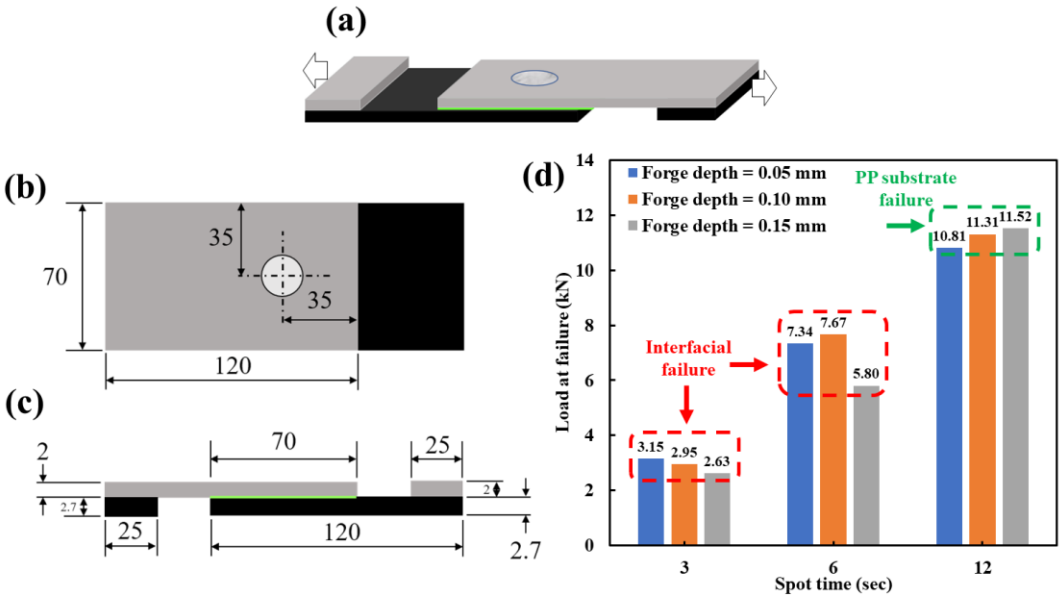


Figure 3.4: (a) Lap shear tensile test schematic, (b) & (c) major dimensions of the specimen used, (d) summary of the peak loads at failure during lap shear tensile test

3.3.2 Joint strengths, failure modes, and key welding parameters

Joint strengths were evaluated using lap-shear specimen design configuration (see Figure 3.4a through 3.4c) typical of those used for spot welded specimens [25,34] under different welding conditions in terms of friction tool forge depth and welding time. The results are shown in Figure 3.4d corresponding to a constant tool rotation rate of 1800 rpm. Two important observations can be made from the lap shear tensile test results obtained in Figure 3.4d. First, the spot weld time has significant effects on the joint load capacity (measured as the load at failure). The load at failure increases with spot weld time and reaches its maximum value when the weld time reaches about 12 seconds, when tensile failure within the PP substrate at some distance away from the spot weld area occurs, hereafter referred to as base material failure mode.

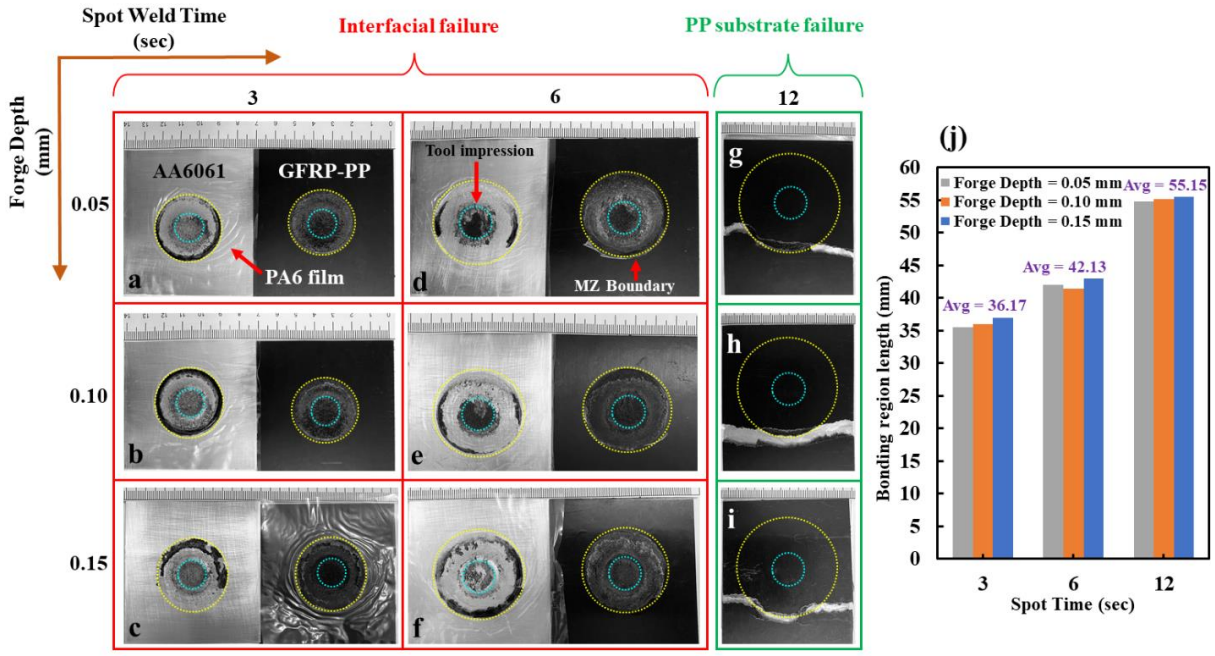


Figure 3.5: (a-i) Failure patterns after lap shear tensile test of AA6061/GFRP-PP joints produced using PA6 thin film inter-layer [1800 RPM, various forge depth and spot weld time], (j) comparison of the bonding region lengths measured as the outer diameters of the bonding region lengths measured as the outer diameters of the melting zone (MZ).

The apparent lower failure loads with weld time of less than about 12 seconds can be related to insufficient bond formation at the interface, leading to the interfacial failure mode, i.e., failure

along the interface between the aluminum and PP substrates, as shown in Figure 3.5(a) through 3.5(f). Second, welding forge depth within the range considered did not influence the joint load capacity in any significant manner. As can be observed from Figure 3.4(d), all three forge-depths resulted in similar levels of loads at failure in all cases. Also, as stated in Section 3.2, an initial contact force of around 150 N was used to keep both material sheets in close contact to avoid any gap between the joining surfaces before starting the process. This suggests that the forge depth does not affect the joint formation significantly as long as an initial minimum contact force is maintained between both the materials.

As substantiated in Figure 3.5(a) through 3.5(f), within the cases exhibiting interface failure mode corresponding to weld time being less than 12 seconds, the increase in failure loads shown in Figure 3.4d can be attributed to the increase in interfacial bonding area indicated by the overall increased area size of PP composite residuals sticking to the aluminum substrates. As the weld time reaches about 12 seconds, the failure mode transitions to base material failure in PP composite substrates (Figures 3.5g through 3.5i) in all cases resulting in the maximum joint load capacity given in Figure 3.4d.

3.3.3 Interfacial microstructure characterization

SEM micrographs of the cross-section in Figure 3.6(a-b) further elucidate the bonding interface and bond-line microstructure features of the joint developed between AA6061 and GFRP-PP at 1800 rpm, 12-sec spot weld time and 0.10 mm forge depth. A mixed network of polymers and randomly distributed glass fibers across the composite side can be seen in Figure 3.6(a) without any fiber penetration through or across the aluminum surface. Since the peak process temperature is above 350 °C (Figure 3.9c), both polymers must generate various chemical compounds through pyrolysis at elevated temperatures. Consequently, gases and bubbles form in

the viscous polymer melt and migrate away from the aluminum surface under high pressure. These bubbles become cavities during polymer re-solidification and are encircled in Figure 3.6(a).

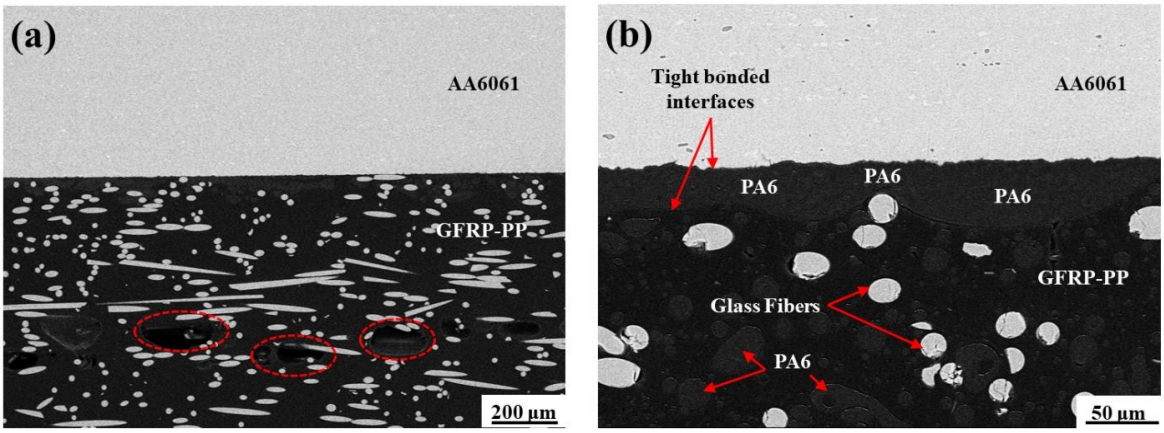


Figure 3.6: Cross-sectional SEM images of AA6061/GFRP-PP joint [1800 rpm, 12-sec and 0.10 mm], (a) low magnification SEM micrograph with visible cavities, (b) high magnification SEM micrograph depicting bonding interface and PA6-fibers-PP network

An intimately bonded interface between AA6061 and PA6 near the aluminum surface and a significant amount of PA6 dispersion towards the GFRP-PP composite side can be further observed in Figure 3.6(b). A network of PP matrix, glass fibers, and PA6 wrapping the glass fibers in the re-solidified polymer melt are highly pronounced below the aluminum surface (Figure 3.6b). It suggests that frictional heat melted the PA6 and PP matrix, and glass fibers were physically inter-mixed again between these polymers. The system then re-solidified as a multi-material composite network near the aluminum surface.

Figures 3.7(a-c) show a tightly bonded AA6061 and PA6 interface. The boundaries are non-distinguishable at the nanoscale and can be seen intimately fused (Figure 3.7c). “Fused boundaries suggest intimate bonding between both materials without any significant mechanical interlocking features”. The intimate bonding between the AA6061 and PA6 consistently prevails for most of the joint bond-line (Figure 3.6a-b), although the spread of PA6 varies with respect to the nugget center location (Figure 3.6b and 3.12).

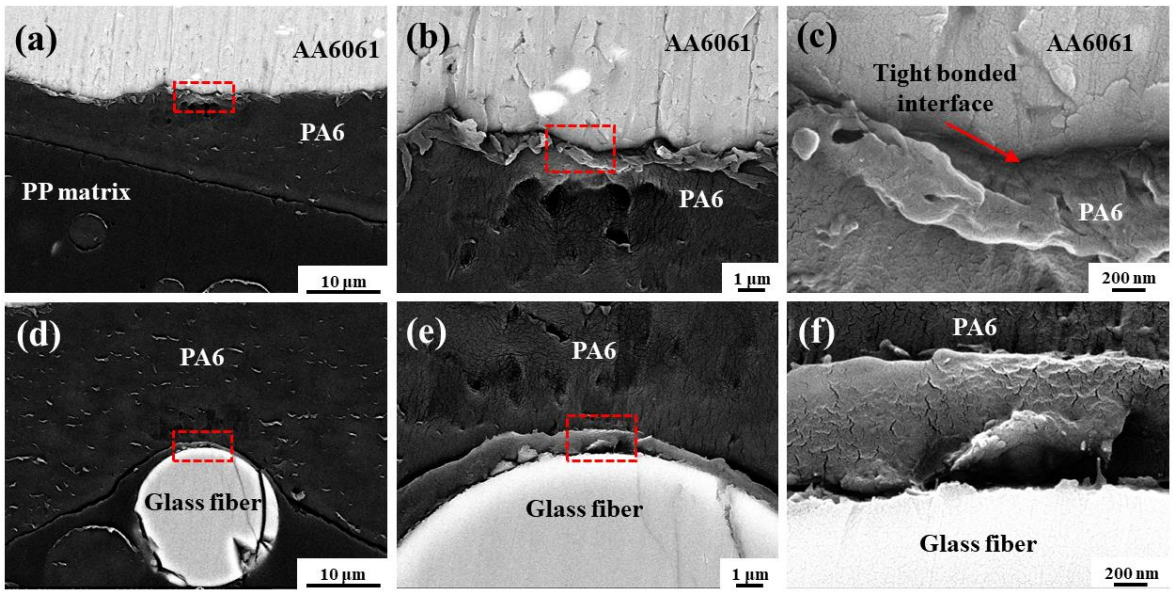


Figure 3.7: SEM images of bonding interfaces in AA6061/GFRP-PP joint [1800 rpm, 0.10 mm and 12 sec], (a-c) Al-PA6 interface, (d-f) PA6-fiber interface

Figure 3.7(d) shows a glass fiber surrounded by the PA6 and another 400 nm thick layer of unidentifiable material which is further observed in Figures 3.7(e-f) between PA6 and the glass fiber. Since PP was reinforced by 40% glass fibers in GFRP-PP, the residual layer may be a layer of PP matrix that remained on the fiber during the melting and re-solidification of polymers. It suggests that despite a thin layer of residual material on the glass fiber, PA6 is surrounding the glass fibers intimately, and formulates a strong multi-material composite network with GFRP-PP. A further molecular level adhesion characterization of this interface is beyond the scope of this article.

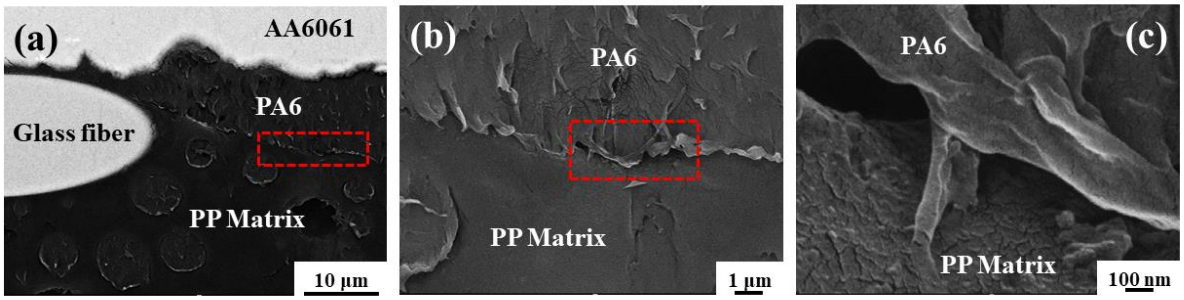


Figure 3.8: SEM images showing possible PA6-PP interface in AA6061/GFRP-PP joint [1800 rpm, 12-sec and 0.10 mm]

Figures 3.8(a-c) illustrate a noteworthy feature between PA6 and PP matrix materials. In general, PA6 and PP polymers are incompatible to mix and do not interact chemically due to their significantly opposite polar characteristics [40,54]. PA6 is polar in nature (Figure 3.1a) due to the presence of oxygen and nitrogen as electronegative species, whereas PP does not have any such electronegative species in its chemical structure (Figure 3.1b), making these two polymers chemically incompatible with each other [54]. However, we can observe an undefined interaction between both polymers at the nano-scale level and three-dimensional fibrillar linkages of PA6 can be seen diffusing in the PP matrix (Figures 3.8b-c). Probable molecular chain entanglement either at a physical level or chemical mixing of both the polymers under high temperature and pressure conditions can be attributed to this phenomenon and, a comprehensive physical and chemical analysis is necessary to provide more meaningful insights further in the future.

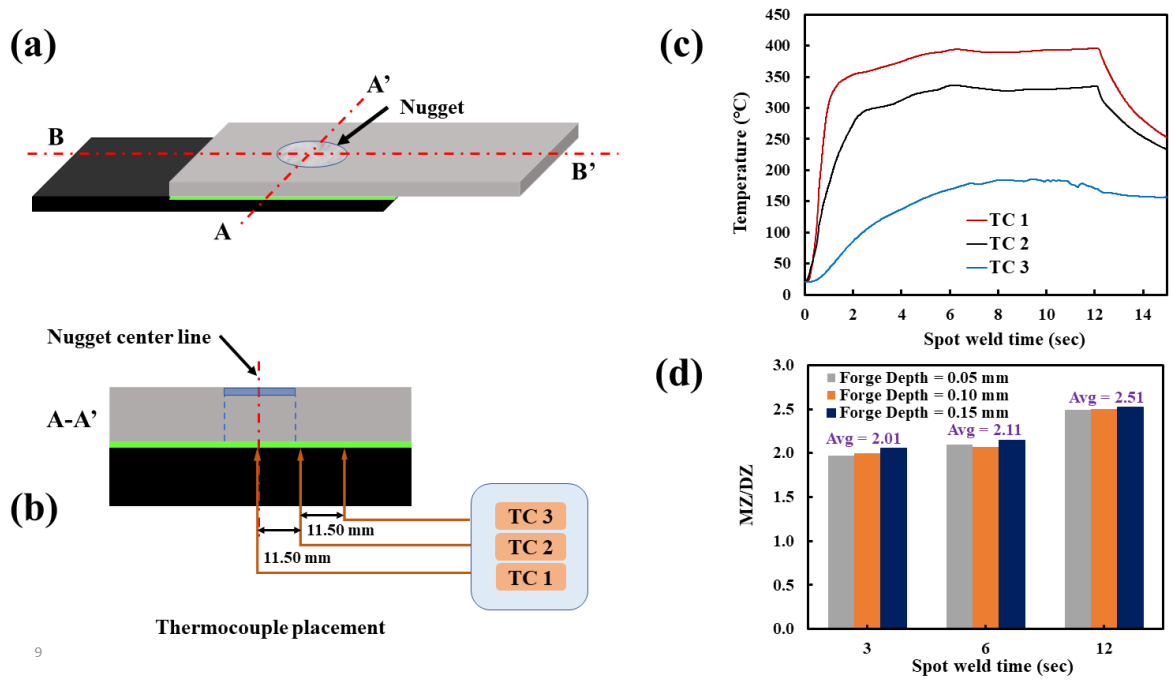


Figure 3.9: Interfacial temperature measurement, (a-b) schematic of thermocouple (TC) placement, (c) temperature measurements for AA6061/GFRP-PP joint [1800 rpm, 12 sec, 0.10 mm] and, (d) ratios of MZ to DZ for various process parameters.

Interfacial temperature histories are examined, as shown in Figure 3.9. Figures 3.9(a-b) show the embedded thermocouple placements during spot welding corresponding to 1800 rpm friction tool rotation, 12-sec spot weld time, and 0.10 mm forge depth. Figure 3.9(c) shows the interfacial temperature history measurement data corresponding to the three interfacial positions described in Figure 3.9(b). As can be seen in Figure 3.9b, thermocouple-1 (TC1) was placed at the centerline of the nugget, TC2 was placed underneath and adjacent to the tool boundary (tool diameter 20 mm) and, TC3 was placed where the through-thickness failure initiation of GFRP-PP was observed (just before 23.50 mm from the nugget center). TC1 provided the temperature profile under the nugget center and reached a maximum of 394 ℃ representing the overall peak process temperature (Figure 3.9c). This indicates a high frictional heat diffusion radially inwards increasing the temperature at the center higher than in other locations. TC2 and TC3 registered maximum temperatures of 336 ℃ and 185 ℃ respectively (Figure 3.9c). Also, TC1 maintained a comparatively higher temperature than TC2 and TC3 throughout the process. This can be attributed to the farther positions of TC2 and TC3 from the nugget center and unavoidable losses of frictional heat while diffusing radially outwards from the center.

As can be seen in Figure 3.9(c) that all the thermocouples maintain temperatures higher than 165 ℃ after a 6-sec spot weld time where 165 ℃ represents the melting point of the PP matrix. The thermal decomposition of pristine PP and PA6 starts above 355 ℃ and 398 ℃ respectively and glass fiber reinforcement can increase the decomposition temperature for GFRP-PP further beyond 425 ℃ [55,56]. Additionally, as shown in Figure 3.9(c), the peak process temperature measured (TC1 peak) is near 400 ℃, and the TC1 temperature profile is above 350 ℃ for most of the joining process duration. This indicates a reasonable possibility of partial thermal decomposition of both the polymers near the tool center. However, TC2 and TC3 temperature

profiles are well below the decomposition temperatures, suggesting no significant thermal decomposition of both the polymers away from the tool center. Corresponding melting zone (MZ) diameter from Figure 3.5(j) and decomposition zone (DZ) diameters are further used to obtain MZ/DZ and are shown in Figure 3.9(d). It can be observed that the 12-sec spot welding significantly increases the MZ/DZ corresponding to the stabilized temperature regime in Figure 3.9(c) beyond 6-sec spot weld time.

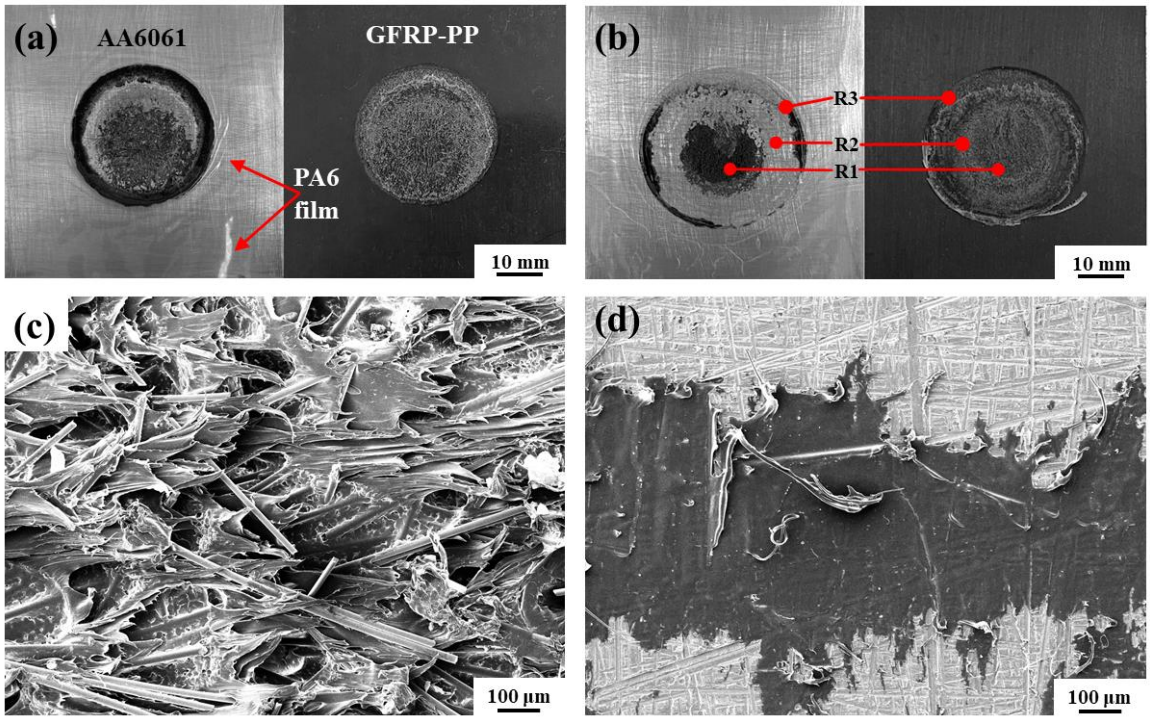


Figure 3.10: Failure features of the produced joints [1800 rpm, 0.10 mm] at, (a) 3-sec spot weld time, (b) 6-sec spot weld time, (c) SEM micrograph of R1 on aluminum side, (d) SEM micrograph of R2 on aluminum side

3.3.4 Fracture surface analysis

Posterior analyses of fracture feature further elucidate the bonding phenomenon between AA6061 and GFRP-PP due to the thin PA6 insert layer and are shown in Figures 3.10(a-d). Joints developed at 1800 rpm and 0.10 mm forge depth was selected owing to the reasons stated in earlier sections. Figures 3.10(a) and 3.10(b) show the interfacial fracture features of 3-sec and 6-sec spot-welded joints respectively. Due to their different failure surface morphologies, three distinct

bonding regions can be observed. Region-1 (R1) contains the area with a noticeable tool impression under the aluminum sheet and receives the highest amount of heat during the joining process to attain the peak process temperature (Figure 3.10b). Region-2 (R2) is the shiny area beyond R1 with a significant amount of PA6 residue on both aluminum and PP composite sides (Figure 3.10b). Region-3 (R3) is the outermost thick ring of re-solidified PP and PA6 residues surrounding R2 (Figure 3.10b). All the regions are shown in Figure 3.10(b) and can be seen evolving, with spot weld time conforming with Figure 3.5. Other researchers [10,25,57] have used different terminologies for such regions responsible for bonding based on similar thermomechanical and adhesion characteristics.

Furthermore, Figure 3.10(a) shows a spread of PP residue (blackened area) and fibers in R1 starting at a 3-sec spot weld time. PP residue and fibers' density increase for the 6-sec spot weld time in R1 on the aluminum side as shown in Figure 3.10(b) and are expected to increase further for the 12-sec spot weld time. Due to high heat input, a large amount of polymer must melt in R1 and flow outside the R1 under high tool pressure, leaving a shiny saddle transition surface surrounding R1 (Figure 3.10b). Similarly, due to high heat, the density of gaseous bubbles must be high in R1 compared to surrounding areas. Consequently, R1 shows interface failure features, and the fracture surfaces on the aluminum side depict the morphology of intermittently broken bubbles, cavities, and polymer network tearing (Figure 3.10c). Dominated by high bubble and cavity concentrations and resultant failure features, R1 alone cannot provide high joint strength.

On the other hand, R2 has a different correlation with spot weld time compared to R1. As can be seen in Figure 3.5 and Figure 3.10(a-b), the width of R2 increased significantly both in aluminum and PP composite sides with spot weld time. R2 has an opaque residue of PA6 material which increases both on aluminum and PP composite sides with increasing spot weld time. The

PA6 residue in R2 is not consistently uniform and spots of shiny aluminum surface also appear in R2 on the aluminum side (Figure 3.10d). Its mixed spread on both aluminum and GFRP-PP sides suggests that R2 has both adhesive and cohesive failure features as can be seen in Figures 3.10(b & d). Furthermore, R2 has only minute traces of glass fibers as can be seen in Figures 3.10(d). The absence of fibers in R2 at the aluminum side, suggests that PA6 film melted and resolidified with glass fibers of GFRP-PP to form a strong multi-material composite network in R2. The fiber network between PA6 and glass fibers is significantly stronger than the PA6 and aluminum bonding in R2 and does not break in PP composite (Figure 3.10d). The absence of any cavity-breaking features in R2 implies that bubbles if formed, should be very few in R2. A further increase in spot weld time from 6-sec must melt and resolidify a higher amount of PA6 and PP matrix in R2 and further increase the bonding strength. Owing to the low possibility of bubbles and a combination of adhesive-cohesive failure features, R2 should provide a high contribution toward overall joint strength. This fact is more pronounced in the 12-sec spot-welded joint (Figure 3.11) which failed in the base PP composite material.

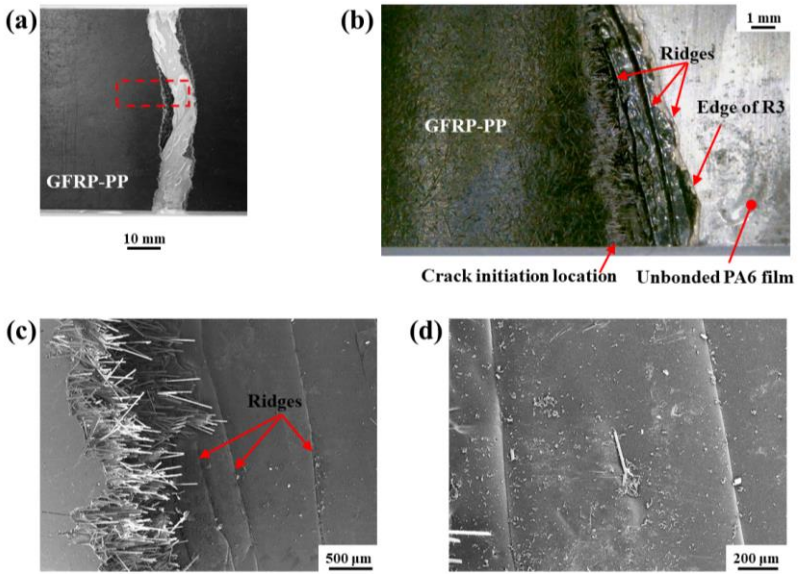


Figure 3.11: Resolidified PA6 near fracture origin in the joint [1800 rpm, 0.10 mm and 12 sec], (a) global view, (b) local view of PA6+PP reconsolidation near through crack fracture region, (c) SEM micrograph of crack front location and ridges, (d) ridges pattern on the aluminum side

The outermost region R3 has a different morphology compared to R1 and R2 as shown in Figure 3.10(b). The outer diameter of R3 increases significantly with spot weld time as can be seen in Figures 3.10(a) and 3.10(b). It has a thick blackened ring of re-solidified material when spot weld time is 3-sec (Figure 3.10a), and it partially diffuses with PA6 when spot weld time increases to 6-sec (Figure 3.10b). The outer edge of R3 for the 12-sec spot-welded specimen suggests that it has ridge patterns (Figure 3.11b-d). Ridges form due to the squeezing action of molten viscous polymers away from the nugget center during the joining process. These ridges further formulate bulk material waviness in R3 when re-solidified, causing material discontinuities. Such melt flow and re-solidification caused material discontinuities in R3 must increase the stress concentration significantly near the outer edge of R3 (Figure 3.11b-d). Consequently, the fracture location appears near the edge of R3 as shown in Figure 3.11(b). It further follows from the morphologies and failure features that; qualitatively, bonding regions should follow a ranking of R2 > R1 > R3 towards the joint strength contribution. In other words, the boundary of the R1 corresponds to the DZ and the boundary of the R3 corresponds to the MZ. As shown in Figures 3.5 and 3.9(d), the fracture mode transitions from the interfacial failure mode for the 3 and 6-sec spot weld time, to BM failure for the 12-sec spot weld time when the MZ/DZ increases to the maximum attainable value.

3.4 Discussions

3.4.1 Bonding mechanisms

It is worth noting that all A6061 aluminum substrates used in this study were subjected to polishing using P400 sandpaper and degreasing with alcohol. The polishing process with P400 sandpaper typically provides surface roughness of around 30 μm without any significant depth and is not sufficient to achieve a strong micro-mechanical interlocking effect [25]. AA6061 and GFRP-

PP did not join without the PA6 inter-layer (Figure 3.2d and Table 3.3) after AA6061 surface polishing and degreasing using P400 sandpaper. However, using the same surface degreasing process, the strong joining between AA6061 and GFRP-PP (Figure 3.3d-f and Fig 3.5) was achieved when using the PA6 inter-layer, and, joining can be solely attributed to the application of functional group seeding inter-layer via PA6 thin film. The temperature profile due to the frictional heating in Figure 3.9c suggested that all the joining regions were either at the melting temperature of the PP matrix or higher and TC1 and TC2 remained above the melting temperature of PA6 throughout the joining process suggesting sufficient melting of both PA6 and PP matrix and mixing with the glass fibers to formulate the multi-material composite network. This multi-material composite network initiated at the AA6061 surface with the PA6 formulated an intimate interface with the AA6061.

Due to the presence of functional groups, PA6 must react strongly with metals and should be the major contributor to the strongly bonded interface between aluminum alloy and PA6 [11,24]. Liu et al., [24] proved that the formation of the C-O-Al type of chemical bond is a highly probable cause for providing intimate bonding between aluminum and PA6 type polymers. In addition, other researchers have suggested other possibilities of different chemical interactions between PA6 and metals [58,59]. AA6061 is an alloy containing various compositional elements and is always prone to have oxide and hydroxide layers when exposed to atmospheric conditions. In addition, hydrocarbon contaminations are likely to be present before and during the welding process, suggesting various combinations of chemical interactions between aluminum surface and PA6. On the other end, both PA6 and PP matrices are found to have a strong network via the glass fibers and form a strong interface at the AA6061. The boundaries of AA6061 and PA6 are indistinguishable in Figure 3.7(c), suggesting a strong and intimate bonding between both

materials at the molecular level. Further quantification of chemical and physical bonding types at an atomic or molecular level is out of the scope of this study.

Another important feature of bonded regions observed in Figure 3.5 is further illustrated in detail in Figure 3.10. All these bonded regions are predominantly circular and are found to be playing a significant role in joint quality. The placement of the friction tool and the distances from all the joint boundaries were maintained to keep the joint geometry symmetric with respect to the tool center and tool surface area. Edges of the joint were maintained square of 70 mm x 70 mm and a minimum one tool diameter distance was maintained between the tool edge and the joint's outer edges providing a significant space to contain the pressure generated during the tool plunging and polymer melting during the joining process. Additionally, the spread of the melting zone increases more compared to the concentration of the decomposition zone around the tool impression (Figures 3.5 a-j and Figure 3.9d) which signifies a fully developed joint under the 12-sec spot weld condition for the said material combination. This can potentially happen when the interfacial contact regions have reached the melting point of both the PA6 and the PP matrix material, as can be seen from the corresponding temperature profiles in Figure 3.9(c) for an approximately stable thermal regime beyond 6-sec spot weld time. Further analysis to understand the effect of pressure containment and optimization corresponding to the tool and joint sizing and tool placement will be considered in future studies.

Based on the macro and microscopic observations discussed above, the bond formation process can be described as illustrated in Figure 3.12, starting from polymer melting, to melt flow and melt re-solidification, leading to a multi-material composite network at the joint interface (see Figures 3.12(a-b)). As seen in the previous sections, spot weld time plays a vital role in forming a strong joint. With a sufficient spot weld time, e.g., 12-sec (see Sec. 3.3.2), the general

characteristics of the bonded region and its development process follow those shown in Figures 3.12(a) and 3.12(b). As such, cavity-rich volume in R1, wide spread of PA6 forming composite with glass fibers of GFRP-PP in R2, and evolution of ridges in R3 are shown in Figure 3.12(a). Fully developed bonding regions on aluminum and GFRP-PP sides along with ridges in R3 are shown in Figure 3.12(b).

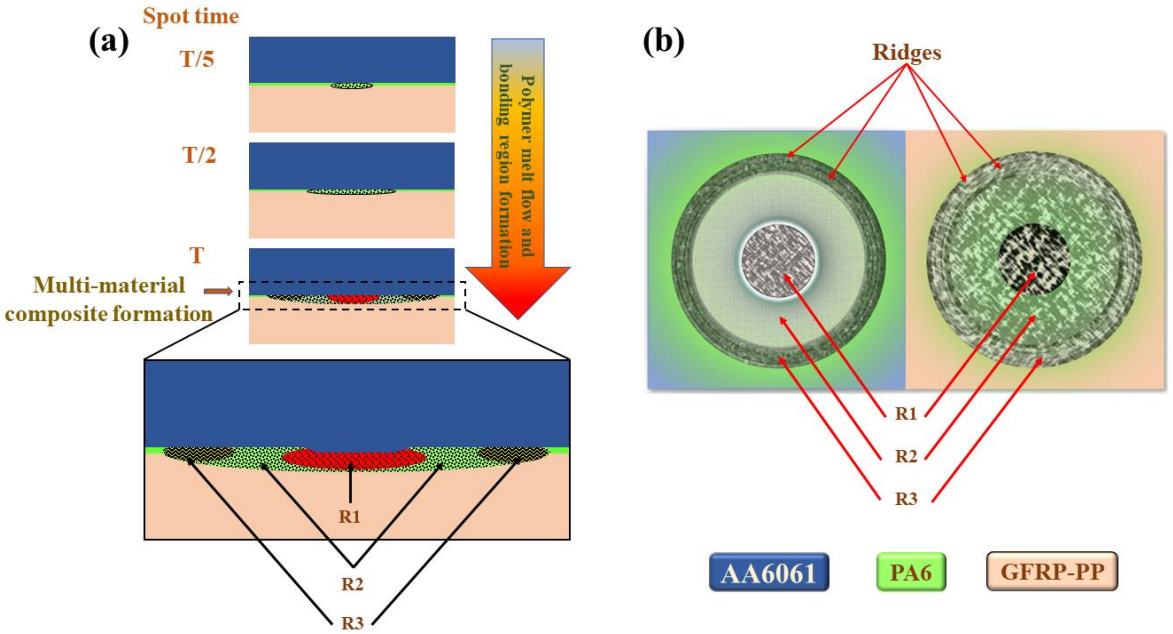


Figure 3.12: (a) Schematic representation of multi-material composite network formation at the cross-section of AA6061/GFRP-PP joint (T = 12-sec), (b) schematic representation of the fully developed bonding regions for a 12-sec spot-welded joint

3.4.2 Process Characteristics

The proposed friction spot joining process for achieving metal-polymer joining has only four process parameters to control (tool dimension, rpm, forge depth, and spot weld time). It can be directly extended for performing friction lap seam welding which can be used to achieve metal-polymer continuous joints and has numerous advantages [9,10]. The process offers several major advantages over existing joining processes, including (i) direct control of the bonded region through friction heating tool dimension, (ii) high welding speed without requiring special surface

or bulk material treatments, (iii) energy-saving and environmentally friendliness due to the absence of filler or masking gas, voltage sparks, and minimal material loss during friction heat generation. In addition, the application of an inexpensive and readily available PA6 thin film interlayer makes the process highly cost-effective. Note that PA6 thin film cost only around 1.50 cents per square inch of the joint produced between AA6061 and GFRP-PP in the laboratory which is significantly lower than other surface and material modification methods necessary to join said materials for load-bearing structural applications. After achieving the high quality joining under the current sample and material conditions, another future study of process parameter optimization is underway and is expected to bring forth an optimally short processing time aptly suited for automotive applications through the acquisition of a dedicated machine and control system.

3.5 Conclusions

A simple and reliable process for joining nonpolar polymer composite to metal is presented and has been successfully demonstrated for joining AA6061 and GFRP-PP in a spot weld configuration by seeding functional groups through a readily available PA6 thin film as an interlayer. The major conclusions of the present work can be summarized as follows.

1. Reliable joining between AA6061 and GFRP-PP, which traditionally cannot be accomplished without special surface or material modifications, can now be achieved through a simple functional group seeding technique using a PA6 thin-film. The joint failure load increases from zero (no joining condition), without the PA6 film insert, to 11.52 kN (BM failure) when using the PA6 film insert. The new process proves to be simple and cost-effective, particularly in a high-volume production environment.
2. Although this study was not intended to develop a detailed process parameter window for a specific application, the experimental results show that the proposed joining process

possesses just a few parameters to control for ensuring bond quality consistency. Chief among them are weld time (12-sec for the material combination used) which governs the final interfacial bonding area and preset forge depth (corresponding to the 150 N preset force) which is to ensure initial intimate contact at the joint interface. As a result, the process can be readily adapted to various applications for joining nonpolar polymeric composites to metals.

3. The application of PA6 provided the necessary interfacial bridging between the non-joinable AA6061 and the GFRP-PP. The interfacial bonding mechanisms observed can be attributed to (1) direct bonding between aluminum and PA6 (resulting from PA6 film) through previously proven C-O-Al type chemical bonding and; (2) the formation of a strong multi-material composite network of PA6, glass fibers, and PP matrix, leading to a strong AA6061/GFRP PP joint.

References

[1] Sperling D, Cannon JS. Reducing climate impacts in the transportation sector. Springer; 2009.

[2] Taub A, Moor E De, Luo A, Matlock DK, Speer JG, Vaidya U. Materials for Automotive Lightweighting. Annu Rev Mater Res 2019;49:327–59. https://doi.org/10.1146/annurev-matsci-070218-010134.

[3] Peter WH, Love LJ, Chesser PC, Gaul KT. Hybrid Multi-Material Endoskeleton Overmolded Structure for Automotive Powertrain. ; Oak Ridge National Lab. (ORNL), Oak Ridge, TN (United States); 2018.

[4] Blanco D, Rubio EM, Marín MM, Davim JP. Advanced materials and multi-materials applied in aeronautical and automotive fields: a systematic review approach. Procedia CIRP 2021;99:196–201. https://doi.org/https://doi.org/10.1016/j.procir.2021.03.027.

[5] Pramanik A, Basak AK, Dong Y, Sarker PK, Uddin MS, Littlefair G, et al. Joining of carbon fibre reinforced polymer (CFRP) composites and aluminium alloys – A review. Compos Part A Appl Sci Manuf 2017;101:1–29. https://doi.org/https://doi.org/10.1016/j.compositesa.2017.06.007.

[6] Amancio-Filho ST, dos Santos JF. Joining of polymers and polymer–metal hybrid structures: Recent developments and trends. Polym Eng Sci 2009;49:1461–76. https://doi.org/https://doi.org/10.1002/pen.21424.

[7] Blaga L, Bancilă R, dos Santos JF, Amancio-Filho ST. Friction Riveting of glass–fibre-reinforced polyetherimide composite and titanium grade 2 hybrid joints. Mater Des 2013;50:825–9. https://doi.org/https://doi.org/10.1016/j.matdes.2013.03.061.

[8] Lambiase F, Scipioni SI, Lee C-J, Ko D-C, Liu F. A State-of-the-Art Review on Advanced Joining Processes for Metal-Composite and Metal-Polymer Hybrid Structures. Materials (Basel) 2021;14:1890.

[9] Lambiase F, Balle F, Blaga L-A, Liu F, Amancio-Filho ST. Friction-based processes for hybrid multi-material joining. Compos Struct 2021;266:113828. https://doi.org/https://doi.org/10.1016/j.compstruct.2021.113828.

[10] Liu FC, Liao J, Nakata K. Joining of metal to plastic using friction lap welding. Mater Des 2014;54:236–44. https://doi.org/https://doi.org/10.1016/j.matdes.2013.08.056.

[11] Liu FC, Dong P, Pei X. A high-speed metal-to-polymer direct joining technique and underlying bonding mechanisms. J Mater Process Technol 2020;280:116610. https://doi.org/https://doi.org/10.1016/j.jmatprotec.2020.116610.

[12] Liu FC, Nakata K, Liao J, Hirota S, Fukui H. Reducing bubbles in friction lap welded joint of magnesium alloy and polyamide. Sci Technol Weld Join 2014;19:578–87. https://doi.org/10.1179/1362171814Y.0000000228.

[13] Liu FC, Liao J, Gao Y, Nakata K. Effect of plasma electrolytic oxidation coating on joining metal to plastic. Sci Technol Weld Join 2015;20:291–6. https://doi.org/10.1179/1362171815Y.0000000012.

[14] Wang B, Sun Z, Xu L, Zhang W, Li X, Zhang H. Friction spot joining of aluminum AA5052 and short glass fiber-reinforced PPS: Effects of material properties and process parameters on joint structure and strength. J Manuf Process 2021;66:549–64. https://doi.org/10.1016/J.JMAPRO.2021.04.047.

[15] Balle F, Wagner G, Eifler D. Ultrasonic metal welding of aluminium sheets to carbon fibre reinforced thermoplastic composites. Adv Eng Mater 2009;11:35–9.

[16] Feistauer EE, Guimarães RPM, Ebel T, dos Santos JF, Amancio-Filho ST. Ultrasonic joining: A novel direct-assembly technique for metal-composite hybrid structures. Mater Lett 2016;170:1–4. https://doi.org/https://doi.org/10.1016/j.matlet.2016.01.137.
[17] Katayama S, Kawahito Y. Laser direct joining of metal and plastic. Scr Mater 2008;59:1247–50.
[18] Wahba M, Kawahito Y, Katayama S. Laser direct joining of AZ91D thixomolded Mg alloy and amorphous polyethylene terephthalate. J Mater Process Technol 2011;211:1166–74. https://doi.org/https://doi.org/10.1016/j.jmatprotec.2011.01.021.
[19] Huang Y, Gao X, Zhang Y, Ma B. Laser joining technology of polymer-metal hybrid structures - A review. J Manuf Process 2022;79:934–61. https://doi.org/10.1016/J.JMAPRO.2022.05.026.
[20] Tao W, Su X, Chen Y, Tian Z. Joint formation and fracture characteristics of laser welded CFRP/TC4 joints. J Manuf Process 2019;45:1–8. https://doi.org/10.1016/J.JMAPRO.2019.05.028.
[21] Mitschang P, Velthuis R, Didi M. Induction Spot Welding of Metal/CFRPC Hybrid Joints. Adv Eng Mater 2013;15:804–13. https://doi.org/https://doi.org/10.1002/adem.201200273.
[22] Nagatsuka K, Xiao B, Wu L, Nakata K, Saeki S, Kitamoto Y, et al. Resistance spot welding of metal/carbon-fibre-reinforced plastics and applying silane coupling treatment. Sci Technol Weld Join 2018;23:181–6.
[23] Nagatsuka K, Kitagawa D, Yamaoka H, Nakata K. Friction Lap Joining of Thermoplastic Materials to Carbon Steel. ISIJ Int 2016;56:1226–31. https://doi.org/10.2355/isijinternational.ISIJINT-2016-042.
[24] Liu FC, Dong P, Lu W, Sun K. On formation of AlOC bonds at aluminum/polyamide joint interface. Appl Surf Sci 2019;466:202–9. https://doi.org/https://doi.org/10.1016/j.apsusc.2018.10.024.
[25] Han SC, Wu LH, Jiang CY, Li N, Jia CL, Xue P, et al. Achieving a strong polypropylene/aluminum alloy friction spot joint via a surface laser processing pretreatment. J Mater Sci Technol 2020;50:103–14. https://doi.org/https://doi.org/10.1016/j.jmst.2020.02.035.
[26] Hussein FI, Akman E, Genc Oztoprak B, Gunes M, Gundogdu O, Kacar E, et al. Evaluation of PMMA joining to stainless steel 304 using pulsed Nd:YAG laser. Opt Laser Technol 2013;49:143–52. https://doi.org/https://doi.org/10.1016/j.optlastec.2012.12.028.
[27] Meiabadi MSSM, Kazerooni A, Moradi M, Torkamany MJ. Laser assisted joining of St12 to polycarbonate: Experimental study and numerical simulation. Optik (Stuttg) 2020;208:164151.
[28] Yusof F, Miyashita Y, Seo N, Mutoh Y, Moshwan R. Utilising friction spot joining for dissimilar joint between aluminium alloy (A5052) and polyethylene terephthalate. Sci Technol Weld Join 2012;17:544–9. https://doi.org/10.1179/136217112x13408696326530.
[29] Al-Sayyad A, Salah F, Bardon J, Hirchenhahn P, Shihata L, Houssiau L, et al. Laser Ablation of Titanium Alloy (Ti64): Effects of Process Parameters on Performance of Laser Welded Ti64–Polyamide 6.6 Joints 2021.
[30] Izadi O, Mosaddegh P, Silani M, Dinari M. An experimental study on mechanical properties of a novel hybrid metal–polymer joining technology based on a reaction between isocyanate and hydroxyl groups. J Manuf Process 2017;30:217–25. https://doi.org/10.1016/J.JMAPRO.2017.09.022.
[31] Alaluss K, Bürkner G. Thermal joining of steel/polymer/steel composite materials using

non-direct arcprocess technique. J Manuf Process 2018;34:523–30. https://doi.org/10.1016/J.JMAPRO.2018.06.032.
[32] Lambiase F, Grossi V, Paoletti A. Defects formation during Friction Assisted Joining of metals and semi crystalline polymers. J Manuf Process 2021;62:833–44. https://doi.org/10.1016/J.JMAPRO.2020.12.063.
[33] Wang Z, Bi X, Liu B, Xu M, Dong Z. Adhesion enhancement of PEEK/6161-T6 FLJ joints via laser surface modification. Compos Part B Eng 2021;216:108797.
[34] Lambiase F, Paoletti A. Mechanical behavior of AA5053/polyetheretherketone (PEEK) made by friction assisted joining. Compos Struct 2018;189:70–8.
[35] Li Y, Bu H, Yang H, Liu G, Yao J, Zhan X. Effect of laser heat input on the interface morphology during laser joining of CFRTP and 6061 aluminum alloy. J Manuf Process 2020;50:366–79. https://doi.org/10.1016/J.JMAPRO.2019.12.023.
[36] Bu H, Zhan X, Yang H, Wang F, Ma W. Numerical simulation of thermal distribution and residual stress characteristic for laser wobble joining of CFRTP and Ti-6Al-4V alloy. J Manuf Process 2022;79:562–75. https://doi.org/10.1016/J.JMAPRO.2022.05.018.
[37] Xie Y, Zhang J, Zhou T. Large-area mechanical interlocking via nanopores: Ultra-high-strength direct bonding of polymer and metal materials. Appl Surf Sci 2019;492:558–70.
[38] Ku JH, Jung IH, Rhee KY, Park SJ. Atmospheric pressure plasma treatment of polypropylene to improve the bonding strength of polypropylene/aluminum composites. Compos Part B Eng 2013;45:1282–7. https://doi.org/https://doi.org/10.1016/j.compositesb.2012.06.016.
[39] Chen J, Du K, Chen X, Li Y, Huang J, Wu Y, et al. Influence of surface microstructure on bonding strength of modified polypropylene/aluminum alloy direct adhesion. Appl Surf Sci 2019;489:392–402.
[40] Ochoa-Putman C, Vaidya UK. Mechanisms of interfacial adhesion in metal–polymer composites – Effect of chemical treatment. Compos Part A Appl Sci Manuf 2011;42:906–15. https://doi.org/https://doi.org/10.1016/j.compositesa.2011.03.019.
[41] Liang C-S, Lv Z-F, Bo Y, Cui J-Y, Xu S-A. Effect of modified polypropylene on the interfacial bonding of polymer–aluminum laminated films. Mater Des 2015;81:141–8. https://doi.org/https://doi.org/10.1016/j.matdes.2015.05.021.
[42] Astigarraga V, Gondra K, Valea Á, Pardo Aurrekoetxea G. Improvement of adhesive bonding of polypropylene and maleic anhydride grafted polypropylene blends to aluminium by means of addition of cyclic butylene terephthalate. J Adhes 2019;95:286–307. https://doi.org/10.1080/00218464.2018.1437415.
[43] Liu L, Wang Z, Yu Y, Fu S, Nie Y, Wang H, et al. Engineering Interfaces toward High-Performance Polypropylene/Coir Fiber Biocomposites with Enhanced Friction and Wear Behavior. ACS Sustain Chem Eng 2019;7:18453–62. https://doi.org/10.1021/acssuschemeng.9b04381.
[44] Kore S, Spencer R, Ghossein H, Slaven L, Knight D, Unser J, et al. Performance of hybridized bamboo-carbon fiber reinforced polypropylene composites processed using wet laid technique. Compos Part C Open Access 2021;6:100185. https://doi.org/10.1016/J.JCOMC.2021.100185.
[45] Alwekar S, Yeole P, Kumar V, Hassen AA, Kunc V, Vaidya UK. Melt extruded versus extrusion compression molded glass-polypropylene long fiber thermoplastic composites. Compos Part A Appl Sci Manuf 2021;144:106349. https://doi.org/https://doi.org/10.1016/j.compositesa.2021.106349.

[46] Kleinbaum S, Jiang C, Logan S. Enabling sustainable transportation through joining of dissimilar lightweight materials. MRS Bull 2019;44:608–12. https://doi.org/DOI: 10.1557/mrs.2019.178.
[47] Link T, Behnisch F, Rosenberg P, Seuffert J, Dörr D, Hohberg M, et al. Hybrid Composites for Automotive Applications–Development and Manufacture of a System-integrated Lightweight floor Structure in multi-material Design. Proc. SPE 19th Annu. Automot. Compos. Conf. Exhib. ACCE, 2019.
[48] Chen M-A, Li H-Z, Zhang X-M. Improvement of shear strength of aluminium-polypropylene lap joints by grafting maleic anhydride onto polypropylene. Int J Adhes Adhes 2007;27:175–87. https://doi.org/https://doi.org/10.1016/j.ijadhadh.2006.01.008.
[49] Zhu XB, Yang X, Li YB, Carlson BE. Reinforcing cross-tension strength of adhesively bonded joints using metallic solder balls. Int J Adhes Adhes 2016;68:263–72. https://doi.org/10.1016/J.IJADHADH.2016.04.009.
[50] Wu T, Zhang Q, Zhang C, Li YB, Carlson BE. Process variables influencing solder reinforced adhesive (SRA) performance. J Manuf Process 2018;31:440–52. https://doi.org/10.1016/J.JMAPRO.2017.12.001.
[51] Kang HT, Dong P, Hong JK. Fatigue analysis of spot welds using a mesh-insensitive structural stress approach. Int J Fatigue 2007;29:1546–53. https://doi.org/10.1016/J.IJFATIGUE.2006.10.025.
[52] Lu H, Dong P, Boppudi S. Strength analysis of fillet welds under longitudinal and transverse shear conditions. Mar Struct 2015;43:87–106. https://doi.org/10.1016/J.MARSTRUC.2015.06.003.
[53] Zhang Y, Dong P, Pei X. Fracture Mechanics Modeling of Fatigue Behaviors of Adhesive-Bonded Aluminum Alloy Components. Metals (Basel) 2022;12. https://doi.org/10.3390/met12081298.
[54] La Mantia FP. Blends of polypropylene and nylon 6: Influence of the compatibilizer, molecular weight, and processing conditions. Adv Polym Technol J Polym Process Inst 1993;12:47–59.
[55] Rahman NA, Hassan A, Yahya R, Lafia-Araga RA. Glass fiber and nanoclay reinforced polypropylene composites:morphological, thermal and mechanical properties, 2013.
[56] Sang L, Wang C, Wang Y, Wei Z. Thermo-oxidative ageing effect on mechanical properties and morphology of short fibre reinforced polyamide composites – comparison of carbon and glass fibres. RSC Adv 2017;7:43334–44. https://doi.org/10.1039/C7RA07884F.
[57] Goushegir SM, dos Santos JF, Amancio-Filho ST. Friction Spot Joining of aluminum AA2024/carbon-fiber reinforced poly(phenylene sulfide) composite single lap joints: Microstructure and mechanical performance. Mater Des 2014;54:196–206. https://doi.org/https://doi.org/10.1016/j.matdes.2013.08.034.
[58] Zhao S, Kimura F, Wang S, Kajihara Y. Chemical interaction at the interface of metal–plastic direct joints fabricated via injection molded direct joining. Appl Surf Sci 2021;540:148339.
[59] Hirchenhahn P, Al Sayyad A, Bardon J, Felten A, Plapper P, Houssiau L. Highlighting chemical bonding between nylon-6.6 and the native oxide from an aluminum sheet assembled by laser welding. ACS Appl Polym Mater 2020;2:2517–27.

Chapter 4 Direct Spot Joining of Thin Gauge Aluminum Alloy to Stainless Steel

4.1 Introduction

A multi-material approach to achieve effective structural lightweighting has gained increasing attention over the last decade [1–3]. As such, effectively combining steel with aluminum alloy can be a cost-effective means of attaining high strength-to-weight ratios in transportation systems, particularly for mass-produced automotive structures [4]. Another promising area of the multi-material applications approach is non-structural. These include thin gauge aluminum and steel combinations for automotive interior and exterior trims, weathering strips, and other related components [5–7]. Due to the nature of the high-volume production of these products, cost-effective dissimilar material joining methods become essential for realizing the potential of multi-material systems. This becomes particularly challenging when dealing with metallurgically incompatible material combinations, e.g., by directly welding an aluminum alloy to a steel substrate [8] (or polymer composite to metal [9–13]).

It is well known that fusion-based welding methods introduce brittle intermetallic compounds (IMCs) at the aluminum alloy and steel (Al/Steel in short) interface [14,15]. The presence of a certain amount of IMCs can cause cracking during welding and degrade joint load capacity for structural applications [16]. In addition, IMCs have been shown to be highly susceptible to galvanic corrosion under service environments [17].

As a result, solid-state joining methods have been considered in the research community. These include friction welding [18] and friction stir welding [19,20], roll bonding [21], magnetic

pulse welding [22], and vaporizing foil actuator welding (VFAW) [23,24] for joining the two incompatible metals directly. The first two methods have shown their potential, but consistently mitigating detrimental IMCs remains to be the major challenge. The last two are mostly investigated for some special applications, and VFAW uses a controlled high velocity impact to join the dissimilar material pairs. In the context of friction based joining processes, Ma et al. [25] showed that heat input during the friction joining of the aluminum alloy and the steel significantly affected the joint strength as a result of IMCs. The heat input during the joining process is further correlated with the IMC layer thickness, and the joint strength is significantly affected by the thickness of the IMCs at the interface. The joint strength was found to show a significant improvement with a reduction in IMC thickness. Kimapong et al. [26] reported that an IMC thickness of ~ 7 μm reduced the joint strength by ~ 60% for a joint compared to its strength when an IMC thickness was ~ 1 μm. Tanaka et al. [27] reported that the joint strength can be affected as much as three times when IMC thickness is reduced from ~ 1μm to ~ 0.1 μm. Watanabe et al. [28] showed that the thickness of the IMC layer in aluminum to steel joint under FSW increased with spot welding time used. There have been attempts of an intermediate transition layer, such as using Zn-based filler material [29] and utilizing the effect of silicon on Al-Si-based filler materials [30]. However, the presence of IMCs still cannot be avoided.

It is well established that aluminum to steel joints are prone to galvanic corrosion, which can be further adversely affected by the presence of IMCs [17]. Wloka et al. [29] demonstrated that the cathodic material (Fe) containing IMCs increases the dissolution of base material under a corrosive environment significantly. Shi et al. [31] showed that IMCs help formulate the galvanic cell at the interface and dissolve the base metals, accelerating the corrosion process further. Sravanthi et al. [32] have shown that the IMCs participate in galvanic corrosion and can further

accelerate the corrosion process with increased layer thickness. Ma et al. [33] have shown that the corrosion potential is severely affected if the IMC layer thickness is high and the corrosion resistance drops. Reducing the IMC layer thickness to the sub-micron level is, hence, critical for achieving structurally applicable and corrosion-resistant joints between aluminum and steel. The corrosion behavior of these dissimilar material joints thus is a defining factor for a successful structural application.

Several efforts have been used to either reduce the IMC layer thickness via controlling the heat input during the joining process or eliminate any IMCs at Al/Steel interface, including the stationary shoulder and buttering technique [25,34–36]. Along this line, noteworthy recent studies by Liu et al. [37] have shown that two dissimilar materials, e.g., aluminum alloy (AA6061-T6) and stainless steel 304, can be successfully joined together using a novel friction stir additive manufacturing (FSAM) method without detrimental IMCs at the interface through a controlled nanoscale shear localization induced amorphization (NSLIAA) process. Liu et al. [37] utilized a flat shoulder friction stir tool with a flat head pin and maintained a certain distance above the steel faying surface after penetrating the tool into the overlapped aluminum sheet. The rotating tool was then moved along the overlap length, maintaining the gap above the steel faying surface, enabling the NSSLIA process. Zhang et al. [38] further proved that the amorphous layer formed between the Al/Steel binary joints is stable and does not degrade or thicken under high-temperature post-heat treatment.

Encouraged by the recently discovered NSSLIA process for thick sheet aluminum alloy and steel combinations, this study is focused on achieving direct spot-joining of thin gauge aluminum alloy to stainless steel sheet by suppressing the IMCs at the interface by the NSSLIA process, develop a continuous amorphous reaction zone compared to discontinuous amorphous

layer achieved for thick metallic sheet pairs and significantly improve the corrosion resistance. After establishing bond quality and probable presence of amorphous phase at the bonding interface, the effects of a well-adopted automotive corrosion cycle on the resulting weld nugget morphology and spot joint strengths are then investigated in detail to explore the applicability of thin sheet spot joints for automotive applications under severe environmental conditions.

Table 4.1: Chemical compositions of stainless steel 316 (wt%).

	Fe	Cr	Ni	Mo	Mn	Cu	C	Si	N	S	P	Ti
SS316	Bal.	16-18.5	10-15	0-3	0-2	0-1	0-0.08	0-1	0-0.1	0.35	0-0.045	0.7 max

Table 4.2: Chemical compositions of AA6061-T6 alloy (wt%).

	Al	Mg	Si	Fe	Cr	Cu	Zn	Mn	Ni	Ti	Other
AA6061	Bal.	1.1	0.73	≤0.7	0.08	0.29	≤0.25	≤0.15	≤0.05	≤0.15	0.15

4.2 Materials and Methods

Aluminum 6061-T6 alloy sheets of 0.60 mm in thickness and SS316 stainless steel sheets of 0.76 mm in thickness were chosen to be joined for consideration in an automotive component. The chemical compositions of SS316 and AA6061-T6 are provided in Table 4.1 and Table 4.2, respectively, and their mechanical properties are listed in Table 4.3. A friction spot joining process was designed for this study by adopting a recently developed nanoscale shear localization process [37], as illustrated in Figure 4.1. The novelty of the shear localization-induced solid-state joining between the aluminum alloy and steel lies in the fact that it is capable of eliminating or minimizing the generation of IMCs. The process implemented here employs a non-consumable flat head tool with a shoulder and pin, as depicted in Figure 4.1. The pin used has a diameter of 8 mm and is maintained at a constant height "h" above the aluminum alloy/steel (Al/Steel) interface, as discussed in [37]. For the present study, it was set as $\frac{h}{t} = \frac{1}{3}$, where t refers to the thickness of

aluminum sheet and maintained throughout the process. The steel surfaces were received with #8 mirror polished surface condition securely covered with an adhesive back polymer film to avoid any contamination, and no surface or bulk material treatment was performed on aluminum alloy sheets. However, both sheets were cleaned using ethanol to remove dirt and grease from the surfaces. Although the perfectly flat steel faying surface without microscopic scratches is the primary requirement for this joining process, a mirror-polished surface was a final product surface requirement.

Table 4.3: Mechanical properties of base metals

	Yield Strength (MPa)	Ultimate Tensile Strength (MPa)	Elongation (%)
AA6061-T6	276	310	12
SS316	290	580	50

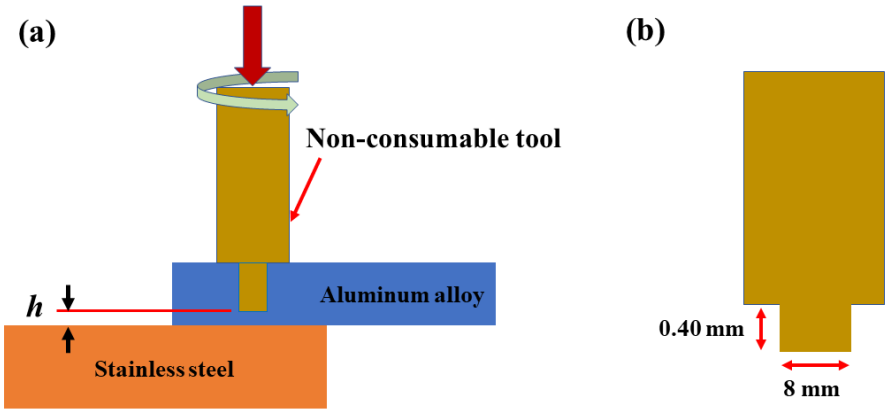


Figure 4.1: Friction spot joining process schematic: (a) tool placement with respect to the aluminum and steel sheets, and (b) critical dimensions of the friction stir tool

The steel sheet was treated as the substrate, and the aluminum alloy sheet was placed on the top in the spot joining configuration, as shown in Figure 4.1. During the process, the non-consumable tool rotation speed was set at 1000 rpm under displacement control mode for 20 seconds. For process characterization purpose, temperature measurements on a number of selected samples were made by placing probe K-type thermocouple near the joint interface under the tool

footprint, as illustrated in Figure 4.2(a). A typical temperature history measured is shown in Figure 4.2(b).

For comparing with and without corrosion effects on joint strengths, one batch of the spot joined specimens was subjected to GMW 14872 automotive-grade corrosion (Cycle C), under which this batch of the samples underwent 18 repeated corrosion cycles. Each cycle consisted of an ambient stage at 25 ℃ for 8 hours, humidity exposure at 100 % relative humidity at 49 ℃ for another 8 hours, and then a water fog chamber with 30% relative humidity at 60 ℃ for the 8 hours as well. The salt mist solution consisted of 0.90 wt% NaCl, 0.10 wt% $CaCl_2$, and 0.075 wt% $NaHCO_3$ in deionized water.

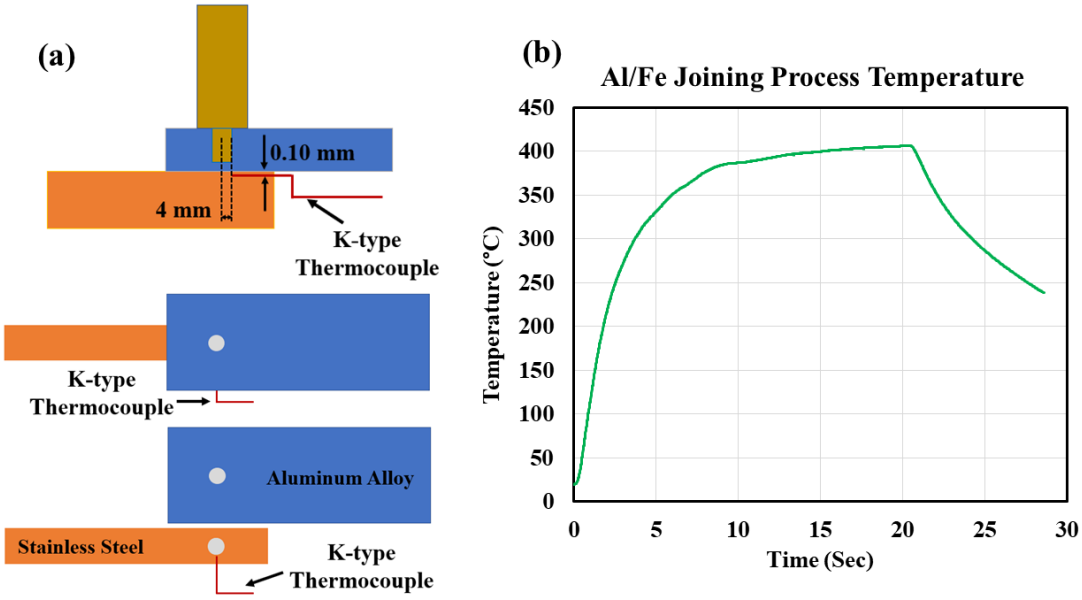


Figure 4.2: Joining process temperature measurements, (a) thermocouple placement schematic, and (b) temperature profile

Weld cross-section analyses were performed on both with and without being subjected to the aforementioned corrosion cycles by using a Nikon optical microscope and TESCAN MIRA 3 FEG scanning electron microscope (SEM). Cross sections across the weld nugget were removed using a wire electric discharge machine (EDM). Samples were ground using silicon carbide grit papers up to P800 size and then were polished up to 1 micron using the diamond polishing solution

for further cross-section examinations. Both secondary electron images and backscattered electron images were collected at 5kV-15kV voltage and 15kV voltage, respectively. In-situ focused ion beam (FIB) liftouts for transmission electron microscopy (TEM) analysis across the Al/Steel bonding interface were prepared using a Thermo-Fisher (TFS) Nova 200 Nanolab FIB/SEM system. A TFS Spectra 300 Probe-Corrected S/TEM with two 60mm^2 SDD detectors attached was used for both imaging and spectroscopy using X-ray signals operated at 300kV in STEM mode.

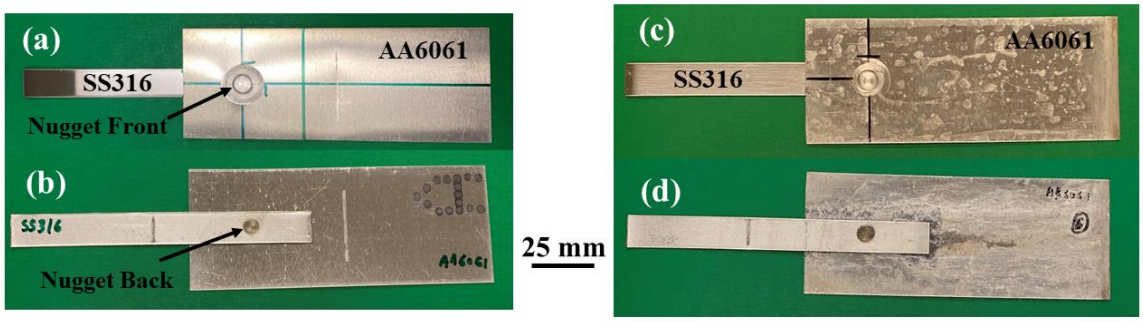


Figure 4.3: Al/Steel joints: (a) & (b) before the corrosion cycle, front and back sides of the sample, respectively, and (c) & (d) post-corrosion cycle, front and back sides of the sample, respectively.

The Al/Steel joint samples before and after subjecting to corrosion cycles are shown in Figure 4.3. Due to the lack of any specific testing standard for directly joined bi-metallic spot joint samples of thin sections, non-standard sample dimensions and testing configurations were adopted in this study to best accommodate the finished product requirements after joining. Three specimens corresponding without and three with corrosion effects were mechanically tested under lap shear tension conditions. A loading rate of 1 mm/min was used to be consistent with the quasi-static loading definition in an Instron 3382 load frame with a 100 kN load cell. To eliminate the global eccentricity with respect to the applied load line generated due to the unequal thickness and lap configuration, rectangular tabs of complementing thicknesses were placed at the gripping locations of the joints during the lap shear tensile experiments, as can be seen in Figure 4.4. The load

capacity of the test specimens or peak load reached prior to final failure (i.e., separation) of the joints under quasi-static loading conditions are summarized in Figure 4.9.

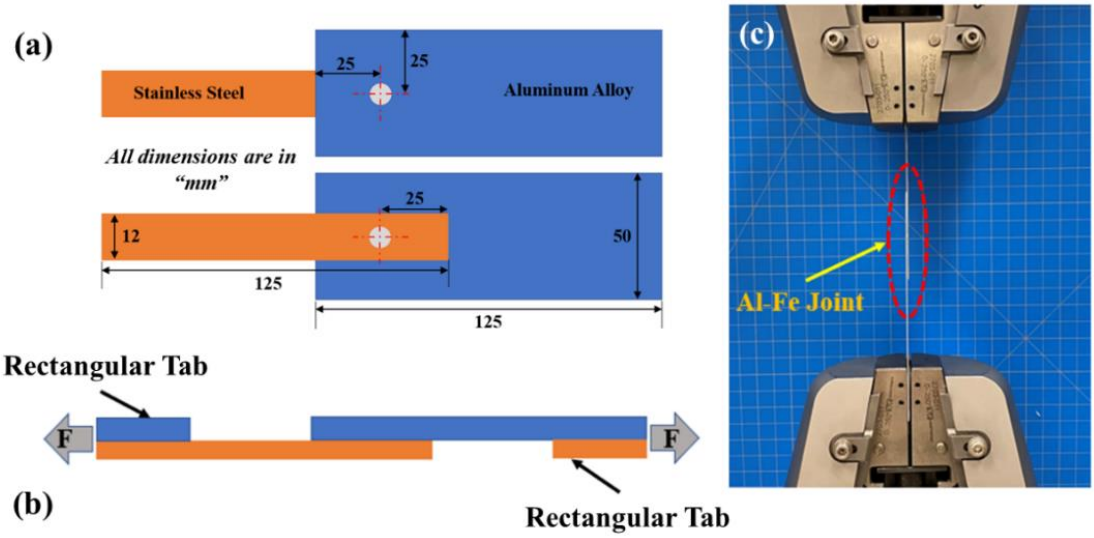


Figure 4.4: Lap shear tensile experimental schematic, (a) & (b) sample dimensions and shims/tab placement, (c) experimental setup with Al/Steel joint sample

4.3 Results

4.3.1 Al/Steel interfacial bond formation characteristics

As described above, a constant value of $\frac{h}{t} = \frac{1}{3}$ was set to generate frictional heating and material flow just above the steel sheet surface to induce shear localization bonding [37] at the aluminum/steel interface. As shown in Figure 4.2(b), the measured temperature follows a continuously increasing profile after the initial transient nonlinear part up to 10 seconds of joining process time. Figure 4.2(b) shows that the maximum temperature during the spot joining process reaches 406°C, which is well below the solidus to liquidus phase transition temperature (652 °C) of AA6061-T6 [39]. As shown in Figure 4.3, the samples indicate a spot joint formation by looking both from the front and back sides (see Figures 4.3a and 4.3b). There seems to be no significant

change in sample surface appearances after being subjected to the corrosion cycles, particularly around the weld nugget regions (see Figure 4.3c and 4.3d).

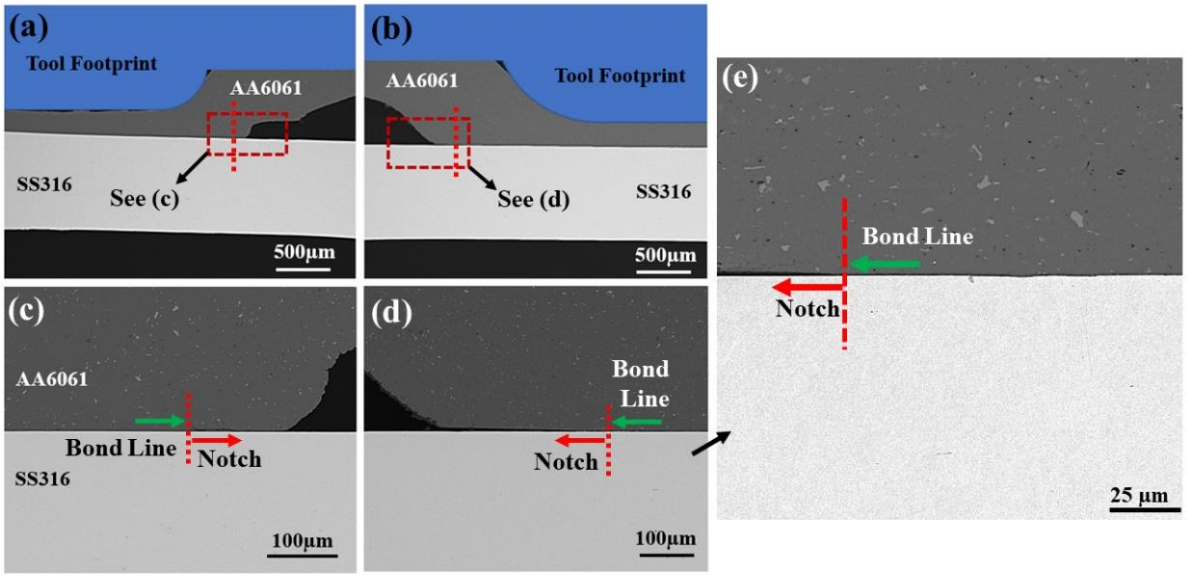


Figure 4.5: Cross-sectional SEM images of Al/Steel joint nugget shoulder, (a) before corrosion cycles; (b) after corrosion cycles; (c) high resolution detailed view from (a); (d) high resolution detailed view (b); and (e) high resolution detailed view near the not

To examine the local effects of corrosion environment exposure on weld nugget region, Figure 4.5 shows macro- and microscopic examinations of one side of the spot joint in different magnification scales. The green arrow lines show that the Al/Steel bonding line ends (i.e., where the interfacial notch begins) slightly beyond the tool footprint edge. Again, there appear to be no significant differences between without and with being subjected to the corrosion cycles by comparing Figures 4.5a and 4.5c with Figures 4.5b and 4.5d. One subtle change in appearance as a result of the corrosion environment can be seen by comparing Figures 4.5c and 4.5d at a 100 µm magnification scale. A light opening of the interfacial notch becomes more obvious in Figure 4.5d after corrosion cycling than that without going through corrosion cycling. This could be attributed to temperature cycling associated with corrosion cycles described earlier. There is no sign of stress corrosion cracking into the weld nugget from the interfacial notch tip, as shown in Figure 4.5e

under an even higher magnification. This was further confirmed by the intimately bonded Al/Steel interface away from the shoulder locations shown in Figure 4.6 (a-d) at higher magnifications SEM images and also by the nugget profile on the post-corrosion sample shown in Figure 4.10d, suggesting that the joining interface at and around the joining nugget is intimately bonded under the tool footprint.

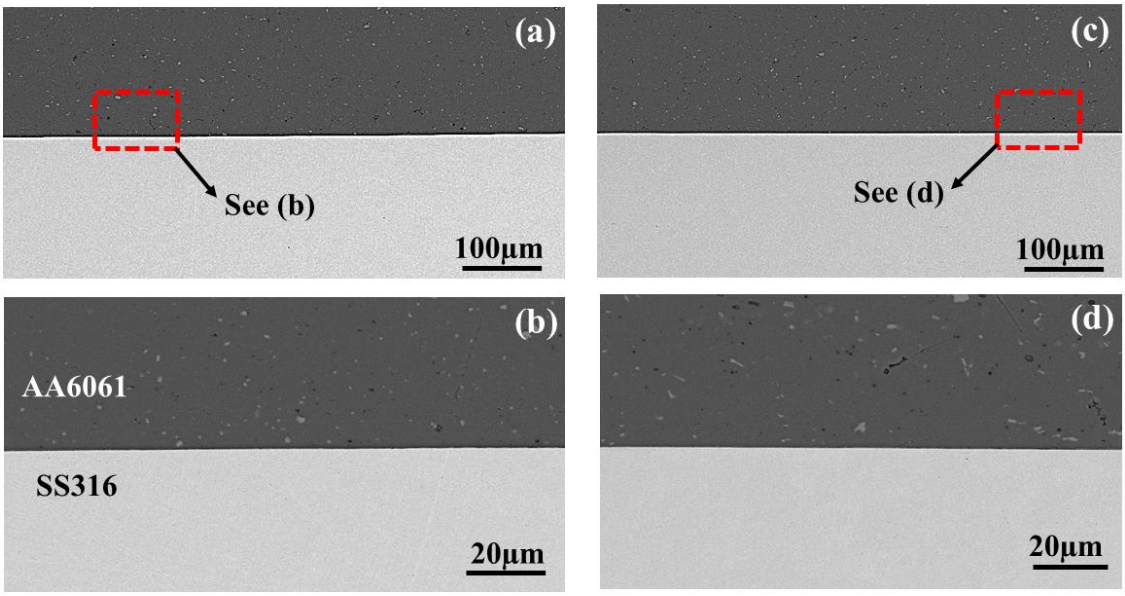


Figure 4.6: Cross-sectional SEM micrographs at the nugget center of Al/Steel joints, (a) & (b) low resolution images before corrosion cycles, and (c) & (d) high resolution images after corrosion cycles

Figure 4.6 shows the Al/Steel cross-section images obtained from SEM at the center of the nugget for both before and after the corrosion cycles. Both before and after the corrosion cycles cases show a significantly flat interface without scratches or mechanical irregularities. It can be observed from Figure 4.6 that the Al/Steel interfaces don't have any cavities or visible voids. It should be noted here that the steel surface used here was industrially mirror-polished and must be significantly flat. Higher resolution images from SEM shown in Figures 4.6b and 4.6d don't show signs of IMCs, implying that the Al/Steel interface is strongly and intimately bonded without noticeable IMCs at the micron length scale. The absence of IMCs at this length scale for the post-

corrosion sample, as shown in Figure 4.6d, also confirms that the corrosion cycle didn't induce any IMCs at the Al/Steel bonding interface.

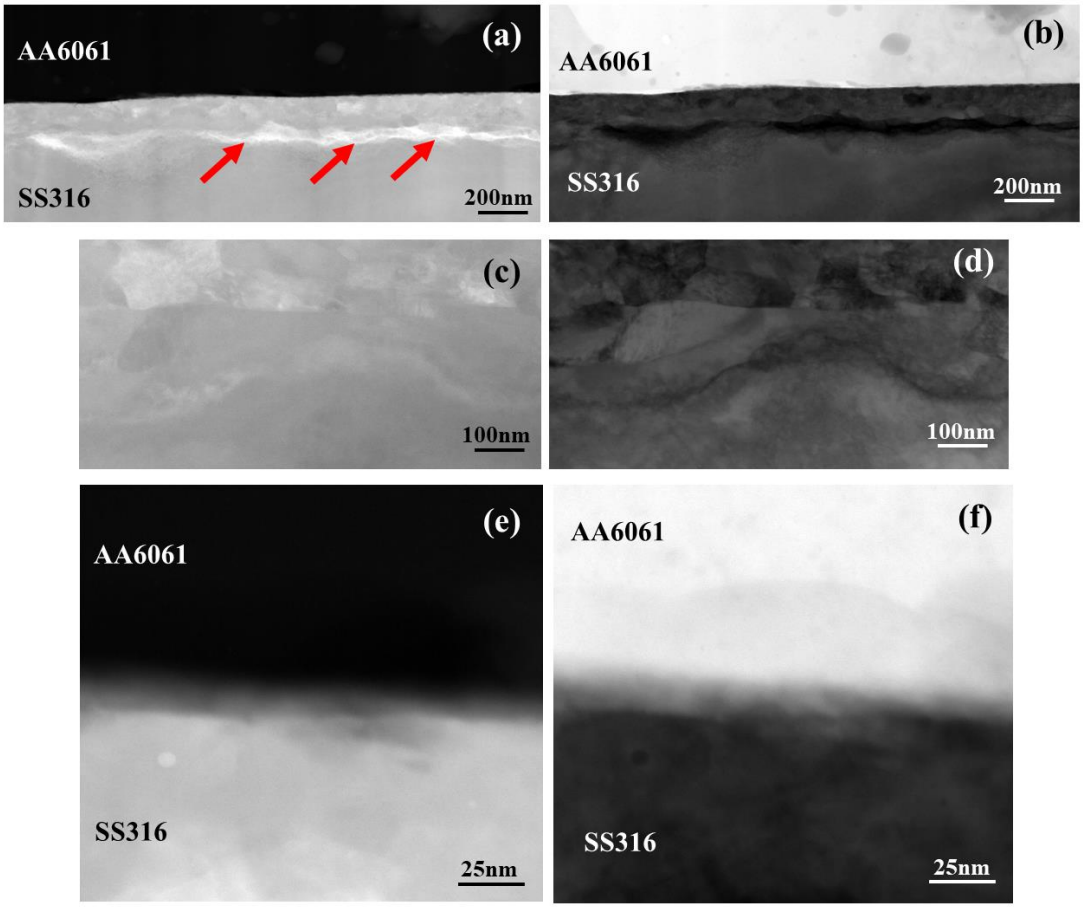


Figure 4.7: High-resolution cross-sectional STEM images of the Al/Steel joints at the nugget center, (a) (c) & (e) high-angle annular dark field (HAADF) images, and (b) (d) & (f) bright-field images, (c) and (d) showing the high-magnification images near the red arrows marked in (a).

4.3.2 Interface chemical composition and nanoscale structure

Figure 4.7 shows an HAADF image and its corresponding STEM BF images. There is no irregularity or discontinuity at the Al/Steel interface throughout the bonding length. Both magnified BF and HAADF images clearly depict an interface without any IMCs up to a 25 nm length scale (see Figure 4.7e and 4.7f). BF image shows a contrastingly darker area in Figure 4.7b, and corresponding brighter areas are marked with red arrows in the HAADF image, as shown in

Figure 4.7a. These areas can be seen more clearly in Figures 4.7d and 4.7c, respectively, at a higher magnification. These brighter areas are adjacent to the Al/Steel interface and are on the steel material. Since the end surface of the tooltip is placed away from the steel surface, the steel material does not experience a direct friction stirring effect. However, the bright areas forming an irregularly shaped band in the HAADF image shown in Figures 4.7a, 4.7c, and 4.7d imply partial crystal distortion induced by the formation of a phase band in the regions. The bright-band regions are up to an average length of 200 nm from the Al/Steel interface due to an indirect effect of high strain rate shear deformation occurring in the aluminum material side under the tool-tip surface.

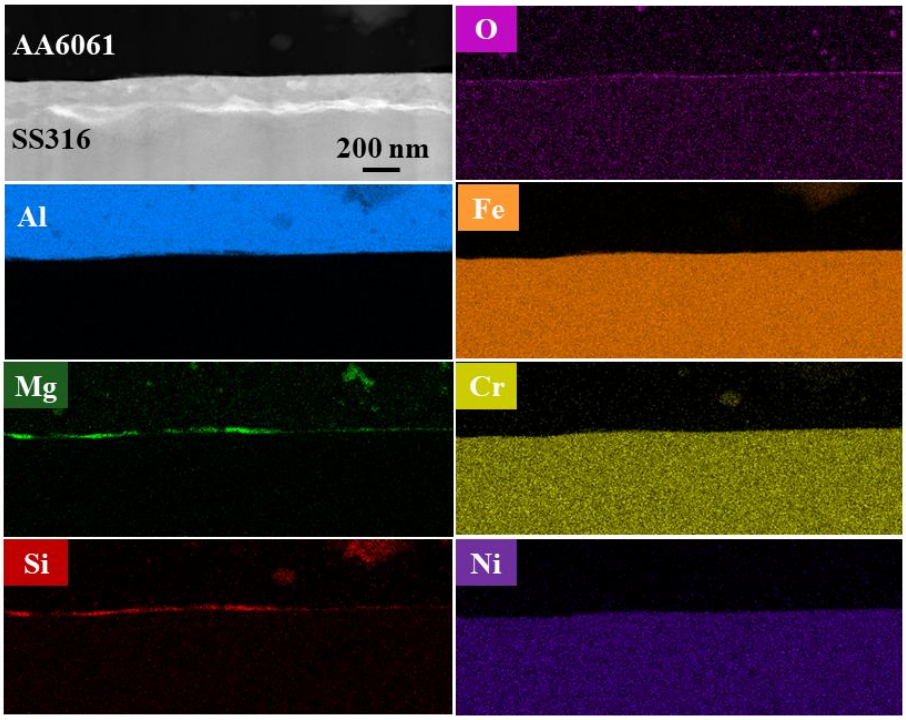


Figure 4.8: STEM HAADF image at the nugget center cross-section of the Al/Steel joint and EDS elemental maps

Figure 4.8 shows corresponding elemental maps obtained from the area shown in HAADF images in Figure 4.7a. The elemental maps further elucidate that aluminum is fully intact above the bonding interface and iron is restricted below the bonding interface. Major alloying elements Mg and Si are spread in a thin layer with an order of 40-50 nm throughout the bonding interface, as shown in Figure 4.8. There is also a very thin layer of O distribution throughout the bonding

interface, as shown in Figure 4.8. This can be attributed to the native aluminum oxide on the surface, which is usually in the range of ~10 nm on the surface before joining occurs [37]. A noteworthy observation can be made from Figure 4.8 and Figure 4.13 that none of these significant alloying elements is cross-distributed in more than 50 nm length across the interface and are found to be contained in very narrow proximity from the Al/Steel interface or the bond line.

The red dashed boundaries shown in Figure 4.13b further depict the alloying elements' reactions or inter-diffusion. This reaction zone's thickness was measured to be around 45 nm. A closer look at the reaction zone provided a noteworthy observation of the presence of Mg and O elements, including Cr and Si, in considerable amounts. As shown in Figures 4.8 and Figure 4.13b, the Mg and O strongly tend to form an amorphous phase and are restricted to 20 nm across the interface similar to how described by [37]. Figure 4.8 and Figure 4.13b also show that the Al and Fe elements have not inter-crossed beyond the 45 nm reaction zone. Furthermore, Al, Fe, and Si in the reaction zone are more likely to form the Al-Fe-Si phase at the nanoscale above the amorphous Mg- and O-rich layer [37]. The addition of Cr, however, changes the threshold of Al-Fe-Si phase formation [37], and a detailed study should be performed to quantify its effect, which is beyond the scope of this article. Similar elemental distributions of alloying elements were found throughout the interface without significant variation in the atomic %, implying a uniform and robustly bonded interface.

4.3.3 Joint strength and failure characteristics

As shown in Figure 4.9, the load capacity of the joint samples without being subjected to the corrosion cycles is at a minimum of 1.788 kN and a maximum of 1.833 kN, averaging at 1.818 kN with standard deviation of 0.026 kN among three specimens. In comparison, the load capacity of the joints after experiencing the corrosion cycles is at a minimum of 1.781 kN and a maximum

of 1.813 kN, averaging at 1.797 kN with standard deviation of 0.016 kN. As can be seen, there is no significant difference between the average values of the joint load capacity before and after the corrosion cycles. It should be pointed out that maximum loads at failure (for with and without being subjected to corrosion cycle case) not the joint strengths are compared to determine the maximum load capacity of the joints. For deriving joint strength in terms of stress or joint strength at failure for comparing with other specimen types (e.g., Coach peel [40]) or structural applications, the mesh-insensitive structural stress methods [40–43] can be used, which is beyond the scope of this study.

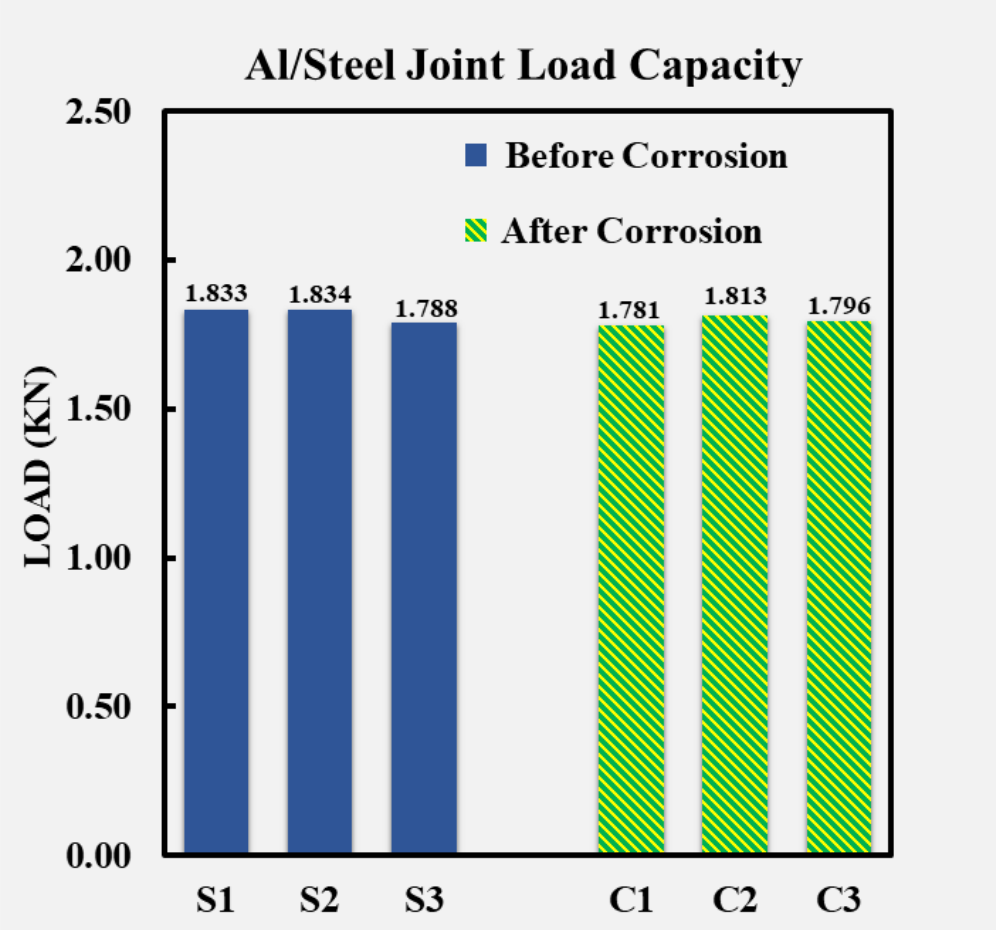


Figure 4.9: Al/Steel joint load capacity during lap shear tensile loading before and after corrosion conditions: S1-S3 represent the samples before corrosion cycles, and C1-C3 represent the samples after corrosion cycles

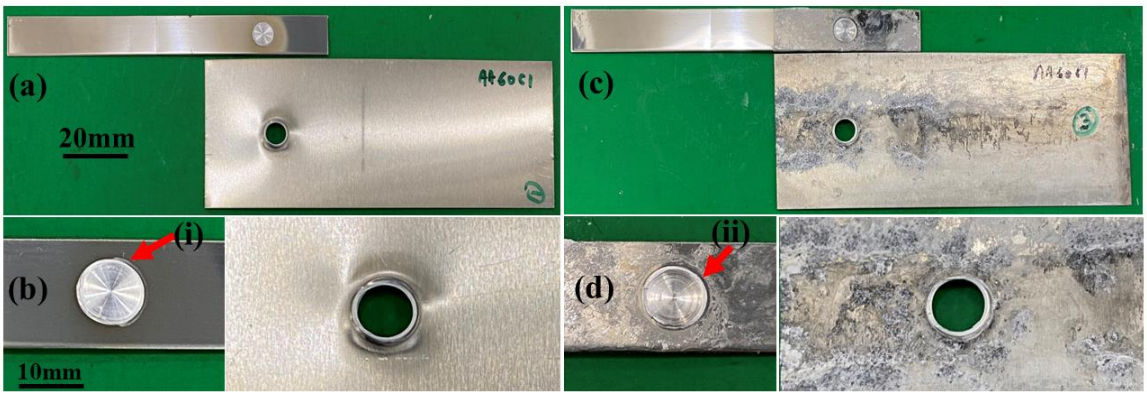


Figure 4.10: Failure features after lap shear tensile experiments, (a) & (b) global and local views before corrosion, and (c) & (d) global and local views after corrosion

Figure 4.10 shows the post-fracture images of the specimens after the lap shear tension testing. As shown in Figure 4.10b and 4.10d, the whole nugget of the spot joint was pulled away from the aluminum sheet and remained attached to the steel sheet post-tensile, often referred to as "pull button" failure mode [44,45], regardless with or without being subjected to the corrosion cycles. It suggests that the corrosion cycle did not have any noticeable detrimental effects on the Al/Steel bond integrity. This is further confirmed by lap shear tension test results shown in Figure 4.9 which shows no noticeable deterioration of joint load capacity after corrosion cycles. It should be noted that such a "pull-button" mode (Figure 4.10) serves as an indication of a sufficient weld nugget strength and bond quality required ensuring adequate static and fatigue load capacity for structural applications [46].

As shown in Figure 4.11, fracture surface morphologies around the weld nugget boundary are consistently ductile for both cases with and without experiencing the corrosion cycles. A closer look at the fracture surface around the aluminum button remaining on the steel sheet in Figure 4.10b, shows significantly elongated dimples in Figure 4.11(i) for the case without experiencing corrosion cycles. Similar fracture surface features are also shown for the case subjected to the corrosion cycles, as shown in Figure 4.11(ii). These elongated dimple features signify the ductile fracture of the aluminum nugget implying that all these specimens did not exhibit any brittle

fracture either due to the presence of IMCs at the Al/Steel joint interface and/or any detrimental effects of corrosion-induced damage.

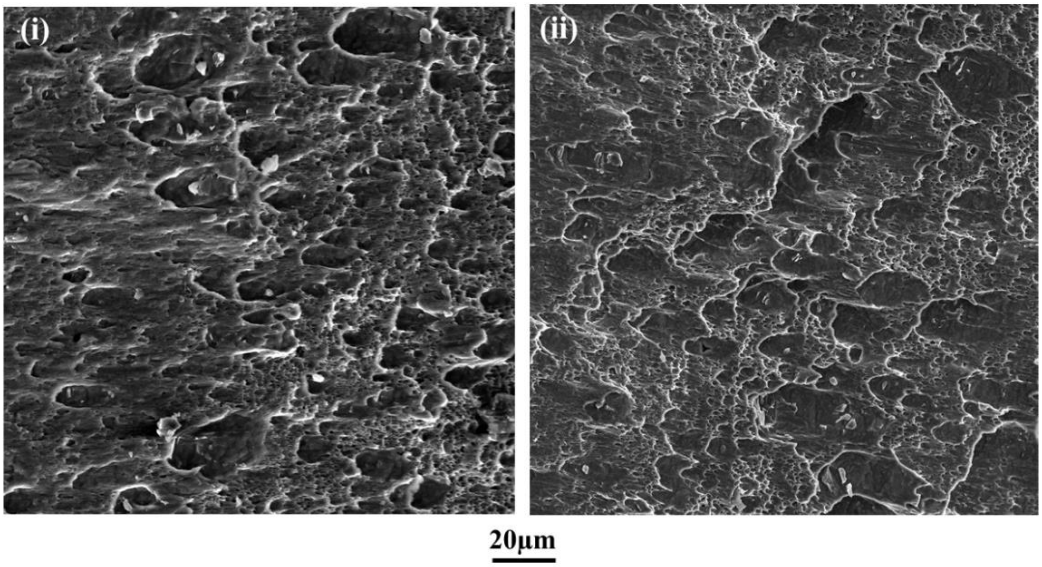


Figure 4.11: SEM micrographs at locations (i) and (ii) near the aluminum nugget shown in Figure 4.10, respectively.

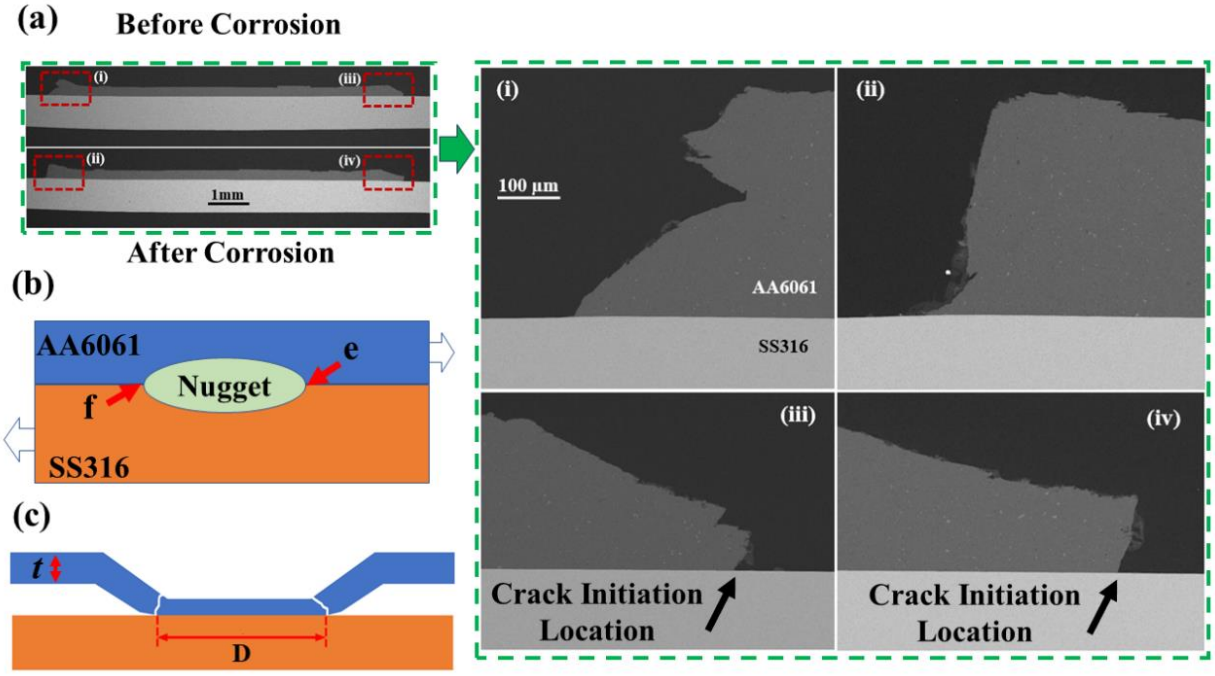


Figure 4.12: Fracture morphologies around the button failure at the nugget boundary, (a) global views, (b) schematic of nugget, (c) failure locations and failure paths during lap shear tensile experiments, (i-iv) detailed views of the locations i-iv shown in (a)

To investigate fracture development processes, Figure 4.12(a) shows the post-fracture weld cross-section images with detailed fracture path features (i) and (ii) (corresponding to location “d”

in Figure 4.12b) and detailed features (iii) and (iv) (corresponding to location "c" in Figure 4.12b). In both cases (with and without experiencing corrosion cycles), the high-resolution images on the right side of Figure 4.12(a) show no evidence of damage or cracking at the Al/Steel interfacial notch tip. Both fracture initiation sites and final failure paths share a great resemblance between without and with corrosion cycling effects. The resulting failure mode is depicted in Figure 4.12(c) with or without considering corrosion cycles. In fact, it has been shown by a rigorous fracture mechanics analysis [9,41] that as long as $D/t \geq 3$, the "pull button" failure mode becomes dominant, where *D* is the bonded nugget diameter shown in Figure 4.12(c). In the present study, such a condition is obviously satisfied, as shown in Figure 4.12(a).

4.4 Discussions

4.4.1 Suppression of IMCs

Development of IMCs at the Al/Steel interface is highly dependent on the diffusion constants of material, which in turn is governed by the interfacial temperature [14,47], relative mobility of the atoms, rate of material deformation, and cooling rate [28]. Liu et al. [48], Tanaka et al. [27], Beygi et al. [49], and Kimapong et al. [26] have shown that developing IMCs at the Al/Steel interface highly depends on the steel tool probe placement near the steel faying surface when joining aluminum alloy and steel plates. They have further found that the IMCs developed in two separate growth categories, one right where the tool probe was inserted in the steel material and the other under the shoulder where temperature distribution was found to be slightly higher than under the tool probe. Watanabe et al. [28] have systematically discussed the growth manner of the IMCs under various joining parameters and have suggested that keeping the stirring probe away from the steel-faying surface and restricting the joining temperature below the solidus temperature of the aluminum alloy favors the suppression of IMCs. Liu et al. [37] further

conformed with the above observations and have achieved a novel form of amorphous phase while joining aluminum alloy to stainless steel under modified friction stir additive manufacturing. Derived by these principles, we have restricted the tool probe above the steel faying surface in spot joining configuration to provide a high shear strain rate and controlled temperature at the joining interface.

Under static diffusion bonding conditions, the inter-diffusion of elements is mainly governed by the diffusion coefficient [28]. The diffusion coefficient of aluminum into iron matrix is zero up to 800 ℃ and diffusion coefficient of iron into aluminum matrix is zero up to 400℃, and above 400℃, the diffusion coefficient of Fe into Al increases significantly [28]. The interfacial temperature measurement at the boundary of the tooltip in our study showed that the maximum temperature was below 406℃ throughout the joining process, suggesting the diffusion coefficient of Fe into Al must remain very small at the reaction zone. Beygi et al. [49] have recently presented a comparative study between carbon steel and stainless steel joining with aluminum alloy under friction stir welding conditions and showed the significance of alloying elements on the IMCs formation. They have observed that the presence of Cr can lower the IMCs thickness under material stirring conditions. On the other hand, Liu et al. [37] have shown that during the friction lap joining of aluminum alloy and stainless steel, the dominant mechanism for forming the joining interface was high shear strain rate driven nanoscale pre-melting that occurs much below the solidus to liquidus phase transition temperature (652 ℃) [39]. Combined with the low cooling and extremely high strain rates, the T-T-T phase profile for such a process avoids the crystallization nose and provides an amorphous phase [39].

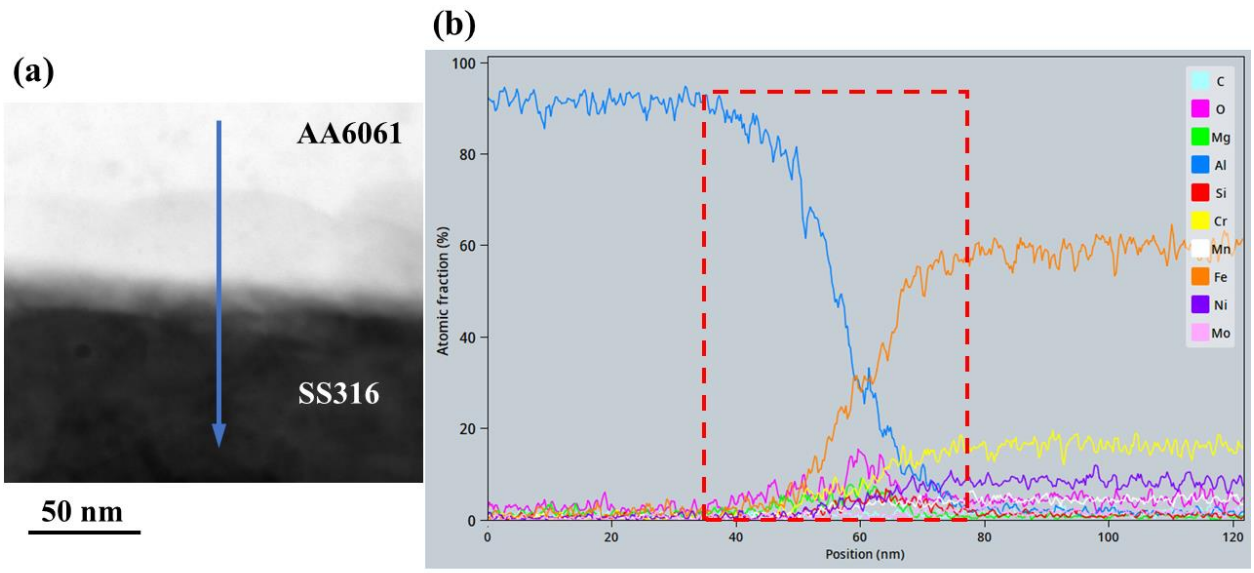


Figure 4.13: (a) EDS line analysis location across Al/Steel interface, and (b) elemental distribution across Al/Steel joint interface

Figure 4.13a shows a HAADF image with a blue arrow drawn running from the center of the image from top to the bottom direction. Figure 4.13b displays element profile curves collected along the arrow line and direction in Figure 4.13a. It can be seen that the reaction zone is 40-50 nm thick, conforming with the findings by Liu et al. [37]. The shear strain rate near the tooltip is ~ 10^9 s^{-1}, reasonably above the minimum required condition for a high shear strain rate stated by Liu et al. [37]. Based on the rationales presented by Liu et al. [37], such a reaction zone must contain ordered short-range structures that cannot be defined as IMCs (IMCs are dominantly in the form of crystalline structures) and must be in the form of an amorphous phase with some degree of nano-crystalline precipitates.

Liu et al. [37] have provided an in-depth discussion about the mechanisms associated with the formation of an amorphous phase at the 6061 aluminum alloy and 304 stainless steel interface, which involves a rapid shear localization induced pre-melting and suppression of atomic diffusion process as a result of a high shear strain rate in the order of 10^9 s^{-1}. The present process follows the same principle, except that the aluminum alloy and stainless substrates are much thinner, i.e., 0.60 mm and 0.75 mm, respectively. The thin thickness combination studied here can be particularly

challenging in maintaining a threshold nominal strain rate at the interface without causing any direct physical contact between the rotational tool face and the stainless substrate. As a result, the offset "*h*" in Figure 4.1 needs at the maximum value possible while still generating a relatively uniform shear strain rate at the interface. From the interface TEM characterization results shown in Figure 4.7, it can be seen that a consistent interfacial bond quality is evident without noticeable signs of IMCs, proving the robustness of the shear localization amorphization formation process presented by Liu et al. [37], even for thin gage aluminum-steel direct joining.

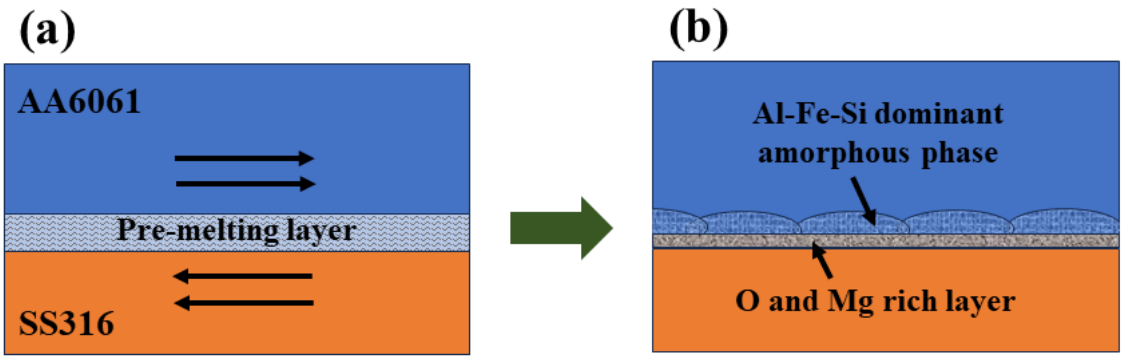


Figure 4.14: Schematic representation of the amorphous phase formation at the aluminum to steel joining interface produced via friction stir spot joining: (a) pre-melting layer formation due to intense friction induced high shear strain rate above the steel faying surface, and (b) amorphous phase formation as a graded reaction zone (or reaction layer) due to rapid quenching effect.

Liu et al. [37] have further demonstrated that the Al-Fe-Si rich phase developed as a q-glass due to the cooling rate achieved by the friction stir additive manufacturing and the Mg and O rich layer developed as an amorphous-crystalline nano-composite. In the current study, the bulk volume is different, and the spot joining process time is relatively shorter than the one used by Liu et al. [37]. Furthermore, the heat dissipation time between the peak temperature and a characteristic temperature of 300 C achieved in the current study is approximately 3 seconds compared to the time obtained in similar processes by Liu et al. [50,51] are approximately above 5 seconds. Thus, it is understandable that the formed amorphous phase and its chemistry are different from the literature [37,49]. The formation mechanism of the amorphous phase can be explained in two steps,

as shown in Figure 4.14. Firstly, a pre-melting liquid forms the interface between aluminum alloy 6061 and the stainless steel 316 faying surface (see Figure 4.14a) due to an intense frictional heating and high shear strain rate 10^9 s^{-1}, similar to Liu et al. [37]. Differently, a faster cooling rate was achieved in the spot joining process configuration in the present study. It did not give sufficient time for diffused elements in the pre-melting layer to cluster themselves once the shear strain rate is removed. Secondly, the amorphous phase is then formed with a much high chemical homogeneity after the shear strain has been released (see Figure 4.14b) due to a high cooling rate achieved along with a much smaller bulk material used here compared to those used in Liu et al. [37,38]. A more sophisticated analytical and experimental analysis is necessary to further elucidate the interface microstructure formation mechanism which is beyond the scope of this article.

4.4.2 Corrosion effects

As stated in the introduction section, IMCs are detrimental to dissimilar material joints as due to their brittle nature which can trigger premature failure under load [52]. IMCs can also form galvanic cells at the Al/Steel joint interface [29]. Wloka et al. [29] reported that Fe-containing IMCs at the joining zone acted as cathode and reduced the open circuit potential (OCP). Next to the IMCs, the corrosion was found to be faster to dissolve the Al-IMC interface. Thus, the joining zone between aluminum alloy and galvanized steel had the most negative corrosion potential and was the first to corrode. Zhang et al. [17] have also shown that the OCP difference between IMCs and aluminum becomes the largest under corrosive conditions, leading to accelerated corrosion of the Al-IMCs interface and weakening the joining interface significantly. Sravanthi et al. [32] have shown that an increased amount of IMCs at the joint interface between aluminum alloy and mild steel was mainly responsible for localized corrosion at the joint interface. They also found that the

increased thickness of IMCs at the joint interface further increased the base material grain boundary widths and weakened the joint interface further.

As it has been well established that IMCs are crystalline solids with well-defined grain boundaries which are highly susceptible to corrosion [53]. Bennett et al. [54] have shown that sensitization in stainless steel was found to be exacerbated by the grain boundaries leading to rapid corrosion at the grain boundaries and intergranular corrosion. For aluminum-based alloys, a sequential pitting initiation, pitting propagation and the intergranular corrosion were found to be accelerated by the depletion of noble Si near the grain boundaries [55]. Hoffman et al. [56] further elucidated that the CoCrMo alloys show preferential grain boundary attacks around high-energy grain boundaries as a consequence of grain boundary sensitization. They further showed that the grain boundaries were mainly responsible for the crevice and intergranular corrosion due to the penetration of the electrolytic ions. In contrast, amorphous phase does not contain any ordered structure or grain boundaries and offers a high degree of resistance to corrosive media [57]. Naka et al. [58] showed that the corrosion resistance of amorphous copper-based alloy was higher than that of crystalline alloys with the same composition. They further confirmed that the chemical homogeneity increments due to the glass formation increased the corrosion resistance in the amorphous metal-metal system. Bakare et al. [59] have shown that the crystalline form of an iron-based alloy showed preferential dissolution of Mo-rich precipitates and shown accelerated corrosion compared to the amorphous form of the alloy with the same composition. They further attributed the improved corrosion resistance of the amorphous material to the chemical homogeneity and resistance of the amorphous phase for electrolytic ions. Based on the above documented findings in the literature, this study further confirms that the amorphous phase formed

at the aluminum alloy 6061 and stainless steel 316 indeed serves as an effective barrier for corrosion attacks, at least under the automotive grade corrosion cycles.

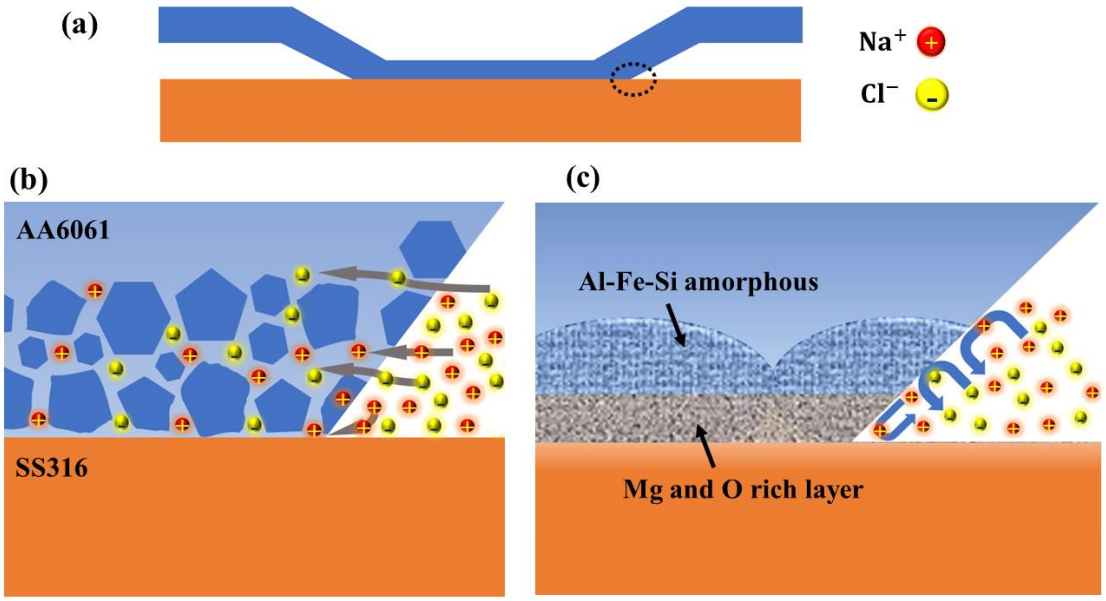


Figure 4.15: Schematic illustration of corrosion resistance via amorphous reaction zone at the aluminum/steel joining interface achieved via NSSLIA: (a) schematic representing spot joining configuration, (b) representation of corrosive media electrolytic ions penetration through grain boundaries of crystalline grain boundaries in IMCs, and (c) barrier effect to prevent the penetration of corrosive media electrolytic ions via the amorphous phase reaction zone

Based on the discussions above and the experimental characterizations performed in this study, the corrosion-resistant nature of the amorphous interfacial layer can be postulated as shown in Figure 4.15 above. It should be noted here that the grain boundaries are exaggerated to schematically depict the electrolytic ion transfer from the corrosive media towards the Al/Steel interface in Figure 4.15b. Since the grain boundaries are the regions of atomic packing discontinuity, the diffusion of ions from the electrolytic media gets accelerated through the grain boundaries. It reaches the steel surface through the crystalline IMCs, easily allowing the preferential grain boundary corrosion attack. Additionally, the potential difference between a single grain and the grain boundaries is always present due to the difference in microstructure homogeneity (due to the presence of defects, slip, and dislocations). The micro-galvanic cell formation is accelerated around the crystalline solids such as IMCs, and ion exchange becomes

faster to corrode the joining interface. On the other hand, the amorphous dominant reaction zone (Figure 4.15c) acts as a barrier to prevent the ion exchange between the bulk electrolytic corrosive media and the joining interface due to its chemical homogeneity. Such a barrier effect does not allow for a preferential corrosion attack or micro-galvanic cell formation around the joining interface, increasing the corrosion resistance of the joints.

Furthermore, as described in Section 4.3, all Al/Steel spot joint samples, with and without being subjected to the corrosion cycles, have consistently exhibited ductile failure mode (see Figure 4.11 and Figure 4.12) in the form of "pull button", as illustrated in Figure 4.12c. There is also a noticeable amount of thinning around the notch near the joining nugget boundaries due to the plunging action of the friction stir tool. This thinning can be observed with a continuous profile from the actual sheet thickness down to the joining sheet thickness in the nugget area (Figures 4.5 and 4.12). However, the amount of thinning is nearly the same in both with and without being subjected to the corrosion cycle cases and has been found to contribute similarly to failure modes in both conditions. The resulting relatively consistent joint strengths in terms of test specimen load capacities shown in Figure 4.9 further prove the corrosion-resistant nature of the spot joints realized by the shear localization-based direct joining method presented in this study.

4.5 Conclusions

A shear localization-based spot-welding method is presented for joining thin gauge aluminum alloy to stainless steel sheets with a consistent bond quality with negligible detrimental intermetallic compounds, if any. Environmental corrosion effects on joint strengths were examined by subjecting a batch of aluminum alloy (6061-T6) and stainless steel (316) joint samples to a well-accepted corrosion environment conditions by the automotive industry. The following represent the key findings:

i. The nanoscale shear localization induced alloy amorphization (NSLIAA) discovered by Liu et al. [37] can be consistently reproduced for direct spot-joining of thin aluminum alloy (AA6061-T6) to thin stainless steel (SS316) substrates without noticeable IMCs. This further proves the robustness of the NSLIAA process for potentially a broad application in the direct joining of incompatible metals.

ii. A continuous amorphous dominant reaction zone was observed at the bimetallic joining interface, consisting of an Mg and O-rich layer adjacent to the steel faying surface in combination with an Al-Fe-Si amorphous phase. The continuous reaction zone was attributed to the faster cooling rate effect observed for the spot joining configuration and high shear strain rate dominant material pre-melting at the joining interface.

iii. The resulting bimetallic spot joints show no degradation in joint strengths, nor any change in failure mode after being subjected to a full automotive grade corrosion test cycle. The continuous and homogeneous amorphous reaction zone did not allow the electrolytic ion penetration at the joining interface and was found to have a barrier effect under the automotive corrosion cycling conditions.

iv. The good corrosion resistance thus observed in the Al/Steel joints investigated in this study can be attributed to the amorphous phase at the joining interface. The results suggest that the NSLIAA process has a strong potential for enabling direct joining between incompatible metals to achieve structural lightweighting for applications in severe and harsh environmental conditions.

References

[1] Skszek T., Conklin J. Multi-material lightweight vehicles acknowledgement. (2014).

[2] S. Kleinbaum, C. Jiang, S. Logan, Enabling sustainable transportation through joining of dissimilar lightweight materials, MRS Bull. 44 (2019) 608–612, https:// doi.org/10.1557/mrs.2019.178.

[3] J.A.C. Pereira, M.M. Kasaei, R.J.C. Carbas, E.A.S. Marques, H. Lim, L.F.M. da Silva, Joining magnesium and aluminum alloy sheets by a novel hole hemming process, Thin-Walled Structures 200 (2024) 111919 12 Thin-Walled Struct. 187 (2023) 110758, https://doi.org/10.1016/j. tws.2023.110758.

[4] A. Gullino, P. Matteis, F.D. Aiuto, Review of aluminum-to-steel welding technologies for car-body applications, Metals (Basel) 9 (2019) 1–28, https://doi. org/10.3390/met9030315.

[5] F. Czerwinski, Current trends in automotive lightweighting strategies and materials, Materials (Basel) 14 (2021), https://doi.org/10.3390/ma14216631.

[6] K.P. Lam, K. Behdinan, W.L. Cleghorn, A material and gauge thickness sensitivity analysis on the NVH and crashworthiness of automotive instrument panel support, Thin-Walled Struct. 41 (2003) 1005–1018, https://doi.org/10.1016/S0263-8231 (03)00050-8.

[7] A. Haran-Nogueira, M.M. Kasaei, A. Akhavan-Safar, R.J.C. Carbas, E.A.S. Marques, L.F.M. da Silva, Failure analysis of hybrid bonded-hole hemmed joints for dissimilar materials, Thin-Walled Struct. 189 (2023) 110907, https://doi.org/ 10.1016/j.tws.2023.110907.

[8] A. Sadeghian, N. Iqbal, A review on dissimilar laser welding of steel-copper, steel-aluminum, aluminum-copper, and steel-nickel for electric vehicle battery manufacturing, Opt. Laser Technol. 146 (2022) 107595, https://doi.org/10.1016/ j.optlastec.2021.107595.

[9] A.S. Khan, P. Dong, F. Liu, Y. Zhang, Directly welding plastic to metal for structural applications: a state-of-the-art review – part 1 promising processes, Weld J 103 (2024) 117–136, https://doi.org/10.29391/2024.103.011.

[10] H.A. Derazkola, A. Simchi, An investigation on the dissimilar friction stir welding of T-joints between AA5754 aluminum alloy and poly(methyl methacrylate), ThinWalled Struct. 135 (2019) 376–384, https://doi.org/10.1016/j.tws.2018.11.027.

[11] Y. Chen, X. Yang, M. Li, K. Wei, S. Li, Mechanical behavior and progressive failure analysis of riveted, bonded and hybrid joints with CFRP-aluminum dissimilar materials, Thin-Walled Struct. 139 (2019) 271–280, https://doi.org/10.1016/j. tws.2019.03.007.

[12] Khan SA Zain-ul-Abidin, H.A. Khan, R. Awais, S Khushbash, Classification of progressive failure and mechanical behavior of dissimilar material hybrid joints at varying temperatures, Thin-Walled Struct. 182 (2023) 110212, https://doi.org/ 10.1016/j.tws.2022.110212.

[13] A.S. Khan, F. Liu, P. Dong, Joining of metal and non-polar polypropylene composite through a simple functional group seeding layer, J. Manuf. Process. 85 (2023) 90–100, https://doi.org/10.1016/j.jmapro.2022.11.022.

[14] B. Pan, H. Sun, S.L. Shang, M. Banu, P.C. Wang, B.E. Carlson, et al., Understanding formation mechanisms of intermetallic compounds in dissimilar Al/steel joint processed by resistance spot welding, J. Manuf. Process. 83 (2022) 212–222, https://doi.org/10.1016/j.jmapro.2022.08.062.

[15] L. Shi, J. Kang, X. Chen, A.S. Haselhuhn, D.R. Sigler, B.E. Carlson, Effect of material inhomogeneity on fracture modes in aluminium–steel resistance spot welds, Fatigue Fract. Eng. Mater. Struct. 43 (2020) 2157–2168, https://doi.org/10.1111/ ffe.13256.
[16] M.M. Atabaki, M. Nikodinovski, P. Chenier, J. Ma, M. Harooni, R. Kovacevic, Welding of aluminum alloys to steels: an overview, J. Manuf. Sci. Prod. 14 (2014) 59–78, https://doi.org/10.1515/jmsp-2014-0007.
[17] P. Dong, Quantitative weld quality acceptance criteria: an enabler for structural lightweighting and additive manufacturing, Weld. J. 99 (2) (2020) 39S–51S.
[18] S. Wu, P. Dong, Modeling of distributed defects and a proposed fatigue interaction criterion for additively manufactured metal parts, Int. J. Press. Vessels Pip. 105048 (2023).
[19] S. Wu, J. Cheng, P. Dong, Y. Zhang, L. Zhang, Defect interactions and effects on fatigue behaviors of additively manufactured parts, in: Pressure Vessels and Piping Conference 87486, American Society of Mechanical Engineers, 2023.
[20] S. Zhang, S. Li, X. Meng, Y. Chen, C. Cheng, Effect of intermetallic compound on the corrosion behaviour of resistance spot welding joints between 5182 aluminium alloy and galvanized DP780 dual-phase steel, Mater. Res. Express 10 (2023), https://doi.org/10.1088/2053-1591/acbbbc.
[21] E. Fereiduni, M. Movahedi, A.H. Kokabi, Aluminum/steel joints made by an alternative friction stir spot welding process, J. Mater. Process. Technol. 224 (2015) 1–10, https://doi.org/10.1016/j.jmatprotec.2015.04.028.
[22] S.A. Hussein, A.S.M. Tahir, A.B. Hadzley, Characteristics of aluminum-to-steel joint made by friction stir welding: a review, Mater. Today Commun. 5 (2015) 32–49, https://doi.org/10.1016/j.mtcomm.2015.09.004.
[23] H. Zhao, Y. Liu, Y. Ma, X. Ping, D. Zhang, Thin-walled structures research on the formation mechanism and mechanical properties of refill friction stir riveting (RFSR) joints of aluminium alloy AA7075-T6, Thin-Walled Struct. 198 (2024) 111696, https://doi.org/10.1016/j.tws.2024.111696.
[24] H.R. Akramifard, H. Mirzadeh, M.H. Parsa, Cladding of aluminum on AISI 304L stainless steel by cold roll bonding: mechanism, microstructure, and mechanical properties, Mater. Sci. Eng. A 613 (2014) 232–239, https://doi.org/10.1016/j. msea.2014.06.109.
[25] T. Aizawa, M. Kashani, K. Okagawa, Application of magnetic pulse welding for aluminum alloys and SPCC steel sheet joints, Weld. J. (Miami, Fla) 86 (2007) 119–124.
[26] S. Chen, G.S. Daehn, A. Vivek, B. Liu, S.R. Hansen, J. Huang, et al., Interfacial microstructures and mechanical property of vaporizing foil actuator welding of aluminum alloy to steel, Mater. Sci. Eng. A 659 (2016) 12–21, https://doi.org/ 10.1016/j.msea.2016.02.040.
[27] A. Vivek, S.R. Hansen, B.C. Liu, G.S. Daehn, Vaporizing foil actuator: a tool for collision welding, J. Mater. Process. Technol. 213 (2013) 2304–2311, https://doi. org/10.1016/j.jmatprotec.2013.07.006.
[28] H. Ma, G. Qin, P. Geng, Z. Ao, Y. Chen, Effect of intermetallic compounds on the mechanical property and corrosion behaviour of aluminium alloy/steel hybrid fusion-brazed welded structure, J. Manuf. Process. 75 (2022) 170–180, https://doi. org/10.1016/j.jmapro.2022.01.004.
[29] K. Kimapong, T. Watanabe, Friction stir welding of aluminum alloy to steel, Weld. J. (Miami, Fla) 83 (2004) 277–282.

[30] T. Tanaka, M. Nezu, S. Uchida, T. Hirata, Mechanism of intermetallic compound formation during the dissimilar friction stir welding of aluminum and steel, J. Mater. Sci. 55 (2020) 3064–3072, https://doi.org/10.1007/s10853-019-04106- 2.
[31] M. Watanabe, K. Feng, Y. Nakamura, S. Kumai, Growth manner of intermetallic compound layer produced at welding interface of friction stir spot welded aluminum/steel lap joint, Mater. Trans. 52 (2011) 953–959, https://doi.org/ 10.2320/matertrans.L-MZ201120.
[32] J. Wloka, H. Laukant, U. Glatzel, S. Virtanen, Corrosion properties of laser beam joints of aluminium with zinc-coated steel, Corros. Sci. 49 (2007) 4243–4258, https://doi.org/10.1016/j.corsci.2007.04.014.
[33] H. Xia, X. Zhao, C. Tan, B. Chen, X. Song, L. Li, Effect of Si content on the interfacial reactions in laser welded-brazed Al/steel dissimilar butted joint, J. Mater. Process. Technol. 258 (2018) 9–21, https://doi.org/10.1016/j.jmatprotec.2018.03.010.
[34] Y. Shi, J. Li, G. Zhang, J. Huang, Y. Gu, Corrosion behavior of aluminum-steel weld-brazing joint, J. Mater. Eng. Perform. 25 (2016) 1916–1923, https://doi.org/ 10.1007/s11665-016-2020-9.
[35] S.S. Sravanthi, S.G. Acharyya, K.V Phani Prabhakar, G Padmanabham, Effect of welding parameters on the corrosion behavior of dissimilar alloy welds of T6 AA6061 Al-galvanized mild steel, J. Mater. Eng. Perform. 27 (2018) 5518–5531, https://doi.org/10.1007/s11665-018-3596-z.
[36] H. Ma, G. Qin, P. Geng, S. Wang, D. Zhang, Microstructural characterisation and corrosion behaviour of aluminium alloy/steel hybrid structure produced by friction welding, J. Manuf. Process. 61 (2021) 349–356, https://doi.org/10.1016/j. jmapro.2020.11.014.
[37] T. Watanabe, H. Takayama, A. Yanagisawa, Joining of aluminum alloy to steel by friction stir welding, J. Mater. Process. Technol. 178 (2006) 342–349, https://doi. org/10.1016/j.jmatprotec.2006.04.117.
[38] R. Beygi, M. Zarezadeh Mehrizi, A. Akhavan-Safar, S. Safaei, A. Loureiro, L.F.M da Silva, Design of friction stir welding for butt joining of aluminum to steel of dissimilar thickness: heat treatment and fracture behavior, Int. J. Adv. Manuf. Technol. 112 (2021) 1951–1964, https://doi.org/10.1007/s00170-020-06406-3.
[39] R. Beygi, R.J.C. Carbas, A.Q. Barbosa, E.A.S. Marques, L.F.M. da Silva, Buttering for FSW: enhancing the fracture toughness of Al-Fe intermetallics through nanocrystallinity and suppressing their growth, J. Manuf. Process. 90 (2023) 233–241, https://doi.org/10.1016/j.jmapro.2023.02.001.
[40] F.C. Liu, P. Dong, A.S. Khan, K. Sun, W. Lu, A. Taub, et al., Amorphous interfacial microstructure and high bonding strength in Al-Fe bimetallic components enabled by a large-area solid-state additive manufacturing technique, J. Mater. Process. Technol. 308 (2022), https://doi.org/10.1016/j.jmatprotec.2022.117721.
[41] M. Zhang, F.C. Liu, Z.Y. Liu, P. Xue, P. Dong, H. Zhang, et al., Highly stable nanoscale amorphous microstructure at steel-aluminum interface enabled by a new solid-state additive manufacturing method, Scr. Mater. 227 (2023), https://doi. org/10.1016/j.scriptamat.2023.115300.
[42] F. Liu, Y. Zhang, P. Dong, Large area friction stir additive manufacturing of intermetallic-free aluminum-steel bimetallic components through interfacial amorphization, J. Manuf. Process. 73 (2022) 725–735, https://doi.org/10.1016/j. jmapro.2021.11.042

[43] A.S. Khan, P. Dong, F. Liu, Y Zhang, A state-of-the-art review on direct welding of polymer to metal for structural applications: part 2 — joint design and property characterization, Weld. J. 103 (2024) 142–150, https://doi.org/10.29391/ 2024.103.013.
[44] Y. Zhang, P. Dong, X Pei, Fracture mechanics modeling of fatigue behaviors of adhesive-bonded aluminum alloy components, Metals (Basel) 12 (2022), https:// doi.org/10.3390/met12081298.
[45] H. Lu, P. Dong, S. Boppudi, Strength analysis of fillet welds under longitudinal and transverse shear conditions, Mar. Struct. 43 (2015) 87–106, https://doi.org/ 10.1016/j.marstruc.2015.06.003.
[46] H.T. Kang, P. Dong, J.K. Hong, Fatigue analysis of spot welds using a meshinsensitive structural stress approach, Int. J. Fatigue 29 (2007) 1546–1553, https://doi.org/10.1016/j.ijfatigue.2006.10.025.
[47] X. Sun, E.V Stephens, M.A. Khaleel, Effects of fusion zone size and failure mode on peak load and energy absorption of advanced high-strength steel spot welds, Weld. J. (Miami, Fla) 86 (2007).
[48] K. Martinsen, S.J. Hu, B.E. Carlson, Joining of dissimilar materials, CIRP Ann. - Manuf. Technol. 64 (2015) 679–699, https://doi.org/10.1016/j.cirp.2015.05.006.
[49] L. Zhang, P. Dong, Y. Wang, J. Mei, A Coarse-Mesh hybrid structural stress method for fatigue evaluation of spot-welded structures, Int. J. Fatigue 164 (2022) 107109, https://doi.org/10.1016/j.ijfatigue.2022.107109.
[50] Y. Luo, S.P. Hu, X.G. Song, A. Aprilia, Y.J. Yang, W. Zhou, A novel method for improving interfacial joining strength of vacuum brazed TiAl/GH3536 thin-walled structure by Au coating, Thin-Walled Struct. 190 (2023), https://doi.org/10.1016/ j.tws.2023.110915.
[51] F.C. Liu, P. Dong, From thick intermetallic to nanoscale amorphous phase at Al-Fe joint interface: roles of friction stir welding conditions, Scr. Mater. 191 (2021) 167–172, https://doi.org/10.1016/j.scriptamat.2020.09.031.
[52] R. Beygi, R. Carbas, A. Queiros, E.A.S. Marques, R. Shi, L.F.M. da Silva, Comparative study between stainless steel and carbon steel during dissimilar friction stir welding with aluminum: kinetics of Al–Fe intermetallic growth, Met. Mater. Int. 28 (2022) 1948–1959, https://doi.org/10.1007/s12540-021-01070-y.
[53] F. Liu, P. Dong, A.S. Khan, Y. Zhang, R. Cheng, A. Taub, et al., 3D printing of finegrained aluminum alloys through extrusion-based additive manufacturing: A.S. Khan et al. Thin-Walled Structures 200 (2024) 111919 13 microstructure and property characterization, J. Mater. Sci. Technol. 139 (2023) 126–136, https://doi.org/10.1016/j.jmst.2022.08.017.
[54] M. Zhang, F.C. Liu, P. Xue, H. Zhang, L.H. Wu, D.R. Ni, et al., Fabrication of largescale steel-aluminum components with homogenously distributed amorphous interfacial layer and enhanced bonding strength using modified friction stir additive manufacturing, J. Mater. Sci. Technol. 194 (2024) 151–166, https://doi. org/10.1016/j.jmst.2024.01.036.
[55] J.L. Song, S.B. Lin, C.L. Yang, G.C. Ma, H. Liu, Spreading behavior and microstructure characteristics of dissimilar metals TIG welding-brazing of aluminum alloy to stainless steel, Mater. Sci. Eng. A 509 (2009) 31–40, https://doi. org/10.1016/j.msea.2009.02.036.
[56] A.R. Paul, M. Mukherjee, D. Singh, A critical review on the properties of intermetallic compounds and their application in the modern manufacturing, Cryst. Res. Technol. 57 (2022) 1–19, https://doi.org/10.1002/crat.202100159.

[57] B.W. Bennett, H.W. Pickering, Effect of grain boundary structure on sensitization and corrosion of stainless steel, Metall. Trans. A 18 (1991) 1117–1124, https://doi. org/10.1007/BF03325722 .
[58] A. Shi, B.A. Shaw, E. Sikora, The role of grain boundary regions in the localized corrosion of a copper-free 6111-like aluminum alloy, Corrosion 61 (2005) 534–547, https://doi.org/10.5006/1.3278189.
[59] E.E. Hoffman, A. Lin, Y. Liao, L.D. Marks, Grain boundary assisted crevice corrosion in CoCrMo alloys, Corrosion 72 (2016) 1445–1461, https://doi.org/ 10.5006/2108.
[60] W.J. Botta, J.E. Berger, C.S. Kiminami, V. Roche, R.P. Nogueira, C. Bolfarini, Corrosion resistance of Fe-based amorphous alloys, J. Alloys Compd. 586 (2014) S105–S110, https://doi.org/10.1016/j.jallcom.2012.12.130.
[61] M. Naka, K. Hashimoto, T. Masumoto, Corrosion behavior of amorphous and crystalline Cu50Ti50 and Cu50Zr50 alloys, J. Non Cryst. Solids 30 (1978) 29–36, https://doi.org/10.1016/0022-3093(78)90053-4.
[62] M.S. Bakare, K.T. Voisey, K. Chokethawai, D.G. McCartney, Corrosion behaviour of crystalline and amorphous forms of the glass forming alloy Fe 43Cr 16Mo 16C 15B 10, J. Alloys Compd. 527 (2012) 210–218, https://doi.org/10.1016/j. jallcom.2012.02.127

Chapter 5 Novel Solid-State Additive Friction Extrusion Deposition Method

5.1 Introduction

Metal manufacturing has traditionally faced hard choices among property, geometry complexity, and cost. Metals can be processed into complex geometries through fusion or sintering based additive manufacturing (AM) methods, such as powder bed fusion, directed energy deposition, or binder jetting [1-5]. However, these methods often lead to inferior mechanical properties due to the formation of columnar grain structure or manufacturing defects [6-8]. The mechanical properties of solidified metals, including tensile strength, fatigue strength, and ductility, can be improved by a subsequent thermomechanical processing [9,10], which inevitably leads to a compromise of the geometry complexity and affordability of the resultant parts. One way to break the property-complexity-affordability tradeoff is to develop new metal processing methods, e.g., by introducing new deformation-based metal AM methods that can cost-effectively print dense metals into complex structural forms.

Thermoplastics can be readily printed into complex geometry through a simple and cost-effective extrusion-based AM [11]. In contrast, extrusion-based AM of metals is only applicable to a limited number of metals, such as some specific bulk metallic glasses and alloys with a sufficiently large difference between the solidus and liquidus temperatures [12]. As a result, the versatility and affordability of metal AM lag significantly behind thermoplastics AM. The asymmetry of the development can be attributed to the inherently different material behavior between thermoplastics and metals at elevated temperatures. Most thermoplastics are either

amorphous or semi-crystalline and, therefore, possess a considerable temperature range in which the thermoplastics are flowable below the melting point. This gives thermoplastics the ability to maintain a suitable range of viscosity within a practical time scale to be processed through extrusion-based AM. Polycrystalline metals can be treated as composites of grains separated by thin "amorphous" grain boundaries [13,14], but the proportion of "amorphous" grain boundaries in conventional coarse-grained meals is extremely low. As a result, most of these metals are either too hard before reaching their melting points or too soft after melting for a stable extrusion-based AM [12].

Introducing more "amorphous" grain boundaries into polycrystalline metals can significantly soften the metals before melting [13,15,16], offering new strategies for developing extrusion-based metal AM. One strategy to introduce denser grain boundaries is through dynamic recrystallization-induced grain refinement. Since the finer the grain size, the less stable the grains at elevated temperatures, a suitable grain structure rather than the finest grain structure is more desirable for low flow stress at high temperatures [17]. The high-angle grain boundaries with large areas of poor fit and a comparatively open structure are more disordered and, therefore, are more desirable to promote grain boundary sliding and reduce the flow stress of the fine-grained alloys at elevated temperatures, which has been quantitatively described by a recently established visco-plastic constitutive equation [18]. It has been demonstrated that an excellent combination of fine-grained structure and a high fraction of high-angle grain boundaries can be achieved by introducing intensive plastic deformation using friction/friction-stir processing [19].

Motivated by these recent findings, the authors developed an extrusion-based AM method, additive friction extrusion deposition (AFED) or "SoftTouch deposition" in the filed patent [20], aiming to offer new solutions for fabricating customized dense metal parts at reduced

manufacturing costs. The principle of AFED is illustrated in Figure 5.1 and can be described as: (1) locally processing the metal to its malleable state through rapid friction between the feedstock and the rotating die before deposition; (2) extruding the softened and refined metals out through an opening as a "paste" onto a targeted location; and (3) continue to deposit until the desired shape is achieved. Different from other extrusion-based AM processes which soften the feedstock mainly through heating [11,12], AFED enables an effective combination of friction energy and grain refinement to soften the metal feedstock before printing.

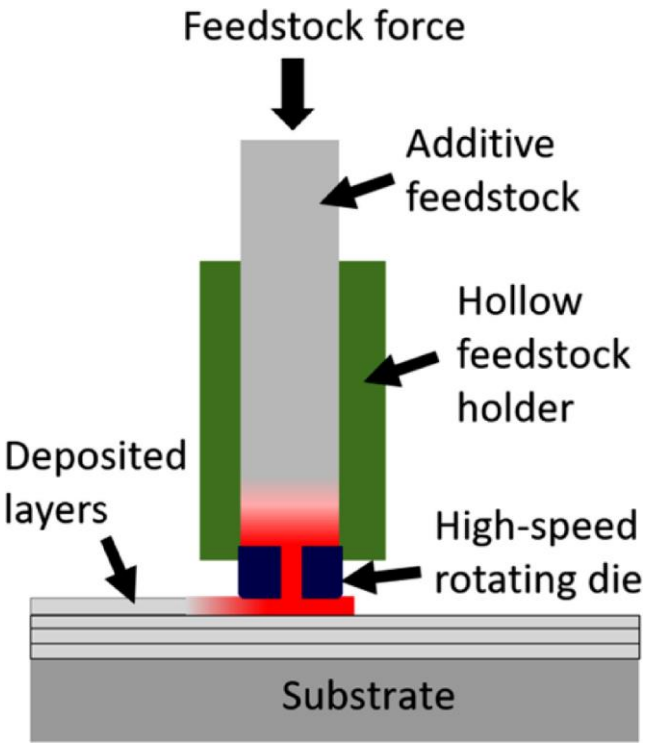


Figure 5.1: Principle of AFED (or SoftTouch deposition).

It should be pointed out that the proposed AFED method is different from other friction stir-related processes, e.g., friction surfacing (FS) [21-23] and additive friction stir deposition (AFSD or MELD) [25-27]. The latter two processes share a rather similar principle and have attracted a great deal of attention from both academia and industry since they can additively

manufacture dense metal parts without reaching melting temperature. The major limitation of FS and AFSD is that these two processes do not have the mechanism to actively soften the feedstock metal just prior to the deposition and therefore require direct friction between the feedstock and the previously deposited metal to soften the metal feedstock [24,25]. A high compressive force or pressure needs to be applied to the substrate or the previously deposited metal layer to enable high-pressure friction. Therefore, the deposition of the following layer needs to wait until the previously deposited layer is stiff enough to support the applied high pressure, which severely limits the process throughput.

AFED has the potential to address this limitation by pre-processing the metal feedstock into its malleable state in a self-reacting module just prior to the deposition. The applied stress on the previously printed layers can be reduced significantly. The manufacturing rate of AFED can be much higher than that of FS and AFSD due to the significantly reduced waiting time between layers. In addition, the pre-processing module enables microstructure uniformity before deposition and a high degree of portability for in-field AM applications. It also makes high-resolution solid-state 3D printing possible by adjusting the size of the die opening.

With the above discussions in mind, the objective of this study is to demonstrate that AFED is a viable solid-state metal AM method for printing dense metals with a significantly reduced pressure against the previously deposited layers. In addition, AFED has been experimentally proven as an effective metal AM method for enabling refined equiaxed grain structure and excellent mechanical properties.

5.2 Materials and Methods

To demonstrate the versatility and cost-effectiveness of the AFED, off-the-shelf 6061 aluminum rods rather than costly metals were used as the metal feedstock. Commercial 6061-T6

aluminum sheets were used as the substrates for deposition. The 6061 aluminum alloy rods consisted of Al (balance), Mg (0.89%), Si (0.75%), Fe (0.38%), Cu (0.33%), Mn (0.11%), Cr (0.09%), Zn (0.04%), and Ti (0.02%), in weight percent while the 6061 aluminum alloy sheets consisted of Al (balance), Mg (0.96%), Si (0.74%), Fe (0.50%), Cu (0.33%), Cr (0.18%), Zn (0.14%), Mn (0.06%), and Ti (0.02%), in weight percent.

An AFED prototype machine was developed and used for the AM experiments. The aluminum alloy rod was inserted into the guiding tube before deposition. The dimension of feedstock used in this study is 15.90 mm in diameter and ~200 mm in length. An anti-rotation protrusion was machined at one end of the aluminum alloy rods and connected to the propulsion rod for preventing the rod to rotate during deposition. The extrusion die was driven to rotate at 1000 rpm to locally soften the aluminum alloy rod during 3D printing. An in-plane velocity of 160 mm/min was used for all the linear or curvilinear deposition. The materials feed rates were varied in such a way that defect-free depositions with the same deposition width, but different layer thicknesses were achieved. Three load cells were installed above the spindle of the AFED so that the compression reaction force applied on the previously printed layer can be measured and recorded. Some of the as deposited samples were subjected to T6 heat treatment: a solution heat treatment at 540 °C for 3 h followed by a water quenching and then an age-hardening at 170 °C for 7 h.

The thermal cycle experienced by the first deposited aluminum alloy during the second layer deposition was measured using Type-K immersion thermocouple probes produced by Omega Engineering. Thermocouple output was recorded using a computer-based data acquisition system. Figure 5.2 shows that the end of the thermocouple probe was placed in the middle of the first deposited layer.

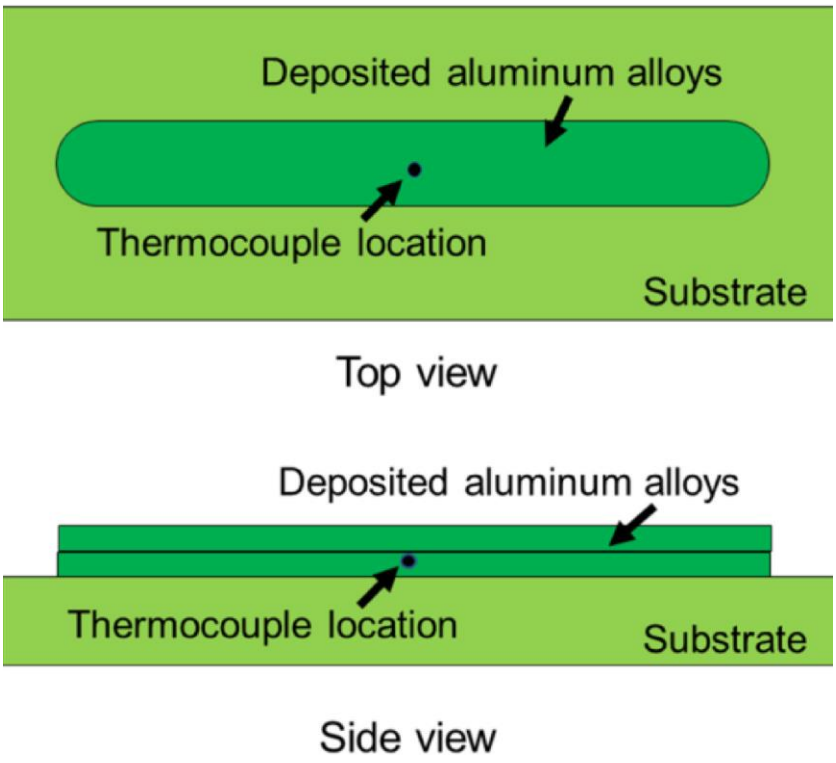


Figure 5.2: Schematic diagram showing the location of the end of the thermocouple during the deposition of the second layer.

The samples for cross-sectional microstructure analysis and mechanical testing were removed from the build plate using wire electro discharge machining (EDM). The samples for microstructure analysis were mechanically polished from P240 sandpaper down to 1 μm diamond paste polishing while the specimens for electron backscattering diffraction (EBSD) analysis were further polished with 0.05 μm colloidal silica using a VibroMet 2 Vibratory Polisher for 4 h. The TEM foils were prepared by twin-jet electropolishing using a solution of 70 pct methanol and 30 pct nitric at 248 K and 12 V.

The polished samples were observed with an optical microscope and scanning electron microscope (SEM). TESCAN MIRA3 FEG-SEM equipped with EDAX Hikari EBSD detector was used for microstructure characterization and EBSD analysis. The acceleration voltage and step size for EBSD were set to be 30 kV and 0.20 μm, respectively. TSL OIM 8.0 software was used for EBSD data analysis. The transmission electron microscope (TEM) analysis was performed

using a Thermos-Fisher Talos F200x at 200 kV. The incident electron beam was adjusted to parallel to a <100> zone axis of the aluminum matrix for identifying the distribution of the precipitates.

Dog-bone-shaped tensile specimens were removed from both the as-deposited samples and heat-treated samples using EDM. The gauge length, thickness, and width of the specimens were 5.0, 1.0, and 1.2 mm, respectively (The ratio of the sample dimensions was referred to the specimen size of ASTM standard E8). Tensile specimens were polished with 400, 800, and 1200-grit sandpaper to eliminate the effect of surface roughness on the tensile properties. Quasi-static uniaxial tensile testing was carried out at room temperature with an initial strain rate of 1.0×10^{-3} s^{-1} using an Instron 3366 frame equipped with a 10 kN Instron load cell.

5.3 Results and Discussion

Figure 5.3(a) shows the SoftTouch prototype machine developed in this study. To demonstrate the versatility and cost-effectiveness of the AFED, off-the-shelf 6061 aluminum rods were used as the metal feedstock (Figure 5.3(b)). The propulsion system applies a compression force to push the feedstock rod against the extrusion die at a constant feed speed while the motor drives the extrusion die to rotate at the targeted speeds. The deposition support table can move relative to the extrusion die in three directions following a computer numerical control (CNC) program. A tie opening of about 70 mm^2 was made at the center of the rotating die to make it easier for the prototype machine to build layers for feasibility demonstration. If high-resolution printing is desired, a smaller circular center orifice can be used. The aluminum alloy feedstock was heated up locally by the friction between the aluminum rod and the rotating die. The softened aluminum alloy was extruded out of the guiding tube through the die opening in solid-state and then was

driven to rub against the substrate/previously printed layer, generating additional friction and plastic deformation to promote the bonding between layers (Figure 5.3(c,d)).

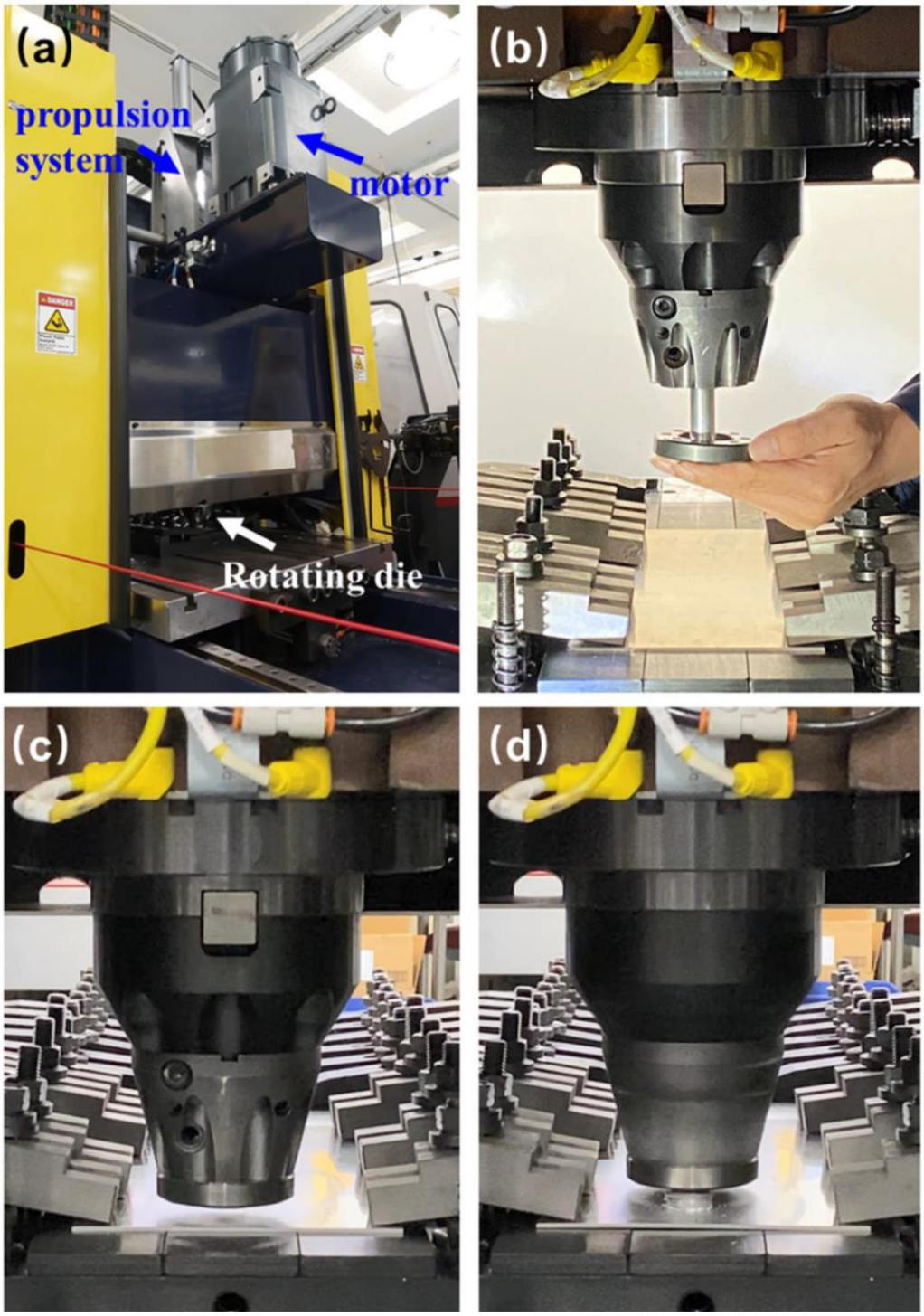


Figure 5.3: AFED: (a) prototype machine, (b) 6061 aluminum alloy feedstock within the system. A snapshot of AFED (c) before and (d) during printing.

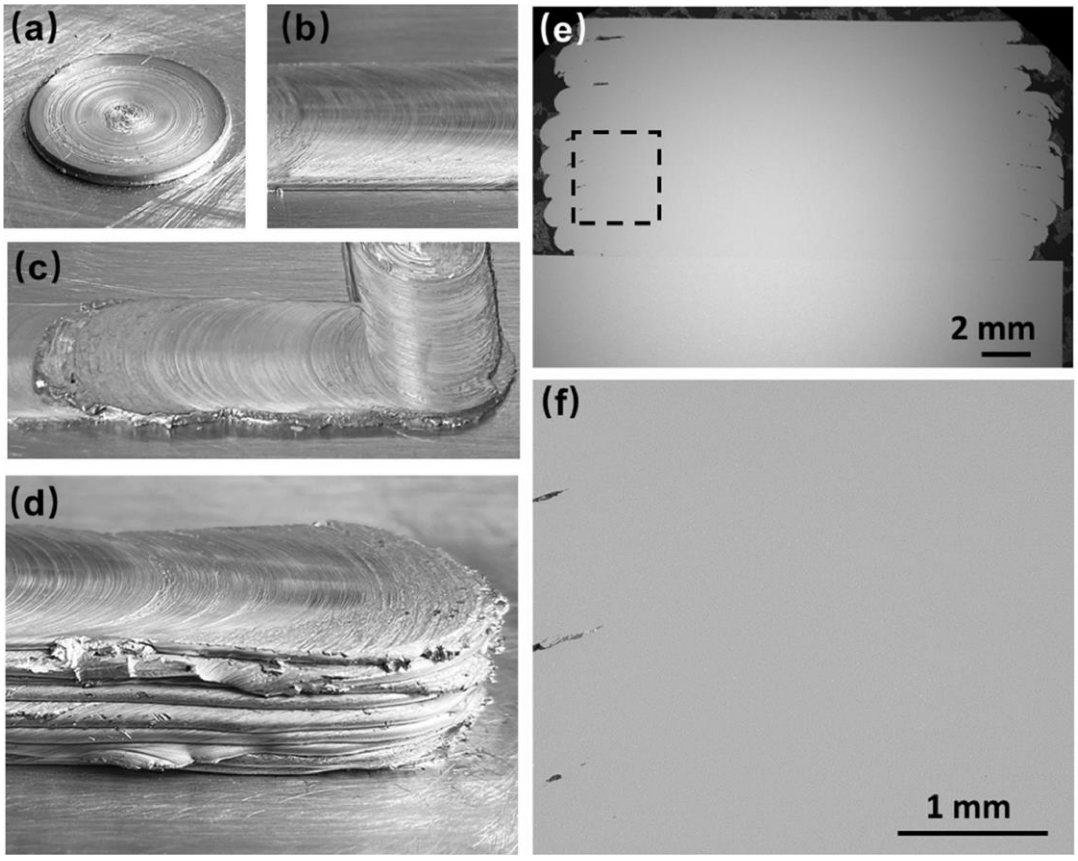


Figure 5.4: Photographs of deposited aluminum alloy in the shape of spot (a), linear (b), curvilinear linear (c), and multiple layers (d). (e) Cross-sectional observation of the deposited metal and (f) a zoom-in view of the deposited metal.

To demonstrate the versatility and capabilities offered by the AFED, as-built aluminum alloys are shown in Figure 5.4, including circular and linear single-layer build patterns (Figure 5.4(a,b), and curvilinear multi-layer and multiple-layer build blocks (Figure 4 (c, d)). In all cases, the printing was controlled such that the layer width is around 20 mm, and the layer thickness is 1 mm, which allows the aluminum extrudate to deform extensively in the lateral directions. Figure 5.4(e,f) shows the cross-section of a typical multiple-layer build block of 6061 aluminum. No porosity defect was observed within the interior of the printed region while voids or kiss bonding were only present at the outer edges of the as-printed block between printed layers. By integrating the AFED with subtractive manufacturing technologies, the outer edges of the as-printed block

can be removed. Therefore, the AFED can be further developed into a hybrid manufacturing method that can build dense metal parts.

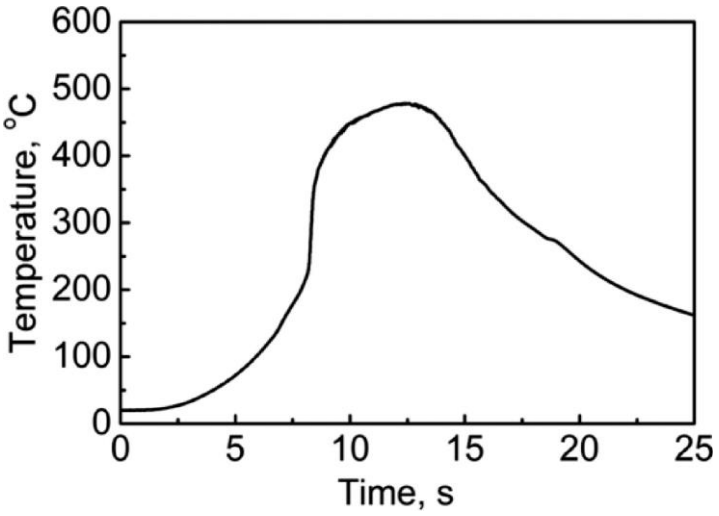


Figure 5.5: Thermal history of the metal in the middle of the first deposited layer during the second layer deposition.

The thermal cycle experienced by the first layer of the deposited aluminum alloy during the second layer deposition was measured using a Type-K immersion thermocouple probe. Figure 5.5 shows that the peak temperature experienced by the first deposited layer during the deposition of the second layer is ~500 °C and the duration time above 400 °C is ~11 s. The melting temperature of the current 6061 aluminum alloy was determined to be ~600 °C (873 K). Therefore, the peak temperature during stable deposition is ~0.87 T_m of the aluminum feedstock, where T_m is the absolute melting temperature (K) of the 6061-aluminum feedstock.

In addition to additive manufacturing of various forms of metal parts, AFED is also well suited for adding geometric features to existing metal parts, repairing damaged metal surfaces, and joining two metals together. Therefore, it is important to evaluate the bonding quality between the deposited metal and the substrate. A comparison of Figure 5.6(a,b) shows that AFED has introduced extensive thermomechanical deformation around the interface between the deposited aluminum alloy and the aluminum alloy substrate, leading to the disappearance of the original

metal surface and the occurrence of recrystallization. The metallurgical bonding between the two metals developed so well that the original surface of the aluminum alloy substrate cannot be identified in the as-deposited sample. Similar microstructures have been observed at the interface between the stir zone and the thermo-mechanically affected zone of friction stir welds which offered excellent bonding strength [28-30].

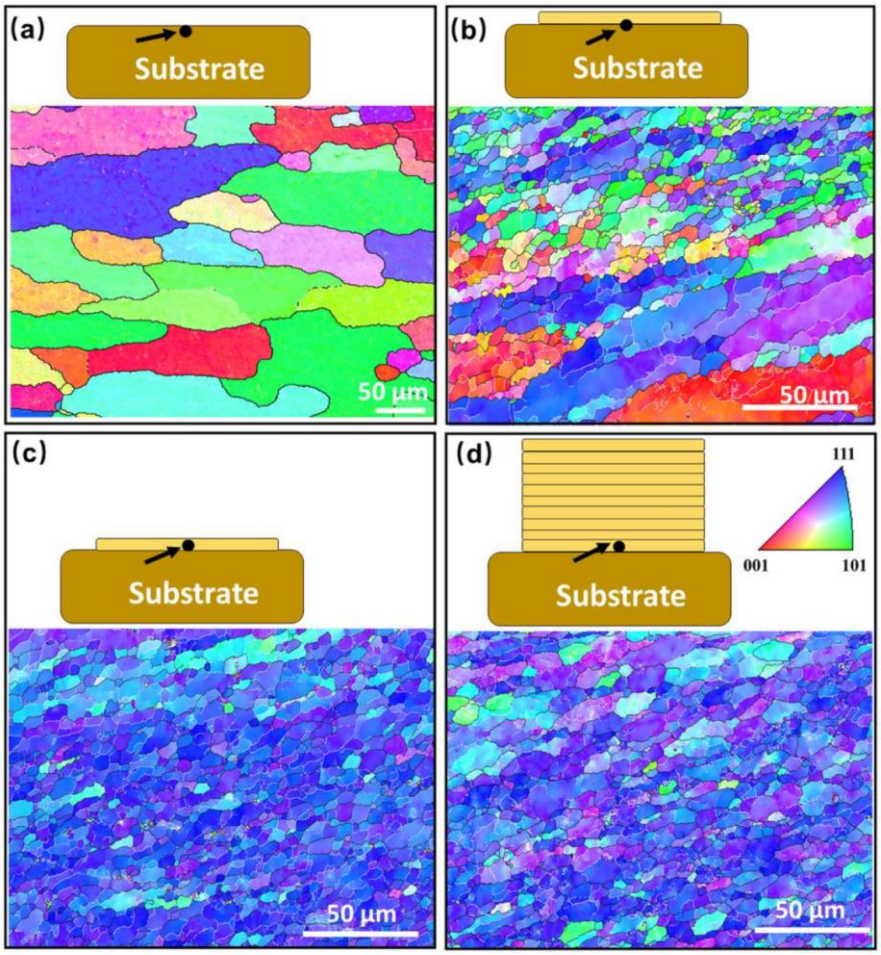


Figure 5.6: Grain structure of (a) 6061aluminum alloy substrate, (b) at the interface between the deposited layer and substrate, at the center of the first printed layer (c) after the first layer of printing, and (d) after 10 layers of printing.

Figure 5.6(c) shows that the first layer of the aluminum alloy printed by AFED was characterized by fine equiaxed grains. The average grain size was determined to be 7.50 µm. The remarkable grain refinement can be ascribed to the deformation-induced recrystallization during FED [16,31]. The grain refinement capability of the AFED is highly desirable as many metals with

fine equiaxed grain structures possess excellent strength, ductility, wear resistance, and superplasticity [15,16,32].

Figure 5.6(d) shows that no significant change in grain structure occurred in the first printed layer even after the completion of a total of 10-layer printing, i.e., the grain structure was not adversely impacted by printing sequence. This is practically attractive since it will significantly simplify the grain structure control during 3D printing. In contrast, the microstructure control in fusion-based AM is very complex as the following printing layers significantly changed the grain structure of previously printed layers [6].

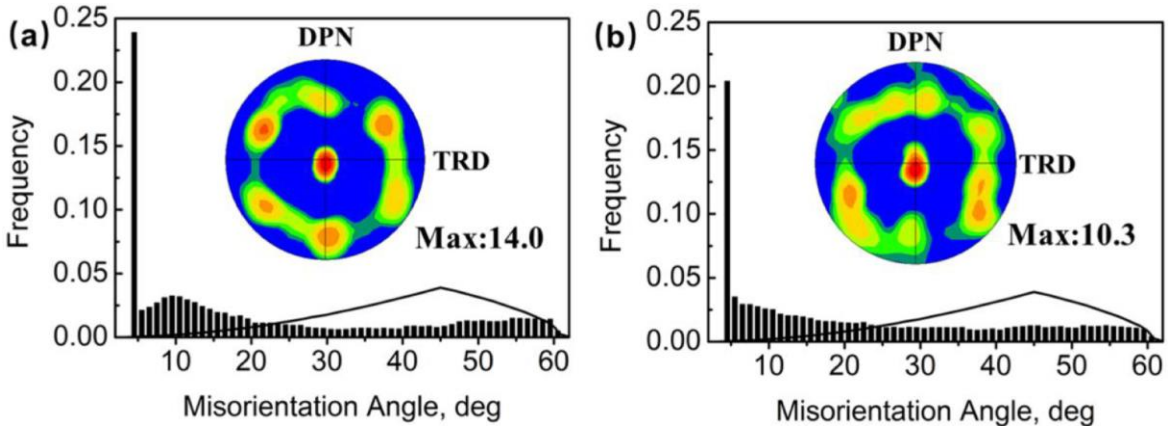


Figure 5.7: Distribution of grain boundary and texture at the center of the first printed layer (a) after the first layer of printing, and (b) after 10 layers of printing (TRD: tool rotation direction; DPN: die plane normal).

Figure 5.7 shows that strong shear texture {112}<110> and a high fraction of low-angle grain boundaries formed in the first printed layer of the as-deposited 6061 aluminum alloy and a completion of a total of 10-layer only slightly weakened the texture. The shear direction and shear plane normal were aligned well with the die rotation direction and the die bottom surface normal, respectively. Previous investigations have shown that the formation of {112}<110> texture in face-centered cubic (fcc) metals is often associated with rapid shear deformation at elevated temperatures [33]. The mechanical properties of the as-deposited 10-layer aluminum alloy block produced by AFED were examined using miniature tensile specimens.

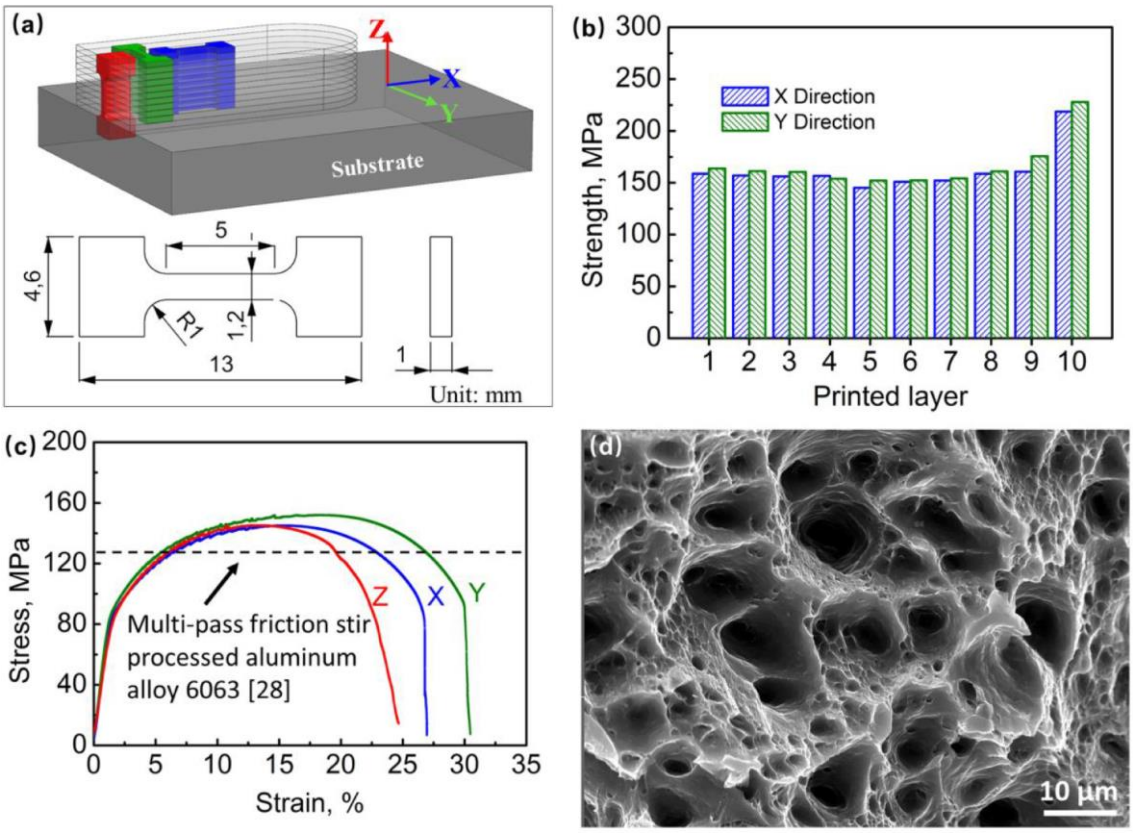


Figure 5.8: Tensile deformation behavior of the as-deposited dense aluminum alloys: (a) schematic showing the locations and dimensions of the tensile test specimens, (b) ultimate tensile strength of each deposited layer in X and Y directions, (c) a comparison of the stress-strain curves in X, Y, and Z directions, and (d) typical fractography of the failed tensile specimen tested in the Z direction.

Figure 5.8(a) shows the position of the miniature tensile specimens relative to the aluminum block. Figure 5.8(b) shows that the last printed layer exhibited the highest ultimate tensile strength (UTS) while the fifth layer exhibited the lowest UTS. The rest of the printed layers exhibited a similar UTS. Since most of the tensile samples in the Z direction failed in the fifth printed layer, the stress-strain curves of the fifth layer in the X and Y directions were summarized in Figure 5.8(c) together with the stress-strain curve in the Z direction for comparison. No significant difference in UTS was observed in the X, Y, and Z directions, demonstrating a weak anisotropy in the as-printed 6061 aluminum alloy and a good bond quality between the deposited layers. Figure 5.8(d) shows the typical fractography of the failed tensile specimen tested in the Z

direction. The fracture surface was fully characterized by dimple-type ductile fracture, which is different from the brittle fracture observed in the 6061-aluminum alloy produced by high-power ultrasonic AM in the Z direction [34]. The poor Z-direction properties of ultrasonic AM samples are correlated to the coalescence of pre-existing shear bands at interfaces into micro-voids, leading to strain localization and spontaneous failure on tensile loading. The results above suggested that SoftTouch AM^{TM} is able to avoid the formation of a weakly bonded interface between deposited layers and, therefore, promote a fully ductile fracture during the tensile test.

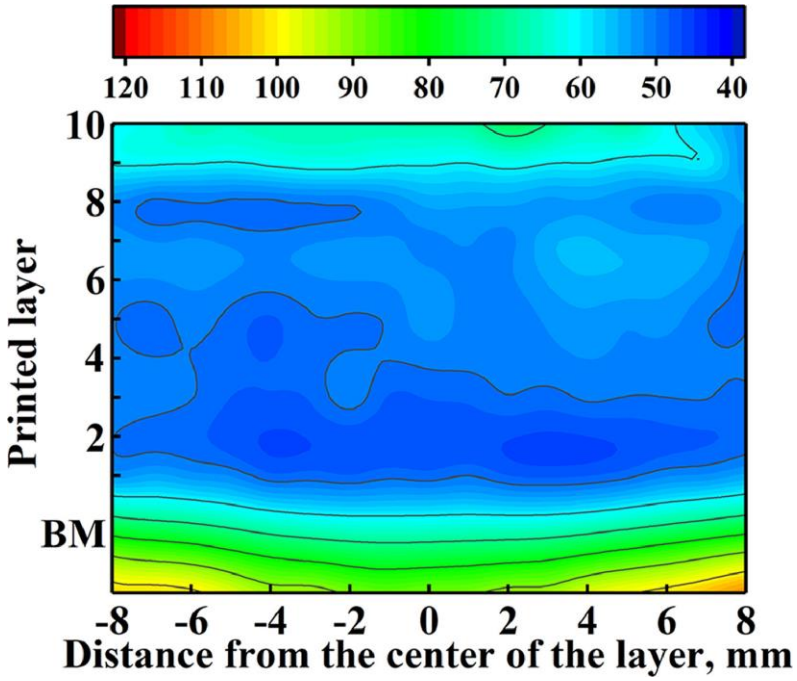


Figure 5.9: Hardness map for the cross-section of the as-deposited sample and the adjacent substrate.

Figure 5.9 shows the hardness distribution of the as-deposited 6061 aluminum alloy layers and the adjacent wrought 6061 aluminum alloy base metal (BM). Compared to the adjacent aluminum alloy BM, a remarkable hardness reduction occurred in all the as-deposited aluminum alloy layers. The tenth printed layer (the last printed layer) exhibited relatively higher hardness than the other layers. 6061 aluminum alloy is a precipitate-hardened aluminum alloy whose

mechanical properties mainly rely on the precipitates rather than the grain structure. A previous investigation [29] showed that even a short exposure of the peak-aged 6061 aluminum alloy to temperatures > 370 °C caused precipitate dissolution, leading to a reduction in strength. Therefore, it is no surprise that the as-printed 6061 aluminum alloy exhibited a reduced hardness compared to the adjacent aluminum alloy BM.

Figure 5.10(a,b) shows the TEM images of the tenth printed layer. A low density of dislocations and spherical precipitates around 100 nm in diameter were observed in the tenth printed layer while the typical needle-shaped β" or rod-shaped Mg_2Si precipitates in the peak aged 6061 aluminum alloy were not observed, suggesting the β" or rod-shaped Mg_2Si precipitates dissolved into the matrix of the 6061-aluminum alloy. Compared to the tenth printed layer, the first printed layer contained a higher density of spherical precipitates and a lower density of dislocations (Figure 5.10 (c,d)). The typical needle-shaped β" or rod-shaped Mg_2Si precipitates were also hardly observed in the first printed layer. Elemental mapping analysis (Figure 5.11) shows that the spherical precipitates were not Mg_2Si precipitates but Si-rich precipitates.

The main alloying elements in the deposited 6061 aluminum alloy are Mg (0.89 wt%) and Si (0.75%). Previous investigations showed that the solubility of Si in the aluminum alloy was 0.86% at 500 °C and decreased to a few parts per million (ppm) at room temperature [35] while the solubility of Mg in aluminum was > 15 wt% at 450 °C and decreased to ~1 wt% at room temperature [36]. Figure 5.10 suggests that high processing temperature during AFED enabled the dissolution of Si and Mg elements into the 6061-aluminum alloy matrix. During the cooling stage of AFED, part of the Si precipitated into Si-rich spherical particles while part of the Si was retained in solution in the aluminum alloy matrix, forming a supersaturated solid solution due to the high cooling rate of FED (Figure 5.10 (a, b)).

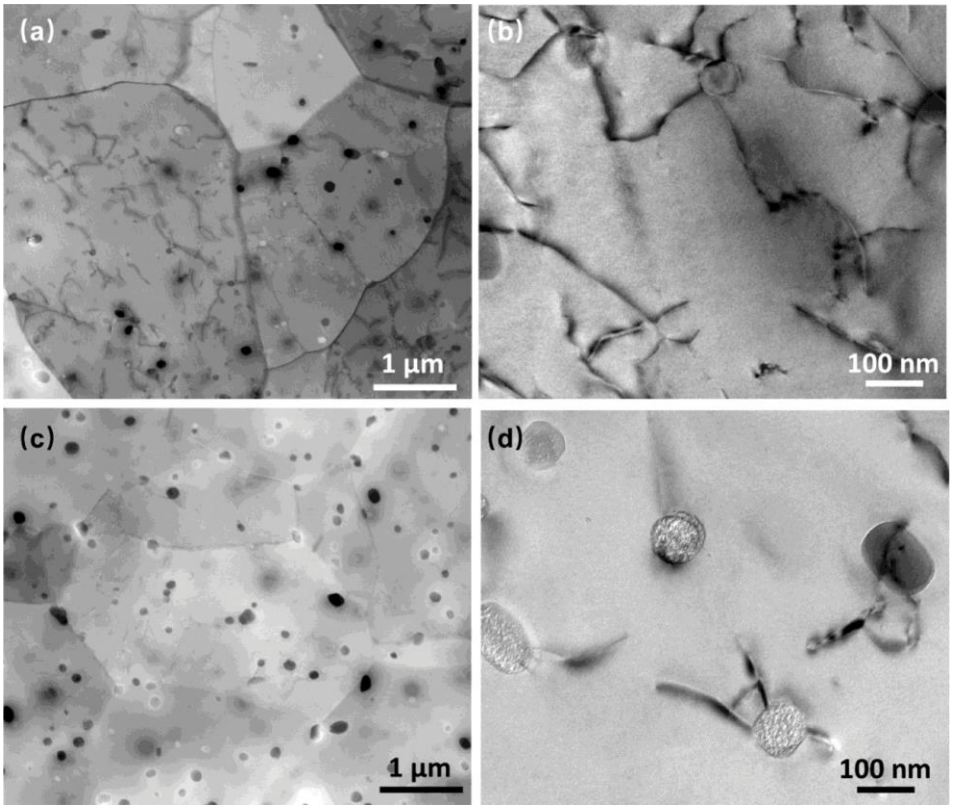


Figure 5.10: TEM micrographs of the tenth layer of the as-deposited sample at (a) low and (b) high magnification; TEM micrographs of the first layer of the as-deposited sample at (c) low and (d) high magnification.

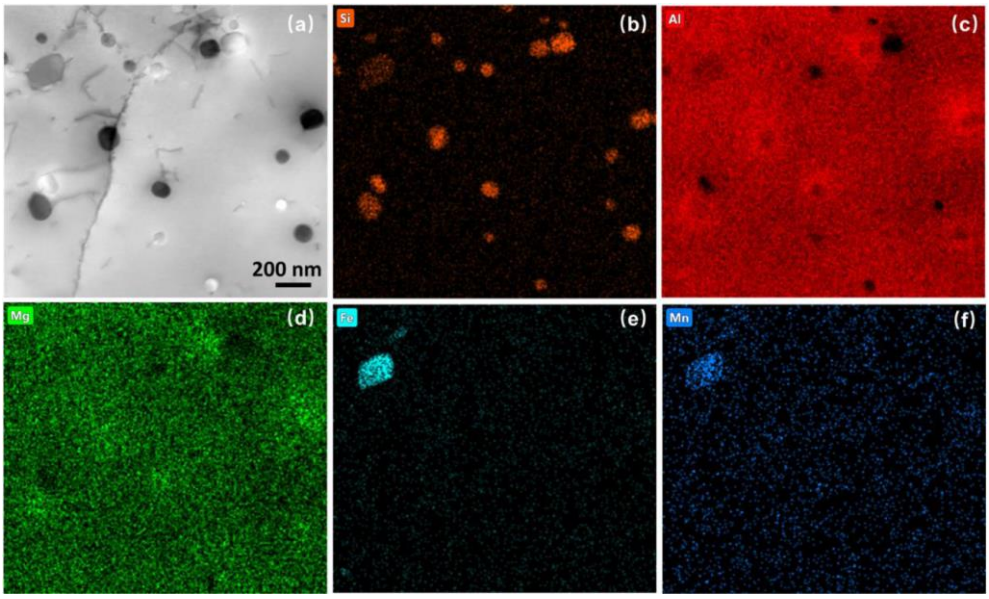


Figure 5.11: Microstructure and element distribution of the first layer of the as-deposited sample.

Figure 5.10 (c, d) shows that more Si in the matrix precipitated into Si-rich spherical particles after experiencing additional thermal cycles during the following deposition processes. The formation of Si-rich spherical particles reduced the degree of Si supersaturation in the aluminum alloy (Figure 5.10 (c, d)) and, therefore, the hardness of the deposited aluminum alloy (Figure 5.9).

Previous investigations showed that the mechanical properties of friction stir processed 6000 series aluminum alloys can be fully recovered after a T6 thermal cycle [37]. Therefore, the temporary softening of the as-printed aluminum alloy is not a major issue for many 3D printing applications. Similar to any other thermomechanical processing or fusion-based processing, a post-processing heat treatment may be needed for the printed parts if high strength is a must, which was experimentally verified in this study.

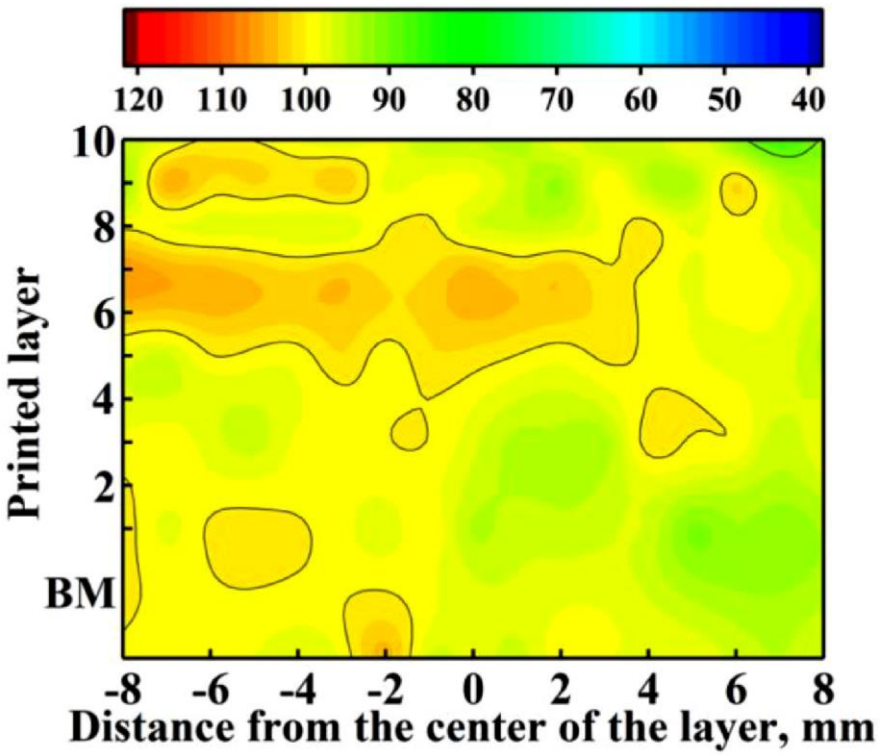


Figure 5.12: Hardness map for the cross-section of the deposited sample and the adjacent substrate after T6 heat treatment.

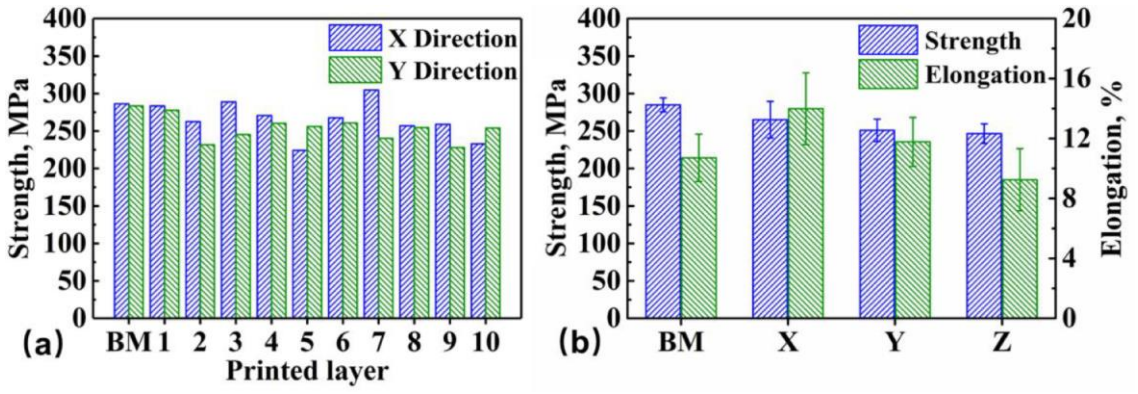


Figure 5.13: Tensile deformation behavior of the deposited alloy and the nearby BM (wrought aluminum alloy) after T6 heat treatment: (a) ultimate tensile strength of each deposited layer in X and Y directions, (b) a comparison of the tensile deformation behavior of the nearby BM and the deposited alloy in X, Y, and Z directions.

Figure 5.12 shows that after the T6 heat treatment (a solution heat treatment at 540 °C for 3 h followed by water quenching and then an age-hardening at 170 °C for 7 h), the majority of the deposited 6061 aluminum alloy and the adjacent 6061 aluminum alloy BM exhibited a similar hardness. A further evaluation of the tensile deformation behavior of the heat-treated samples shows that the wrought BM and all the printed layers exhibited a similar UTS in both X and Y directions (Figure 5.13 (a)). Compared to the BM, the deposited 6061 aluminum alloy exhibited a slight increase in ductility in both the X and Y directions and a slight decrease in UTS and ductility in the Z direction (Figure 5.13(b)). Overall, the deposited 6061 aluminum alloy and the wrought 6061 exhibited comparable tensile deformation behavior. The average UTS and ductility of the deposited 6061 aluminum alloy were determined to be 254 MPa and 12%, respectively. The average UTS and ductility of the wrought aluminum alloy were determined to be 280 MPa and 10%, respectively. High-density needle-shaped β” precipitates, which are the most strengthening precipitates in the peak-aged 6061 aluminum alloy, were observed in both the BM and deposited 6061 aluminum alloy after the T6 heat treatment (Figure 5.14).

Considerable high strength has been achieved in the 6061 aluminum alloys produced by cold spray and fusion-based AM. However, the high strength is often associated with a remarkably

reduced elongation [38-40]. The current study showed that the bulk 6061 aluminum alloys produced by AFED exhibited a UTS and elongation comparable to wrought AA6061 after T6 heat treatment although with a slightly reduced UTS and ductility in the Z direction.

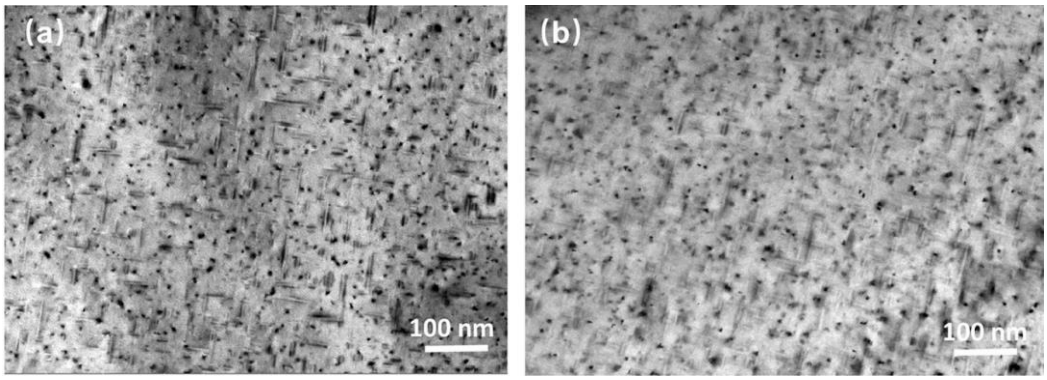


Figure 5.14: TEM micrographs of the (a) BM and (b) the first layer of the deposited sample after T6 heat treatment.

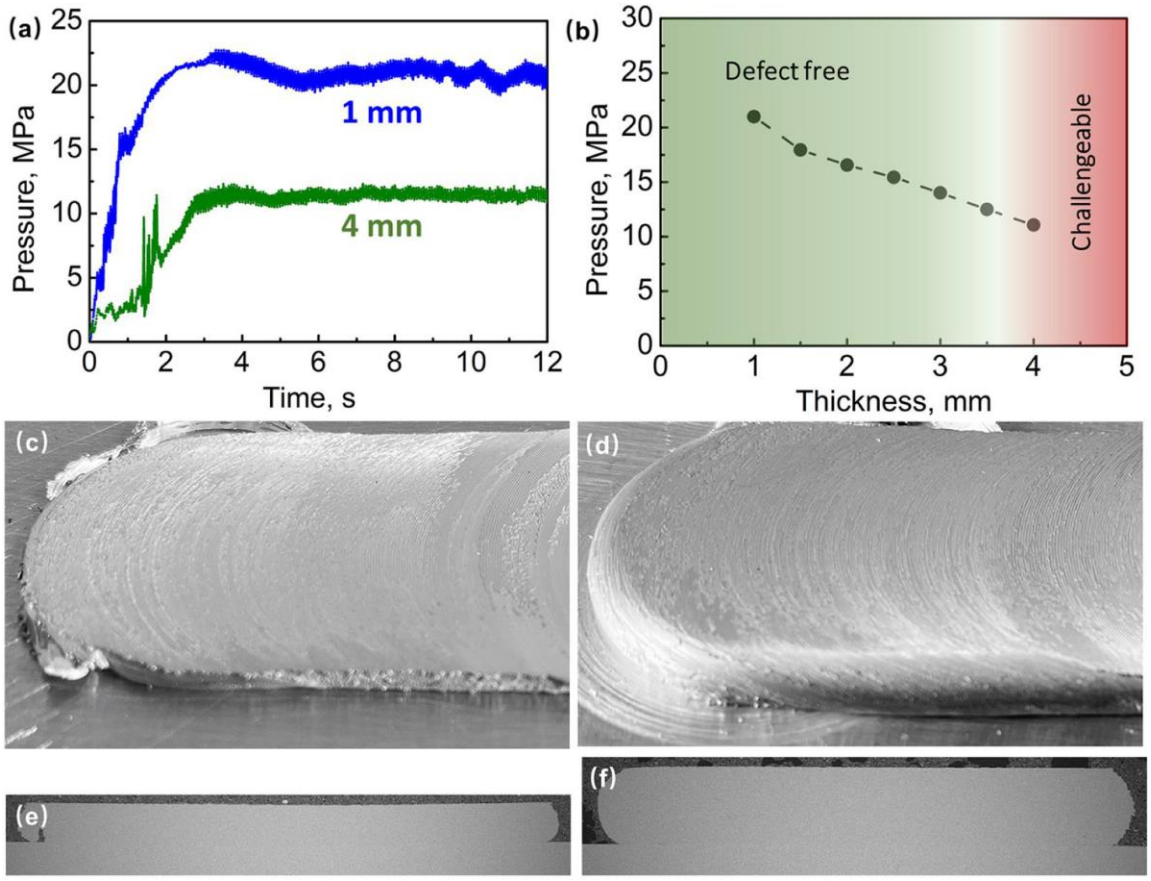


Figure 5.15: Effect of printing layer thickness on the printing process and bonding quality: (a) compression pressure applied on the substrate during AFED, and (b) compression pressure as a function of printing layer thickness. Photographs of as-deposited aluminum alloy with a deposition layer thickness of 1.5 mm (c) and 3 mm (d), respectively. Cross-section of as-deposited aluminum alloy with a layer thickness of 1.5 mm (e) and 3 mm (f), respectively.

Figure 5.15 (a, b) shows that the compression pressure applied on the substrate is only ~21 MPa during deposition when the layer thickness is 1 mm. The compression pressure was reduced to ~10 MPa after increasing the layer thickness to 4 mm. The low deposition compression pressure is advantageous in that it will allow continuous layer-by-layer printing without needing a dwell time for the previously printed layer to recover sufficient strength to endure the compression pressure. A further increase in deposition layer thickness is desirable for large-scale additive manufacturing since it allows a higher building rate. Further investigation is necessary to understand the relation between the printing layer thickness and bonding quality since interfacial defects started to appear when the layer thickness was beyond a certain limit, as shown in this study (Figure 5.15(c-f)).

This study shows that FED can be a key enabler for achieving cost-effective dense metal 3D printing at high manufacturing speed, therefore offering a disruptive solution to the property-complexity-affordability tradeoff dilemma. The absence of metal melting avoids the solidification-induced hot cracking, large shrinkage, and voids defects associated with fusion-based AM. The thermomechanical deformation of FED ensured a dense fine-grained microstructure. Sound mechanical properties can be achieved in the as-printed state and after a post-processing heat treatment.

The geometry complexity of the printed dense metal can be increased by either a size reduction of the die opening or a combination of the AFED with a subtractive manufacturing process. In this regard, AFED offers innovation opportunities in tools, facilities, and system integrations. The capability of using off-the-shelf metal rods as feedstock and printing in the open air makes the SoftTouch deposition avoid pricy metal powders, and costly inert or vacuum conditions. Compared to additive friction stir deposition, SoftTouch deposition has a unique

capability of softening the metal prior to deposition, leading to a soft metal deposition in a solid state. This can significantly increase the manufacturing speed and reduce the manufacturing cost as the waiting time between layers can now be removed, particularly for large-volume AM applications.

The AFED has the potential to unlock unprecedented freedoms for innovations in the field of materials and manufacturing. The capacity of the AFED can be further exploited after strategic control of alloying, precipitates, dislocations, grain size, grain boundaries, texture, and phase distribution of the printed metals. To make the SoftTouch process robust in various applications, an in-depth understanding of the underlying process physics will become critical. Since AFED is an extrusion-based direct printing process operable in an open-air environment, it can be implemented for adding features to existing parts, repairing damaged metal surfaces, joining different pieces of metals, and developing novel fine-grained metals and composites in addition to AM applications. To that end, the authors are confident that the AFED process will significantly advance our metal manufacturing capability through an improved understanding of its process physics and implementation of novel process control algorithms in the coming years, making printing fine-grained dense metals cost-effective.

5.4 Conclusions

In summary, we presented an extrusion based SoftTouch/AFED process that can build dense metal of complex structural forms in an open-air environment using off-the-shelf metal rods as feedstock. During AFED, the feedstock metal was softened by severe plastic deformation-induced grain refinement at elevated temperatures prior to deposition, enabling low compression pressure in the previously deposited layer during the AM process, which is critical for continuous layer-by-layer printing since it can eliminate or remarkably reduce the waiting time between layers

for cooling down the previously printed layer to recover sufficient strength to endure high compression pressure.

The bulk 6061 aluminum alloys produced by AFED exhibited a UTS and ductility comparable to the wrought 6061 aluminum alloys after the same T6 heat treatment. The current study showed that compression pressure applied on the substrate by SoftTouch was in the range of 10−21 MPa during AFED. With an improved understanding of the process physics and implementation of the process control algorithms, the new AM process will be advanced in the coming years for making fine-grained dense metal printing cost-effective, breaking the property-complexity-affordability tradeoff in metal manufacturing.

References

[1] T. DebRoy, T. Mukherjee, J.O. Milewski, J.W. Elmer, B. Ribic, J.J. Blecher, W. Zhang, Nat. Mater. 18 (2019) 1026–1032.

[2] J.H. Martin, B.D. Yahata, J.M. Hundley, J.A. Mayer, T.A. Schaedler, T.M. Pollock, Nature 549 (2017) 365–369.

[3] D. Zhang, D. Qiu, M.A. Gibson, Y. Zheng, H.L. Fraser, D.H. StJohn, M.A. Easton, Nature 576 (2019) 91–95.

[4] L.E. Murr, J. Mater. Sci. Technol. 35 (2019) 231–241.

[5] N. Li, G.Zhang S.Huang, R. Qin, W. Liu, H. Xiong, G. Shi, J. Blackburn, J. Mater. Sci. Technol. 35 (2019) 242–269.

[6] T. DebRoy, H.L. Wei, J.S. Zuback, T. Mukherjee, J.W. Elmer, J.O. Milewski, A .M. Beese, A .D. Wilson-Heid, A. De, W. Zhang, Prog. Mater. Sci. 92 (2018) 112–224.

[7] A .A. Martin, N.P. Calta, S.A. Khairallah, J. Wang, P.J. Depond, A.Y. Fong, V. Thampy, G.M. Guss, A.M. Kiss, K.H. Stone, Nat. Commun. 10 (2019) 1987.

[8] M.-S. Pham, B. Dovgyy, P.A. Hooper, C.M. Gourlay, A. Piglione, Nat. Commun. 11 (2020) 749.

[9] P.A. Colegrove, J. Donoghue, F. Martina, J. Gu, P. Prangnell, J. Hönnige, Scr. Mater. 135 (2017) 111–118.

[10] A.R. McAndrew, M.A. Rosales, P.A. Colegrove, J.R. Hönnige, A. Ho, R. Fayolle, K. Eyitayo, I. Stan, P. Sukrongpang, A. Crochemore, Addit. Manuf. 21 (2018) 340–349.

[11] A .D. Valino, J.R.C. Dizon, A .H. Espera Jr, Q. Chen, J. Messman, R.C. Advincula, Prog. Polym. Sci. 98 (2019) 101162.

[12] M.A. Gibson, N.M. Mykulowycz, J. Shim, R. Fontana, P. Schmitt, A. Roberts, J. Ketkaew, L. Shao, W. Chen, P. Bordeenithikasem, Mater. Today 21 (2018) 697–702.

[13] H. Zhang, D.J. Srolovitz, J.F. Douglas, J.A. Warren, Proc. Natl. Acad. Sci. U. S. A. 106 (2009) 7735–7740.

[14] J. Han, V. Vitek, D.J. Srolovitz, Acta Mater. 104 (2016) 259–273.

[15] F.C. Liu, Z.Y. Ma, Scr. Mater. 59 (2008) 882–885.

[16] Z.Y. Ma, F.C. Liu, R.S. Mishra, Acta Mater. 58 (2010) 4693–4704.

[17] F.C. Liu, Z.Y. Ma, Mater. Sci. Eng. A-Struct. Mater. Prop. Microstruct. Process. 530 (2011) 548–558.

[18] K. Wang, F.C. Liu, P. Xue, D. Wang, B.L. Xiao, Z.Y. Ma, Metall. Mater. Trans. A Phys. Metall. Mater. Sci. 47 (2016) 546–559.

[19] F.C. Liu, P. Xue, Z.Y. Ma, Mater. Sci. Eng. A Struct. Mater. Prop. Microstruct. Pro-cess. 547 (2012) 55–63.

[20] F. Liu, P. Dong, Solid-State Manufacturing System and Process Suitable for Extrusion, Additive Manufacturing, Coating, Repair, Welding, Forming and Mate- rial Fabrication, 2021 US Patent, No. 20210053283.

[21] J. Gandra, H. Krohn, R.M. Miranda, P. Vilaça, L. Quintino, J.F. dos Santos, J. Mater. Process. Technol. 214 (2014) 1062–1093.

[22] Y. Huang, Z. Lv, L. Wan, J. Shen, J.F. dos Santos, Mater. Lett. 207 (2017) 172–175.

[23] G.K. Padhy, C.S. Wu, S. Gao, J. Mater. Sci. Technol. 34 (2018) 1–38.

[24] F. Khodabakhshi, A.P. Gerlich, J. Manuf. Process. 36 (2018) 77–92.

[25] H.Z. Yu, R.S. Mishra, Mater. Res. Lett. 9 (2021) 71–83.

[26] Z.Y. Hang, M.E. Jones, G.W. Brady, R.J. Griffiths, D. Garcia, H.A. Rauch, C.D. Cox,

N. Hardwick, Scr. Mater. 153 (2018) 122–130.
[27] J.B. Jordon, P.G. Allison, B.J. Phillips, D.Z. Avery, R.P. Kinser, L.N. Brewer, C. Cox, K. Doherty, Mater. Des. 193 (2020) 108850.
[28] R.S. Mishra, Z.Y. Ma, Mater. Sci. Eng. R Rep. 50 (2005) 1–78.
[29] F.C. Liu, Z.Y. Ma, Metall. Metall. Mater. Trans. A Phys. Metall. Mater. Sci. 39 (2008) 2378–2388.
[30] A. Heidarzadeh, S. Mironov, R. Kaibyshev, G. Çam, A. Simar, A. Gerlich, F. Khodabakhshi, A. Mostafaei, D.P. Field, J.D. Robson, Prog. Mater. Sci. 117 (2021) 100752.
[31] X. Li, W. Tang, A.P. Reynolds, W.A. Tayon, C.A. Brice, J. Mater. Process. Technol. 229 (2016) 191–198.
[32] Z.Y. Ma, A.H. Feng, D.L. Chen, J. Shen, Crit. Rev. Solid State Mater. Sci. 43 (2018) 269333.
[33] R.W. Fonda, K.E. Knipling, Sci. Technol. Weld. Join. 16 (2011) 288–294.
[34] N. Sridharan, M. Gussev, R. Seibert, C. Parish, M. Norfolk, K. Terrani, S.S. Babu, Acta Mater. 117 (2016) 228–237.
[35] S. Fujikawa, Y. Oyobiki, K. Hirano, J. Jpn. Inst. Light Met. 29 (1979) 331–339.
[36] I.J. Polmear, K.R. Sargant, Nature 200 (1963) 669–670.
[37] K.J. Al-Fadhalah, A.I. Almazrouee, A.S. Aloraier, Mater. Des. 53 (2014) 550–560.
[38] M.R. Rokni, C.A. Widener, O.C. Ozdemir, G.A. Crawford, Surf. Coat. Technol. 309 (2017) 641–650.
[39] S.Z. Uddin, L.E. Murr, C.A. Terrazas, P. Morton, D.A. Roberson, R.B. Wicker, Addit. Manuf. 22 (2018) 405–415.
[40] F.R. Chen, Y.H. Yang, H.L. Feng, Materials 14 (2021) 1061.

Chapter 6 Further Exploratory Study on Friction Extrusion-Based Solid-State Deposition of Dissimilar Material Systems

6.1 Background

3D metal printing or additive manufacturing (AM) processes have shown enormous potential for both repairing existing structures and developing optimized structures by achieving near-net shapes [1]. However, one of the key challenges in fusion-based AM processes is solidification-induced anomalies or defects, e.g., gas pores, solidification cracking, incomplete fusion, inclusion, etc. Fusion-based dissimilar metal AM is particularly challenging due to the formation of intermetallic compounds (IMCs), which can cause microcracking. The impact of some of these types of defects must be carefully evaluated on their implications on structural performance [2]. Specifically for multi-material structure applications, such as a light water reactor where stainless-steel cladding is used on the low carbon steel pressure vessels, a fusion-based cladding process can induce tensile stresses, which can cause stress corrosion cracking. Therefore, alternative AM processes, particularly solid-state AM, can be highly desirable for eliminating solidification-induced defects and enabling dissimilar metal AM [3,4].

Furthermore, fusion-based processes, due to their high input, decarburize at the LCS side near the welding interface [5,6]. Such a migration of carbon from the heat-affected zone (HAZ) leaves the region for coarse-graining, and softening takes place weakening the region. Similarly, due to the high input of fusion welding and fusion-based 3D printing, significant chromium carbide precipitation takes place when the temperature reaches above 700°C for a prolonged period of time

[7]. Precipitation of chromium carbide occurs more rapidly around the grain boundaries, and such a sensitization of steel makes the region around the weld more prone to corrosion, leading to a reduction of the service life of the welded components [5].

Combining the grain refinement achieved in AFED presented in Chapter 5, and with the controlled and strategically induced localized shear strain between the steel surface and the depositing aluminum alloy 6061 (AA6061) in large-area friction stir additive manufacturing (FSAM) presented by Liu et al [8,9] in Chapter 4, this chapter presents an exploratory study on the solid-state deposition of stainless steel 316 (SS316) on carbon steel 1018 (AISI1018) (section 6.2.1) and aluminum alloy 6061 (AA6061) deposition on stainless steel 304 (SS304) (section 6.2.2) to achieve dissimilar material systems. This study is intended to provide a multi-fold solution to achieve structural lightweighting and on-demand structural repair by AFED to develop dissimilar material structures using stainless steel on mild steel for various surface cladding applications, and aluminum alloy on steel with suppressed IMCs and robust interfacial bonding.

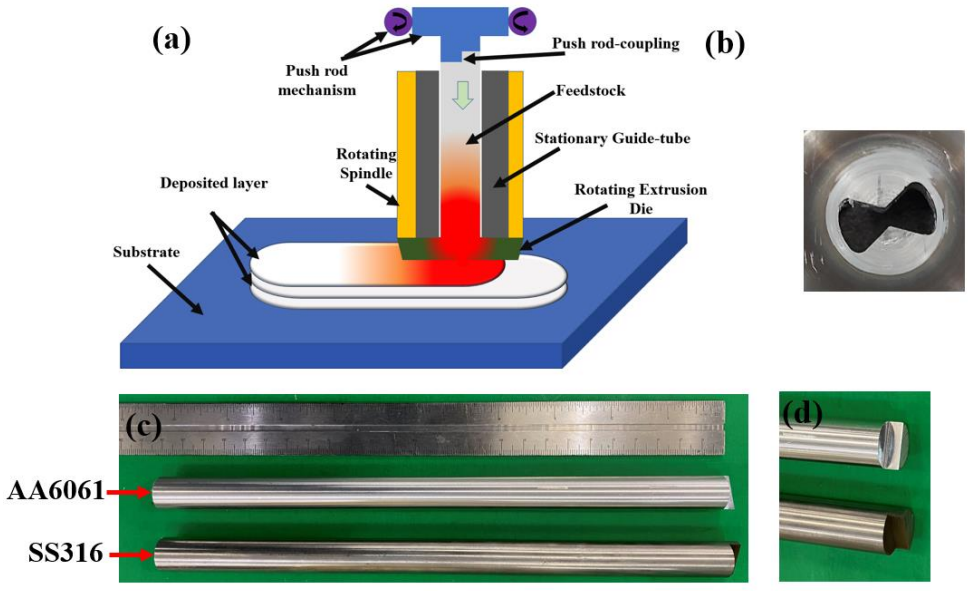


Figure 6.1:(a) Schematic of the AFED (SoftTouch AM^{TM}) process, (b) bow-tie extrusion profile, (c) off-the-shelf round feedstock of aluminum alloy 6061 (AA6061) and stainless steel 316 (SS316), (d) anti-locking feature on the top end of feedstocks

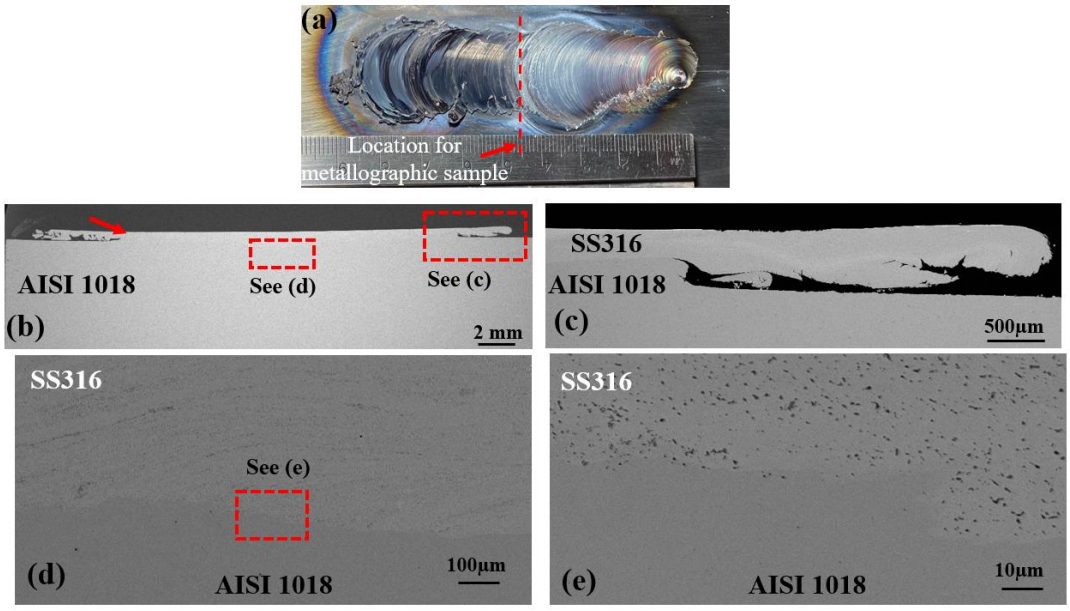


Figure 6.2: (a) SS316 deposition on AISI1018, (b) cross-sectional SEM image showing a global view of deposition, (c) detailed features of flash overhang indicated in (b), (d) higher magnification image showing banded structure between SS316 deposition and AISI1018 substrate, (e) higher magnification image showing inter-penetration of SS316 deposited layer with AISI1018 substrate top surface indicated in (d)

6.2 Results and Implications

6.2.1 Stainless steel 316 deposition on carbon steel AISI1018

AFED is a novel solid-state additive manufacturing process, and the design of the material printing nozzle has been achieved by numerous combinations of systems and component-level design iterations. As shown in Figure 6.1, the feedstock and guiding tube remain stationary at all times, and only the extrusion die rotates at the end of the feedstock without letting feedstock pass through the extrusion die directly, making it different than the commercially available technologies such as AFSD by MELD Inc [3]. AFED system assembly does not contact with the substrate and the extrusion die shown in Figure 6.1(b) uses a bow-tie extrusion profile. The round feedstocks of aluminum alloy 6061 and SS316 shown in Figure 6.1(c) have an anti-rotation feature shown in Figure 6.1 (d) to prevent any rotation of feedstock when the extrusion die is rotating at the other end to plasticize the feedstock. A single continuous layer of SS316 was deposited on mild steel

1018, developing a dissimilar material SS316/AISI1018 interface. Figure 6.2(a) shows the top view of SS316 deposition on AISI1018 with approximately 85 mm printed length, 25 mm width, and 0.80 mm average thickness. It was deposited at 1000 RPM, 20 mm/min federate, and 60 mm/min printing velocity.

Figure 6.2(b) shows a cross-sectional macrograph with SS316 deposited on AISI1018 mild steel. Two distinct overhangs can be observed on either side of the printed layer widths (Figure 6.2b). The SEM backscatter detector image shown in Figure 6.2(c) shows strong stirring and mixing features at the overhanging flash adjacent to the substrate material. The overhangs on the advancing and retreating sides were 4.50 mm (top right corner in Figure 2b) and 2.50 mm (top left corner in Figure 6.2b), respectively. Longer overhanging flashes on the retreating side can be attributed to a material flow in the extrudate deposited material between the rotating extrusion die exterior plane and the substrate implying insufficient forced mixing of deposited material between the SS316 deposition and the AISI1018 substrate.

The higher magnification image shown in Figure 6.2(d) represents the deposition-processing or friction-processing zone of SS316 and the inter-mixed substrate boundary. It can be seen from Figure 6.2(d) that the SS316 deposited material underwent a significant amount of frictional processing to mix and adhere with the AISI1018 substrate. It can be further confirmed with even higher magnification images in Figure 6.2(e). Visible shear bands or banded structures [10] developed by the mixing and interpenetration of elemental alloys of SS316 and AISI1018 can be seen with slightly varying contrast in Figure 6.2(d). A further higher inter-penetration of deposited material and the substrate material can be verified by Figure 6.2(e) at a much higher magnification image showing clear inter-mixing and inter-penetration of SS316 and AISI1018 materials. There were no visible voids or gaps at the interface of SS316 and AISI1018 materials

in any of the depicted cross-sectional images shown in Figure 6.2 implying a strongly bonded interface.

Figure 6.3(b) shows the EBSD IPF map for the SS316 feedstock rod material cross-section. The preliminary observation from Figure 6.3(b) shows typical coarse grains with grain size between 35 and 98 µm. We can observe a significant density of annealing twins and shear bands with strong texture from the EBSD IPF map shown in Figure 6.3(b), with well-defined grain boundaries. Figure 6.3(c-d) represents the IPF maps of EBSD scans collected for the SS316 deposition on AISI1018 steel substrate and respective pole figures at locations marked in Figure 6.3(a). The IPF map shown in Figure 6.3(c) at the top of the layer (point "c" in Figure 6.3(a)) depicts nearly equiaxed smaller grains with disappeared annealing twins compared to the base feedstock material grain structure. It has an average grain size of around 7.60 µm (see Figure 6.4c) with random texture distribution as shown in Figure 6.4(a).

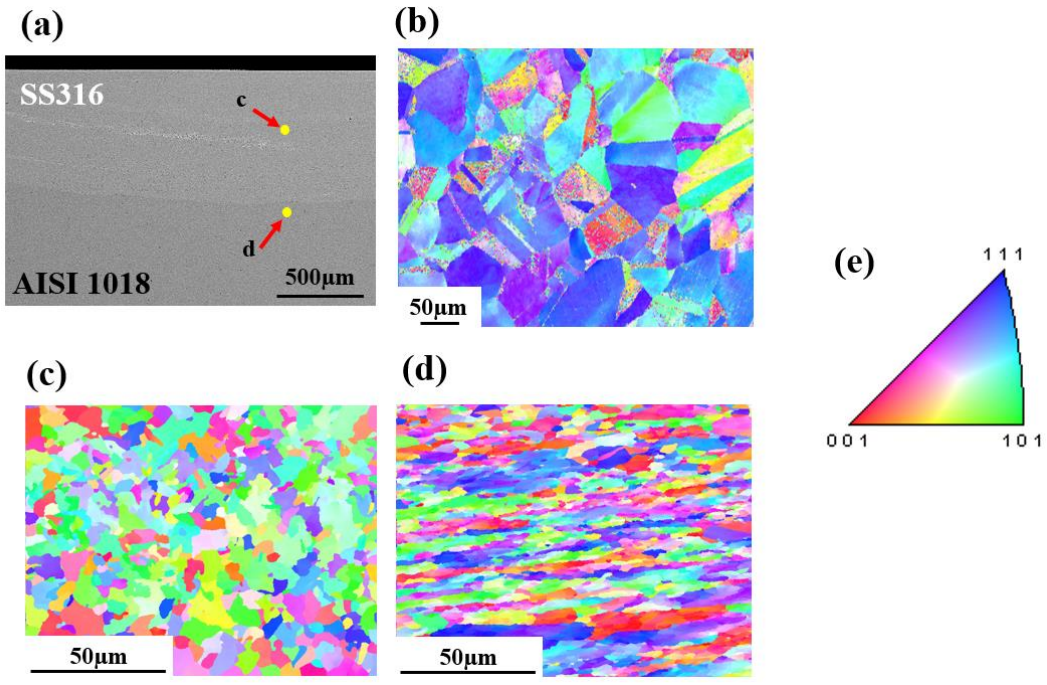


Figure 6.3: (a) EBSD scanning locations in the SS316 deposited layer and top of the AISI1018 substrate, (b) EBSD IPF maps for SS316 base material, (c) inverse pole figure (IPF) maps at the location shown for the SS316 deposited layer, (d) IPF maps at the top of the AISI1018 layer adjacent to the SS316 deposited layer, (e) IPF triangle

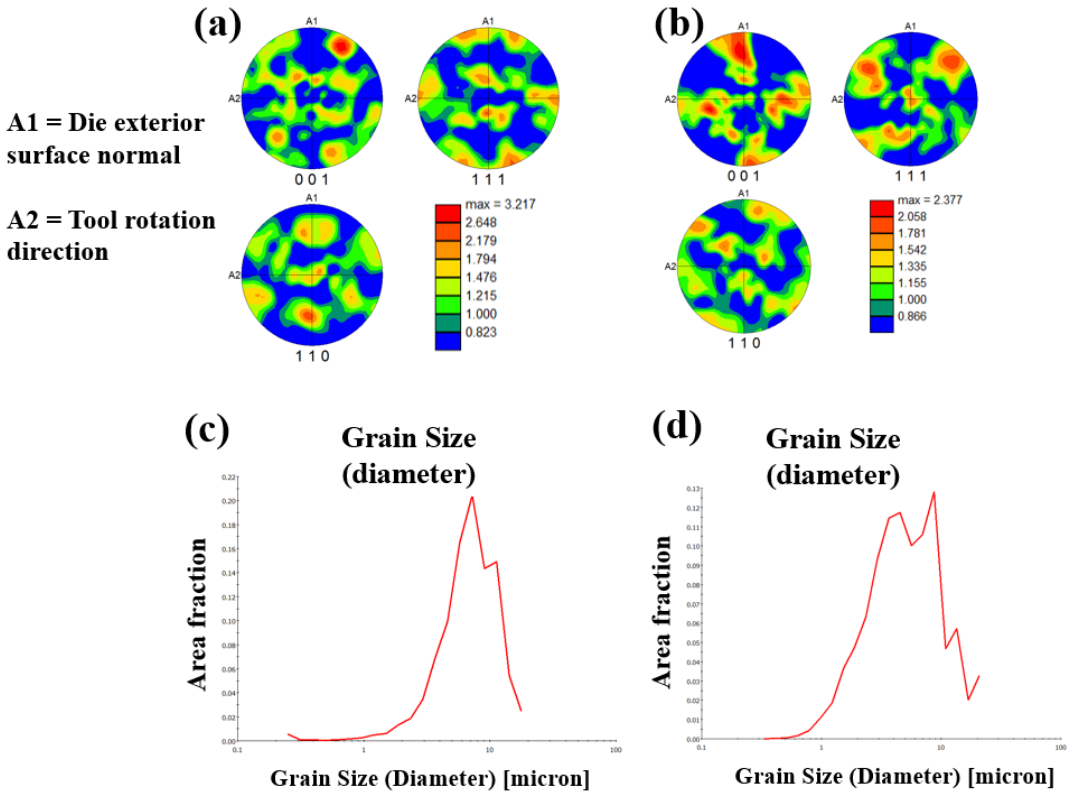


Figure 6.4: (a) Texture plot for the IPF maps shown in Figure 6.3(c), (b) texture plot for the IPF maps shown in Figure 6.3(d), (c) grain size distribution w.r.t. area fraction for the IPF maps shown in Figure 6.3(c), (d) grain size distribution w.r.t. area fraction for the IPF maps shown in Figure 6.3(d)

On the other hand, the EBSD scanning location in the AISI1018 substrate top surface has a slightly different microstructure, as shown in Figure 6.3(d), depicting a more pronounced shear banding phenomenon generally seen in the friction stir zone [11,12]. The grains in Figure 6.3(d) show more elongated and friction stir deformation-induced banded patterns. It has an average grain size of 5.50 µm as shown in Figure 6.4(d). Corresponding pole figures shown in Figures 6.4(a) and (b) show weak textures for both the grain distribution shown in Figures 6.3(c) and 6.3(d), indicating strong frictional processing. Such a frictional processing must shear and elongate the grains and deform the microstructure at a high shear strain rate inducing severe plastic deformation and grain refinement throughout the deposited SS316 layer and adjacent AISI1018 substrate material.

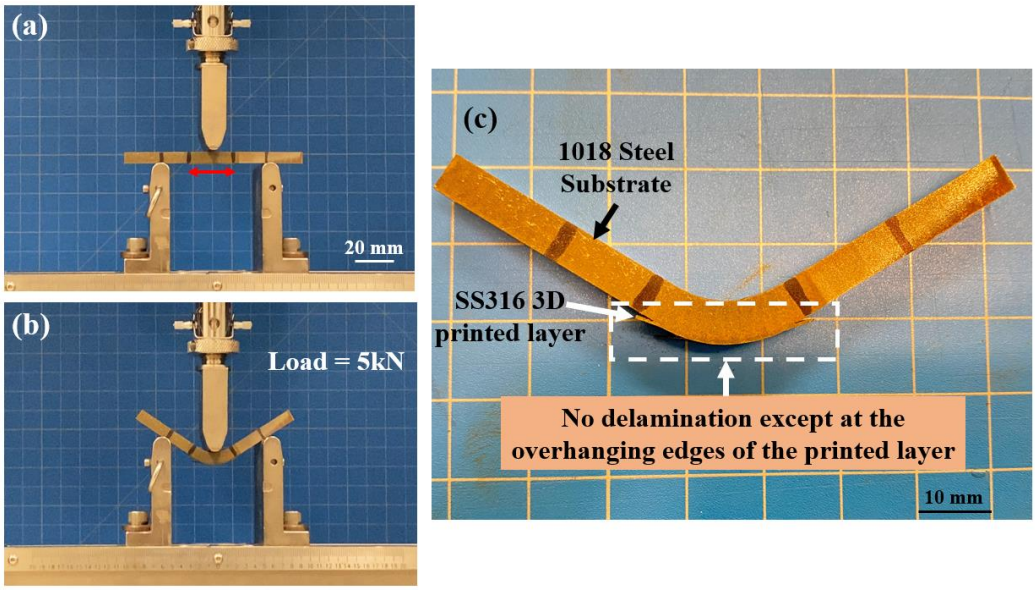


Figure 6.5: Illustration of three-point bending test; (a) testing setup before the loading begins, (b) sample under 5kN loading condition, and (c) optical image showing bonding and delamination between SS316 deposited layer and AISI1018 substrate.

In order to assess the interlayer bonding characteristics for SS316 deposition on AISI1018, a three-point bending test was performed. Figure 6.5(a) shows the loading configuration of the three-point bending specimen (100mm X 10mm X 6.25mm) with a deposited layer indicated by the double-sided red arrow. After a peak load of 5kN, the bent and sufficiently yielded profile of the substrate AISI1018 with unaffected SS316 deposited layer was recovered and is shown in Figure 6.5(b). As can be seen in Figure 6.5(c), the delamination occurred only at the outer edges of the deposited SS316 layer, and no delamination was seen away from the edges of the deposited layer. This implies a strong stirring between SS316 deposited material and AISI1018 substrate leading to a strongly bonded interface.

Stacking fault energy (SFE) is the governing factor for grain refinement in metallic materials because it controls the dislocation movements directly [10,13]. Materials with low SFE have higher stacking fault width between two partial dislocations, and hence, the cross slip and climb of dislocations suffer from recombination, leaving concentrated regions of dislocations in the grains. On the other hand, materials with high SFE are easier to allow dislocations to

redistribute, recover, and recrystallize [10,14]. AFED process generates a high strain rate frictional processing of materials at temperatures significantly high, yet below the melting point. Such a dynamic state imparts superplastic deformation at high temperatures, and refinement of grains must occur.

The AFED process discussed in this research uses the rotatory extrusion tool on the solid feedstock to first deform the metallic materials superplastically at a high shear strain rate. Grain refinement takes place partially once at the exit of the extrusion die opening. Then deposited material is frictionally processed again vigorously with the substrate by frictional stirring and severe plastic deformation must take place adjacent to the substrate. Both processes undergo a significant amount of frictional shear processing below melting temperature of materials, and severe plastic deformation (sever cold working) must occur to homogeneously refine the grains depending upon their SFE [10,15].

6.2.2 Aluminum alloy-6061 deposition on stainless steel 304 substrate

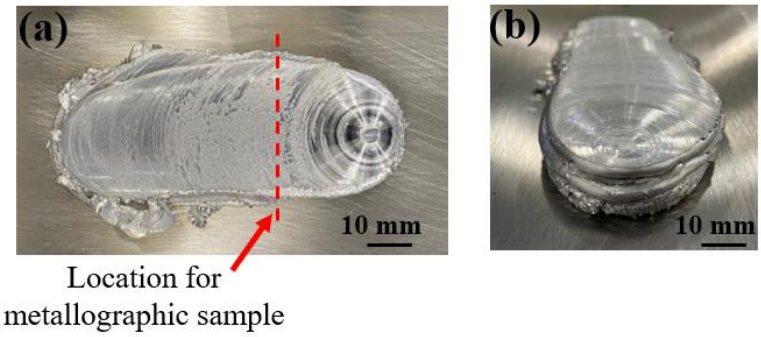


Figure 6.6: (a) Top view of multi-layer 6061 aluminum deposition on SS304 substrate, (b) front of view of multi-layer 6061 aluminum deposition on SS304 substrate.

Figure 6.6 shows the multilayer 6061 aluminum alloy deposition on the SS304 substrate, with Figure 6.6a representing the top view and Figure 6.6b representing the front view of the multi-

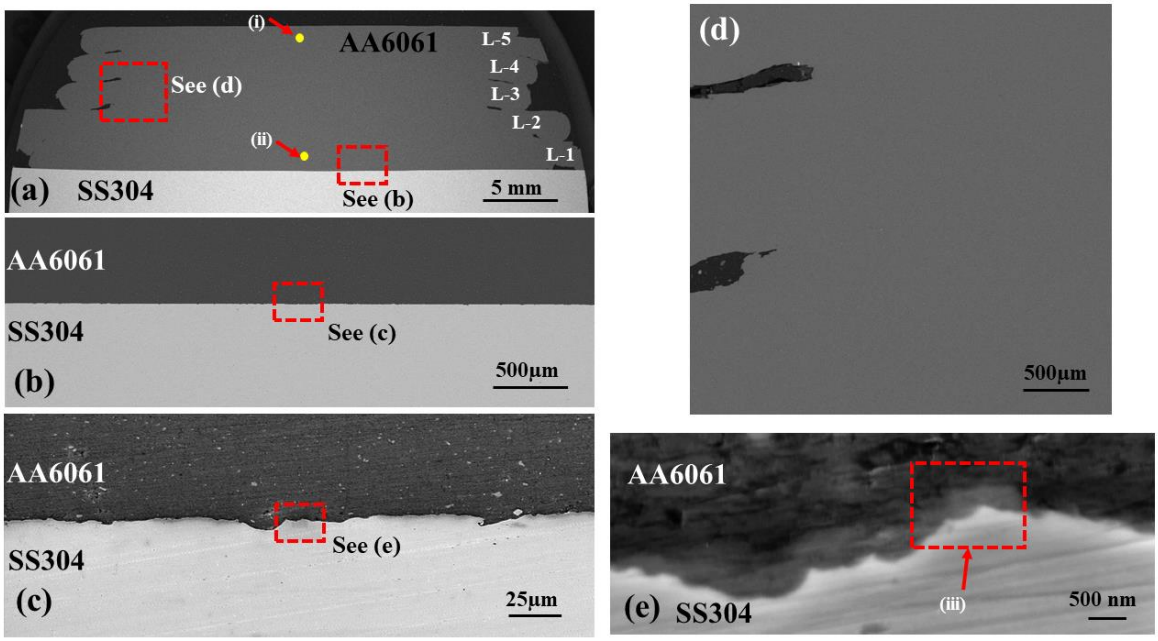


Figure 6.7: Cross-sectional SEM images of multi-layer 6061 aluminum alloy deposition on SS304 substrate; (a) multi-layer deposited sample cross-section with marked layers 1-5 and locations (i) and (ii) for EBSD scanning, (b) intimately bonded AA6061/SS304 interface, (c) higher magnification image showing tightly bonded interface, dispersion of white Mg_2Si precipitates, and surface unevenness of SS304, (d) inter-layer bonding features near the overhang shown in (a), and (e) nanoscale interfacial reaction zone indicated in (c) with location (iii) marked for TEM sample analysis

layer deposit. A layer thickness of 1.50 mm with 25 mm width, 75 mm printing length, 1000 RPM, 800 psi, and 120 mm/min printing velocity was used to deposit 5 layers of 6061-aluminum alloy on SS304 substrate. Figure 6.7 represents cross-sectional images at various magnifications of 6061 aluminum alloy multi-layer deposition on SS304 substrate. As shown in Figure 6.7(a), layers 1-5 are marked as L1, L2, L3, L4, and L5 respectively. It can be observed from Figures 6.7(a-c) that the first 6061 aluminum layer deposition on SS304 shows no visible voids or gaps at the bonded interface. There was a noticeable amount of surface unevenness on the SS304 material shown in Figure 6.7(c), which can be attributed to the surface condition of the SS304 substrate (brushed condition) and the initial action of friction processing of the extruded 6061 aluminum alloy. Despite the surface unevenness on the SS304 substrate, the bonding interface shown in Figures 6.7(a) and 6.7(b) shows intimate bonding between aluminum alloy 6061 and SS304. Higher magnification images 6.7(c) and 6.7(e) further confirm the close and tight bondedness of the

interface without any visible voids or gaps. The deposition-bonded interface in Figure 6.7(e) further shows a nanoscale interfacial feature adjacent to the SS304 faying surface. It resembles similarities with intermetallic compounds (IMCs) and is discussed in detail in later sections.

The multi-layer deposited regions in Figure 6.7(a) are further investigated in detail and are shown in Figure 6.7(d) with L-3 and L-4 interfaces at higher magnification. It can be observed from Figure 6.7(d) that the aluminum 6061 deposited layers have been adequately processed and don't show any signs of visible delamination or inter-layer voids.

Another important observation can be made from Figure 6.7(c) above the SS304 substrate line about the broken and dissolved precipitates. Since 6061 aluminum alloy is a precipitate-hardened alloy with the Mg2Si phase as the dominant precipitation phase [4], such precipitates must be dissolved and redistributed homogeneously via friction processing. This can be observed from Figure 6.7(c) at multiple spatial locations with white precipitate nodules distributed throughout the deposited layer. It can be further attributed to the high shear strain rate induced agitation achieved during the primary friction at the feedstock end to soften the feedstock material and then secondary friction to additively deposit the layer-by-layer structural build. Also, since the dual friction processing reduces the deposition processing temperature (as shown in Liu et al. [4]) and substrate back-response pressure, such a mixing must happen at lower temperatures compared to the solidus to liquidus temperature transition temperature leading to more uniform precipitate redistribution.

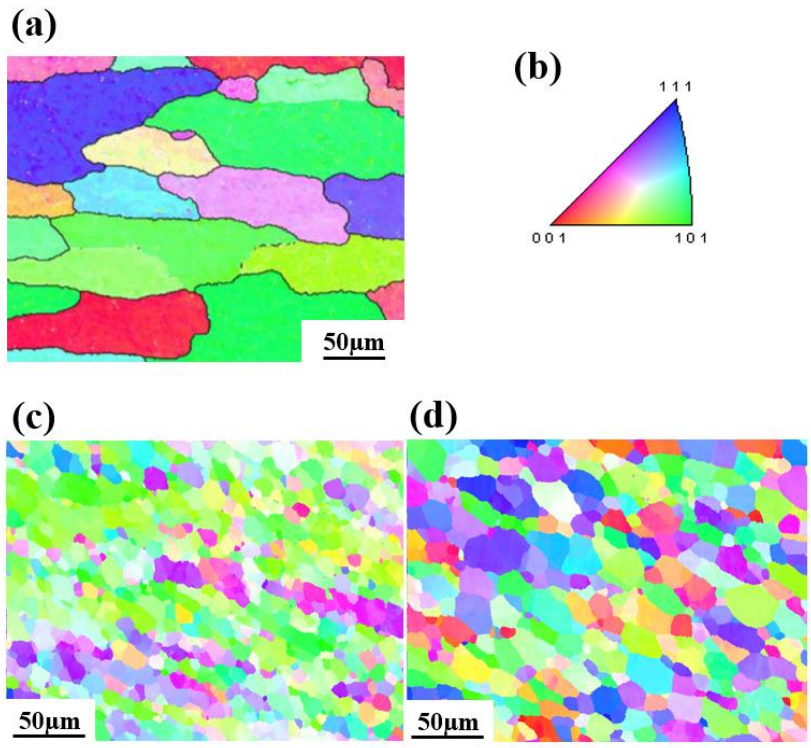


Figure 6.8: EBSD IPF (a) AA6061 base material, (b) IPF triangle, (c) IPF maps showing grain refinement at location (i) in L5 shown in Figure 6.7(a), (d) IPF maps showing grain refinement at location (ii) in L1 shown in Figure 6.7(a)

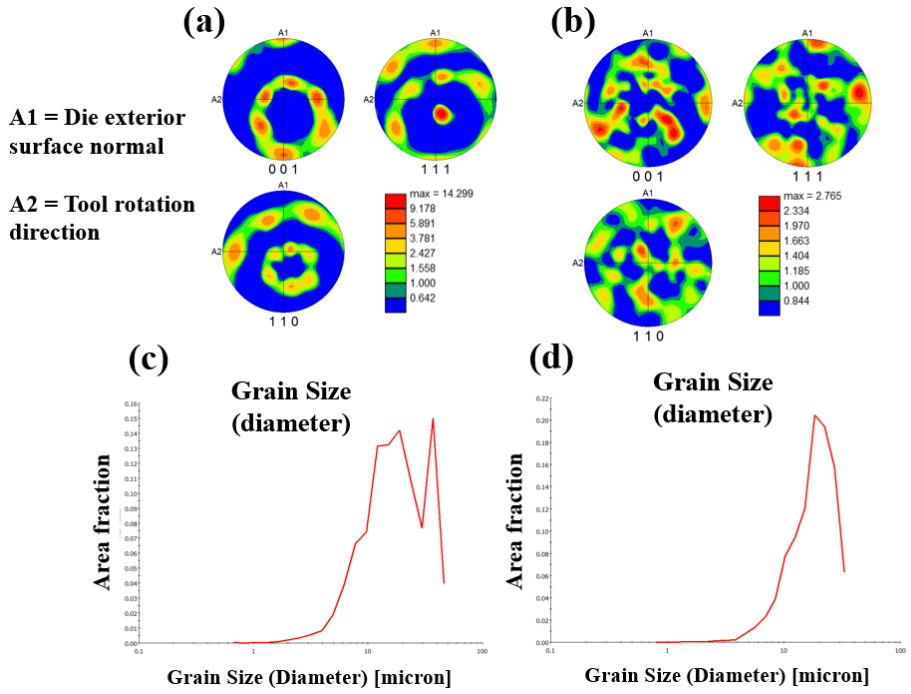


Figure 6.9: (a) Texture plots for IPF maps in 6.8(c), (b) texture plots for IPF maps in 6.8(d), (c) grain size distribution and area fraction for IPF maps in 6.8(c), and (d) rain size distribution and area fraction for IPF maps in 6.8(d)

Figure 6.8 represents EBSD IPF maps for 6061 aluminum deposition on SS304. Figure 6.8(a) shows the 6061-aluminum alloy coarse grains for the base material with grain size between 90 and 170 µm. Figure 6.8(b) represents the IPF triangle. The EBSD scan collected at the top layer mid-thickness (location (i) in L5 shown in Figure 6.7a), shows uniformly distributed equiaxed grains with an average grain size of around 11 µm in Figure 6.8(c) compared to around 130 µm diameter grains shown in Figure 6.8(a). Corresponding pole figures in Figure 6.9(a) show a strong texture, which can be attributed to the low heating rate associated with the friction processing of aluminum 6061 alloys [4]. Figure 6.8(d) shows the grain distribution IPF collected at the first layer (adjacent to the SS304 substrate, location (ii) in L1 shown in Figure 6.7a) mid-thickness with an average grain size of 18 µm and a weak texture (Figure 6.9(b)). It is interesting to note here that there is a slight increase in average grain size from L5 to L1. 6061 aluminum alloys' grain growth is highly driven by the heating cycles around the recrystallization temperature and the grain size increases with temperature [16-18]. Such a noticeable increment in grain size can be attributed to the higher heat associated with frictionally heating the steel substrate during the first layer (L1) of deposition, which does not happen during the last layer (L5) deposition.

Figure 6.10(a-e) further represents the bonding strength assessment steps using small-scale tensile coupons. Tensile coupons were carefully machined using an Electrical Discharge Machining (EDM) such that the gauge length comprises equal lengths of the substrate and deposited aluminum 6061 layers, as shown in Figures 6.10(b) and 6.10(d). These tensile coupons were then subjected to uniaxial tensile loading, and the corresponding stress-strain response is presented in Figure 6.10(e). As can be seen from Figure 6.10(e), sample-1 follows an initial sudden drop in stress after reaching the peak stress. Samples 2 and 3 follow a prolonged flattened plateau of load drop with respect to the strain axis indicating delayed failure of the tensile coupons after

reaching the peak stresses. It can be further observed from Figure 6.10(e) that none of the samples showed an immediate and sharp drop in load vertically. This implies that there was a significant amount of elongation before the final failure of the samples.

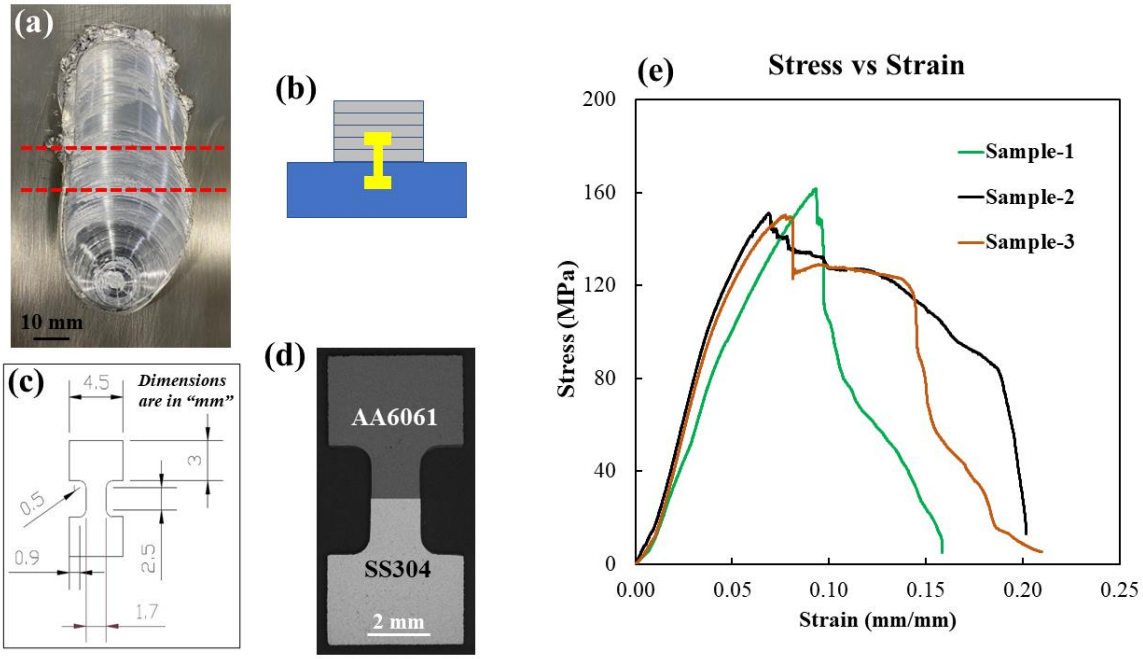


Figure 6.10: (a) dotted lines showing the location for mini-tensile sample machining, (b) configuration of the mini-tensile sample extraction, (c) dimensions for the mini-tensile samples, (d) physical sample after EDM machining and surface cleaning, and (e) stress-strain curves obtained after tensile testing

This phenomenon can be further confirmed by material failure at the aluminum 6061 alloy side presented in Figures 6.11(a) and 6.11(b). As shown in Figure 6.11(a), there is an apparent necking and gauge width reduction in the aluminum side of the tensile sample, corresponding to the flattened plateau shown for sample 2 in Figure 6.10(e). Respective ductile failure features from the necking region in Figure 6.11(a) are shown in Figure 6.11(c) depicting broken dimpled structures. The density of these broken dimpled features is significantly uniform and homogeneous indicating a well-homogenized friction extrusion deposited material volume, typically an indication of wrought microstructure [4,3].

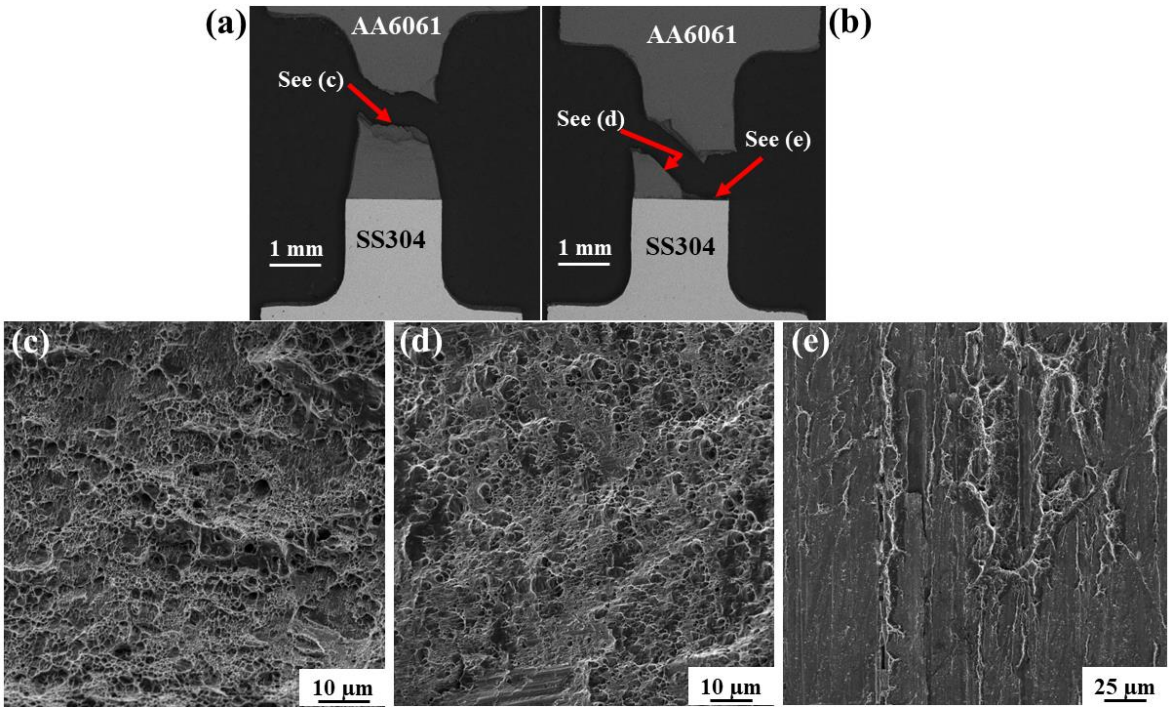


Figure 6.11: Post-tensile failure features of mini-tensile samples: (a) and (b) SEM images showing global failure features, (c) local ductile failure features indicated in (a), (d), ductile and shear failure features indicated at aluminum side in (b), and (e) residual 6061 aluminum alloy on SS304 indicated in (b)

On the other hand, Figure 6.11(b) represents a progressive failure starting at the AA6061/SS304 interfacial location at the right end of the gauge width and traversing interfacially before transitioning into the aluminum 6061 alloy side for final shear mode failure. Such a progressive failure conforms adequately with the stress-strain curve shown for sample 3 in Figure 6.10(e) before the final sample failure regime. A detailed look at the significant amount of residual aluminum on the SS304 surface shown in Figure 6.11(e) further indicates that the crack must initiate at the aluminum 6061 alloy side. Once the crack is initiated at the softer material (AA6061) side, it propagates along the interface through the aluminum alloy until the loading branch is weakened significantly (reaches up to half gauge width). From that point, it proceeds with the shear dominant route, and the final failure takes place along almost 45° shear and ductile failure mode. The ductile failure mode can be further confirmed by the sheared dimpled and ductile failure features shown in Figure 6.11(d).

Aluminum alloy has a much higher SFE value ranging above 150 mJ m^{-2} [13,16]. With such a high SFE, the dislocation movements are easily facilitated by the shear deformation caused by the friction extrusion deposition process, and homogeneous equiaxed grain refinement can easily occur compared to SS316. This can be evidently seen from Figures 6.7(b) and 6.7(c) with uniform grain refinement both at the first layer (L1) and at the last layer (L5) of aluminum 6061 alloy deposition on the SS304 substrate. The top layer (L1), however, shows a stronger texture compared to the bottom layer (L5) of aluminum 6061 deposition on SS304 due to a high fraction of low-angle grain boundaries form in the last deposited layer (L5) and repetition of multi-layer deposition weakened the texture of the first deposited layer (L1) as described by Liu et al [4].

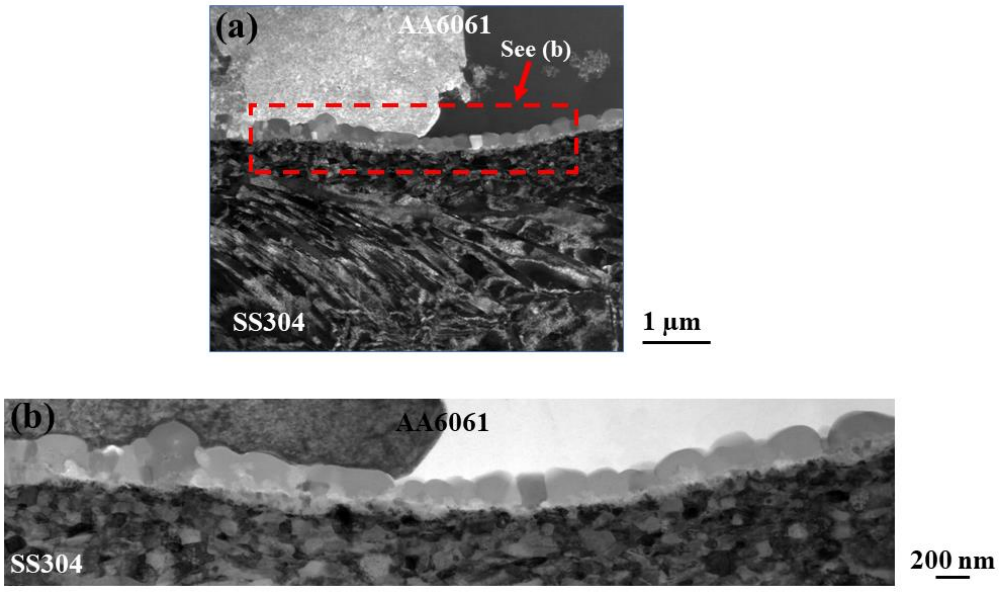


Figure 6.12: (a) TEM dark field image taken at the location (iii) shown in Figure 6.7(e), showing the interface between aluminum alloy 6061 and SS304 with small grains, reaction zone, and distorted crystals on SS304 side, and (b) detailed view of reaction zone indicated in (a)

For the case of aluminum 6061 deposition on SS304 to develop a dissimilar material interface, a noteworthy phenomenon can be further illustrated using TEM dark-field (Figure 6.12a) and bright-field (Figure 6.12b) images taken at the interface before tensile testing of AA6061 deposition on SS304 (location (iii) in Figure 6.7e). A continuous horizontal stacking of spherical

nodules with overlapping regions can be seen at the interface between aluminum alloy 6061 and SS304, shown in Figure 6.12(a), and can be more clearly seen in Figure 6.12(b) at a higher magnification image. Liu et al [8,9] have identified similar features during 6061 aluminum alloy friction stir additive manufacturing (FSAM) with SS304 and defined this to be a reaction zone where nanoscale shear localization takes place. Since the deposited aluminum 6061 material had undergone a significant amount of grain refinement, two distinct grains adjacent to each other can be seen situated immediately above this reaction zone. There is some evidence of crystallographic distortions on the SS304 side (Figure 6.12a), which can be attributed to the initial frictional processing necessary for the interfacial bonding between aluminum 6061 and SS304 to take place [8,9].

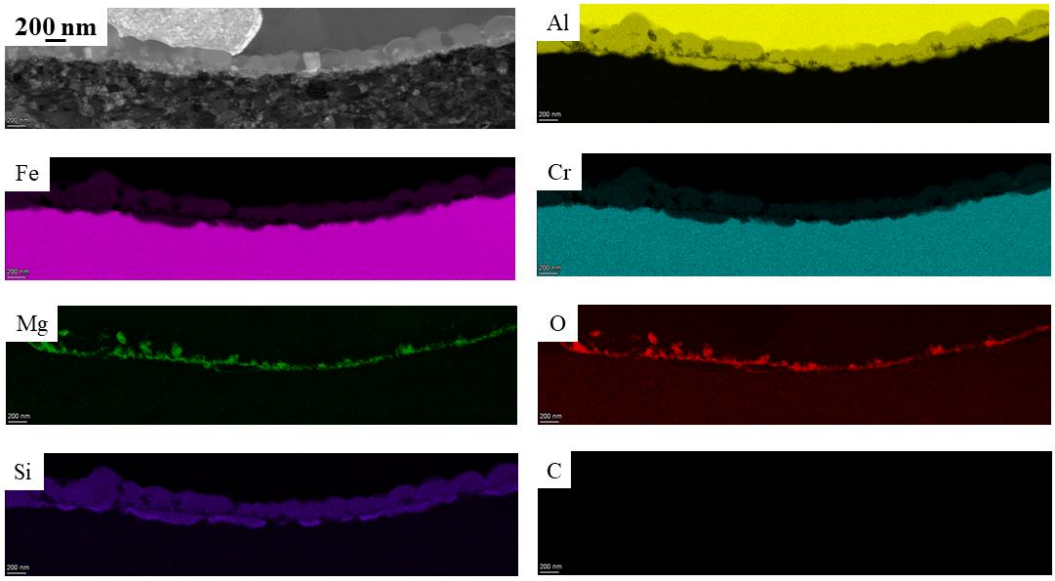


Figure 6.13: Elemental distribution across the reaction zone developed between aluminum 6061 ally and SS304 during AFED

To identify the chemical composition of the reaction zone described above, elemental analysis was performed for the area shown in Figure 6.12(b) and elemental distribution is shown in Figure 6.13 at the reaction zone between aluminum 6061 alloy and SS304. It can be observed from the concentrations of alloying elements at the reaction zone that Si has concentrated strongly,

and a partial width of Mg and O are distributed at the SS304 faying surface compared to Cr, which is very minute. The base alloying elements of Al and Fe can be seen forming a reaction zone with Si as the dominant alloying element with the graded distribution of Mg and O at the SS304 surface. Based on these observations, the reaction zone is not in the form of a dominant intermetallic composition of Al and Fe alone [9] and has a significant amount of Si, Mg, O, and a trace amount of Cr in the reaction zone.

Liu et al. [9] have provided an in-depth discussion about the mechanisms associated with the formation of an amorphous phase at the 6061 aluminum alloy and 304 stainless steel interface under friction stir additive manufacturing using nanoscale shear localization induced amorphization (NSLIAA). The NSLIAA process involves a rapid shear localization-induced pre-melting and suppression of the atomic diffusion process as a result of a high shear strain rate in the order of 10^9 s^{-1}. The present process follows the same principle, except that the aluminum alloy has been processed to soften first and deposit on the SS304 under localized shear deformation. Based on the rationales presented by Liu et al. [8,9], such a reaction zone must contain ordered short-range structures that cannot be defined as IMCs (IMCs are dominantly in the form of crystalline structures) and must be in the form of an amorphous phase with some degree of nano-crystalline precipitates. A detailed TEM analysis of such a reaction zone is beyond the scope of this dissertation research work.

6.3 Summary

Using a two-step friction extrusion deposition process (SoftTouch AM^{TM}) recently invented by Liu et al. [4], a single layer of SS316 and five layers of aluminum 6061 alloy were deposited on carbon steel AISI1018 and SS304 substrates, respectively. Three-point bending and micro tensile testing confirmed robustly bonded SS316/AISI1018 and AA6061/SS304 dissimilar

material interfaces. Severe plastic deformation was achieved during the AFED processing, and more than an order of magnitude grain size reduction with a significant amount of grain refinement was achieved. On the other hand, a nanoscale reaction zone was observed with multi-element (Al, Fe, Si, Mg, O, and a trace amount of Cr) distributions, and corresponding failure modes in tensile loading were found to be ductile and not brittle, indicating suppression of IMCs. Nanoscale shear localization-induced alloy amorphization (NSLIAA) [8,9] was found to be a dominating mechanism for generating nanoscale reaction zones and suppression of IMCs.

AFED has proven to utilize off-the-shelf metallic feedstock without any special feedstock preparation and has shown strong potential to be utilized as an alternative solid-state additive manufacturing technology. Current research has further demonstrated the dissimilar material and multi-material additive manufacturing capabilities intended for future industrial, energy, and sustainability applications via advanced manufacturing.

References

[1] DebRoy T, Wei HL, Zuback JS, Mukherjee T, Elmer JW, Milewski JO, et al. Additive manufacturing of metallic components – Process, structure and properties. Prog Mater Sci 2018;92:112–224. https://doi.org/10.1016/j.pmatsci.2017.10.001.

[2] Wu S, Dong P. Modeling of distributed defects and a proposed fatigue interaction criterion for additively manufactured metal parts. Int J Press Vessel Pip 2023;206:105048. https://doi.org/10.1016/j.ijpvp.2023.105048.

[3] Shao J, Samaei A, Xue T, Xie X, Guo S, Cao J, et al. Additive friction stir deposition of metallic materials: Process, structure and properties. Mater Des 2023;234:112356. https://doi.org/10.1016/j.matdes.2023.112356.

[4] Liu F, Dong P, Khan AS, Zhang Y, Cheng R. 3D printing of fine-grained aluminum alloys through extrusion-based additive manufacturing: Microstructure and property characterization. J Mater Sci Technol 2022. https://doi.org/10.1016/J.JMST.2022.08.017.

[5] Shushan SM, Charles EA, Congleton J. The environment assisted cracking of diffusion bonded stainless to carbon steel joints in an aqueous chloride solution. Corros Sci 1996;38:673–86. https://doi.org/10.1016/0010-938X(96)00158-8.

[6] Govardhan D, Kumar ACS, Murti KGK, Madhusudhan Reddy G. Characterization of austenitic stainless steel friction surfaced deposit over low carbon steel. Mater Des 2012;36:206–14. https://doi.org/10.1016/j.matdes.2011.07.040.

[7] Sundaresan S. Metallurgy of welding stainless steels. Adv Mater Res 2013;794:274–88. https://doi.org/10.4028/www.scientific.net/AMR.794.274.

[8] Liu FC, Dong P. From thick intermetallic to nanoscale amorphous phase at Al-Fe joint interface: roles of friction stir welding conditions. Scr Mater 2021;191:167–72. https://doi.org/10.1016/j.scriptamat.2020.09.031.

[9] Liu FC, Dong P, Khan AS, Sun K, Lu W, Taub A, et al. Amorphous interfacial microstructure and high bonding strength in Al-Fe bimetallic components enabled by a large-area solid-state additive manufacturing technique. J Mater Process Technol 2022;308. https://doi.org/10.1016/j.jmatprotec.2022.117721.

[10] Agrawal P, Haridas RS, Yadav S, Thapliyal S, Dhal A, Mishra RS. Additive friction stir deposition of SS316: Effect of process parameters on microstructure evolution. Mater Charact 2023;195:112470. https://doi.org/10.1016/j.matchar.2022.112470.

[11] Pei X, Dong P. An improved friction stir shear localization model and applications in understanding weld formation process in alloy Ti-6-4. Int J Adv Manuf Technol 2018;95:3549–62. https://doi.org/10.1007/s00170-017-1467-7.

[12] Pei X, Dong P. A selectively-coupled shear localization model for friction stir welding process window estimation. Int J Mach Tools Manuf 2017;123:89–104. https://doi.org/10.1016/j.ijmachtools.2017.08.003.

[13] Sarma VS, Wang J, Jian WW, Kauffmann A, Conrad H, Freudenberger J, et al. Role of stacking fault energy in strengthening due to cryo-deformation of FCC metals. Mater Sci Eng A 2010;527:7624–30. https://doi.org/10.1016/j.msea.2010.08.015.

[14] Molnár D, Sun X, Lu S, Li W, Engberg G, Vitos L. Effect of temperature on the stacking fault energy and deformation behaviour in 316L austenitic stainless steel. Mater Sci Eng A 2019;759:490–7. https://doi.org/10.1016/j.msea.2019.05.079.

[15] Lu J, Hultman L, Holmström E, Antonsson KH, Grehk M, Li W, et al. Stacking fault energies in austenitic stainless steels. Acta Mater 2016;111:39–46.

https://doi.org/10.1016/j.actamat.2016.03.042.
[16] Mishra RS, Ma ZY. Friction stir welding and processing. Mater Sci Eng R Reports 2005;50:1–78. https://doi.org/10.1016/j.mser.2005.07.001.
[17] Huda Z, Zaharinie T. Kinetics of grain growth in 2024-T3: An aerospace aluminum alloy. J Alloys Compd 2009;478:128–32. https://doi.org/10.1016/j.jallcom.2008.11.071.
[18] Wu Q, Li J, Long L, Liu L. Simulating the effect of temperature gradient on grain growth of 6061-T6 aluminum alloy via Monte Carlo Potts algorithm. C - Comput Model Eng Sci 2021;129:99–116. https://doi.org/10.32604/cmes.2021.015669.

Chapter 7 Conclusions

7.1 Key Research Findings

In this dissertation, robust, and repeatable solid-state advanced joining and additive manufacturing methods have been investigated by solving fundamental material incompatibility issues between dissimilar materials. These methods are highly translational for industrial and structural joint development and solid-state dissimilar material large-area additive manufacturing at a higher deposition rate compared to conventional and fusion-based manufacturing. These objectives were achieved by following four major steps and key contributions and conclusions in each of the major areas are as follows:

1) **Direct method for direct joining polymer composite to metal and underlying bonding mechanisms.**
    a) A reliable joining between aluminum alloy 6061 (AA6061) and glass fiber reinforced polypropylene composite (GFRP-PP), which was traditionally not accomplished without special surface or material modifications, was successfully achieved through a simple functional group seeding technique using a Nylon or polyamide-6 (PA6) thin film. The Nylon thin film enabled the joining and provided a joint stronger than the base material compared to a no-joining scenario. It is further intended to enable the use of polypropylene-type non-polar polymer composites directly in conjunction with metallic materials.

b) Local temperature and local pressure are the most important factors governing the metal-to-polymer direct joining. They are responsible for locally melting the polymer to chemically interact with the metal surface directly, governing the bonding, and determining the overall joint load capacity.

c) The application of Nylon provided the necessary interfacial bridging between the non-joinable aluminum alloy 6061 and the glass fiber-reinforced polypropylene composite sheets. The interfacial bonding mechanisms observed were attributed to:

    i. Direct bonding between the aluminum sheet and Nylon (resulting from Nylon film) through previously proven carbon-oxygen-aluminum (C-O-Al) type chemical bonding and,

    ii. The formation of a strong multi-material composite network of Nylon, glass fibers, and polypropylene matrix, leading to a strong aluminum alloy 6061 and glass fiber reinforced polypropylene joint.

d) Metal-to-polymer direct joining has proven to be applicable directly in conjunction with metallic materials, enabling applications of metal-polymer hybrid joints for structural and non-structural applications for achieving lightweighting goals.

2) Direct method for direct joining between dissimilar metals and underlying bonding mechanisms.

a) The nanoscale shear localization-induced alloy amorphization (NSLIAA), previously discovered, was successfully reproduced for direct spot-joining of thin aluminum alloy (AA6061-T6) to thin stainless steel (SS316) substrates without noticeable intermetallic compounds (IMCs). This further proved the robustness of the NSLIAA process for potentially a broad application in the direct joining of incompatible metals.

b) A continuous amorphous dominant reaction zone was observed at the bimetallic joining interface, consisting of an Mg and O-rich layer adjacent to the steel faying surface in combination with an Al-Fe-Si amorphous phase. The continuous reaction zone was attributed to the high shear strain rate combined with the cooling rate effect observed for the spot joining configuration and high shear strain rate dominant material pre-melting at the joining interface.

c) The resulting bimetallic spot joints showed no degradation in joint strengths, nor any change in failure mode after being subjected to a full automotive-grade corrosion test cycle. The continuous and homogeneous amorphous reaction zone was found to restrict the electrolytic ion penetration at the joining interface and was found to have a barrier effect under the automotive corrosion cycling conditions.

d) The good corrosion resistance thus observed in the Al/Steel joints investigated was attributed to the amorphous phase at the joining interface. The results suggested that the NSLIAA process has a strong potential for enabling direct joining between incompatible metals to achieve structural lightweighting for applications in severe and harsh environmental conditions.

3) Characterize bond quality and joint properties.

a) Metal-to-polypropylene composite and aluminum-to-steel directly bonded interface was assessed using lap shear tensile testing, and the joint failure loads were recorded as 11.52 kN and 1.80 kN, respectively.

b) A simple load/area (P/A) based nominal stress as bonding strength, often used in the literature, was found to be ineffective as it accounts for only the membrane stress and

does not account for the bending stress associated with the inherent local bending moment induced by eccentricity present in the joints.

c) To address the bending stress present in the joints, a preliminary case study was performed using a mechanics-based mesh-insensitive structural stress method. A widely adopted "membrane and bending stress interaction diagram" provided by ASME BP&V code Section VIII Division 2, which is based on a plastic limit solution, was further used to validate the results.

d) The joint strengths calculated by the structural stress methods fell well within the bounds provided by the interaction diagram, further justifying the guidelines for CAE designers to use the structural stress-based methods for joint strength calculations and adoption in industrial applications for directly bonded joints.

4) Novel solid-state dissimilar metal additive manufacturing.

a) An extrusion-based solid-state SoftTouch/Additive Friction Extrusion Deposition (AFED) process that can build dense metal of complex structural forms in an open-air environment using off-the-shelf metal rods as feedstock was conceptualized, developed, and demonstrated to deposit aluminum alloy and stainless steel both under similar material and dissimilar material combinatorial systems additively. Such an additive manufacturing system avoids pricy powder materials and is fully capable of utilizing various types of off-the-shelf feedstock designs without any special material treatment, showing strong potential for future sustainability through solid-state additive manufacturing.

b) The bulk 6061 aluminum alloy was first deposited on the 6061 aluminum alloy substrate to investigate the feasibility of the AFED process and systems. The ultimate

tensile strength (UTS) and ductility of AFED layers were comparable to the wrought 6061 aluminum alloy after the same T6 heat treatment. Utilizing the knowledge gained for depositing 6061 aluminum alloy on 6061 aluminum alloy substrates, a design of experiment (DOE) was carried out to deposit stainless steel on mild steel substrate for corrosion and wear-resistant cladding operation intended for applications in light water reactor (LWR) in-situ repair and aluminum alloy on stainless steel substrate for structural lightweighting purposes.

c) The process parameters developed for dissimilar material deposition provided an in-depth understanding of AFED process initiation and the importance of pre-heating time for dissimilar material systems, especially for ferrous-based materials. The feedstock metal was softened by severe plastic deformation-induced grain refinement at elevated temperatures prior to deposition, enabling low compression pressure in the previously deposited layer during the additive manufacturing process and eliminating substrate instability concerns.

d) Microstructure analysis revealed that stainless steel and aluminum alloy underwent a significant amount of grain refinement, and the grain size was reduced by more than an order of magnitude below the bulk melting temperatures of the materials. Bond-line analysis revealed that the deposited layer of feedstock materials (aluminum alloy and stainless steel) makes intimate void-free bonding and doesn't show any signs of microscopic or solidification-induced defects at the microscopic scale. The similar material deposition of 6061 aluminum alloy showed strong inter-layer adhesion without any signs of delamination. The stainless-steel deposition layer bonded with the mild steel substrate by inter-penetration of the respective material matrix. The bond

line analysis of aluminum deposition on stainless steel revealed nanoscale shear localization induced amorphization and thick reaction zone between Fe and Al matrix different than typical intermetallic compounds (IMCs) of Al and Fe materials.

e) Mechanical testing to analyze the bonding strength revealed that a similar material deposition of 6061 aluminum alloy had a strongly bonded inter-layer bonding strength, and the Z-direction (build direction) tensile strength was equivalent to the longitudinal (X) or lateral (Y) direction tensile strength. The dissimilar material stainless steel 316/carbon steel 1018 (SS316/AISI1018) interface does not crack or open under a severe three-point bending test, indicating an intimately bonded interface. Micro-tensile testing of the aluminum alloy 6061/stainless steel 304 (AA6061/SS304) material system revealed well-formed ductile failure features in the aluminum matrix, indicating stronger and more robust interfacial bonding compared to the bulk of 6061 aluminum alloy deposited layers.

f) Dissimilar material deposition through AFED thus can be optimized by improved design and process parameter control for structural applications such as corrosion and wear-resistant cladding, to avoid stress corrosion cracking during crack repairs in pressure vessels, light water reactors, underwater marine pipe applications, and structural lightweighting.

7.2 Contributions to Existing Body of Knowledge and Broad Impacts

1) Proposed a new carbon-oxygen-metal (C-O-M) type covalent bond formation mechanism between non-polar polypropylene composite and metals through an intermediary functional layer. It is intended to serve as a guiding principle for achieving metal-to-

polymer direct bonding by leveraging in-situ functionalities in incompatible material systems for various structural and non-structural applications.

2) It was discovered that if the amorphous phase is present at the Al/Steel joining interface, then the electrolytic ions from the corrosive media cannot penetrate the amorphous phase as they occur through the grain boundaries in crystalline intermetallic compounds. It is further intended to develop corrosion-resistant multi-material systems and novel corrosion-resistant coating processes, material morphologies, and material systems.
3) Developed novel SoftTouch AM^{TM} process concepts and laboratory implementation for consistent solid-state deposition of aluminum to aluminum, aluminum to stainless steel, carbon steel to carbon steel, and stainless steel to carbon steel, which potentially offers rapid large-area deposition of similar and dissimilar material systems.
4) Introduced a novel modular multi-material insert die design and rotational stability requirements in the additive friction extrusion deposition (AFED) AM or SoftTouch AM^{TM} system for achieving consistent solid-state deposition of aluminum and steel materials.
5) Conceptualized, developed, and validated effective nozzle cooling strategies, including an efficient underwater submerged continuous carbon steel deposition platform using the University of Michigan's in-house resources. It is intended to further develop, mature, and optimize a controlled and steady-state stainless steel deposition framework underwater with enhanced heat dissipation capabilities.

7.3 Future Work

1) **Process parameter optimization platform for dissimilar material direct joining**

Based on the fundamental joining mechanisms established in this dissertation research work, a correlation among the material melting temperature, surface conditions of the

joining surfaces, material chemistry and process parameters to achieve a strong joint was observed. Hence a robust process optimization platform for dissimilar material direct joining needs to be developed utilizing these variables of consideration. Such a platform can benefit more from specific industrial material, joint property, and service condition requirements for tailored structural applications.

2) **Joint mechanical property and fatigue life evaluation of directly bonded joints**

With the advent of electrical vehicles, there is a significant demand for dissimilar material direct joining for structural lightweighting. To effectively transfer the properties to CAE designers for better design, optimization, and implementation of the structural components for intended applications, a mechanics-based joint property evaluation must first be developed. Once that's established, a robust fatigue life evaluation process can further provide more realistic measures to develop the joints for various service conditions and final structural applications.

3) **Optimized nozzle material and cooling system for AFED system**

Additive friction extrusion deposition (AFED) is a novel solid-state additive manufacturing method that requires a robust system design for the 3D printing nozzle, tooling material corresponding to the feedstock material, and cooling systems for effective implementation. A multi-physics-based system modeling approach can further reduce the design time and provide a strong material and part design and selection matrix for various types of feedstock materials and deposition requirements.

4) **Steady-state AFED process development for ferrous materials**

Ferrous materials are of the utmost importance for nuclear power generation equipment repair, corrosion and wear resistance cladding, and other structural applications. A due

effort should be invested in developing steady-state process parameters for AFED of iron-based metallic alloys based on the process initiation established in the current research work.

5) **Characterize residual stress state in dissimilar AFED process**

Although AFED imparts a significantly small amount of compressive force on the substrate, it certainly frictional heats the substrate and previously deposited layers. Since this heating leads to temperatures slightly below the melting points of the substrate and deposited materials, particularly when dealing with dissimilar metal deposition, both the residual stress development process and the final residual stress state can be rather complex. Their effects on both additive manufacturability and final product performance must be addressed, particularly for safety-critical applications.